UNIVERSITY OF CALIFORNIA,
IRVINE

Nanoscale Systems for Conversion of Light into Chemical Fuels and Localized Electric Fields

DISSERTATION

submitted in partial satisfaction of the requirements
for the degree of

DOCTOR OF PHILOSOPHY

in Chemistry

by

Yash Gargasya

Dissertation Committee:
Professor Matthew D. Law, Chair
Distinguished Professor Robert M. Corn
Professor Erik Potma

2022

DEDICATION

To

My family and friends

TABLE OF CONTENTS

Page

LIST OF FIGURES iv

LIST OF TABLES v

ACKNOWLEDGEMENTS vi

VITA vii

ABSTRACT OF THE DISSERTATION viii

Contents

1. Introduction 1

1.1. Conversion of light into fuel 1

1.1.1. Availability of solar energy 1

1.1.2. Solar fuels: a true terawatt-scale solution 2

1.1.3. Strategies for water splitting 4

1.1.4. Single absorber system 6

1.1.5. Potential for D4 strategy 8

1.1.6. Stability of semiconductors in corrosive electrolytes 9

1.1.7. Requirements for potential photoanode 9

1.1.8. Manganese vanadate 9

1.1.9. Screening of other ternary metal oxides 10

1.2. Conversion of light into heat and field 11

1.2.1. Plasmon and localized surface plasmon resonance (LSPR) 11

1.2.2. Factors affecting LSPR 13

1.2.3. LSPR dynamics 17

1.2.4. Modelling of SPR 19

1.2.5. Application of LSPR 21

2. Evaluation of nanostructured β-Mn2V2O7 thin films as photoanodes for photoelectrochemical water oxidation 24

2.1. Introduction 25

2.2. Results and Discussion 27

2.2.1. Film fabrication and characterization 27
2.2.2. Film stability in different solutions 35
2.2.3. Behavior of β-MVO films at pH 13 38
2.2.4. Femtosecond transient absorption spectroscopy 42
2.3. Conclusions 47
2.4. Experimental 48
3. Screening of other ternary metal oxides thin films as potential photoanodes for photoelectrochemical water oxidation 54
3.1. Introduction 55
3.2. Bismuth oxyiodide (BiOI) 55
3.2.1. Electrochemical deposition of BiOI 55
3.2.2. Thermal stability of BiOI 59
3.2.3. Optical properties of BiOI thin films 61
3.2.4. XPS studies of film surface 61
3.2.5. Photoelectrochemical and photochemical properties 64
3.2.6. Stability status 66
3.2.7. Conclusion 67
3.3. Bismuth Ferrite ($BiFeO_3$) 68
3.3.1. Film fabrication and characterization 68
3.3.2. Optical properties and band gap tuning 69
3.3.3. Stability and device testing 71
3.3.4. Conclusion 72
3.4. Iron tungstate ($FeWO_4$) 73
3.4.1. Film fabrication and characterization 73
3.4.2. Optical properties 75
3.4.3. PEC device testing 76
3.4.4. Conclusion 77
4. Deterministic Dimerization of Gold Nanoparticles for Precision Plasmonics 78
4.1. Main idea 79
4.2. Gold nanocrystal synthesis 81
4.2.1. Citrate capped gold nanocrystals 81
4.2.2. HEGDT concentration effect 83
4.2.3. Thiol cocktail effect 84

4.2.4. pH effect 86
4.3. Passivation chemistries 90
4.4. Thiol ene click chemistry 91
4.4.1. Passivation chemistry at room temperature 92
4.5. Silica growth on gold surface 93
4.5.1. Preparation of $Au@SiO_2$ NPs 95
4.5.2. Analysis of *in-situ* UV Vis spectra 95
4.5.3. Kinetics analysis of $Au@SiO_2$ NP formation 98
4.5.4. Time dependance of silica growth 102
4.6. Temperature accelerated passivation 104
4.6.1. Click chemistry led passivation 105
4.6.2. Silica growth led passivation 107
4.7. Illumination accelerated passivation 108
4.8. Outstanding challenges 109
4.9. Experimental 110
Appendix 1 (A1) 112
Appendix 2 (A2) 146
Appendix 3 (A3) 147
Bibliography 158

LIST OF FIGURES

Page

Figure 1.1 Global energy demand..... 2
Figure 1.2 Spectral irradiance of sunlight..... 4
Figure 1.3 Schematic of material components of suspended particle reactors 6
Figure 1.4 Working of photoelectrochemical water splitting device with a nanostructured single absorber n-type semiconductor electrode. 7
Figure1.5 Graphical illustration of a plasmon. 12

Figure 2.1 Characterization of nanostructured MVO thin films on FTO-coated glass substrates 28
Figure 2.2 Absorptivity spectra and Tauc-style plots for MVO films on quartz substrates.. 31
Figure 2.3 Aqueous photoelectrochemical measurements..... 33
Figure 2.4 Chemical stability of MVO films in various aqueous solutions in the dark and without applied bias. 36
Figure 2.5 Chemical stability of MVO films in pH 13 NaOH solution in the absence of applied bias and light.. 41
Figure 2.6 Transient absorption spectra. 43

Figure 3.1 Electrodeposition of bismuth oxyiodide (BiOI). 57
Figure 3.2 Crystal properties of BiOI.. 57
Figure 3.3 Plan view SEM images of BiOI. 58
Figure 3.4 BiOI films with variable thickness. 58
Figure 3.5 Temperature effect on BiOI crystal structure.. 60
Figure 3.6 Optical properties of BiOI. 61
Figure 3.7 Chemical properties of BiOI films. 63
Figure 3.8 Photoelectrochemical properties of BiOI films. 65
Figure 3.9 Gold photo deposition on BiOI films. 66
Figure 3.10 Electrochemical stability of BiOI films.. 67
Figure 3.11 Crystal and morphological properties of bismuth ferrite films**.**. 69
Figure 3.12 Optical properties of pristine and doped BFO films..... 70
Figure 3. 13 Photoelectrochemical properties of pristine and Mn doped BFO films.). 71
Figure 3.14 Crystal and morphological properties of Iron tungstate films. 74
Figure 3.15 Optical properties of Iron tungstate films. 76
Figure 3.16 Photoelectrochemical properties of FeWO films**.**. 77

Figure 4.1 FDTD calculations for gold nanoparticle dimers. 79

Figure 4.2 Schematics of light driven gold nanoparticle dimerization Kinetics..... 80
Figure 4.3 Optical and morphological characterization of citrate capped gold nanoparticles..... 82
Figure 4.4 Gold NPs aggregation kinetics as a function of HEGDT concentration.. 83
Figure 4.5 Stability of gold NPs upon addition of MPA.. 84
Figure 4.6 Cocktail effect under 200uM net thiol concentration. 85
Figure 4.7 Cocktail effect under 20 uM net thiol concentration. 86
Figure 4.8 pH effect on aggregation rate of gold NPs with 100% HEGDT 87
Figure 4.9 pH effect with 40-60 MPA-HEGDT 88
Figure 4.10 pH effect on 50-50 MPA -HEGDT system. 88
Figure 4.11 pH effect on 75-25 MPA - HEGDT system. 89
Figure 4.12 pH effect on 90-10 MPA - HEGDT system 89
Figure 4.13 Schematic diagram of various classes of thiol ene click reactions..... 91
Figure 4.14 Ene effect at room temperature. 92
Figure 4.15 Preparation of Au@SiO2 NPs..... 95
Figure 4.16 Analysis of in situ UV–vis spectra shown for standard reaction conditions (20 ± 1 °C, 2 mM TEOS)..... 96
Figure 4.17 Kinetics analysis of Au@SiO2 NP formation. 100
Figure 4.18 Silica coating mechanism at initial stage. 103
Figure 4.19 HEGDT-DEE reaction at 80 °C 105
Figure 4.20 Aggregation profile with acrylate, cocktail, and pH effect 106
Figure 4.21 Thermal driven arrest of gold NP aggregation via silica growth on NP surface.... 107
Figure 4.22 Laser driven arrest of gold NP aggregation..... 108

LIST OF TABLES

Page

Table 1.1 Summary of different computational methods for the SPR in Au NPs. 20

Table 2.1 Electrolyte compositions used in PEC tests of standard β-MVO films 32
Table 2.2 XPS elemental quantification of films aged in various solutions for 20 hours..... 36
Table 2.3 Fitting parameters for ground state bleach (520 nm) and visible photoinduced absorption (715 nm) for dry and electrolyte-immersed β-MVO films 44

Table 3. 1 Film thickness as a function of growth current..... 146

ACKNOWLEDGEMENTS

First and foremost, I would like to thank my advisor Prof Matthew D law. I enjoyed immense intellectual freedom, received constant encouragement to try something new, and gained valuable skills regarding systematically approaching and critically analyzing scientific problems under his guidance. I am grateful to my committee members Prof Erik Potma, Prof Robert Corn, Prof Reginald Penner and Prof John Hemminger, for their constant support throughout my Ph.D. I am also grateful to other UCI faculty members like Prof Ara Apkarian, Prof Shane Ardo and Dr. Dmitry Fishman for multiple intellectually stimulating discussions that allowed me to view the scientific problem from a broader perspective.

My research work would have been incomplete without the instrumentation support provided by Irvine Materials Research Institute (IMRI), Laser Spectroscopy Laboratory (LSL), UCI NMR facility and several other research labs in the department of chemistry. In the lab, I was fortunate to work with erudite and encouraging post-doctoral fellows like Dr Darren Neo and Dr Christian Engelbrekt, and share my workspace with awesome lab mates Nima Farhi, Trenton Salk, Zhongyue Luan, Kan Fu, Julliette Micone, Alex Abelson, Caroline Qian, and Andy Yang. They made the workplace fun and welcoming.

This work has been supported by CASTL (Center for Chemistry as Space-Time Limit), UC Solar Institute (UC Multicampus Research Programs and Initiatives grant MR-15-328386), and National Science Foundation (Award number 2109067).

VITA

Yash Gargasya

2016	Integrated MSc. in chemistry
	Indian Institute of Technology, Roorkee
2022	Ph.D. in Chemistry,
	University of California, Irvine

FIELD OF STUDY

Materials chemistry for conversion of solar light into fuel, electricity, and localized electric fields.

PUBLICATIONS

Y. Gargasya, M. K. Gish, V. V. Nair, J. C. Johnson and M. Law, Evaluation of Nanostructured Manganese Vanadate (β-Mn2V2O7) thin-films for Photoelectrochemical Water Oxidation. *Chem. Mater.* 33(19), **2021**, 7743-7754

C. Engelbrekt, Y. Gargasya and M. Law, Silica Shell Growth on Vitreophobic Gold Nanoparticles Probed by Plasmon Resonance Dynamics. *J. Phys. Chem. C* **2021**, 125, 45, 25119-25125

ABSTRACT OF THE DISSERTATION

Nanoscale systems for efficient conversion of light into fuel and localized electric field

by

Yash Gargasya

Doctor of Philosophy in Chemistry

University of California, Irvine, 2022

Professor Matthew D. Law, Chair

The interaction of light and matter is at the core of many of our day-to-day technologies and life processes. Upon excitation by photons, electrons (in a material) move into a higher energy state. This electronic energy is then harnessed into electricity, fuel, heat, and localized electric fields by various devices and chemical/biochemical systems. This thesis focuses on two such applications namely - the conversion of light into chemical fuels and localized electric fields, using nanoscale systems.

The first section of this work focuses on the generation of chemical fuel – hydrogen from water upon illumination with sunlight – Photoelectrochemical (PEC) water splitting. An efficient, cost-effective, and stable photoanode is the bottleneck of this technology. Chapter 2 and 3 have been dedicated to the fabrication and crystal, morphological, chemical, optical, and photoelectrochemical characterization of nanostructured high surface area ternary metal oxide semiconductor photoanodes. Particular emphasis has been paid to the evaluation of β-$Mn_2V_2O_7$ which was recently reported as a promising photoanode material for water oxidation. Other materials like BiOI, which is interesting for its internal electric fields for charge separation, and $BiFO_3$ – for potential ferroelectricity enhanced charge separation have been covered in chapter 3.

$FeWO_4$ stands out as a promising candidate owing to its optimal bandgap and exceptional stability in both acidic and alkaline electrolytes.

The second section of this thesis deals with developing nanoscale chemical systems for converting light into localized electric fields. A nm^3 region of intense electric field is created due to plasmonic coupling when two gold nanoparticles come together to form a dimer. The hotspot generated in the gap can be utilized for single-molecule detection using surface-enhanced Raman spectroscopy (SERS). However, a simple, scalable, single-pot synthesis of gold nanocrystal dimers remains a challenge decades after the discovery of SERS. We propose a light directed synthesis of gold nanocrystal dimers in chapter 4 with four key milestones, 1) gold nanocrystal synthesis, 2) their controlled aggregation using dithiols, 3) their passivation using thiol-ene click chemistry and silica shell growth and 4) light directed aggregation arrest at the dimer stage.

1. Introduction

The interaction of matter, especially electrons, with light can happen in a variety of ways. Electrons can interact with a photon individually as a fermion or collectively as a boson. Both interactions lead to high-energy hot electrons which can be utilized, and their energy can be harnessed as either electrical energy in terms of electric potential or as chemical energy in terms of reduced chemical species, called fuels. If unharnessed at this stage, these high-energy electrons lose energy first via electron-electron scattering and later via electron-phonon coupling, thus, transferring their electronic energy into thermal energy, first to hot electronic cloud, and then as, lattice heat.

Materials and their properties can be tuned to selectively convert photon energy into electricity, fuel, heat, or localized electric fields. The first section of this thesis critically evaluates potential materials to efficiently convert solar photons into chemical fuels in a cost-effective manner. The second section of this thesis develops a single-step process for synthesizing gold nanocrystal dimers for precision plasmonics. The process exploits the efficient photon-to-heat conversion of gold nanoparticles to selectively arrest the aggregation of gold nanocrystal at the dimer stage upon their selective excitation.

1.1. Conversion of light into fuel

1.1.1. Availability of solar energy

Sun provides a staggering amount of energy to not just earth but the whole milky way. This energy powers oceanic and atmospheric currents; runs evaporation, and condensation cycles that are responsible for freshwater reserves, and is the main energy source for photosynthesis – a process that provides nutrition, directly or indirectly, to almost every species on earth. To put into

perspective, the ultimately recoverable oil reserve on earth is around 3 trillion barrels – 1.7 x 10^{22} joules of energy, something that the sun provides in less than 1.5 days.[1]

1.1.2. Solar fuels: a true terawatt-scale solution

The annual energy demand for humans for sustaining current economic growth is around 20 TWyr and is expected to grow to ~35 TWyr by 2050.[2] (Figure 1.1a) 83% of this demand is met by burning fossil fuels (figure 1.1b)[3] that leads to major carbon emission into the atmosphere. The three potential sources that can achieve the terawatt (TW) scale are 1) continued use of coal followed by carbon sequestration,[4] 2) harnessing nuclear energy, especially with breeder reactors[5], and 3) solar. Sun provides more than four orders of magnitude of it - around 12000 TW, in an hour.[6]

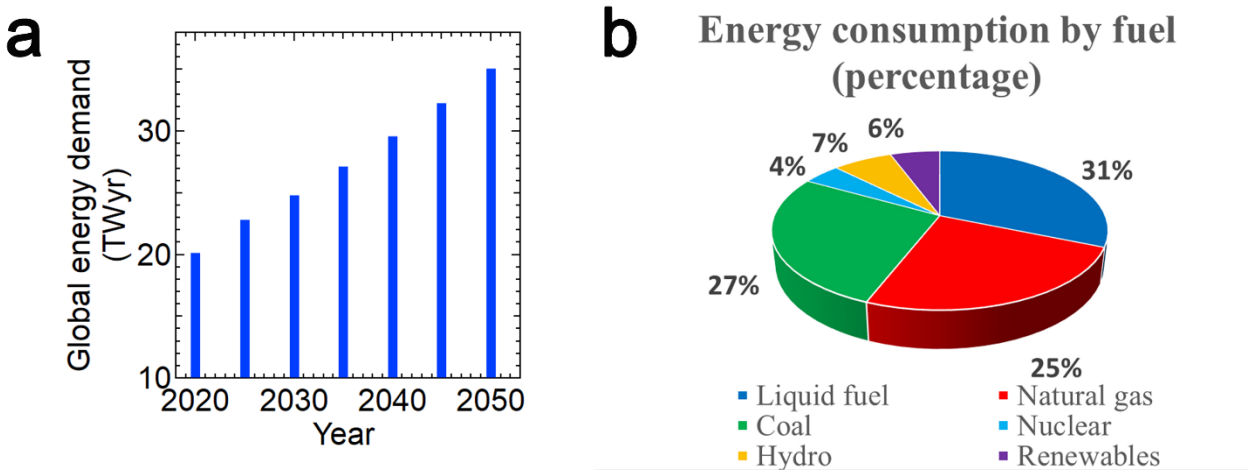

Figure 1.1 Global energy demand. a) global energy demand predicted[2] and b) share of different energy sources to meet the current demand[3]

The world energy assessment report estimates 50 - 150 years of oil reserves, 207 - 590 years of gas reserves, and 1000-2000 years of coal reserves, enough to support 25 - 30 TWyr at least for a few centuries.[6] However, this will produce a significant amount of CO_2 to levels earth hasn't experienced in last 650, 000 years. Carbon capture and storage in underground aquafers can be one possible approach. However, globally averaged CO_2 leak rates must not exceed 1% for the

timescale of centuries, else, the emitted flux will be greater than or equal to intended mitigated carbon initially.[7]

Second option is nuclear energy, especially with breeder reactors. Current Uranium reserves are enough for producing 100 TWyr, using conventional once through reactor technology. Hence if 10 TWyr is obtained by conventional fission, all the U reserves will be exhausted in 10 years. Moreover, there is a public sentiment, after Fukushima, against nuclear reactors regarding the safety.

The third approach is to use the renewable energy, especially solar, with more than enough energy falling on earth surface hourly than annual global energy demand. Two challenges with the solar are 1. its diffuse nature and 2. its intermittency. To account for the first, the material costs should be very low to make solar based technologies affordable. And to account for the second, there should be a mechanism for solar energy storage.

There are two technologies where the solar energy can be stored, 1. in batteries – as electrical energy, and 2. in chemical fuels as chemical energy. However, given the scale of the storage, poor energy density in batteries (in both per mass as well as per volume) coupled with the use of rare earth metals make them unfit for large scale energy storage, leaving chemical fuels as the only viable option if solar energy has to be made affordable.

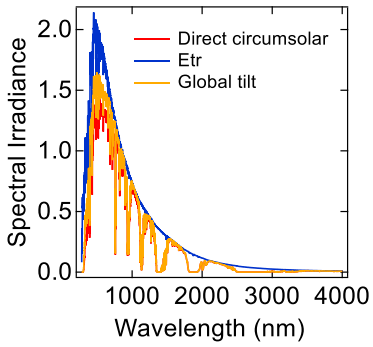

Figure 1.2 Spectral irradiance of sunlight

1.1.3. Strategies for water splitting

Given the scale of energy storage, it is important that the raw material for solar fuel is highly abundant and inexpensive to a large section of human population for good penetration and adoption of this alternate energy technology. Water covers almost 71% of earth surface and close to 70% of global population lives within 5 km of a water body.[8] This makes water an ideal raw material for solar fuels.

Water can be reduced to Hydrogen (H_2) gas. Gibbs free energy change for converting a mole of water into a mole of H_2 and 0.5 mole of O_2 is 237.3 KJ. According to Nernst equation, that converts to ΔE = 1.23 eV per electron, so the semiconductor must absorb an incoming photon with energy greater than 1.23 eV (equal to a wavelength of ~1000 nm or shorter) and convert this energy into

H_2 and O_2. This process must generate two electron-hole pairs for every H_2 molecule and four electron-hole pairs per O_2 molecule.

Currently, majority of hydrogen demand for industry is met by processes like coal gasification and methane reforming which have stayed overall cost effective compared to renewable means despite of fluctuations in the fossil fuel prices. To compete, solar hydrogen needs to be cheaper than $2 per kg.[9]

There have been largely three types of reactor designs for solar hydrogen generation. 1. PV + electrolyzer, 2. Suspended particles, and 3. Photoelectrochemical cells. Each category comes with its own challenges and advantages. The first design - PV + electrolyzer technology, is the closest to market. In this reactor design, the light absorption happens in a separate PV section that is electronically connected to an electrolyzer which carries out the electrolysis. It has the advantage of building upon the achievements of silicon photovoltaics community however, the most competitive systems and startups still lag in terms of cost effectiveness and provide a rather costly hydrogen at the rate of $7.6 per kg.[10,11]

The second reactor designs involve the use of suspended particles. Here the Light absorption and gas evolution happens on the same particle. (Figure 1.3a) Production of hydrogen and oxygen on the same particle in the same reactor provides with a challenge of post catalysis separation and the system can be potentially explosive at high performance. An electrochemically mediated tandem

water splitting system with two different semiconductors in two different bags can be one promising option.[12,13](Figure 1.3b)

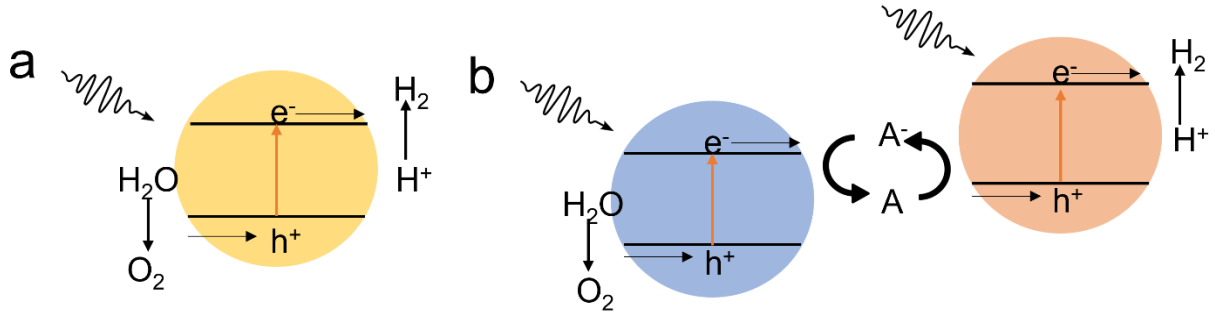

Figure 1.3 Schematic of material components of suspended particle reactors for a) single absorber and b) dual absorber.[13]

The third type of reactors, called photoelectrochemical cells (PEC), involve an optically and catalytically active semiconductor thin films which carries out two halves of the water splitting reaction on two separate electrodes, thus providing a mechanism for gas separation. (Figure 1.4) These are, in a way similar to electrochemically mediated dual particle systems with a difference that here, two sides of electrodes are connected electronically rather than electrochemically.[12] This thesis studies potential materials for this type of systems, which then, can be potentially employed in electrochemically mediated suspended particle systems as well.

1.1.4. Single absorber system

Shown in the figure 1.4 is a diagram of a single absorber photoelectrochemical cell. In a typical cell, light absorption at the semiconductor leads to generation of electrons and holes. The difference between the fermi-level of semiconductor and redox potential of electrolyte leads to the formation of a space charge region at the semiconductor-electrolyte interface resulting in development of an electric fields that facilitates the movement of minority carriers (holes in the case of n-type semiconductor as shown in the figure 1.4) towards the surface and of majority

carriers away from the surface towards the counter electrode via the back contact of working electrode. On reaching the surface, holes oxidize water to oxygen whereas electrons reduced water to hydrogen.

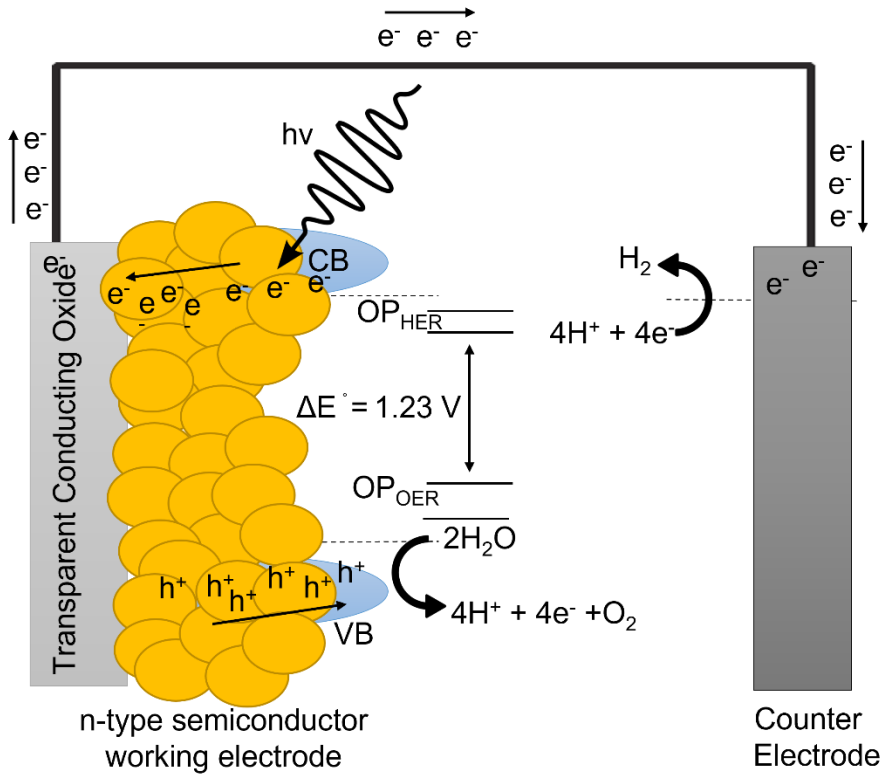

Figure 1.4 Working of photoelectrochemical water splitting device with a nanostructured single absorber n-type semiconductor electrode.

The thermodynamics requirement for splitting water is 1.23 eV, plus the kinetic overpotentials for hydrogen evolution ~ 10 meV (on platinum surface) and water oxidation ~ 300 meV (with best of OER catalysts at pH 13) and ohmic losses ~ 200 meV. The total comes about 1.83 eV which should be provided by the photovoltage generated by the semiconductor.

Assuming the charge separation and catalytic efficiency to be unity and photovoltage to be same as bandgap, the ideal and the realistic efficiency limits for a single absorber PEC cell are 30.6 5 (1.59 V bandgap) and 15.1% (2.09 eV bandgap).[14] The state of the art photoelectrochemical water

splitting semiconductor like TiO_2,[15] WO_3[16] or $BiVO_4$[17] cannot provide a 10% efficient system due to their large bandgap.

1.1.5. Potential for D4 strategy

The photovoltage generated in a semiconductor upon illumination is not equal to its band gap, rather it is the difference between quasi fermi levels for electrons and holes, respectively. It is not more than 70% for the best performing solar materials.[18] This makes carrying out unassisted water splitting with more than 10% efficiency with a single absorber nearly impossible due to lack of driving force for running all thermodynamic, kinetic and ohmic processes. Employing dual absorbers and constructing a tandem cell with D4 strategy can be one possible solution to tackle this problem. D4 stands for dual light absorber – four photons per hydrogen molecule. In a D4 strategy or z scheme, light absorption is carried out by two semiconductors with mutually complementary absorption in the solar spectrum. The optimum band gaps for the two semiconductors are 0.92 eV and 1.59 eV respectively (for a high performance realistic case) to maximize the efficiency to 28.3%.[14] In this scheme the solar spectrum first falls on the 1.59 eV band gap semiconductor leading to the absorption of electromagnetic spectrum with wavelength below 688 nm, transmitting higher wavelengths to be finally absorbed by the bottom lower band gap (0.9 eV) semiconductor. This strategy has a dual advantage of inherent charge separation and higher photovoltage as net photovoltage is the sum of the photovoltages of each light absorber. Thus a ~2 eV bandgap semiconductor comes out to be ideal (for a realistic case) for both single absorber as well as tandem water splitting cells, with Silicon as the potential bottom light absorber.

1.1.6. Stability of semiconductors in corrosive electrolytes

It is electrostatically favorable to dump a positively charged hole on a negatively charged hydroxide ion for oxidation, rather than on neutral water molecule, and to dump an electron on positively charged proton than neutral water for reduction. Moreover, electrochemical cells require decent ionic strength to be conductive and minimize ohmic losses.[19] These effects are reflective in low kinetic overpotentials for water reduction at pH 0 and for water oxidation at pH 14 and increase in overpotentials with deviation from highly acidic or alkaline conditions. This puts an extremely challenging condition for the photocatalyst to be stable in highly corrosive electrolyte solutions.

1.1.7. Requirements for potential photoanode

Given silicon as a well-established potential photocathode or bottom half for tandem cell, a promising photoanode, thus, should have a sub 2eV band gap, stability in highly alkaline solutions, and should have valence band positive of water oxidation potential of 1.23 V vs RHE. The first section of this thesis critically evaluates the nanostructured thin films of potential photoanode materials. Chapter 2 goes into an in-depth study to check the potential of β-$Mn_2V_2O_7$ as the potential photoanode material. Chapter 3 evaluate the potential of BiOI, $BiFeO_3$ and $FeWO_4$ as potential photoanode materials.

1.1.8. Manganese vanadate

β-$Mn_2V_2O_7$ was recently reported to be a promising candidate for photoelectrochemical water splitting, with a suitable bandgap and band edge positions and reasonable stability and photoactivity in preliminary tests in alkaline solution. Here, we present an in-depth evaluation of the photoelectrochemical performance and stability of phase-pure nanostructured β-$Mn_2V_2O_7$ films made by calcination of a spin-cast molecular ink. We show that β-$Mn_2V_2O_7$ dissolves in pure

water corrodes in aqueous electrolytes at pH 7 and 9, and converts to amorphous manganese (hydr)oxides within minutes at pH 13. Our β-$Mn_2V_2O_7$ films yielded only miniscule photocurrents (~μA cm^{-2}) for the oxidation of iodide, sulfite, or water and the reduction of iodate or water in borate- and phosphate-buffered electrolytes at pH 7 and 9, the oxidation of $[Fe(CN)_6]^{4-}$ or water at pH 13, and the oxidation of bromide in acetonitrile, regardless of film calcination temperature and time, film thickness, and illumination geometry. Minimal photoactivity was observed even in electrolytes in which film degradation was insignificant throughout the photoelectrochemical tests. Ultrafast transient absorption spectroscopy shows that the poor photoactivity is mainly the result of fast hole trapping and recombination at the MVO surface that leaves few free charge carriers beyond the picosecond time scale. Given its poor charge transport/extraction and chemical stability, β-$Mn_2V_2O_7$ is not a particularly promising photoanode material for solar water splitting. This work underscores the importance of careful follow-up studies of materials identified as "hits" in combinatorial materials discovery campaigns.

1.1.9. Screening of other ternary metal oxides

In chapter 3 we undertake a screening of potential photoanode materials – bismuth oxyiodide (BiOI), bismuth ferrite ($BiFeO_3$) and iron tungstate ($FeWO_4$). Bismuth oxyiodide is a ~1.9 eV bandgap (bandgap can depend on iodide content) semiconductor with layered structure. Upon illumination, an electron and hole move to two separate layers thus facilitating charge separation. Bismuth ferrite (BFO) is a 2.4 eV band gap, multiferroic, perovskite material. It shows stability in pH 13 electrolytes. It is interesting for its ferroelectricity led charge separation, defect and grain boundary mediated charge carrier conduction and bandgap tuning with substitutional doping at B sites. Iron tungstate (FeWO) is a ~2 eV (direct bandgap) semiconductor with earth abundant

elemental constituents. It can be stable in both acidic as well as alkaline solutions due to passivation by tungsten and iron oxides.

1.2. Conversion of light into heat and field

So far, we have covered semiconductor-based systems where the electron interacts individually with a photon and behaves like a fermion. However, loosely bound conduction band electrons behave like a collective in nanoparticles of coinage metals like copper, silver, and gold. Upon illumination, these excited electrons lead to localized surface fields that can be utilized for single molecule spectroscopy. These excited electrons lose their energy, first by electron – electron scattering and then, by electron phonon coupling to the lattice as heat. This illumination driven lattice heat can be utilized to accelerate chemistry selectively on the nanoparticle surface. This section delves into the phenomenon of excitation of collective oscillations called plasmons in gold nanoparticles upon illumination, the conversion of light into heat and formation of near field intense electric fields on the gold nanoparticle surface and junctions, and their utilization for Raman cross section enhancements for single molecule spectroscopy.

1.2.1. Plasmon and localized surface plasmon resonance (LSPR)

Plasmons are collective longitudinal oscillations of free elections in metal nanoparticles in resonance with a spatially and/or temporally varying external electric field, for example - light. The presence of an oscillating external electric field leads to a coherent displacement of the electronic cloud from the equilibrium position. (Figure 1.5a) The positively charged lattice exerts a restoring force pulling the electronic cloud back towards the equilibrium position displaying an antenna-like behavior.[20] Overall, it can be described as a negatively charged electron cloud

coherently oscillating about the positively charged metal lattice, similar to a mass-spring harmonic oscillator (Figure 1.5b). [21,22]

Due to a sea of loosely bound electrons in a metal, an external electric field cannot penetrate the bulk beyond the skin depth. It can, however, create propagating surface plasmon polaritons like propagating phonon polaritons due to the interaction of parallel components of an electric field to

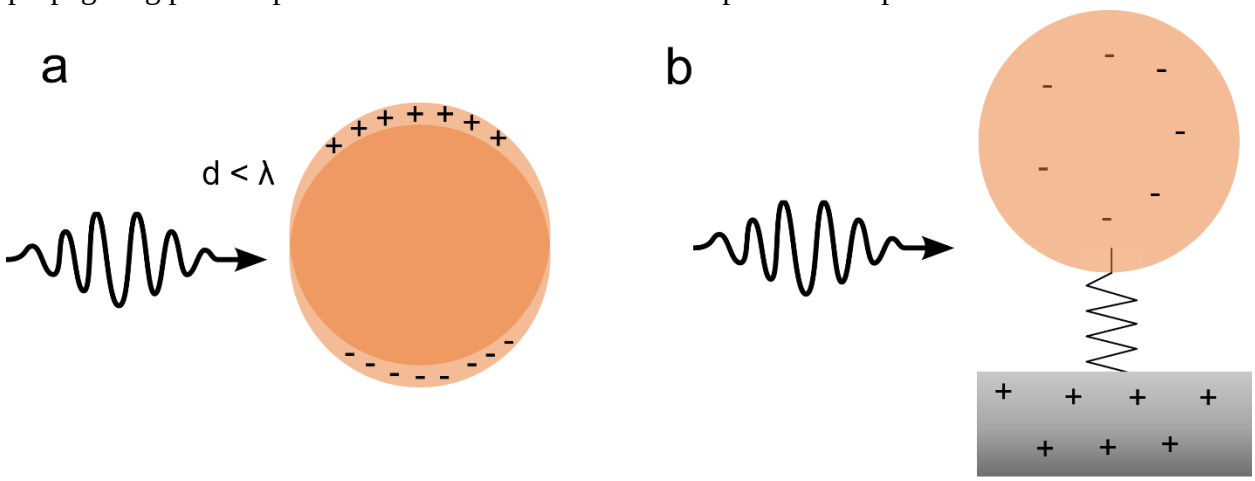

Figure1.5 Graphical illustration of a plasmon in a) a gold nanoparticle and b) comparison with mass-spring harmonic oscillator.

the metal surface. In the case of metallic nanoparticles with skin depth comparable size, light can penetrate through the whole particle and polarize the electron cloud.[22] For a nanoparticle much smaller than the wavelength of light, the phase of the oscillating external electric field is practically constant and the particle can be assumed to be in an electrostatic field – quasistatic approximation. The polarizability $\alpha(\lambda)$ in such a particle can be calculated as:

Equation 1.1 $$\alpha(\lambda) = 3\varepsilon_m(\lambda)V_{NP}\frac{\varepsilon(\lambda)-\varepsilon m(\lambda)}{\varepsilon(\lambda)+X\varepsilon m(\lambda)}$$

Where λ is light wavelength, ε_m is the dielectric constant of the non-absorbing medium, V_{NP} is the volume of the nanoparticle, X is the geometrical factor (2 for sphere), and ε is the frequency dependent complex dielectric function for the metal. And the corresponding extinction cross-section can be calculated as[23]:

Equation 1.2 $$\sigma(\lambda) = \frac{18\pi[\varepsilon m(\lambda)]^{3/2}}{\lambda} V_{NP} \frac{Im[\varepsilon(\lambda)]}{[Re[\varepsilon]+2\varepsilon m(\lambda)]^2+[Im[\varepsilon(\lambda)]]^2}$$

A few takeaways from the above equations are 1) plasmonic properties of a metal are a function of its complex dielectric function, 2) extinction cross section increases linearly with nanoparticle volume, and 3) the extinction coefficient is maximum when denominator is minimum for the SPR condition –> $Re[\varepsilon_m(\omega)] \approx -\chi\, \varepsilon_m(\omega)$.[24] The resonance frequency is predominantly decided by the dielectric function of the material but can be tuned by the dielectric constant of non-absorbing medium, nanoparticle shape, size and composition.[24] For the higher sized metal nanoparticles, light cannot uniformly excite the whole particle and this leads to higher order modes.[25]

For gold and silver nanoparticles, this resonant frequency falls in the visible region leading to the striking colors exhibited by them due to enhanced absorption and scattering.[21] Between the two, gold has a substantial Im(ε) in the visible region due to d-sp intraband transition. This transition competes with the plasmonic excitation and its resultant excited electron-hole pairs lead to enhanced electron-electron scattering and smaller plasmon lifetime. A good measure of plasmon quality can be quantified as plasmonic quality factor $Q_{SPR}(\omega) = -Re[\varepsilon]/Im[\varepsilon]$. However, it should be noted that the chemical stability of gold is much better than silver, which leads to higher volume of research on colloidal gold plasmonics.

1.2.2. Factors affecting LSPR

Following the equation 2, the LSPR can be tuned by tuning dielectric function of metal, of medium, and volume, shape and composition of the nanoparticle.

Dielectric and physical chemical environment

Non absorbing dielectric medium: for a non-absorbing medium, the imaginary component of the dielectric function for medium is non-existent. Since the $Re[\varepsilon_{Au}]$ decreases on

increasing wavelength, the SPR band should redshift on increasing ε_m and should blueshift on decreasing ε_m. Due to a very high surface to bulk atom ratio in nanoparticles, the SPR is very sensitive to the surface ligands and external environment.

Absorbing dielectric medium*:* With the complex dielectric function for the medium, the real component (refractive index) causes the spectral shift as described in the last section. The imaginary component of dielectric constant of the medium leads to absorption of photon that causes shielding effect. Shielding effect is a function of shape, size thickness and geometry of the absorbing medium. Additionally, the presence of an absorbing medium can cause a highly distance dependent plasmon quenching or enhancement effect as well, for example graphene kept in the vicinity can substantially quench the plasmon enhancement.[26,27]

Surface chemical interaction*:* Being a nanoparticle, there are relatively large number of surface atoms compared to bulk, making a plasmonic peak extremely sensitive to the adsorbed surface atoms. These surface atoms affect the plasmon is largely three ways. 1) By increasing the pure dephasing rate by introducing a new electron relaxation pathway. One of the many examples can be a coupling between the LUMO of the molecule and conduction band of the gold leading to reversible transfer of electron to and from the metal to the molecule.[28] Adsorbed molecules have also been reported to alter the surface density of states and polarizability of gold nanocrystals with thiols having stronger interface damping effects than amines.[29] 2) By formation of a non-metallic gold-ligand complex on the surface, thereby reducing the net size of metal nanoparticle.[30,31] and 3) By changing the dielectric properties of the matrix, especially the real part and shifting the plasmonic peak.[32]

Temperature: For nanoparticles embedded in solid matrix or suspended in liquid solutions, the change in dielectric properties of the matrix or structural modification in the nanoparticle induced

by local plasmonic heating drives the major changes in the LSPR. For nanospheres in air, an increase in temperature leads to the lattice dilation and a decrease in electron density. In nanocrystals, the LSPR frequency is proportional to bulk plasma frequency which, in turn, is proportional to $n_e^{1./2}$ according to the following expression from drude model.[33,34]

$$\omega_p(T) = \sqrt{\frac{e^2 n_e(T)}{m_{eff}\varepsilon_0}}$$

Where e is the electronic charge, m_{eff} the electron effective mass and ε_0 permittivity in vacuum.

An increase in temperature leads to a redshift and an LSPR broadening which means an increase in Γ_{nr} leading to higher electron scattering. The heating caused at ultrafast time scales with femtosecond pulses majorly lead to the increase in electron scattering while the steady state heating by convectional means of continuous wave laser led to higher electron phonon coupling.[34]

Nanoparticle Size

Absorption and scattering cross section: The optical extinction spectra of SPR is a sum of absorption and scattering spectra.

$$\boldsymbol{\sigma_{ext} = \sigma_{abs} + \sigma_{scat}}$$

Assuming a monodisperse gold nanoparticle colloidal solution, the transmittance T(ω) and absorbance A(ω) can be represented as following.

$$T(\omega) = \frac{I(\omega)}{I_0(\omega)} = e^{-lc\boldsymbol{\sigma_{ext}}} = e^{-lc\boldsymbol{\sigma_{abs}} + \boldsymbol{\sigma_{scat}}}$$

$$A(\omega) = -\log(e^{-lc\boldsymbol{\sigma_{abs}} + \boldsymbol{\sigma_{scat}}})$$

Here, c is the particle concentration in the colloidal solution, l is the path length, $\boldsymbol{\sigma_{abs}}$ and $\boldsymbol{\sigma_{scat}}$ are cross sections for absorption and scattering, respectively. Transmittance increases exponentially and absorbance increases linearly with the absorption cross section, which in turn is linearly dependent and particle volume and cubically dependent on particle size. (Equation 1)

Absorption and scattering scale with the third and sixth power of the particle size.[23] Hence, absorption dominates for smaller particles, however scattering starts contributing substantially to optical extinction once particle size crosses ~50 nm.

Extrinsic size effect: Quasistatic approximation of Mie theory holds as long as the particle size is much smaller than the resonant wavelength and the size parameter x is less than 0.1.

$$x = \frac{\pi d}{\lambda}$$

However, when x is close to 1, the electric field is no longer uniform and in phase throughout the particle and it leads to excitation of multipolar plasmon oscillation modes. This generally causes redshift and broadening of the dipolar peak, and excitation of a very broad multipolar peak.

Intrinsic size effect: Mean free path for an electron in gold is approximately 30 nm. A nanoparticle size smaller than 30 nm leads to higher electron scattering at the surface, thereby increasing the non-radiative decay rate $\boldsymbol{\Gamma nr}$ and broadened and damped plasmonic peak. This effect increases with a decrease in particle size such that SPR is completely quenched for nanoparticles size below 2 nm.[25]

Nanoparticle Shape

The FWHM, position and intensity and number of plasmon bands can also be tuned by the shape of a nanoparticle. Sophisticated approaches in synthesis have led to the geometries like spheres,

triangular prisms, rods, wires, cubes, cones, and starts etc.[35] Notable examples are core shell nanoparticle or shapes like triangular prisms and rods that move the plasmonic peak substantially towards the IR and away from the lossy intraband transition thus improving the quality factor of LSPR.

Assembly of nanoparticles

Plasmons on nanoparticles in proximity can reciprocally affect each other depending on the particle distance, nanoparticle geometry etc. with the generation of hybrid modes.[36,37] The simplest case of assembly is a dimer which will be covered in more detail in chapter 4. For specific NP assembly geometries, the mutual interaction between plasmon oscillations can originate constructive and destructive interference phenomena yielding to asymmetric SPR band shapes and sharp dips or spikes in the optical extinction spectrum, known as Fano resonances as shown.

Thirdly, both electric as well as magnetic component of light can excite a plasmon. Magnetic effects are generally feeble in individual nanoparticles. However, magnetic plasmonic resonance effects can dominate the optical spectrum in an assembly of non-touching nanoparticles in a loop.

1.2.3. LSPR dynamics

Absorption of a photon leads to the coherent oscillation of the electronic cloud which start dephasing/ dampening in a lifetime of 2-50 fs. The dephasing lifetime is a function of particle size, shape, and chemical environment. Lifetime of plasmon is also reflected in the bandwidth of the plasmonic peak, assuming complete monodispersity. The smaller is the decoherence time, larger is the plasmonic bandwidth. The dephasing can either be through a radiative or a non-radiative mechanism. The total linewidth of the plasmon band can be represented as a function of an elastically scattered radiative rate term – Γ_r and an non-radiative electronic relaxation term - Γ_{nr}.[38,39]

$$\Gamma = \Gamma nr + \omega^2 \Gamma r$$

Where, Γ is the net dephasing rate and ω is the SPR angular frequency.

Radiative decay: The classical electrodynamics necessitates that an accelerating charge must emit electromagnetic radiation. This radiation comes from the lost kinetic energy of the coherently oscillating electronic cloud and is generally added as a radiation reaction or Abraham - Lorentz force in the overall differential equation for harmonic dampening harmonic oscillator.[40,41] This emitted radiation leads to far field scattering phenomenon from gold nanoparticles. The radiative decay or scattering is largely a function of nanoparticle size, and to a lesser extent, of nanoparticle shape and environment. For a smaller particle, < 40 nm, this makes up less than 5% of the far field extinction spectrum.[42]

Non radiative decay: Non radiative decay has been extensively studied following a variety of ultrafast spectroscopy techniques. Several dephasing mechanisms, like landau dampening, electron- electron scattering ($\boldsymbol{te-e}$), electron phonon scattering ($\boldsymbol{te-ph}$), surface scattering ($\boldsymbol{ts}$), etc., contribute to the non-radiative decay. Non-radiative decay rate can be summarized in the following equation.[43]

$$\Gamma nr = \frac{1}{te-e} + \frac{1}{te-ph} + \frac{1}{te-d} + \frac{1}{ts}$$

The excited plasmon dephases in the 2-50 fs, followed by the landau dampening in which the plasmon energy is transferred into low energy single or multiple electron hole pairs by 100 fs.[43] This leads to multiple high energy – hot electrons. These electrons undergo electron-electron scattering at the time scale of ~500 fs. Given that the intraband d – sp transition in gold overlaps with the dipolar plasmonic excitation in gold spheroidal nanoparticles, plasmons in these

nanoparticles have shorter lifetime to higher chances of scattering due to extra electrons excited due to intraband transition, which ultimately leads to a poorer plasmon quality factor in gold compared to silver.[44] High energy hot electrons transfer some of their energy to low energy conduction band electrons upon scattering leading to thermalization where the average electron energy distribution looks more like quasi equilibrium Fermi-Dirac distribution. System energy at this point is thermal energy plus absorbed photon energy distributed among conduction band electrons. The electronic temperature is higher than the lattice temperature until this stage.[38,45]

In 1-5 ps, hot electrons start scattering by the lattice transferring their energy into lattice vibrations and leading to the electron-phonon coupling. Finally, hot nanoparticle lattices transfers its energy to the surrounding via phonon-phonon coupling and the phenomenon happens at the timescale of 50 ps to tens of nanoseconds.[38]

All these processes are overlapping and the timescales are a function of illumination intensity, particle size, and the external temperature.[46,47]

1.2.4. Modelling of SPR

There have been primarily two types of approach taken for theoretical calculations. 1) analytical (Mie scattering theory) and 2) Numerical (DDA, FDTD, FEM, BEM, etc.).

Analytical methods (Mie theory)

Mie theory provides the analytical solutions for simple, spherically symmetrical nanoparticles dispersed in a non-absorbing medium.[23,48] It involves solving maxwell equations and multipole expansion of the electromagnetic field. For a small sphere (~ 20 nm) under quasistatic conditions, the solutions converge well for the dipole LSP, and a simple analytical solution can be achieved Multipole expansion is required to converge the solutions for larger particles.

Numerical methods

In majority of situations, plasmonic systems do not have spherical symmetry and a simple analytical solution cannot be achieved for these systems. Such systems are solved using numerical calculations approach. Below is a table that summarizes the major approaches for solving complex plasmonic systems numerically.

Table 1.1 Summary of different computational methods for the SPR in Au NPs.

Method	Type	Structure allowed	Grid type
Mie theory	Analytical	Spherically symmetrical	No grid
DDA	Numerical (Frequency domain)	Any	Cubic
FDTD	Numerical (time domain)	Any	Rectangular
FEM	Numerical (frequency domain)	Any	Triangular or tetrahedral
BEM	Numerical (frequency domain)	Any	Adaptive
T-Matrix	Analytical	Spheres and their assembly	No grid

*****Rectangular grids may cause computation inaccuracies in the case of curved or highly dynamic surfaces

DDA: It is generally known as discreet dipole approximation or coupled dipole method. It was originally introduced by Purcell and Pennypacker[49] and was further developed by Draine et al.[50,51,52] DDA divides a plasmonic particle into N point dipoles of known polarizability tensors organized in a cubic lattice. Each dipole interacts with the incoming electromagnetic wave and re-radiated wave form other dipoles. The accuracy depends upon the size a dipole compared to the incoming wavelength of light. The method can produce artefacts when the dipole size is not small enough.[53]

FDTD: FDTD stands for finite difference time domain, also known as Yee's method, and is a widely used technique for optical studies of plasmonic nanostructures.

BEM: BEM stands for boundary element method and is based on vector diffraction theory.[54]

FEM: FEM stands for finite element method. In this method, total simulation volume is divided into a set of finite elements whose shape is chosen to best describe the target geometry.

T-matrix: T-matrix is a powerful approach to study the optical properties of randomly oriented particles and interacting plasmonic aggregates using a transition (T) matrix.[55]

1.2.5. Application of LSPR

There have been numerous applications of LSPR based on its different aspects. For example, optical absorption, chemical and dielectric sensitivity, intense electric field enhancement, hot-electron generation, heat generation etc. We have covered select few in the following sections.

Sensing: A very high extinction coefficient (σ_{ext}) and its equally high chemical and dielectric sensitivity and possibility of modulation makes plasmonic nanostructures excellent transducers. This coupled with easy synthesis, chemically inert nature, photostability, biocompatibility and ease of functionalization of plasmonic gold nanoparticles makes them well-suited for biological, diagnostic and medical applications. Moreover, optical properties can be studied using a simple, nondestructive, easily available, UV Vis spectrophotometry. This makes their application of optical properties based sensing highly widespread. These can be colorimetric sensing with NC assemblies led band formation in the red, ligand adsorption led SPR shifting etc [56,57, 58,59]

The binding of analyte on nanoparticle surface can cause the colloidal aggregation changing the suspension color from red to blue (for gold nanoparticles). In last two decades several such sensors have been built for the detection of metal ions[6061], organic molecules[6263], proteins[64], DNA[6566] and living cells[67].

Dar field imaging: Isolated and aggregated nanoparticles with size larger than 40 nm possess a large Rayleigh-scattering cross section that is utilized for conventional dark field imaging. This has been used to locate the localization of gold nanoparticle assemblies in a particular compartment of cell.[68]

Photothermal effects: Conversion of light into heat is extremely efficient in gold nanoparticles. Gold nanoparticles have a tunable band in visible in the water transparency window with absorption cross section several orders of magnitude larger than organic chromophores. This couples with poor luminescence yield and rapid relaxation of SPR makes them an ideal candidate to dump heat efficiently, especially for biological applications. This has been utilized for selectively killing tumor cells with illumination. Chapter 4 is based on using this aspect of gold nanocrystals for their deterministic dimerization.

Plasmon induced hot carrier effects: The first product of dephasing of plasmons are hot electrons and holes that can be utilized for filling the acceptor states or accepting from the donor states of adsorbed molecules on the gold surface. This aspect of LSPR in gold nanoparticles is utilized for photocatalysis and charge injection application for energy harvesting.

Local field enhancement: One of the main reasons of interest in plasmonic gold nanoparticles is their ability to absorb far field radiation and transform into intense electric fields of sub wavelength dimensions thus, acting like a lens. This can be exploited to enhance several types of optical phenomena such as Raman scattering,[69] fluorescence,[70] visible,[71] IR, coherent antistokes Raman scattering,[72,73] hyper Raman scattering[74,75] and a series of other linear and non linear optical effects in absorbed molecules and materials.

SERS: Raman spectroscopy vibrational spectroscopic technique based on incoherent scattering of light to use for fingerprint recognition of an analyte. In general, Raman cross section is typically poor, and the scattering efficiency is around $10^{-29} – 10^{-31}cm^2$/molecule. However, this cross section can be improved by orders of magnitude if the molecule is kept in the vicinity of a metal nanoparticle, or better at the gap between two gold nanoparticles due to two enhancement effects. 1. Chemical enhancement, and 2) electromagnetic enhancement. Chemical enhancement corresponds to the modification of Raman cross section of a molecule adsorbed on a metal. The order of this enhancement is ~ 10^2.[69] Electromagnetic enhancement is when a molecule is in the hotspot caused by plasmonic coupling and can be of the order of $10^9 – 10^{10}$ inside a single hot spot. In principle this can allow us to detect a single molecule. In chapter 4, we have attempted to design simple, single pot synthesis for the gold nanoparticle dimers with tunable gap.

2. Evaluation of nanostructured β-Mn2V2O7 thin films as photoanodes for photoelectrochemical water oxidation

A major portion of this chapter has been adapted from a research article [Gargasya, Y.; Gish, M. K.; Nair, V. V.; Johnson, J. C.; Law, M. Evaluation of Nanostructured β-Mn2V2O7 Thin Films as Photoanodes for Photoelectrochemical Water Oxidation. *Chem. Mater.* **2021,** *33* (19), 7743-7754]

2.1. Introduction

The discovery of efficient, stable, and inexpensive photoanode materials for use in tandem photoelectrochemical water-splitting devices remains a major challenge to the realization of practical solar-driven hydrogen production.[76,77,78] In 2015, Yan et al. reported β-$Mn_2V_2O_7$ as a highly promising *n*-type semiconductor for solar water splitting, with a near-optimal optical band gap energy of 1.75 ± 0.1 eV,[14] band edge energies that straddle the water oxidation and reduction potentials, and electrochemical stability under illumination in pH 13 electrolyte.[79] These authors prepared bulk powders by chloride salt calcination. X-ray diffraction (XRD) showed that the powders consisted of a mixture of β-$Mn_2V_2O_7$, α-$Mn_2V_2O_7$, and at least one unidentified crystalline phase. Diffuse reflectance spectra of these mixed-phase samples were used to estimate the optical band gap of β-$Mn_2V_2O_7$. Films with a composition of "$Mn_{0.5}V_{0.5}O_x$" were then made by a similar but different procedure and evaluated for their photoactivity in pH 13 electrolyte. However, no characterization of the phase composition or optical properties of the films before or after photoelectrochemical testing was presented. An anodic photocurrent of ~0.1 mA cm^{-2} was reported for the $Mn_{0.5}V_{0.5}O_x$ films in 0.1 M NaOH (*aq*) with $[Fe(CN)_6]^{3-/4-}$ (a fast redox couple) when biased at ~1.1 V vs. the reversible hydrogen electrode (RHE) and illuminated with chopped ultraviolet light (3.2 eV), but no photocurrent was observed in the absence of the $[Fe(CN)_6]^{4-}$ hole scavenger, indicating that the samples were not appreciably photoactive for the oxygen evolution reaction (OER). The report by Yan et al. generated significant interest in β-$Mn_2V_2O_7$ as a candidate water splitting material,[1,2,3,80,81,82,83]. Still, it also raised many questions, including whether their films were, in fact, β-$Mn_2V_2O_7$ and stable in base.

There has been little subsequent experimental work on $Mn_2V_2O_7$ in the context of water splitting. Abdi and Berglund mentioned parenthetically that transient microwave conductivity

measurements revealed β-$Mn_2V_2O_7$ to have a low mobility of ~10^{-4} cm^2 V^{-1} s^{-1}, suggesting that the small photocurrent reported by Yan et al. is caused by a short carrier diffusion length in this material.[2] Very recently, Seenivasan and co-workers reported a surprisingly long minority carrier diffusion length of ~235 nm and photocurrents of up to ~0.15 mA cm^{-2} from mixed-phase β-$Mn_2V_2O_7$ films that contained molybdenum and were encapsulated in a TiO_2 coating by atomic layer deposition and measured under simulated sunlight in borate buffer at pH 9.[9] $Mn_2V_2O_7$ has two well-known polymorphs, a low-temperature triclinic phase (α-$Mn_2V_2O_7$) and the high-temperature monoclinic phase (β-$Mn_2V_2O_7$), which reversibly interconvert via a thermally-hysteretic first-order phase transition over a temperature range of 285-310 K.[84,85,86] Most experimental studies of $Mn_2V_2O_7$ have focused either on its β-α phase transition and low-temperature magnetic ordering[10,11,12,87,88,89] or applications in lithium ion batteries,[90,91,92] solar cells,[93] and (electro)catalysis.[94,95,96]

Here, we evaluate the stability and photoelectrochemical performance of phase-pure films of nanostructured β-$Mn_2V_2O_7$ made by the calcination of a spin-cast molecular ink. We show that β-$Mn_2V_2O_7$ is unstable in pure water at pH 5.8 and aqueous electrolytes at pH 7 and 9. At pH 13, it corrodes within minutes to form amorphous $Mn_xO_y(OH)_z$ phases. Our β-$Mn_2V_2O_7$ films yielded only miniscule photocurrents (~μA cm^{-2}) for the oxidation of iodide, sulfite, or water and the reduction of iodate or water in borate- and phosphate-buffered electrolytes at pH 7 and 9, the oxidation of $[Fe(CN)_6]^{4-}$ or water at pH 13, and the oxidation of bromide in acetonitrile, regardless of calcination temperature and time (which tune crystallite size), film thickness, and illumination geometry. Minimal photoactivity was observed even in electrolytes in which film degradation was insignificant over the duration of the photoelectrochemical tests. Ultrafast transient absorption spectroscopy shows that the poor photoactivity is mainly the result of fast hole trapping and

recombination at the MVO surface that leaves few free charge carriers beyond the ps time scale. Given its poor charge transport and stability – particularly in an alkaline solution – β-$Mn_2V_2O_7$ is not a promising photoanode material for solar water splitting, but systematic studies of doping, heterostructuring and surface protection and catalyst coatings may still prove fruitful.

2.2. Results and Discussion

2.2.1. Film fabrication and characterization

Monoclinic $Mn_2V_2O_7$ (β-MVO, Figure 1a) thin-films were fabricated by spin-coating an acidified water-ethylene glycol ink of manganese(II) acetate hydrate ($Mn(CH_3COO)_2 \cdot 4H_2O$), vanadium(IV) oxide acetylacetonate ($VO(acac)_2$) and a polyethylene-polypropylene-polyethylene triblock copolymer (Pluronic F-108) onto a substrate and calcining the dried ink layer in air (see Methods). The acid in the ink prevents the precipitation of vanadium, while the triblock copolymer is a thickening and structure-directing agent that produces porous nanocrystalline MVO films of tunable thickness, as we reported in the synthesis of similar $BiVO_4$ (BVO) films.[97] Figure 1 presents structural characterization data of our standard ~580 nm-thick MVO films made on FTO-coated glass substrates using a 30 minute calcination at 500 °C. The films are bright orange, uniform across many square inches, optically smooth, and highly transparent (Fig. 1b). X-ray diffraction patterns of the films are consistent with phase-pure, untextured β-MVO (Fig. 1c), but the presence of a trace α-MVO impurity cannot be ruled out from these data alone. High-resolution synchrotron powder XRD of powdered films showed phase-pure β-MVO and no evidence for α-MVO or other phase impurities (Figure A1.1). Films grown on quartz substrates also appeared pure, untextured β-MVO by XRD (Figure A1.2). Given the unknown effect of α-MVO impurities on the photoelectrochemical behavior of β-MVO films, we restricted our study to these pure β-MVO films, leaving the investigation of α-β mixtures and pure α-MVO films for future work.

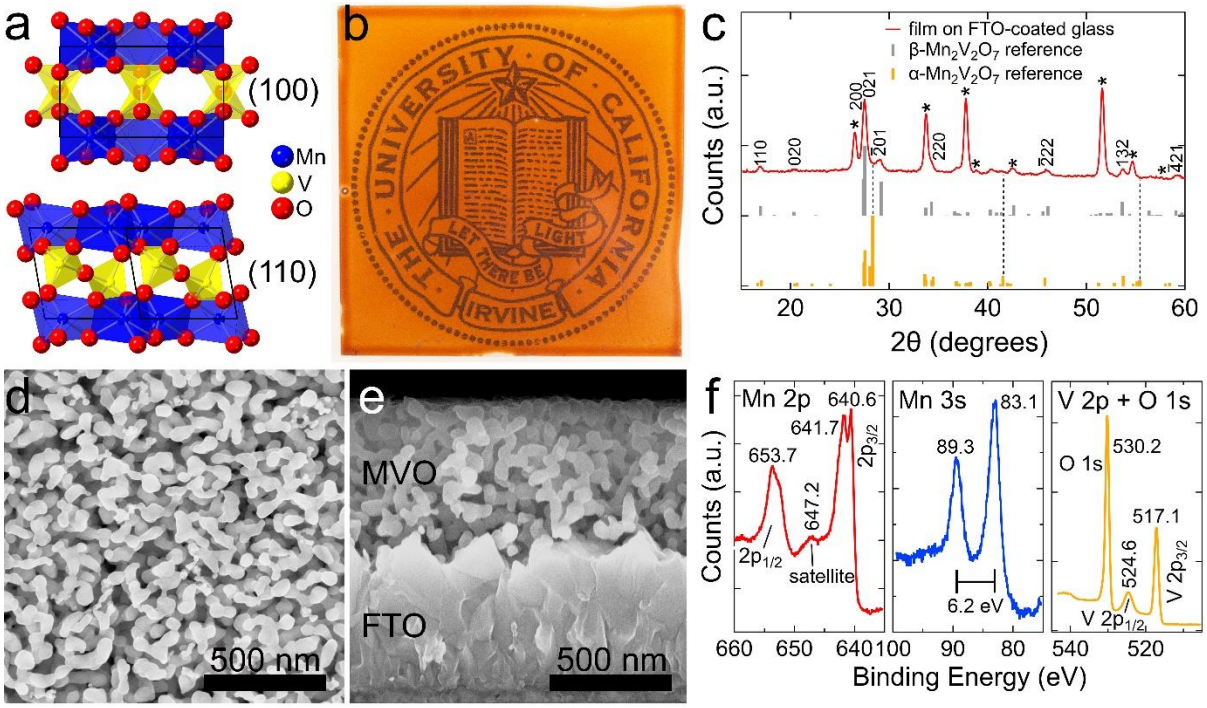

Figure 2.1 Characterization of nanostructured MVO thin films on FTO-coated glass substrates. (a) Polyhedral representations of the monoclinic β-$Mn_2V_2O_7$ crystal structure. (100) and (110) projections highlight the layered structure and isolated $V_2O_7^{4-}$ units (yellow). The unit cell is outlined with black lines. (b) Photograph of a 580 ± 60 nm thick β-MVO film deposited on a 3 × 3 inch FTO-coated glass substrate by spin coating and calcining the molecular ink. (c) XRD pattern of a duplicate film. All peaks index to β-$Mn_2V_2O_7$ (PDF# 01-089-0484, grey bars), although the presence of a trace amount of α-$Mn_2V_2O_7$ (PDF# 01-089-0483, orange bars) cannot be ruled out in these data (dotted lines). FTO substrate peaks are denoted with asterisks. (d-e) Plan view and cross-section SEM images of the film. (f) XP spectra of the Mn 2p, Mn 3s, and V 2p regions with binding energies labeled. See Figure A1.1 for synchrotron XRD data, Figure A1.2 for corresponding data for films on quartz substrates, Figure A1.3 for Raman spectra of films on both substrates, and Figure A1.4 for characterization of nonporous MVO films made from inks without the triblock copolymer.

The β-MVO films have a comparable morphology and thickness on FTO-coated glass and quartz substrates. SEM images show that the standard films consist of a highly-porous, sponge-like network of fused nanocrystals with a crystallite diameter of 53 ± 11 nm and a total film thickness of ~575 nm (Fig. 1d-e and Fig. A1.2). This morphology offers a reasonable balance of small crystallite size, large film surface area, and good inter-crystallite connectivity, which together are expected to favor the efficient transport of photogenerated holes to the MVO/water

interface and electrons into the substrate. BVO films with a nearly identical microstructure made by a similar process were highly photoactive for both sulfite and water oxidation.[23]

We used X-ray photoemission spectroscopy (XPS) to determine the surface composition of the as-made MVO films on FTO-coated glass substrates. Manganese, vanadium, oxygen, carbon, potassium, and tin (from the substrate) were the only elements detected in XPS survey scans (Figure A1.5). High-resolution Mn 2p, Mn 3s, and V 2p spectra are consistent with Mn^{2+} and V^{5+}, with no evidence for other oxidation states (Figs. 1f and A1.5).[98,99,100]

An Mn: V:O atomic ratio of 1.09:1:4.86 was determined from the XPS data. This value agrees well with a bulk Mn: V ratio of 1.02 ± 0.05 determined by inductively-coupled plasma mass spectrometry (ICP-MS) of digested films and suggests that the as-made films are stoichiometric or nearly-stoichiometric $Mn_2V_2O_7$, possibly with a small excess of surface Mn.

We found that the thickness and average crystallite size of the *β*-MVO films could be independently tuned by adjusting the ink composition and film fabrication conditions. The film thickness was tuned from 150 nm to 4.6 μm – while maintaining phase purity, average crystallite size, and film morphology – by changing the solvent volume and spin speed while keeping the ink stoichiometry, annealing temperature, and annealing time constant (Table A1.1). XRD shows that all of the films were pure *β*-MVO, and SEM indicates an average crystallite diameter of 55-65 nm (Figure A1.6). The average crystallite diameter was tuned from 25 to 160 nm by changing the calcination temperature or time. For example, films calcined at 500 °C for 15, 60, or 120 minutes yielded a crystallite diameter of 39 ± 13 nm, 89 ± 21 nm, and 110 ± 33 nm, respectively, without substantially altering film thickness (550 ± 30 nm), phase, or morphology (Figure A1.7). The crystallite diameter could be made as small as ~25 nm by decreasing the annealing temperature and time to 475 °C and 15 minutes, again while maintaining phase purity (not shown). Our method

for making nanoporous β-MVO films provides substantial flexibility to independently tune film thickness and crystallite size, parameters that often play key roles in the performance of nanostructured photoelectrodes.

The optical absorptivity spectra and band gaps of the films were measured using an integrating sphere. Figure 2a shows the absorptivity spectra of films of different thickness grown on quartz substrates. We find an absorptivity of ~10^4 cm^{-1} at a wavelength of 500 nm. The absorptance spectra were multiplied by the AM1.5G solar photon flux and integrated to obtain a maximum possible photocurrent density and water-splitting efficiency of 2.6, 4.9, and 11.2 mA cm^{-2} and 3.2%, 6.0%, and 13.8% for the films with a thickness of 190, 460, and 990 nm, respectively (Fig. 2b). Tauc-style plots of the absorptivity spectra suggest an indirect allowed band gap of 1.65-1.70 eV (Fig. 2c), a direct forbidden gap of ~1.85 eV (Fig. 2d), and a direct allowed gap of 2.25-2.30 eV (Fig. 2e). Yan et al. reported a direct band gap of 1.75 ± 0.1 eV based on diffuse reflectance data from a multi-phase bulk powder.[5] The same authors concluded from density functional theory band structure calculations that β-MVO has a near-direct band gap, meaning that the indirect gap is smaller but within kT of the direct gap at room temperature, which is qualitatively consistent with our results. Figure S8 compares the absorptivity spectra and Tauc fits of our β-MVO films on FTO-coated glass versus quartz substrates. The FTO-coated glass substrates absorb light in the ultraviolet and infrared (Figure A1.9), but they have little effect on the absorptance spectra of the MVO films, again showing that the β-MVO films grown on FTO-coated glass and quartz substrates are very similar.

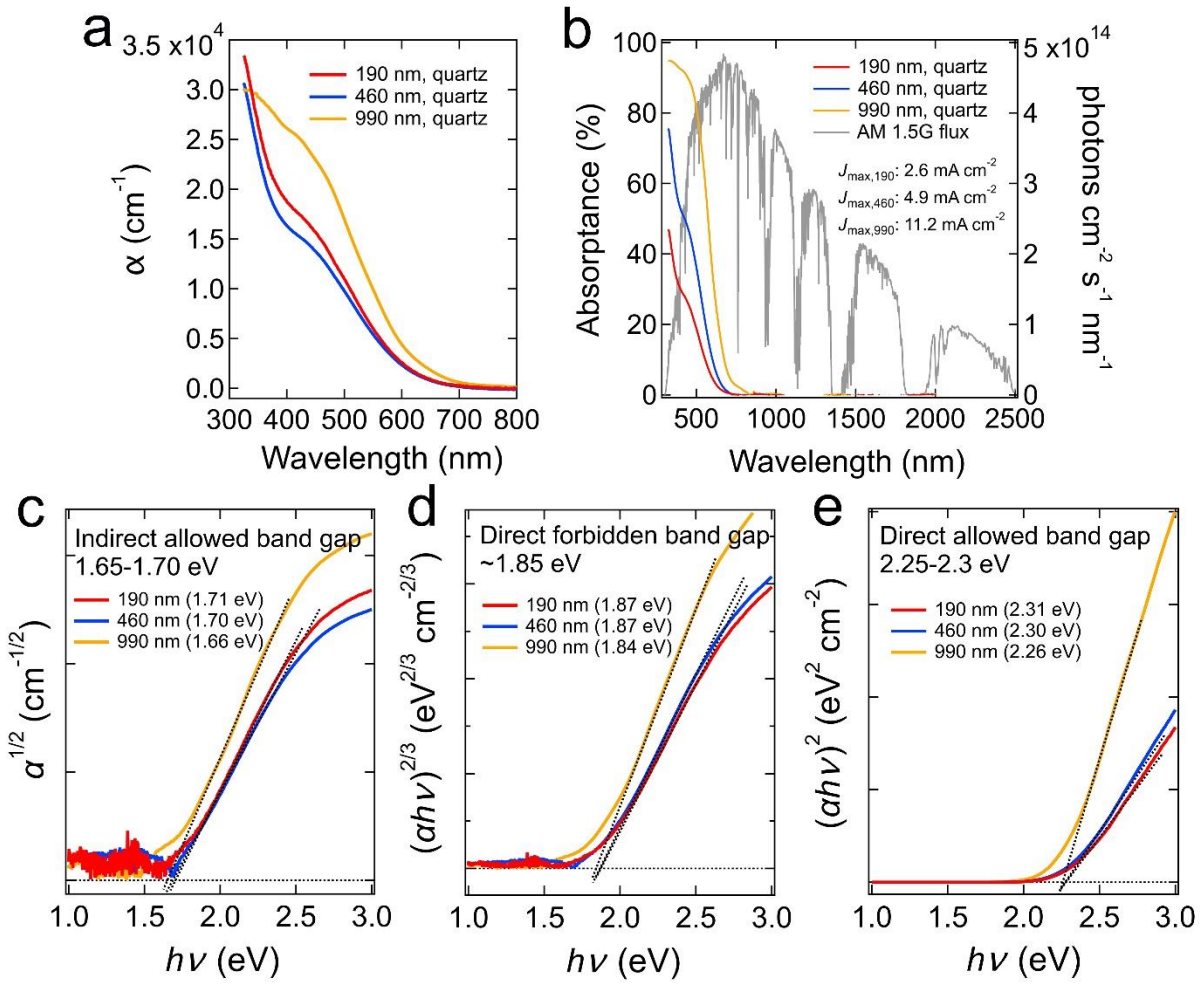

Figure 2.2 Absorptivity spectra and Tauc-style plots for MVO films on quartz substrates. (a) Absorptivity spectra for 190, 460, and 990 nm thick MVO films. (b) Overlap of the absorptance spectra with the AM1.5G solar photon flux used to determine the maximum theoretical photocurrent for these films. Tauc plots and fits for an (c) indirect allowed transition, (d) direct forbidden transition, and (e) direct allowed transition. The estimated bandgap of each sample is listed in the legends.

Aqueous photoelectrochemical testing of the MVO films was performed unstirred in air using a three-electrode cell with both electrolyte-electrode (EE) and substrate-electrode (SE) illumination geometries (Figure 3a). According to the calculated Pourbaix diagram of Ref 5, MVO is thermodynamically stable in mild base (pH 8-10.5) within a 0.3 V window between the water redox potentials when the dissolved Mn and V ion concentrations are 10^{-4} mol kg^{-1}. We tested samples in several different electrolytes (Table 1) and found in all cases only extremely small photocurrents (~μA cm^{-2}) by constant-potential chronoamperometry under chopped 100 mW cm^{-}

^{2} AM1.5G simulated sunlight. Figure 3 shows representative current density versus potential (*J-E*) and current density versus time (*J-t*) data for our standard ~580 nm thick *β*-MVO films in pH 9 borate buffer containing 0.1 M potassium iodide as a hole scavenger. *J-E* sweeps at 50 mV/s showed small photocurrent (100s of μA cm^{-2}) at potentials >1 V vs. RHE, but this photocurrent decayed in potentiostatic conditions to just a few μA cm^{-2} (Fig. 3b-c). The dark current was also much smaller in *J-t* than in *J-E* measurements. The smaller currents obtained in the potentiostatic *J-t* measurements indicate that the currents measured in the *J-E* sweeps are influenced by transient processes such as charge trapping and interface charging. In contrast, nanostructured $BiVO_4$ films measured with the same setup and conditions produced much larger photocurrents (~0.66 mA cm^{-2} at 1.23 V vs. RHE) and featured *J-E* and *J-t* data with self-consistent dark currents and photocurrents (Figure A1.10). These BVO control samples show that the transient *J-E* behavior and very small photocurrent densities of the MVO films are caused by the samples, not the setup. Similarly tiny photocurrents were obtained for the oxidation of water and sulfite and the reduction of water and iodate by MVO in all of the electrolytes listed in Table 1 (Figures A 1.11 - A1.14). Optical spectra showed that ~65% of these samples changed significantly during the photoelectrochemical tests (e.g., Fig. 3d), indicating that that the MVO films were unstable under most of the conditions investigated here (*vide infra*).

Table 2.1 Electrolyte compositions used in PEC tests of standard β-MVO films*

	Hole/electron scavenger				
Electrolyte	no scavenger	KI	Na_2SO_3	$NaIO_3$	TBABr
pH 9 borate	✓	✓	✓	✓	
pH 9 phosphate	✓	✓	✓	✓	
pH 7 phosphate	✓	✓	✓	✓	
pH 13 (NaOH)	✓	✓	✓		
acetonitrile					✓

* These tests employed ~580 nm thick films. The electrolytes did not contain added Mn or V.

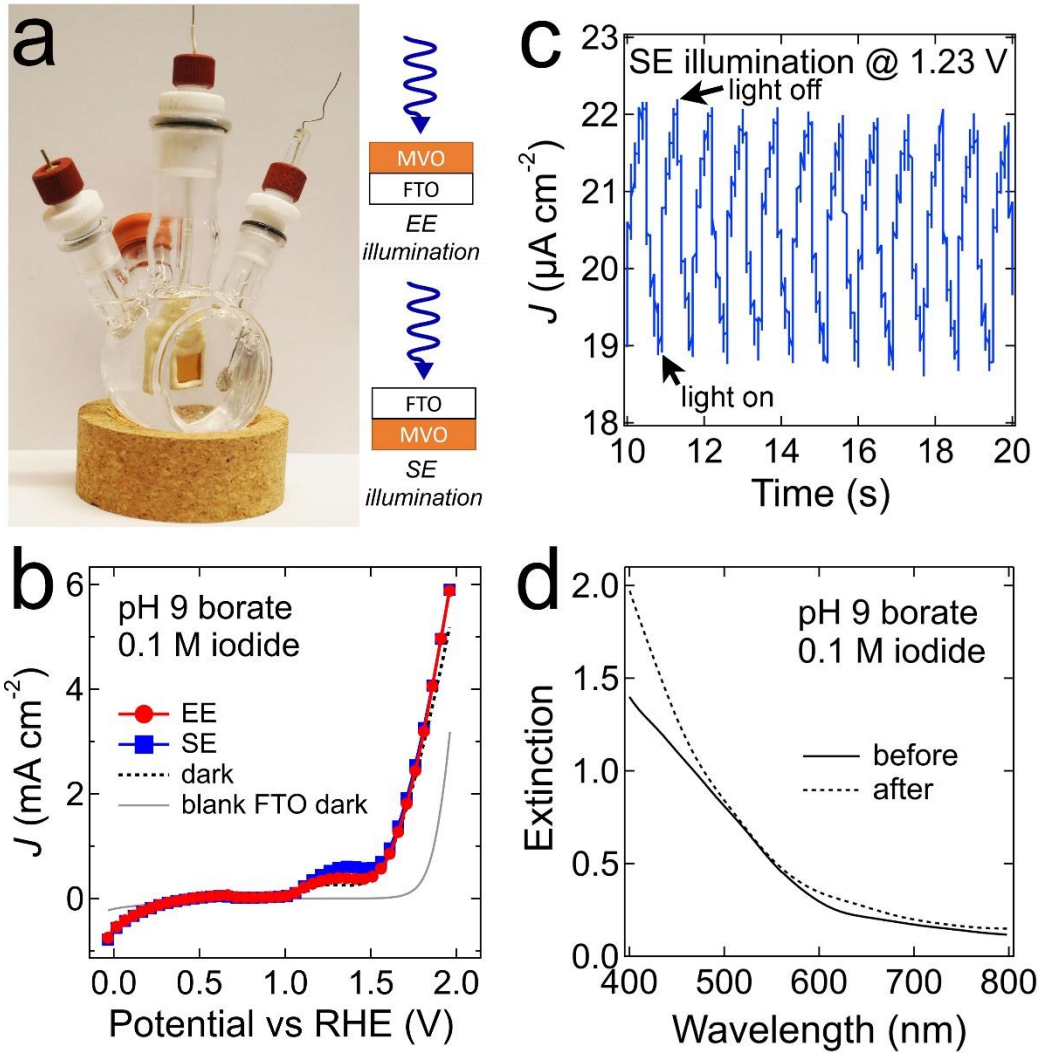

Figure 2.3 Aqueous photoelectrochemical measurements. (a) Photograph of the PEC cell and cartoons of the EE and SE illumination geometries. (b) Current-potential (*J-E*) plots of a standard *β*-MVO film in pH 9 borate buffer with 0.1 M potassium iodide as a hole scavenger. *J-E* data were collected at a scan rate of 50 mV/s using 1 Sun AM1.5G illumination. Data for a blank FTO-coated glass substrate in the dark are also shown (grey line). (c) Current-time (*J-t*) data acquired at 1.23 V vs. RHE using chopped 1 Sun illumination (1.25 Hz) in the SE geometry. We observe a very small photocurrent of ~3 μA cm^{-2}. (d) Optical extinction spectra of the film immediately before and after the photoelectrochemical tests. See Methods for full experimental details, Figures A1.11-A1.14 for data in other electrolytes, and Figure A1.15 for PEC data of a blank FTO-glass substrate.

We also tested MVO films of different thickness and average crystallite size to check whether the negligible photoresponse was specific to our standard ~580 nm thick films. However, changing the film thickness (Figure A1.16), annealing time (Figure A1.17) or annealing temperature (Figure A1.18) did not meaningfully improve the photocurrent for iodide oxidation in borate electrolyte. While by no means exhaustive, this exploration of film parameters (Table A1.1) and electrolyte compositions (Table 1) demonstrates a general lack of photoactivity from these *β*-MVO films. It is possible that MVO samples with significantly different composition (doping/alloying) and/or fabricated by a different method would show better photoactivity.

The absence of photocurrent from an illuminated semiconductor-electrolyte junction is typically caused by some combination of fast carrier recombination (bulk and/or surface) and fast photocorrosion (light-driven redox reactions that alter the electrode). We used post-mortem optical extinction spectra to check for degradation of the films during the *J-E* and *J-t* measurements. Most of the films tested in pH 9 phosphate buffer showed negligible changes after photoelectrochemical testing (Fig. A1.12), suggesting that the films have short-term stability in this electrolyte and that the lack of photocurrent is due to fast recombination rather than photocorrosion in this case. In contrast, most of the films tested in the other electrolytes changed significantly during testing (Figs. 3d, A1.11, and A1.13- A1.14). For example, the films in pH 7 phosphate electrolyte partially corroded during the measurements (Fig. A1.13). However, as discussed in more detail in the next section, these changes occurred even in the dark without applied bias and were not strongly enhanced by illumination. A simple comparison of the total charge generated by light over the course of the photoelectrochemical testing of each film (5-10 C cm^{-2}) with the charge that would be required to completely photocorrode each film (~0.065 C cm^{-2}, assuming two holes per formula unit of $Mn_2V_2O_7$) shows that at least 99% of the photogenerated carriers recombined instead of

participating in local redox processes leading to photocorrosion. We conclude that the miniscule MVO photocurrent is the result of massive electron-hole recombination rather than photocorrosion.

Additional evidence that fast corrosion is not the main cause of the poor MVO photoresponse comes from photoelectrochemical tests carried out in dry acetonitrile. Films measured in 0.1 M tetrabutylammonium bromide in acetonitrile were reasonably stable yet showed only μA cm^{-2} photocurrents (Figure A1.19), again implying that the photogenerated carriers are quantitatively lost to recombination. BVO electrodes measured under the same conditions produced photocurrents of ~0.8 mA cm^{-2} in both illumination geometries (Figure A1.20).

2.2.2. Film stability in different solutions

The chemical stability of the standard MVO films was assessed in several electrolytes using a combination of *in situ* optical extinction spectroscopy and post-mortem XPS and SEM imaging. Figure 4a shows the behavior of an MVO film immersed in pure water (pH 5.8) in the dark for 20 hours without applied bias or stirring. We see that the film extinction decreased monotonically with time and nearly stabilized by the end of the experiment at ~85% of its initial value. The corresponding XP spectra showed an increase in the Mn:V ratio from 1.09 to 1.71, indicating preferential loss of surface vanadium upon aging in water (Figure A1.21 and Table 2). In principle, these changes can be explained by either partial dissolution of the MVO film to form a saturated solution of Mn and V species or the self-limited growth of a surface corrosion layer. To distinguish between these two possibilities, we transferred the aged film to a vial of fresh water and found that the decrease in optical extinction resumed (Fig. 4a). These results are consistent with dissolution of *β*-MVO in water, not self-passivated corrosion of MVO to form a stable manganese-rich surface layer. In a sufficient volume of water, the films would likely fully dissolve within days.

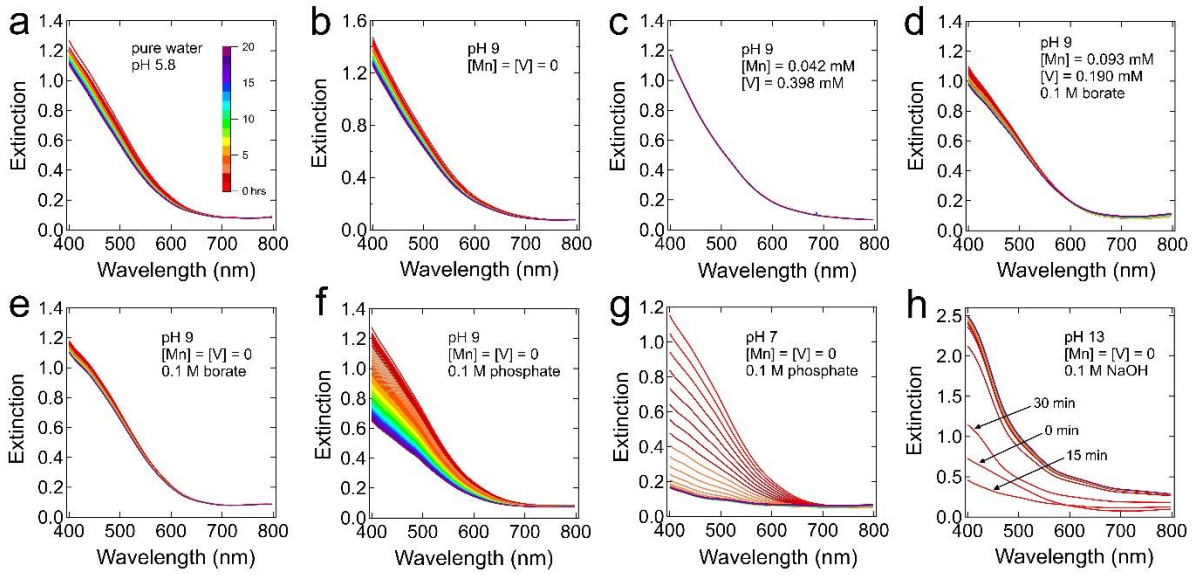

Figure 2.4 Chemical stability of MVO films in various aqueous solutions in the dark and without applied bias. Representative spectral time series for standard MVO films aged for 20 hours in (a) pure water (pH 5.8), (b) pH 9 solution without added Mn and V, (c) pH 9 solution containing 0.042 ± 0.002 mM of Mn and 0.198 ± 0.006 mM of V, (d) pH 9 solution containing 0.093 ± 0.004 mM of Mn and 0.190 ± 0.007 mM of V plus 0.1 M borate buffer, (e) pH 9 solution containing only 0.1 M borate buffer, (f) pH 9 solution containing only 0.1 M phosphate buffer, (g) pH 7 solution containing only 0.1 M phosphate buffer, and (h) 0.1 M NaOH (pH 13). Scans were acquired every 15 minutes for 20 hours. After 20 hours, the sample in aged in pure water was transferred to a second vial of pure water and aged for another 20 hours (double rainbow). See Figures A1.23-A1.25 for corresponding photographs, SEM images and XRD patterns for (e-g).

Table 2.2 XPS elemental quantification of films aged in various solutions for 20 hours*

	Atomic Concentration (%)**					Atomic Ratio		
Solution	Mn	V	O	C	P	Mn:V	O:Mn	Mn:P
none (control)	14.5	13.3	64.6	7.62	-	1.09	4.46	-
water (pH 5.8)	18.0	10.5	62.9	8.60	-	1.71	3.49	-
pH 9 borate	11.8	7.94	57.9	22.4	-	1.49	4.91	-
pH 9 phosphate	11.2	4.33	67.5	9.65	7.33	2.59	6.03	1.53
pH 7 phosphate	12.6	0.229	65.2	6.54	15.4	55.0	5.18	0.82
pH 13 NaOH	23.3	0.466	67.9	8.36	-	50.0	2.91	-

* Experiments employed ~575 nm thick *β*-MVO films. Solutions did not contain added Mn or V.
** Excluding Sn, K and Na.

We next evaluated the stability of our films within the purported stability field of *β*-MVO reported in Ref 5. The electrolyte was a saturated aqueous solution of Mn and V at pH 9 made by

completely dissolving an MVO film in 1 mM HCl, raising the pH to 9 with NaOH, and removing the resulting precipitate by centrifugation. The Mn and V concentrations were measured by ICP-MS to be 0.042 ± 0.002 mM and 0.198 ± 0.006 mM, respectively. Films aged in this electrolyte for 20 hours exhibited completely stable extinction spectra (Fig. 4c) indicating that MVO may be thermodynamically stable at these conditions, as predicted by the calculated Pourbaix diagram of Ref 5. The presence of dissolved Mn and V species is essential to the observed stability. Films aged in pH 9 solution without added Mn and V were not stable (Fig. 4b). We also found that the addition of other ions to the Mn- and V-saturated pH 9 solution (e.g., 0.1 M borate, 0.1 M NaCl or 0.1 M KI) destabilized the films (Figs. 4d and A1.22). Unfortunately, use of Mn- and V-saturated pH 9 electrolytes did not improve the photocurrent for iodide oxidation, which remained at only ~μA cm^{-2} levels (Figure A1.22).

Dark stability tests performed in the buffered electrolytes used for the PEC measurements in Figures 3 and A1.11- A1.13 (no added Mn or V) show that MVO stability increased in borate buffer and decreased in phosphate buffer compared to unbuffered solution at the same pH (Fig. 4e-f). Films aged for 20 hours in 0.1 M borate buffer at pH 9 showed a moderate increase in Mn:V ratio by XPS (from 1.09 to 1.49) and slight surface etching of the MVO crystallites, but no major changes in optical extinction, morphology or phase (Table 2 and Figures A1.21 and A1.23). This increased stability may result from borate anions binding to cations on the MVO surface and slowing surface corrosion. However, increasing the borate concentration from 0.1 to 1 M only decreased film stability (Figure A1.26). We speculate that the concentration-dependent speciation of polyborate ions (i.e., $[B(OH)_4]^-$, $[B_2(OH)_7]^-$, $[B_3O_3(OH)_4]^-$, $[B_4O_5(OH)_4]^{2-}$, etc.) may be responsible for the loss of MVO stability at higher borate concentrations.[101] In contrast to borate buffer, films aged in phosphate buffer dramatically degraded to form a dense layer of amorphous

manganese phosphates and manganese oxides, with the degradation significantly faster at pH 7 than pH 9 (Table 2 and Figures A1.21 and A1.24- A1.25).

Overall, we find that *β*-MVO is unstable in water even in the absence of light and applied bias. It dissolves or corrodes in both pure water and at pH 9. The corrosion is slowed in dilute borate buffer and accelerated in concentrated borate buffer. Phosphate converts MVO to other compounds. We found that the addition of 0.1 M NaCl, $NaClO_4$ or K_2SO_4 to water at pH 9 also reduced the stability of the films (not shown). MVO does appear to be stable in Mn- and V-saturated water at pH 9, but this stability is lost upon addition of supporting electrolytes or hole scavengers, and only tiny photocurrents are obtained in Mn- and V-saturated electrolytes. The stability of the films further decreases under applied bias and illumination (e.g., compare Figs. 4e and 3d). In addition, its near lack of photoactivity, the poor stability of $Mn_2V_2O_7$ makes it an unlikely candidate for practical solar water splitting.

We also tested dark stability in two non-aqueous solvents, ethanol and acetonitrile. Films in ethanol exhibited some initial minor changes in extinction that stopped within a few hours, while films in acetonitrile had completely stable extinction spectra over the entire 20-hour aging tests (Figure A1.27). Photoelectrochemical testing in acetonitrile resulted in a small change (increase) in extinction but only μA cm^{-2} photocurrents (Figure S19), consistent with quantitative electron-hole recombination.

2.2.3. Behavior of *β*-MVO films at pH 13

The performance of OER photoanodes in strong base (pH ≥ 13) is important because resistance losses are low and many OER catalysts work best at high pH.[102] Ref 5 stated that MVO is thermodynamically unstable in strong base and should

decompose to Mn_xO_y and soluble vanadium oxyanions. Regardless, these authors reported that a film of composition $Mn_{0.5}V_{0.5}O_x$ placed in 0.1 M NaOH solution (pH 13) with 0.05 M $[Fe(CN)_6]^{3-/4-}$ redox couple produced a stable anodic photocurrent of ~0.1 mA cm^{-2} under chopped 385 nm illumination. Repeating the measurement on a duplicate sample with 0.1 M NaOH and without the facile redox couple yielded no measureable photocurrent.[5] Based solely on these photocurrent data and without characterizing film phase purity or elemental composition, the authors concluded that β-MVO is kinetically stable under illumination at pH 13. Photoelectrochemical stability of MVO in concentrated base at the OER potential would be surprising and encouraging for water splitting applications. However, the lack of proof of phase and elemental composition calls into question whether the samples measured in Ref 5 were in fact MVO rather than some other phase or phase assemblage.

Our stability tests at pH 13 show that β-MVO films rapidly degrade to form amorphous manganese oxides and hydroxides. This degradation occurred regardless of illumination or the presence of $[Fe(CN)_6]^{3-/4-}$ redox couple (0.05 M). We found no evidence for significant kinetic stability of β-MVO in concentrated base. Optical spectra show that the film extinction first dramatically decreased within seconds and minutes, then rapidly increased and stabilized within ~1 hour to a new spectrum with extinction values ~2x higher than those of the initial MVO film (Fig. 4h). These optical changes were also apparent in photographic time series (Figure 5a). SEM time series show that the films rapidly (~1 hr) convert into a ~800 nm thick, porous layer of interconnected, crumpled nanoscale sheets sitting on a ~200 nm thick, much denser interlayer on the FTO. Films aged for 20 hours were nearly amorphous by XRD (Fig. 5c), with the MVO peaks replaced by weak, broad peaks at 25.0 and 36.2 degrees that may be due to MnO(OH) (PDF # 01-

088-0649) and Mn_3O_4 (PDF # 00-001-1127), respectively. Films immersed in pH 13 for even 5 minutes were amorphous by XRD (Figure A1.28). Meanwhile, XPS of the 20-hour films showed nearly complete loss of vanadium, an Mn 3s peak separation consistent with Mn^{4+}, and a sharp oxygen peak at 529.9 eV with weak high-energy features that we assign to the bulk oxygen of MnO_2 plus surface hydroxides (Fig. A1.21), consistent with the O:Mn atomic ratio of 2.91 in Table 2. These data indicate that β-MVO films at pH 13 quickly degrade to manganese oxides and hydroxides. There was some hope that a self-passivating layer of MnO_x would form on the MVO surface, protecting it from bulk corrosion and acting as a reasonable water oxidation catalyst, but this appears not to happen. We conclude that the samples tested at pH 13 in Ref 5 were probably not MVO, but rather some mixture of $Mn_xO_y(OH)_z$ decomposition products.

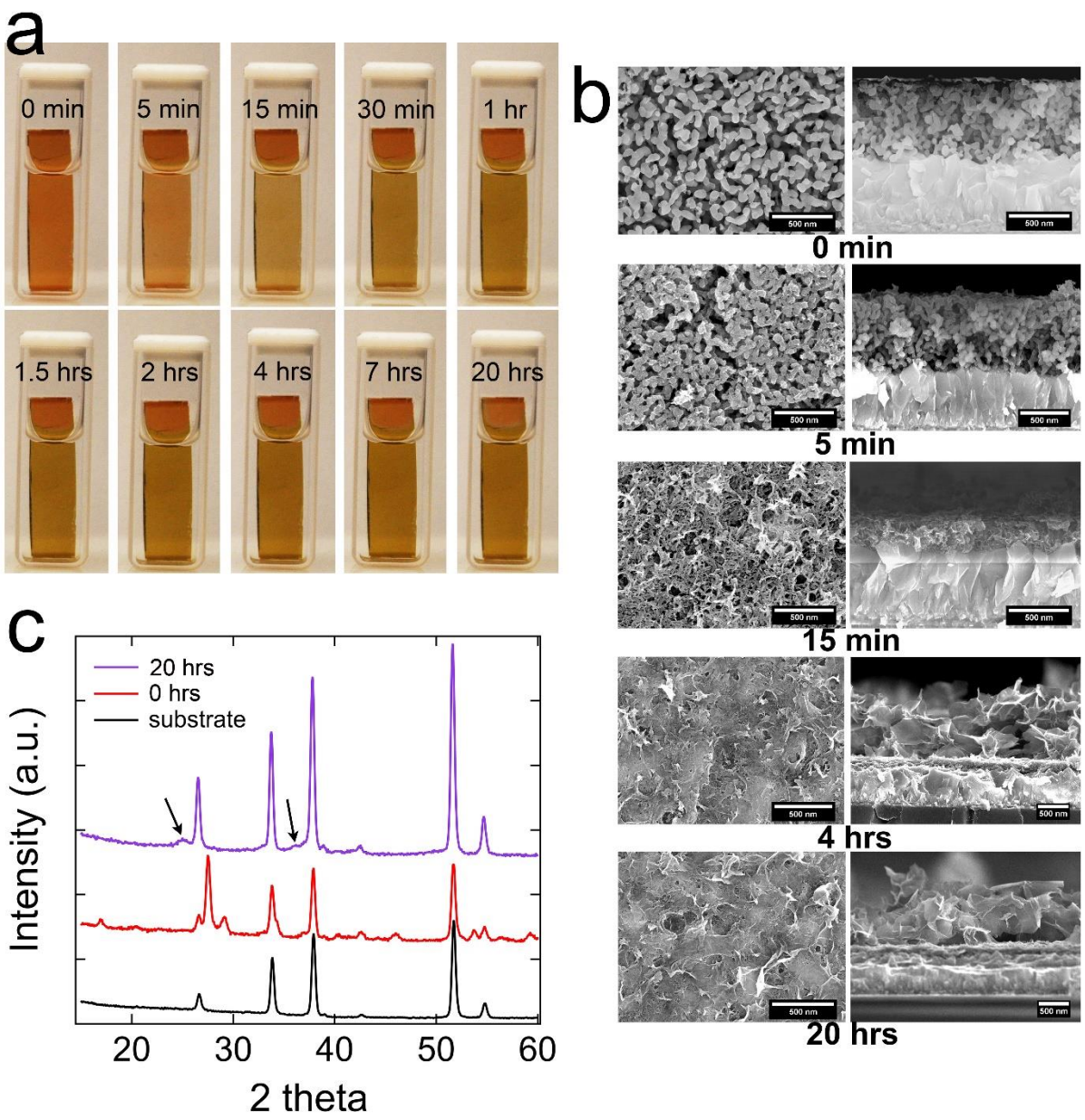

Figure 2.5 Chemical stability of MVO films in pH 13 NaOH solution in the absence of applied bias and light. (a) Photographic time series of a film from 0 min to 20 hours of immersion in the solution. The immersed part of the film begins to change color within seconds and stabilizes with a distinct brownish hue after ~1 hour. (b) Plan-view and cross-section SEM images of films aged in solution for 0 min, 5 min, 15 min, 4 hrs, and 20 hrs. (c) XRD patterns of an MVO film before immersion (red) and after 20 hrs of immersion (purple). The pattern of a clean FTO-coated glass substrate is also shown (black). The pattern of the aged film shows a complete loss of MVO peaks and the appearance of weak, broad peaks at 25.0 and 36.2 degrees (labelled with arrows). The peak at 25.0 degrees may be due to MnO(OH) (PDF # 01-088-0649), while the peak at 36.2 may be due to Mn_3O_4 (PDF # 00-001-1127). All patterns were acquired with an angle of incidence of 0.5 degrees.

Unfortunately, *J-E* and *J-t* measurements of films in 0.1 M NaOH showed nearly zero photocurrent (μA cm^{-2} or less) for the oxidation of $[Fe(CN)_6]^{4-}$, iodide, sulphite or water at any time during the 20-hour aging experiments (Figures A1.29 and A1.14). Given the extreme instability of *β*-MVO at this pH, we can only speculate that the photocurrent reported in Ref 5 for $[Fe(CN)_6]^{4-}$ oxidation originated from some unique phase mixture produced by the degradation of those "$Mn_{0.5}V_{0.5}O_x$" films in strong base. It is also possible, though we believe less likely, that the particular composition or microstructure of those films imbued them with better stability and photoactivity than the nanostructured *β*-MVO films explored here.

2.2.4. Femtosecond transient absorption spectroscopy

The hypothesis that fast recombination contributes to the poor photoelectrochemical performance of the MVO films was tested using visible, near-IR and mid-IR femtosecond transient absorption spectroscopy (TAS). For all MVO films and all conditions investigated, a ground state bleach (GSB) centred at 475-500 nm and a broad photoinduced absorption (PIA) centred at 600-625 nm arose within the instrument response time after photoexcitation at 500 nm (Figure 6a). For dry samples, about half of the initial amplitude of the visible PIA was lost with a sub-ps time constant, with additional slower decays of 7 ps (30%) and 7 ns (20%) (See Table 3 for a full list of fitted time constants). A small portion (<20%) of the PIA signal persisted beyond the 10 ns timescale, decaying with time constants of 128 ns and 8.6 μs (Fig. 6b). We note that the decay kinetics were not strongly power dependent. The rapid decay of the PIA also occurred with a red shift, which uncovers additional GSB at 550 nm that does not decay significantly within the course of 5 ns. Due to the peak shifting, it is difficult to judge the relative amplitudes of fast versus slow GSB decay, but the long-lived bleach could comprise up to 70% of the total signal. In the NIR

there is a broad PIA spanning the entire spectral window that decays to 25% of its initial amplitude by 5 ps and completely by ~0.5 ns (Fig. 6a). There was no substantive change in dynamics with or without air exposure. The mid-IR PIA dynamics lack the ps-scale initial decay, instead possessing ~200 ps and ~1 ns decay components (Figure A1.30 and Table A1.2). Mid-IR kinetics could not be probed at delay times greater than 5 ns due to instrument limitations, or in the presence of electrolyte due to strong absorption by solvent in the infrared region.

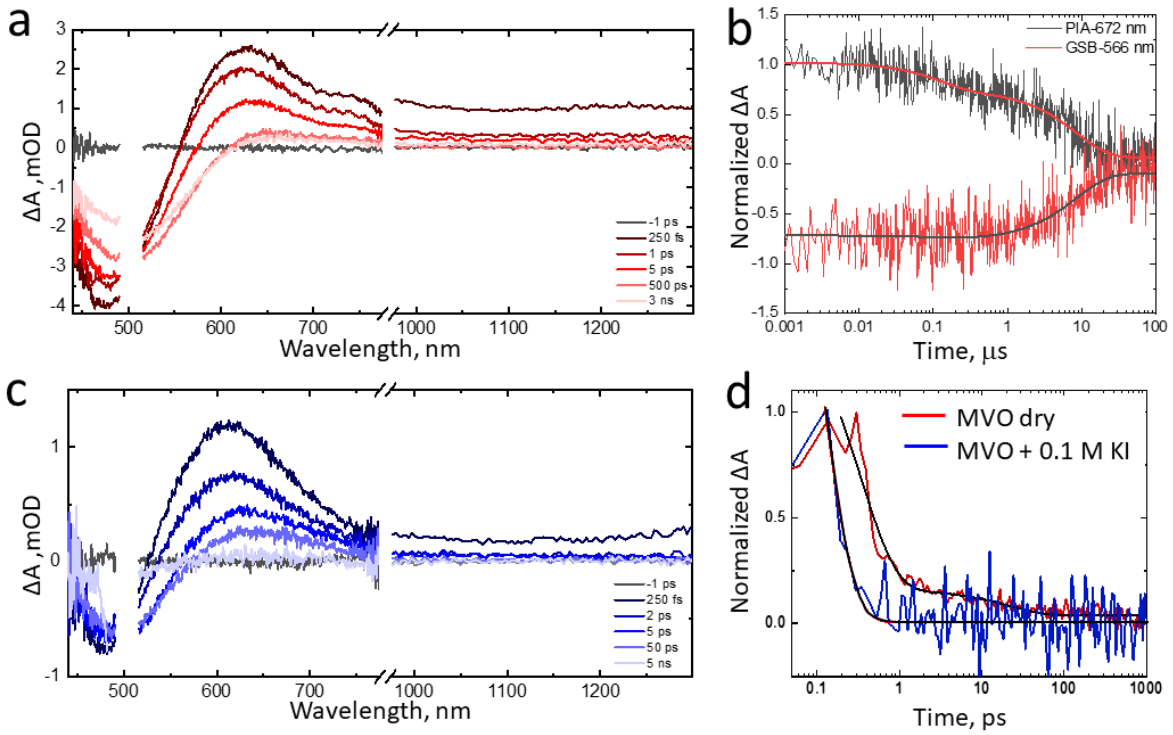

Figure 2.6 Transient absorption spectra. TA spectra in the visible and near-infrared regions at various delay times after 500 nm excitation of a (a) dry β-MVO film and (c) a β-MVO film immersed in 0.1 M aqueous borate buffer at pH 9. (b) Kinetics of the bleach and PIA decay at representative wavelengths on the ns-μs timescales for the dry film. (d) NIR decay kinetics and fits (1100 nm probe) for a dry film and a film immersed in pH 9 borate buffer solution containing 0.1 M KI hole scavenger.

Transient absorption spectra collected in the visible and near-IR for films immersed in a 0.1 M aqueous borate buffer solution at pH 9 under the same excitation conditions as the dry films (λ_{pump} = 500 nm) reveal a significant quenching of the long-lived (>0.5 ns) GSB and complete quenching

of NIR PIA signals beyond a few ps, as compared to dry films, while the faster decays are mostly unaffected (Fig. 6c). We found that adding a hole scavenger (0.1 M KI) to the borate buffer accelerates the decay of the NIR PIA (Fig. 6d, Fig. A1.31a) such that all signal is lost within 1 ps, whereas some long-lived GSB remains. Adding an electron scavenger (0.1 M $NaIO_3$) to the buffer solution had the same effect as the buffer alone, significantly reducing the >0.5 ns component but not altering the faster decay components (Fig. A1.31b).

Table 2.3 Fitting parameters for ground state bleach (520 nm) and visible photoinduced absorption (715 nm) for dry and electrolyte-immersed β-MVO films. Fit uncertainties are given in parentheses.

	dry		0.1 M borate (pH 9)		buffer + 0.1 M KI		buffer + 0.1 M $NaIO_3$	
	520 nm	715 nm	520 nm	715 nm	520 nm	715 nm	520 nm	715 nm
A_1	16%	48%	57%	65%	68%	68%	53%	64%
t_1 (ps)	262 (157)	0.48 (0.04)	106 (18)	3.65 (0.5)	257 (37)	2.0 (0.1)	79 (21)	1.6 (0.2)
A_2	14%	33%	43%	35%	32%	32%	47%	36%
t_2 (ps)	3135 (1289)	7.7 (0.53)	828 (129)	582 (80)	1971 (1164)	478 (40)	671 (146)	128 (15)
A_3	70%	19%	-	-	-	-	-	-
t_3 (ps)	>10000	7197 (633)	-	-	-	-	-	-

Prior work on BVO provides some guidance about the likely origin of the transient absorption signals in MVO.[103,104] The sub-ps PIA features in the visible region are initially blue-shifted from the band edge, likely resulting from band gap renormalization and related screening effects that temporarily shift and broaden spectral features shortly after photoexcitation. As charge carriers relax on a ps time scale, these contributions diminish. Although it is tempting to assign the persistent GSB and associated strong PIA peaking around 650 nm (Fig. 6a-b) to long-lived free charge carriers, we believe that other factors account for most, if not all, of this signal. One

contribution is thermally induced absorption change, which manifests as a derivative-like spectral feature near the band edge that decays over microseconds after laser excitation by heat dissipation to the surroundings. Variable-temperature steady-state difference spectra, Figure A1.32, reveal a close match with the TA spectra at long delay times (dashed red curve in Figure A1.33). We note that a rise in temperature of only a few degrees could produce the roughly 1 mOD of long-lived GSB observed for the dry films, consistent with the predicted temperature rise.[30]

A second contribution to the TAS signal is transient reflectivity (TR) that results from a change in refractive index upon photoexcitation and produces a derivative-like spectral contribution similar to the effect that transient heating has on absorption. Although signals were too weak to be quantitatively analysed, TR spectral features and their associated kinetics overlap strongly with GSB and visible PIA from TAS (Figure A1.33). The relative contributions of the TR and thermal effects are difficult to disentangle given their similar spectral profiles. Addition of the borate buffer solution ameliorates the thermal effect by reducing the temperature rise of the film through the solvent heat capacity, and thus effectively eliminates the residual PIA and GSB on □s timescales (Table 3). The TR contribution is also reduced upon buffer addition through improved index matching between film and solvent compared with gaseous N_2.[105] Therefore, the TAS data for the MVO films immersed in electrolyte, which possess no GSB signal beyond a few ns, more accurately reflect the true excited state population dynamics than does TAS on the dry MVO films.

Additional evidence against the existence of long-lived free holes is found in the PIA spectral features far from the MVO band edge (>800 nm), which are not influenced by the thermal effect or TR signals. This portion of the NIR spectrum does not possess the long-lived decay component present near the band edge, and the addition of the KI hole scavenger further reduces the decay time to < 1 ps (Figure 6d, Table A1.3). This behaviour concurs with the prior assignment of NIR

PIA features in BVO to hole absorption and further suggests that scavenging with KI markedly accelerates loss of the hole population[106] The mid-IR transient absorption, although undoubtedly associated with free carriers, cannot be *a priori* assigned to electron or hole absorption due to our inability to make mid-IR measurements in the presence of a scavenger. Nevertheless, the lack of a sub-ps decay compared with the NIR kinetics implies that the opposite carriers (i.e., electrons) are responsible for the mid-IR absorption. As such, we infer that electrons undergo slower trapping kinetics than holes, including up to one-third of the electron population remaining as free carriers with lifetimes > 1 ns. The residual GSB with lifetime > 1 ns also represents roughly one-third of the total amplitude (Figure S34b), which likely reflects the band filling contribution of the free electrons detected in mid-IR TAS. The amplitude of this long-lived GSB increases further when the hole scavenger KI is introduced, suggesting that faster separation of holes from free electrons reduces recombination.

We note that the faster NIR decay in the presence of the KI hole scavenger shows that photogenerated holes reach the MVO surface. We can conclude that (1) the hole diffusion length is not *extremely* short and (b) the miniscule photocurrents observed in our photoelectrochemical tests are caused mainly by fast surface trapping and recombination. Surface recombination seems to be the major loss channel for holes in these MVO films.

The scenario presented here for MVO is less favorable for water oxidation than BVO, for which comprehensive TAS analysis has shown that a significant fraction of free holes persists to the ns time scale, while electrons are quickly trapped. Common experimental artifacts present near the band edge initially clouded our interpretation, but probing in the presence of electrolytes and in the NIR provides clarity that the free hole population is exceedingly fleeting due to a combination

of bulk and surface trapping and recombination. Mid-IR probing reveals the existence of a significant free electron population with distributed decay times between 100 ps and 1 ns.

2.3. Conclusions

We evaluated the stability and photoelectrochemical performance of nanostructured *β*-$Mn_2V_2O_7$ films made by calcination of a spin-cast molecular ink. *β*-MVO was found to dissolve in pure water and corrode in neutral and alkaline aqueous electrolytes even in the absence of light and applied bias. At pH 13 it corrodes within minutes to form amorphous manganese (hydr)oxides. While *β*-MVO appears to be stable in saturated solutions of Mn and V at pH 9, this stability is lost upon addition of other ions, including supporting electrolytes, buffers, and hole scavengers. The extreme instability of *β*-MVO in water presents a major challenge to its use in water splitting devices.

In addition to poor stability, the *β*-MVO films showed extremely small photocurrents (<3 μA cm^{-2}, equivalent to an overall external quantum efficiency of <0.05%) for the oxidation of iodide, sulfite, bromide and water and the reduction of iodate and water in all of the aqueous and non-aqueous electrolytes that we tested. Comparison of post-mortem optical extinction spectra with the photogenerated (but uncollected) charge and the charge needed for complete corrosion of the tested films shows that photocorrosion cannot account for this lack of photocurrent. Instead, the *β*-MVO films must suffer from some mix of massive bulk recombination (i.e., an ultrashort carrier diffusion length) and a high surface recombination velocity (i.e., fast electron-hole recombination at the MVO surface). Femtosecond transient absorption spectra show that the vast majority of photogenerated holes are trapped within a few picoseconds and recombine with free electrons on timescales of up to a few nanoseconds. The short hole lifetime (τ_h ~ 50 ps for films immersed in borate buffer) may result in a very short hole diffusion length (<5 nm) that severely limits the

photocurrent of our films despite their nanostructured morphology. However, the markedly faster TA decay kinetics of films immersed in electrolyte containing a hole scavenger indicate that most photogenerated carriers do reach the MVO surface, pointing to fast surface recombination as the main reason for the miniscule photocurrents generated by these samples. Coating the β-MVO surface with a passivating, protective and catalytic layer may boost the photoactivity and stability of this material enough to justify further study of its potential for solar water splitting.

2.4. Experimental

Materials. All chemicals were used as received unless otherwise noted. 18.2 MΩ water (Millipore Milli-Q Gradient) was used in all experiments. Fused quartz substrates and quartz tubes were purchased from GM Associates, Inc. FTO-coated glass substrates (TEC 8, Pilkington) were purchased from Hartford Glass Company. Hellmanex III detergent, manganese acetate tetrahydrate (>99.99%), K_2SO_4 (99%), acetonitrile (>99.8%), and NaOH (99.99%) were purchased from Sigma Aldrich. Vanadyl acetylacetonate (>99%) was purchased from Acros Organics. Poly(ethylene glycol)-block-poly(propylene glycol)-block-poly(ethylene glycol) Pluronic F-108 (average M_n ~ 14,600, 82.5 wt% PEG) was purchased from Aldrich. KH_2PO_4 (>99.0%) was purchased from Sigma Life Sciences. Potassium ferrocyanide (>99.3%), $NaIO_3$ (99.0 %), Na_2SO_3 (98.2%), and isopropyl alcohol (99.9%) were purchased from Fisher Scientific. Trace Metal Grade nitric acid for ICP-MS measurements was purchased from Fisher chemicals. Potassium ferricyanide (>99.9%) was purchased from J.T. Baker Chemical company. Ethylene glycol (>99%) and concentrated nitric acid (for the MVO inks) were purchased from Macron Fine Chemicals. KI (99.9%) was purchased from Alfa Aesar. Boric acid (reagent grade) was purchased from Ward's Science. Tetrabutylammonium bromide (>99%) was purchased from TCI. Silver

paint (Lietsilber 200) was purchased from Ted Pella. Loctite 9462 epoxy was purchased from McMaster-Carr. Ag/AgCl (4 M KCl) and non-aqueous Ag/Ag^+ reference electrodes were purchased from CH Instruments.

Film fabrication. All procedures were carried out in air. Fused quartz and FTO-coated glass substrates were cleaned by sequential sonication in a 5% (v/v) aqueous solution of Hellmanex III detergent, pure water, and isopropyl alcohol (15 minutes each). After sonication, the substrates were dried in a furnace at 110 °C for one hour. Molecular inks for spin coating were prepared by adding 1 mmol (0.265 g) of $VO(acac)_2$ followed by 0.32 g of concentrated nitric acid to a mixture of ethylene glycol and water (1 g each). The mixture was sonicated for 5 minutes to completely dissolve the vanadium salt. Next, 1 mmol (0.245 g) of $Mn(CH_3COO)_2{\cdot}4H_2O$ was added to the solution and sonicated until a clear bluish-green solution was obtained, to which 0.4 g of the triblock copolymer Pluronic F-108 was added as a structure-directing agent for making porous MVO films. The solution was sonicated for an additional 3 hours to obtain a dark blue-green viscous ink for spin coating. Our standard films were spin cast at 2000 rpm for 20 seconds followed by 3000 rpm for 40 seconds. After drying, the films were annealed at 500 °C for 30 minutes using a 10 °C min^{-1} heating rate and then cooled naturally to room temperature. This procedure yielded nanostructured β-MVO films with a thickness of ~575 nm and average crystallite diameter of ~53 nm.

Physical characterization. Grazing-incidence X-ray diffraction patterns were obtained on a Rigaku SmartLab diffractometer (Cu Kα radiation) at room temperature. Unless otherwise stated, the angle of incidence (ω) was selected to maximize the intensity of the 111 reflection of β-MVO at $2\theta = 27.5°$. Synchrotron powder XRD was performed on beamline 11 of the Advanced Photon Source (APS), Argonne National Laboratory using an X-ray wavelength of 0.458092 Å, a step size

of 0.001° and a scan speed of 0.01 °/s. Scanning electron microscopy (SEM) was performed on an FEI Magellan 400L XHR SEM operating at 10 kV with a 13 pA beam current. Low-conductivity samples were sputtered with 1 nm of iridium prior to imaging. Raman spectra were obtained using a Renishaw inVia confocal Raman microscope with a 50x objective lens and $\lambda_{incident}$ = 532 nm at 1% power and a 60 s acquisition time. The Mn and V content of the MVO films and electrolyte solutions was quantified by inductively coupled plasma mass spectrometry (ICP-MS) using a ThermoFisher Scientific iCAP RQ C2 Inductively Coupled Plasma Mass Spectrometer (ICP-MS). IV-ICPMS-71A (Inorganic Ventures) was used as the calibration standard. MVO films were dissolved in 10% nitric acid for elemental analysis. Dissolved film solution was diluted 100 times with 1% nitric acid before measurement. The Mn- and V-containing electrolytes were made by dissolving an MVO film in 1% nitric acid, raising the pH to 9.0 using aqueous NaOH, centrifuging the resulting suspension to remove precipitates, and diluting the mother liquor 100-fold with 1% nitric acid prior to ICP-MS measurements.

Optical characterization. Room-temperature optical measurements to determine the absorptance spectra and band gap of the MVO films were performed on a PerkinElmer Lambda 950 spectrophotometer equipped with a 60 mm integrating sphere. Variable-temperature data were acquired by placing films grown on sapphire substrates (Edmund Optics) in a Janis ST-100 cryostat mounted in the spectrophotometer. For sample stability tests, films grown on FTO-coated glass substrates were placed in electrolyte-filled cuvettes and their extinction spectra were measured at 15-minute intervals for 20 hours.

X-ray photoemission spectroscopy. X-ray photoemission spectra were acquired on a Kratos AXIS Supra spectrometer using monochromatic Al Kα radiation (1487 eV). Survey and high-resolution core-level spectra were collected at 160 eV and 20 eV pass energies, respectively. All spectra were

charge corrected using the C 1s peak of adventitious carbon at 184.8 eV. Relative atomic compositions were calculated by integrating the Mn $2p_{3/2}$, O 1s, C 1s and V $2p_{3/2}$ peaks in CasaXPS using its library of relative sensitivity factors. For stability studies, MVO films on FTO-coated glass substrates were immersed in the electrolyte of interest for 20 hours, briefly doused with water, and dried with a nitrogen gun.

Photoelectrochemical measurements. Three electrode measurements were performed in a degassed four-neck electrochemical cell fitted with a quartz window. Working electrodes were prepared from films by affixing a long wire to a bare region of the FTO-coated glass substrate using silver paint, threading the wire through a hollow quartz tube and mounting the sample to the end of the tube with epoxy. The epoxy encased the entire substrate except a square-shaped area of 1-1.4 cm^2 exposed to the solution. Biased three electrode measurements used a Ag/AgCl (4 M KCl) reference electrode and a platinum mesh counter electrode. The primary aqueous electrolytes used were 0.1 M phosphate buffer at pH 7, 0.1 M phosphate buffer at pH 9, 0.1 M borate buffer at pH 9, and 0.1 M NaOH at pH 13. Use of supporting electrolytes was avoided due to their negative impact on β-MVO stability. 0.1 M KI and 0.1 M Na_2SO_3 were used as hole scavengers and 0.1 M $NaIO_3$ as an electron scavenger. Electrolyte conditions from Ref 5 were recreated with 0.1 M NaOH and 50 mM $[Fe(CN)_6]^{4-/3-}$ as a facile redox couple. Nonaqueous photoelectrochemistry was carried out in acetonitrile containing 0.1 M TBABr as a hole scavenger and electrolyte.

J-E measurements utilized a PalmSens electrochemical interface controlled by PSTrace 5.7. A Newport 91160 Class A solar simulator fitted with 300 W xenon arc lamp and an AM 1.5G filter was used as a light source. The power density at the sample position was measured with a pyroelectric radiometer (RkP-575 power probe and Rk-5710 power meter, Laser Probe, Inc.). The absolute spectral irradiance of the solar simulator was measured using a USB4000 spectrometer

(Ocean Optics) and a calibrated light source (HL-2000-Cal, Ocean Optics). *J-E* measurements were performed using linear sweep voltammetry (LSV) in the dark and under 1 sun illumination incident from either the electrolyte (EE illumination) or substrate (SE Illumination). Five cyclic voltammetry (CV) scans were performed immediately prior to each LSV scan to ensure stable electrochemical behaviour at each measurement condition. The potential range was -0.1 V to 2.0 V for anodic scans and 0.2 V to -1.0 V for cathodic scans, with a scan rate of 50 mV/s for both CV and LSV experiments. *J-t* measurements were carried out at a constant potential of 1.23 V vs. RHE for oxidations and -0.6 V vs. RHE for reductions using 1 Sun SE illumination chopped at 1.25 Hz.

Transient absorption spectroscopy. Ultrafast transient absorption measurements were carried out using a Coherent Libra Ti:Sapphire laser with a 1 kHz, 800 nm output (150 fs pulse width) in a pump-probe configuration. The 500 nm pump pulse was generated with a TOPAS-C optical parametric amplifier. Visible (λ_{probe} = 440-800 nm) and near-IR (NIR) probe (λ_{probe} = 750-1600 nm) pulses were generated by focusing a portion of the 800 nm fundamental into a thin or thick sapphire window, respectively. A portion of the probe was picked off before reaching the sample as a reference to reduce signal-to-noise. The time between pump and probe was controlled by a mechanical delay stage and data were collected using the Helios software package from Ultrafast Systems. Data were chirp-corrected and analyzed using SurfaceXplorer from Ultrafast Systems. A second TOPAS-C optical parametric amplifier was used to generate ~150 fs 3500-4500 nm probe pulses for mid-IR TAS. The spectrally dispersed probe was detected with liquid nitrogen cooled HgCdTe array detectors.

Nanosecond-microsecond (1 ns - 400 μs) transient absorption measurements (EOS, Ultrafast Systems) were collected using the same pump pulse as the ultrafast measurements. The probe pulse

was produced in a diode-laser pumped photonic crystal fiber and electronically delayed relative to the pump pulse with a digital delay generator.

Acknowledgments

This work was supported by the UC Solar Institute (UC Multicampus Research Programs and Initiatives grant MR-15-328386). M.G. and J.C.J. acknowledge support for transient spectroscopy and analysis by the U.S. Department of Energy, Office of Basic Energy Sciences, Division of Chemical Sciences, Biosciences, and Geosciences under Contract No. DE-AC36-08GO28308 with the National Renewable Energy Laboratory. The authors acknowledge the use of facilities and instrumentation at the UC Irvine Materials Research Institute (IMRI), which is supported in part by the National Science Foundation through the UC Irvine Materials Research Science and Engineering Center (DMR-2011967). XPS studies utilized equipment funded in part by the Major Research Instrumentation program of the National Science Foundation under grant CHE-1338173. Raman spectroscopy was performed at the Laser Spectroscopy Facility (LSF) at UC Irvine. Use of the Advanced Photon Source at Argonne National Laboratory was supported by the U. S. Department of Energy, Office of Science, Office of Basic Energy Sciences, under Contract No. DE-AC02-06CH11357. The views expressed in the article do not necessarily represent the views of the DOE or the U.S. Government. The U.S. Government retains and the publisher, by accepting the article for publication, acknowledges that the U.S. Government retains a nonexclusive, paid-up, irrevocable, worldwide license to publish or reproduce the published form of this work, or allow others to do so, for U.S. Government purposes.

3. Screening of other ternary metal oxides thin films as potential photoanodes for photoelectrochemical water oxidation

3.1. Introduction

In the recent years, several metal oxides, oxynitrides and oxyhalides have been introduced as promising photoanode materials. This chapters delves into the solution processible thin film fabrication, characterization, and device testing of three such materials. These materials are 1. bismuth oxyiodide (BiOI), 2. bismuth ferrite ($BiFeO_3$), and 3. iron tungstate ($FeWO_4$).

3.2. Bismuth oxyiodide (BiOI)

Post discovery of inorganic-organic lead halide perovskite as a leading next generation solar material, several bismuth based materials too received great attention due to the inert pair – ns^2 cations and large dielectric constant leading high mobility, better defect screening, and interesting optoelectronic properties with non-toxicity and stability as added advantages, unlike lead (Pb).[107]

In this class of compounds, Bismuth Oxyiodide (BiOI) stands out specifically for solar applications due to its sub 2 eV band gap, air and ambient temperature stability, dispersive band, low effective masses for electrons as well as holes, and layered structure with internal electric fields providing an inherent mechanism for charge separation upon photon absorption. [107]

BiOI (space group P4/nmm) has a layered tetragonal structure (figure 3.2a) with alternate layers of Bi_2O_2 and I_2. The dielectric difference between the two layers creates internal electric fields. Resultantly, electrons and holes created upon photoexcitation move to two different layers of Bi_2O_2 and I_2, thus facilitating charge separation.

3.2.1. Electrochemical deposition of BiOI

The highly textured BOI film was grown electrochemically at room temperature with a slightly modified Choi's method.[108][109] 15mM Bismuth nitrate was slowly added in a solution of 0.4M KI and 40 mM lactic acid using constant sonication. The otherwise insoluble bismuth salts in water

form a bright orange Bismuth tetraiodate complex. The pH of this solution was adjusted to 1.8 using 3M Nitric acid. 45mM ethanolic solution of benzoquinone was added to the former, drop by drop using constant stirring and the pH of the resultant solution was adjusted to 3.4. This was used as an electroplating solution with Pt flag counter, SCE reference and FTO working electrodes. 20 pulses (0.5 seconds each) of -0.4V vs SCE were applied for nucleation followed by 15 minutes of constant potential of -0.15V vs SCE for growth. Here nucleation was carried out using pulse amperometry rather than constant potential to get higher nuclei density. The resultant dark red film was washed with DI water thoroughly and were used for further analysis.

The crystalline phase of the film was checked using GIXRD and was found to be matching with BiOI PDF Card # 01-073-2026. Films were considerably textured in (110) direction with texture increasing with film thickness. (Figure 3.2b). Film had textured BiOI nanosheets grown perpendicular to the surface whose length increases with electrodeposition time almost linearly up to 1.5-micron thickness. (Figure 3.4, table 3.1) The film morphology did not show much difference with increased thickness suggesting a good separation between nucleation and growth phase and growth being largely unidirectional. The sheets appear to be thin which is particularly important for better hole collection as sheet materials tend to have conductivity only in the plane and tend to be very resistive in perpendicular direction. Thin sheets ensure that holes do not have to hop

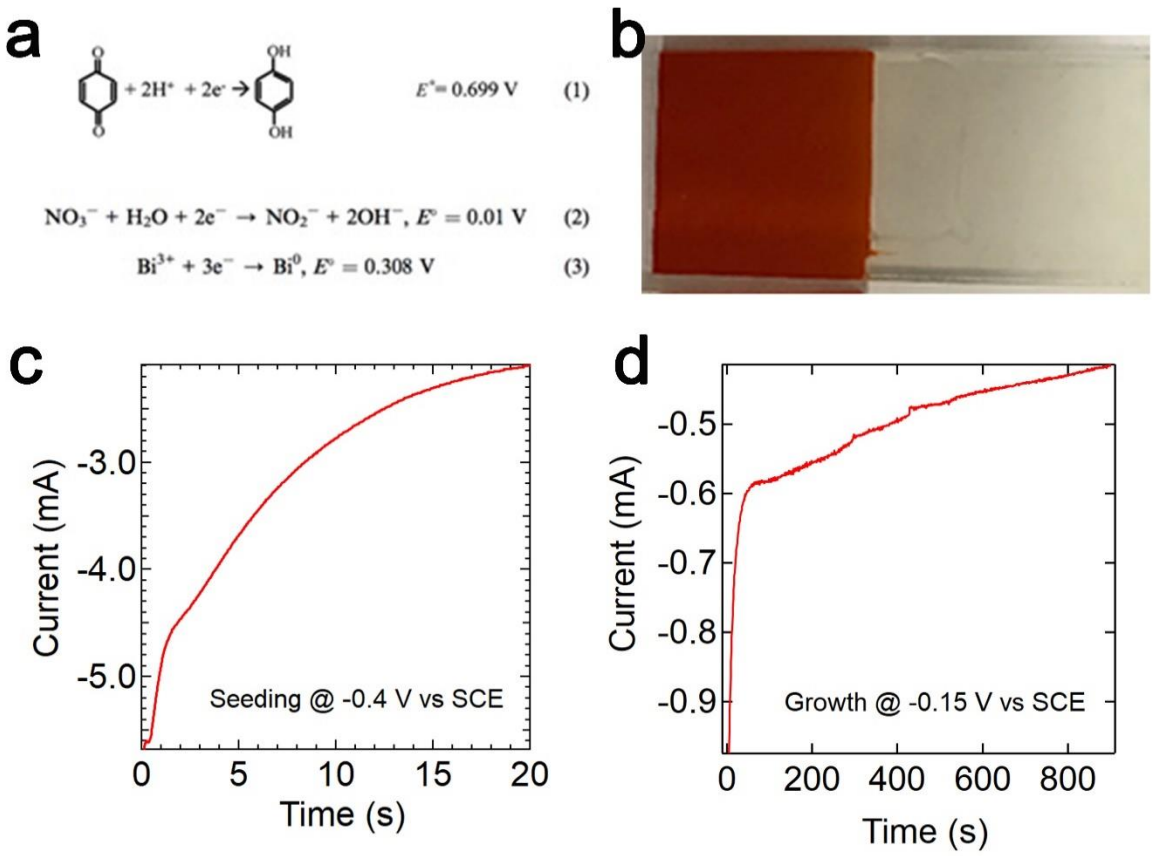

Figure 3.1 Electrodeposition of bismuth oxyiodide (BiOI). a) Relevant electrochemical equations, b) optical image of a 15. Micron thick BiOI film, c) chronoamperometric profile for bismuth nucleation, and d) chronoamperometric profile for BiOI growth.

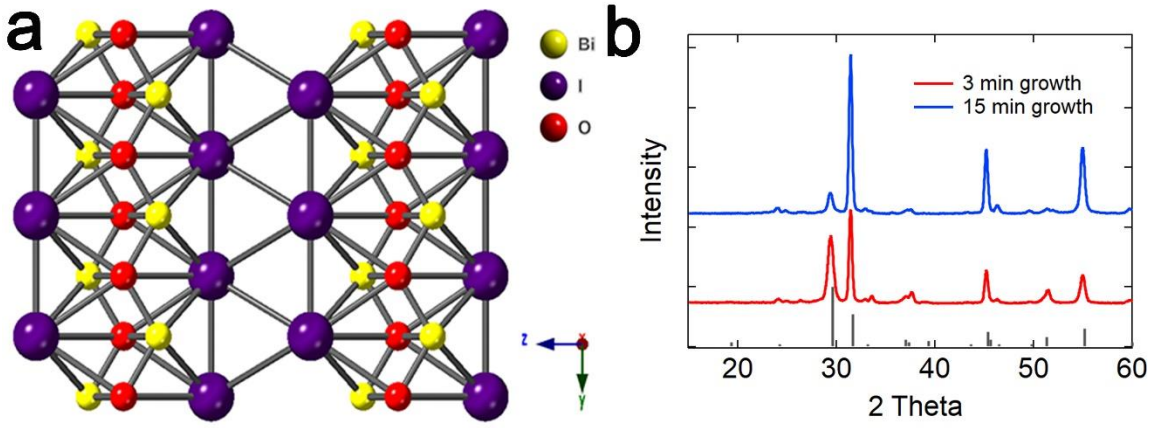

Figure 3.2 Crystal properties of BiOI. a) BiOI unit cell and b) XRD patterns of electrodeposited BiOI films on FTO for 3 and 15 minutes.

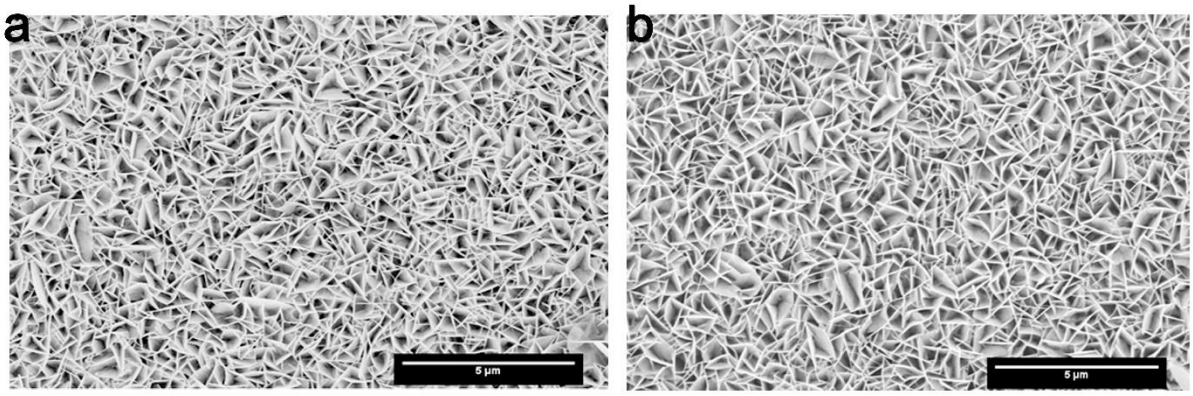

Figure 3.3 Plan view SEM images of BiOI. a) 300 nm thick film and b) 1500 nm thick film.

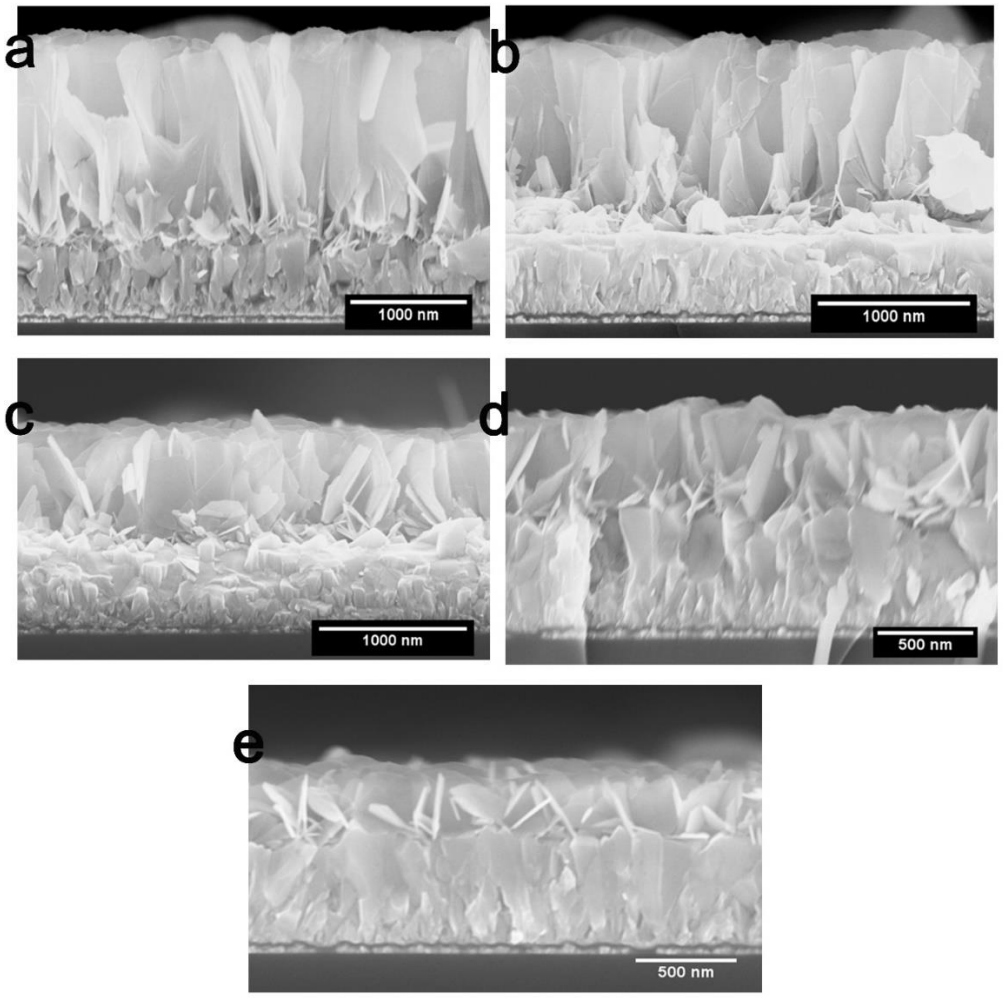

Figure 3.4 BiOI films with variable thickness a) 1500 nm, b) 1200 nm, c) 900 nm, d) 600 nm, and 300 nm.

through very large number of electron rich Bi-O sheets to reach the surface, and most of the surface is not dead catalytically.

3.2.2. Thermal stability of BiOI

With iodide as constituent, BiOI is prone to thermal instability in the oxidative environments. Here we have studied the thermal stability of electrodeposited BiOI films in air with XRD (Figure 3.5) and XPS (Table 3.1). The room temperature electrodeposited films had bismuth excess and iodine deficiency on the surface. This is understandable as iodine is a labile ion and can be easily replaced by hydroxides on the surface in water. The chemical and crystal properties stay largely the same with minor improvement in the crystallinity upon heating to 250 °C in air for 30 minutes. However, the peaks start to broaden, and new peaks start to form upon increasing the temperature to 350 °C. Upon increasing the temperature to 475 °C, new peaks grow in intensity and iodine percentage decreases to 10% from 19%, suggesting the loss of iodine from the film. This is the temperature at which films lose their characteristic red color. Upon raising the temperature to 550 °C, the crystal structure has completely changed, the characteristic 110 peak at 31 ° is completely gone and iodine percentage has reduced to mere 2%, with ~33% bismuth and ~66% oxygen suggesting complete sublimation of iodine from the film crystalline Bi_2O_3 behind.

Table 3.1 XPS studies on thermal stability of BiOI

Sample	Bi (%)	O (%)	I (%)
Control	48.33	32.68	19.O
250 C	44.51	35.89	19.61
350 C	40.49	36.59	22.92
475 C	56.55	30.48	10.17
550 C	30.51	66.52	2.97

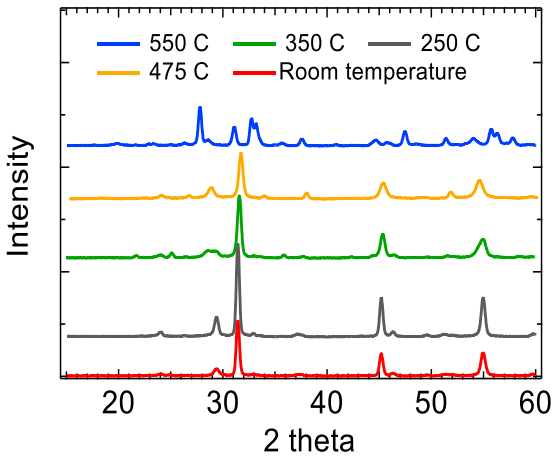

Figure 3.5 Temperature effect on BiOI crystal structure. XRD patterns for BiOI films annealed at different temperatures for 30 minutes in air.

3.2.3. Optical properties of BiOI thin films

The aspect that makes BiOI particularly interesting for solar application is its sub 2 eV band gap that makes it an interesting candidate for both, photovoltaics as well as photoelectrochemical applications. Figure 3.6 shows the optical properties of a typical electrodeposited BiOI film with

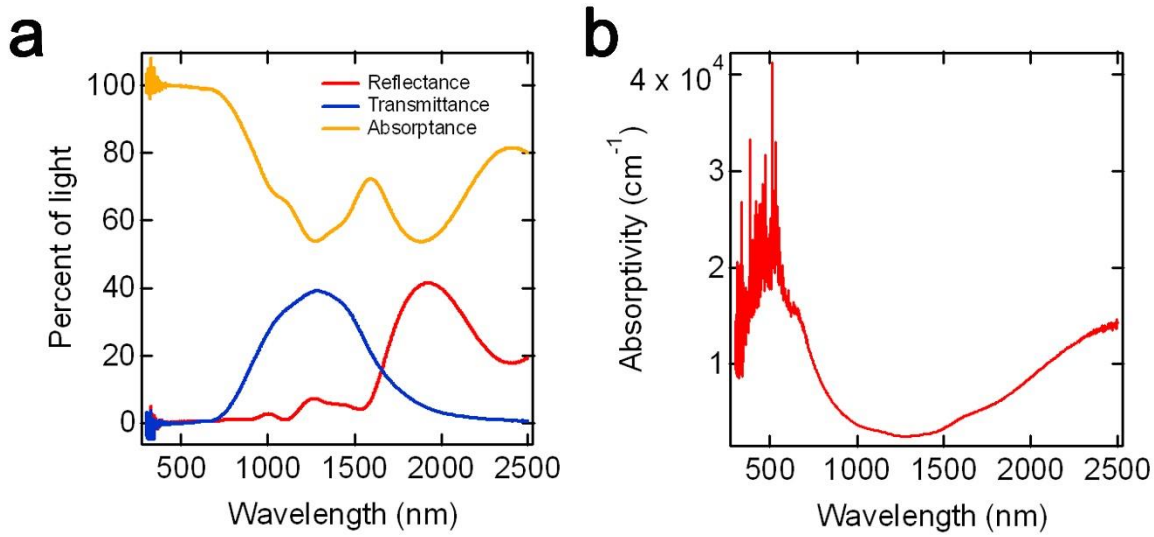

Figure 3.6 Optical properties of BiOI. a) ATR spectra for BiOI films grown on FTO coated glass substrate and b) absorptivity data for the same film.

absorptivity in the range of 3-4 x 10^4 cm^{-1} above the band gap and a considerable light absorption in the visible and even NIR region. However, it should be noted that due to the large micron sized sheet like morphology, the films scatter a lot of photons and are opaque red above the thickness of 600 nm.

3.2.4. XPS studies of film surface

XPS was used to gain insight into the chemical nature of the film (Figure 3.7). The observed elements in the survey scan were Bi, I, O, C and K. All the region as well as survey spectra were charge corrected by the saturated carbon peak at 284.8eV. The usual symmetric Bi^{3+} peaks were

found at 158.7eV and 164.0eV ($\Delta = 5.3\ eV$). Iodine 3d peaks appeared at usual 618.45eV and 629.95eV giving well separated spin orbit components and $\Delta = 11.5\ eV$. The small humps around 623.5eV and 635eV can possibly be due to iodates. The oxygen peak was deconvoluted into three sub peaks. First one at 529.4eV was assigned to the oxygen in the BOI lattice, second one at 530.7eV was assigned to carboxylic oxygen in lactic acid and the third step peak was assigned to adsorbed OH or alcoholic oxygen from lactic acid as well as ethanol from electroplating solution. After sputtering the surface with 1KeV monoatomic argon beam, the potassium peaks were gone, suggesting that it was only absorbed on the surface and was not a part of the crystal. Since, the

electroplating solution contained 0.4M potassium ions, it was natural for some potassium to be and lactic acid to be sticking around on the surface and contributing to the XPS signals.

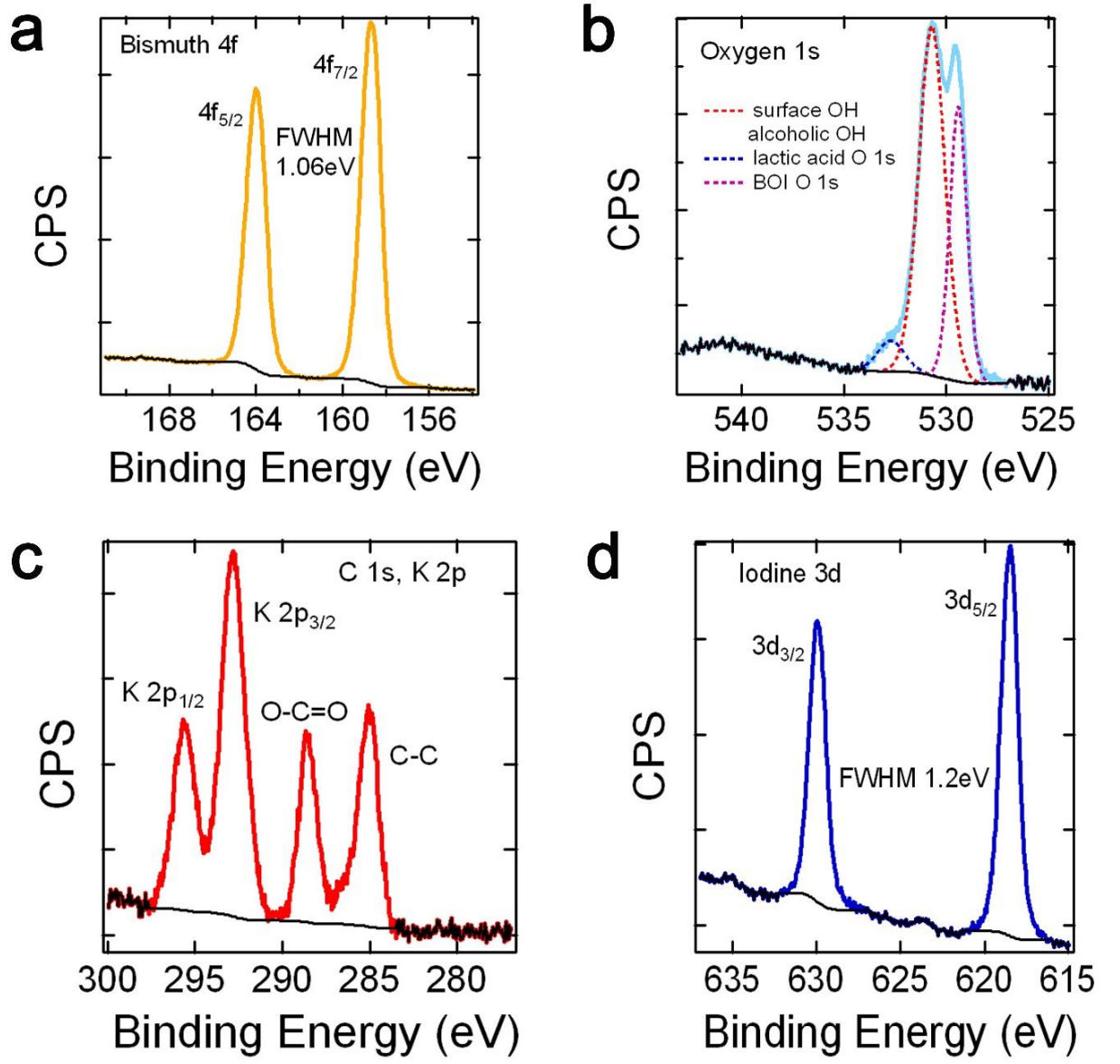

Figure 3.7 Chemical properties of BiOI films. XPS spectra for a) Bi-4f, b) O-1s, c) C-1s, and d)Iodine-3d.

3.2.5. Photoelectrochemical and photochemical properties

Pristine BOI did not show any appreciable photoactivity (Figure 3.8a), and the linear sweep voltammogram looks almost same in light and dark. However, photocurrents could be observed on films stabilized by ~1.5 nm ZnO grown by atomic layer deposition. (Figure 3.8b). One possible reason for the complete absence of photocurrent could be either excessive hole trapping and recombination on the surface or photo corrosion of the surface by photogenerated holes in the presence of water. The resumption of photocurrent upon surface stabilization rules out the bulk recombination as major bottleneck for photoactivity. However, it can play a role in reducing photoactivity.

Given the high overpotential for water oxidation, initial photoactivity was tested with a variety of common hole scavengers like iodide, sulfite, methanol, and ferrocyanide. Iodide performed the best and provided the highest photocurrent for the films. Ferrocyanide corroded the films and provided high photocurrent onset potential with lowest photocurrents. Sulfite provided the lowest and record photocurrent onset of 0.2 V vs RHE. Figure 3.8c shows the chronoamperometric at 1.23 V vs RHE with chopped illumination. There appears to be transient effects with steady state currents much lower than the initial photocurrents, most likely due to bulk and interfacial recombination.

After photon absorption, the electron and hole move to Bi-O and I layer, respectively, in the crystal. Since, interfaces are often the place for charge accumulation and recombination, it was expected that the iodine rich BiOI -ZnO interface could sustain holes for longer, thus improving their lifetime and photocurrent. BOI films were treated with a BI_3 solution (in acetonitrile) before ALD. These films provided more than twice the photocurrent density with the best performing hole

scavenger. These films give one of the best fill factors so far and have a considerably low photocurrent onset potential of 0.3 V vs RHE.

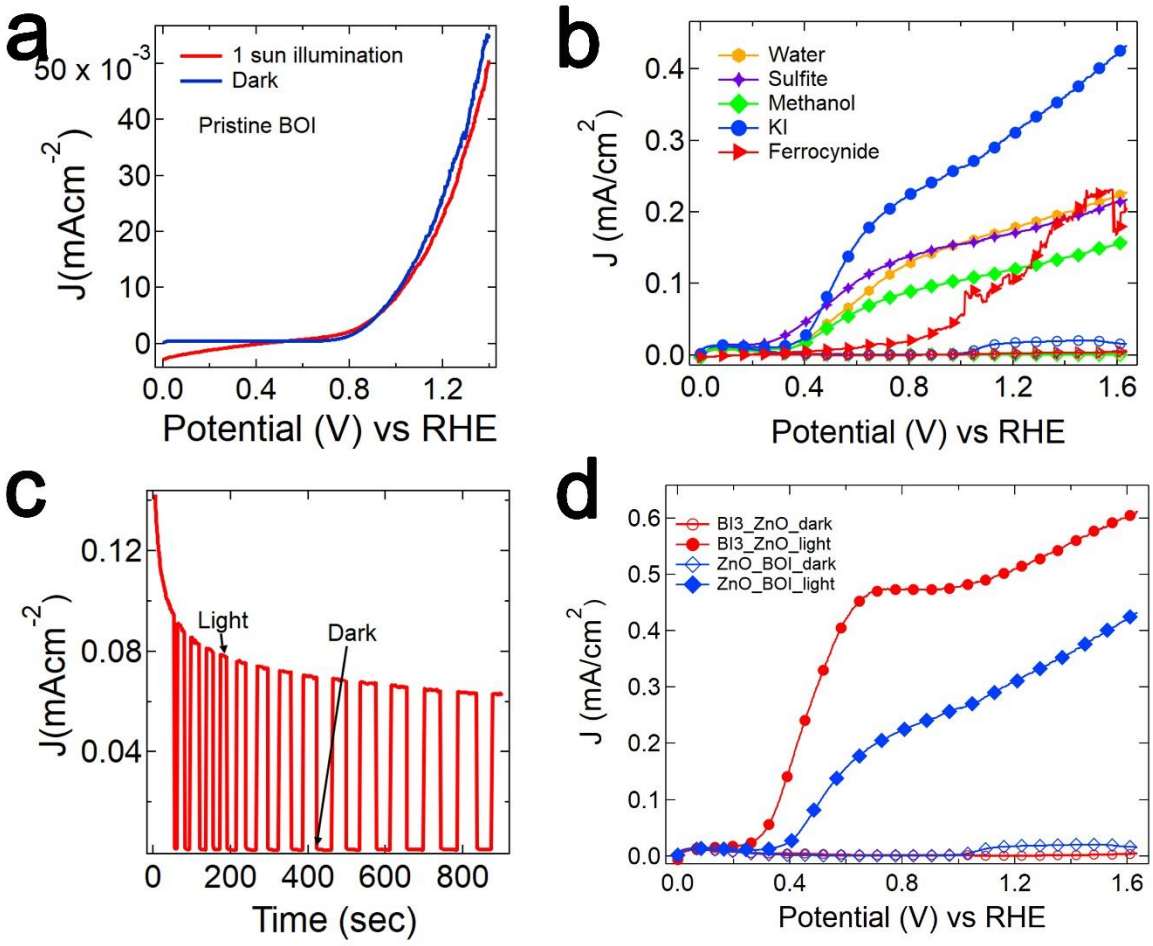

Figure 3.8 Photoelectrochemical properties of BiOI films. A) J-V measurements for pristine BiOI films, b) J-V measurements for ZnO stabilized BiOI films with various hole scavengers, c) J-t measurements on ZnO stabilized BiOI films at 1.23 V vs RHE with chopped illumination, and d) J-V measurements with iodide as hole scavenger for BI_3 treated ZnO stabilized films.

In a sheet like material such as BOI, there is often a huge charge mobility in a direction parallel to sheets and very poor charge transport property in the perpendicular direction. If this is true, and the layers of BOI are indeed bound by Vander Waal interaction, most of the surface would be catalytically dead. To check this, BOI electrode was kept in a solution composed of Auric acid, methanol and water. When exposed to 1 sun illumination, gold deposited on the whole surface and

not just on the periphery of sheets (Figure 3.9), proving that the whole surface is catalytically active rather than just the periphery. Also, the photo deposited gold nanoparticle density improved considerably on ZnO stabilized films, corroborating the photoelectrochemical J-V measurements results.

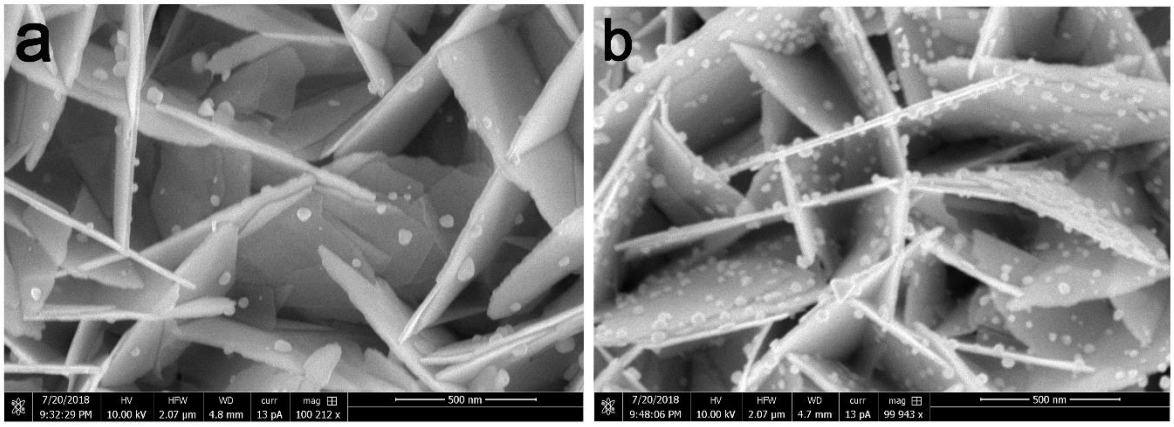

Figure 3.9 Gold photo deposition on BiOI films. Plan view SEM image of photo deposited gold on a) pristine BiOI films and b) ZnO stabilized BiOI films.

3.2.6. Stability status

Bismuth Oxyiodide, with its interesting optoelectronic properties, is chemically and electrochemically unstable. Like many other bismuth and Lead compounds, BOI is susceptible to degradation on applying negative potentials. The film turns black and eventually delaminates from the substrate. Degradation always starts from the surface and can be controlled if one limits the space for ions to reassemble and undergo a phase change. This electrochemical instability has been improved, to some extent, by depositing a sub nm conformal layer of titania or ZnO on the electrodes using atomic layer deposition, such that we can get half a mA of photocurrents but these photocurrents decay fast on successive scans.

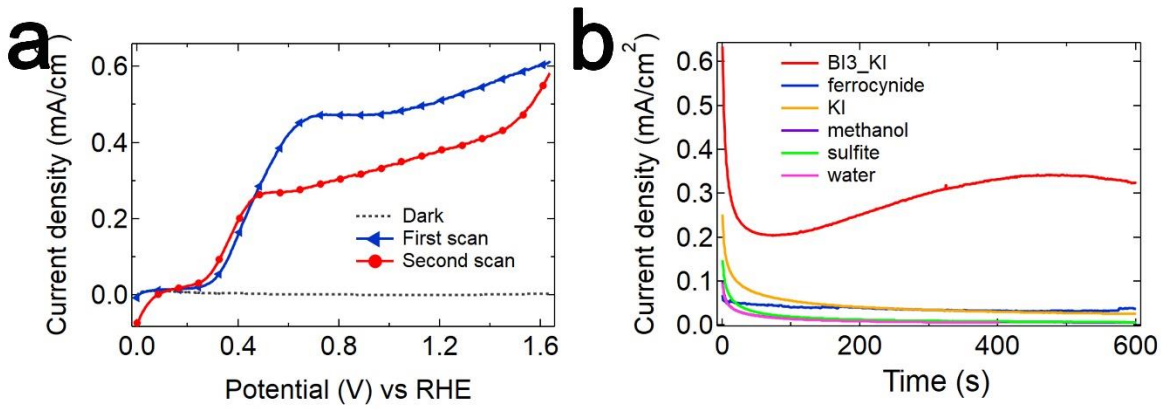

Figure 3.10 Electrochemical stability of BiOI films. a) First and second J-V scans of a BI_3 treated ZnO stabilized BiOI film showing almost 30% drop in photoactivity after the first scan and b) chronoamperometry data of different BiOI films with a variety of electrolytes under illumination.

3.2.7. Conclusion

Bismuth oxyiodide is a promising material with sub 2 eV bandgap, small effective masses for electrons and holes, and inherent mechanism for charge separation, however material stability in aqueous electrolytes turns out to be its Achilles' heels. This material can be employed for organic photocatalysis or its stabilized and ALD protected films can be used for water oxidation. However, this makes it less attractive from the cost of manufacturing considerations with an added cost of bismuth as a non-abundant metal ion.

3.3. Bismuth Ferrite ($BiFeO_3$)

Bismuth ferrite (BFO) is a multiferroic material with a perovskite structure. It is a 2.4 eV bandgap semiconductor with good electrochemical stability in highly alkaline electrolytes. The presence of ferroelectric domains provides internal electric fields that can be utilized for internal charge separation. Given the grain boundary and defects[110,111] led conductivity in this material, a BFO alloy (to lower the band gap) can be employed for photoelectrochemical water oxidation.

3.3.1. Film fabrication and characterization

Bismuth ferrite (BFO) films were fabricated by a spin coating a molecular ink on an FTO coated glass substrate and annealing the dry ink in air at 475 °C for 30 minutes. A typical ink had 1:1 water-ethylene glycol mixture as solvent, 0.5 ml acetic acid to dissolve bismuth salt, 1mmol $Bi(NO_3).5H_2O$ and $Fe(NO_3)_3.9H_2O$ as metal precursors and 400 mg Pluronic F-108 polymer as structure directing agent. Ink turned from yellow to orange upon addition of acetic due to formation of iron acetate. Spin coating followed by annealing of this ink provides a 300 nm thick uniformly yellow BFO film as shown in Figure 3.11b.

BFO has a perovskite – Rhombohedral (R_3C) structure (Figure 3.11a). The deviation from cubic structure is due to the presence of ns^2 lone pairs of bismuth. The crystal phase of the films was ascertained by grazing incidence X-ray diffraction. All the peaks present indexed to the PDF card # 01-0746717. The broadness of peaks suggests the presence of nanostructures which is confirmed by the plan view SEM images in Figure 3.11d. A typical film has an average grain size around 50 ± 8 nm and a thickness of 256 ± 11 nm. Both grain size as well as film thickness can be readily tuned by tuning the annealing temperature, annealing time, amount of polymer, and spin coating parameters.

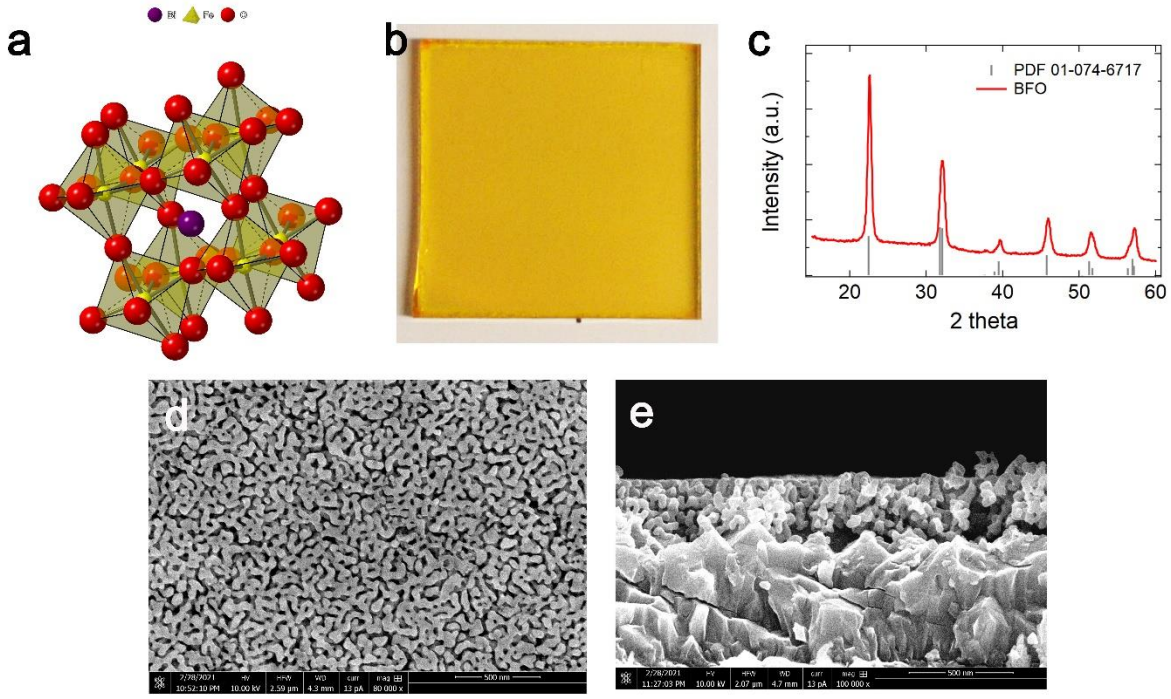

Figure 3.11 Crystal and morphological properties of bismuth ferrite films. a) A bismuth ferrite unit cell, b) optical image of a uniform yellow BFO film grown on FTO, c) grazing incidence X-ray diffraction pattern of BFO films grown on FTO, d) plan view SEM image, and e) cross section SEM image.

3.3.2. Optical properties and band gap tuning

A typical unalloyed BFO film has a shiny yellow color with 2.5 eV band gap with absorptivity of the order of 10^4 cm^{-1}. Band gap in bismuth ferrite can be tuned by alloying and replacing b cation – Fe (in the case of BFO). Three replacements studied are 10% chromium, 10% manganese and 10% cobalt substitutional alloying. Film color changed substantially from yellow to orange to lighter brown and to dark brown upon alloying with chromium, manganese and cobalt respectively. (Figure 3.12e) There is a small dip in absorptivity upon alloying. (Figure 3.12b) Direct band gap fitting suggests a reduction of band gap from 2.5 to 2.2 eV. However, this does not agree strongly with the optical images. Indirect band gap Tauc plot fittings suggest a marked change in the band gap of films from 2.2 eV for pristine BFO films to 1.9 eV for 10% chromium alloyed, 1.6 eV for 105 manganese alloyed and 1.4 eV for 10% cobalt alloyed BFO films.

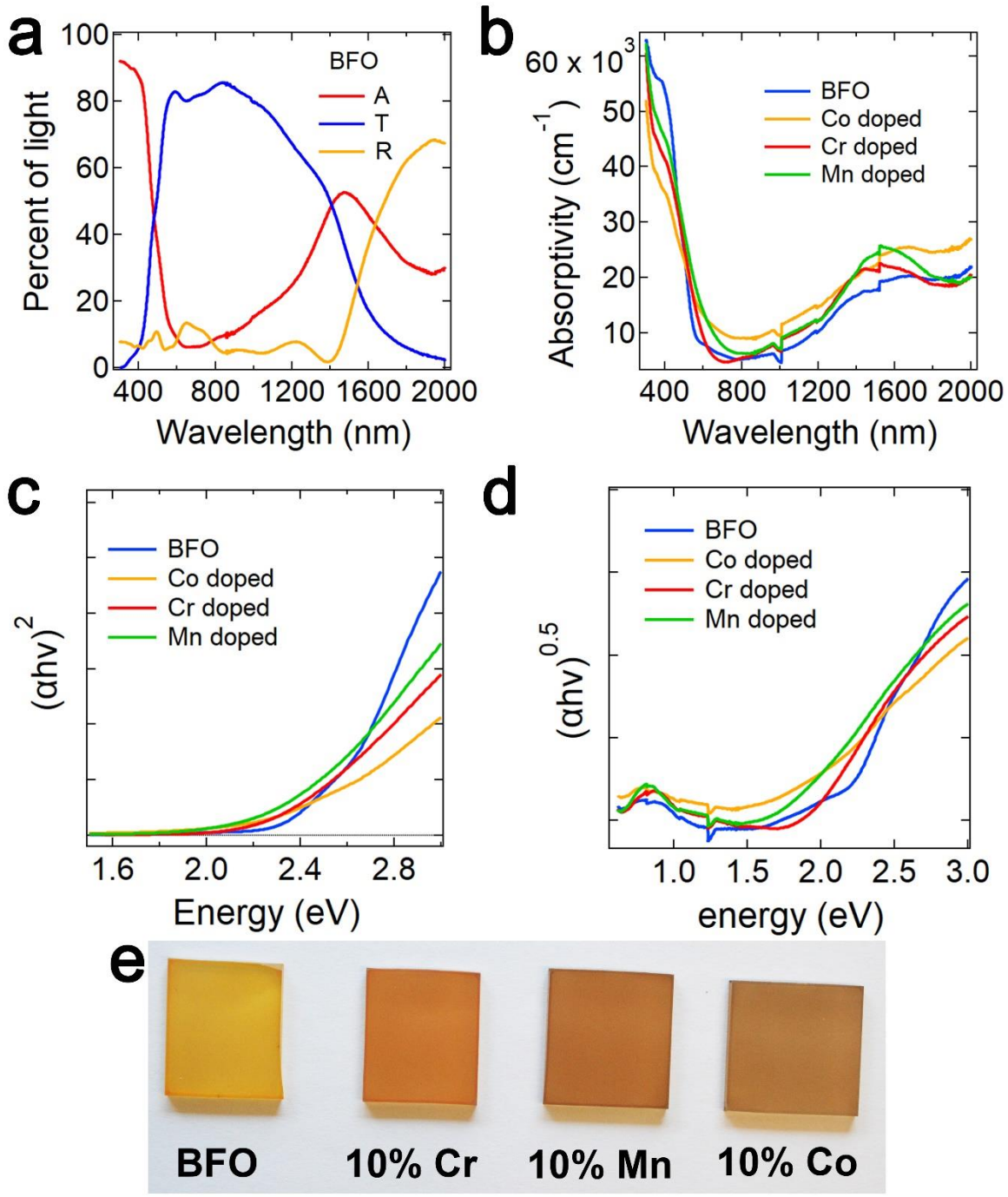

Figure 3.12 Optical properties of pristine and doped BFO films. a) Absorptance, reflectance and transmittance spectra of a pristine BFO film grown on FTO coated glass substrate, b) absorptivity measurements of pristine, 10% cobalt doped, 10% chromium doped and 10% manganese doped BFO films, c) direct band gap Tauc plot fitting for pristine and alloyed BFO films, d) indirect bandgap Tauc plot fittings for pristine and alloyed BFO films, and e) optical images of pristine and alloyed BFO films.

3.3.3. Stability and device testing

BFO films were tested for water oxidation and reduction at pH 7 with 0.1 M phosphate buffer as electrolyte and 0.1 M sulfite as hole scavenger. A clean electrochemical window from 0.2 – 1.23 V suggests minimal or low mid gap defects.

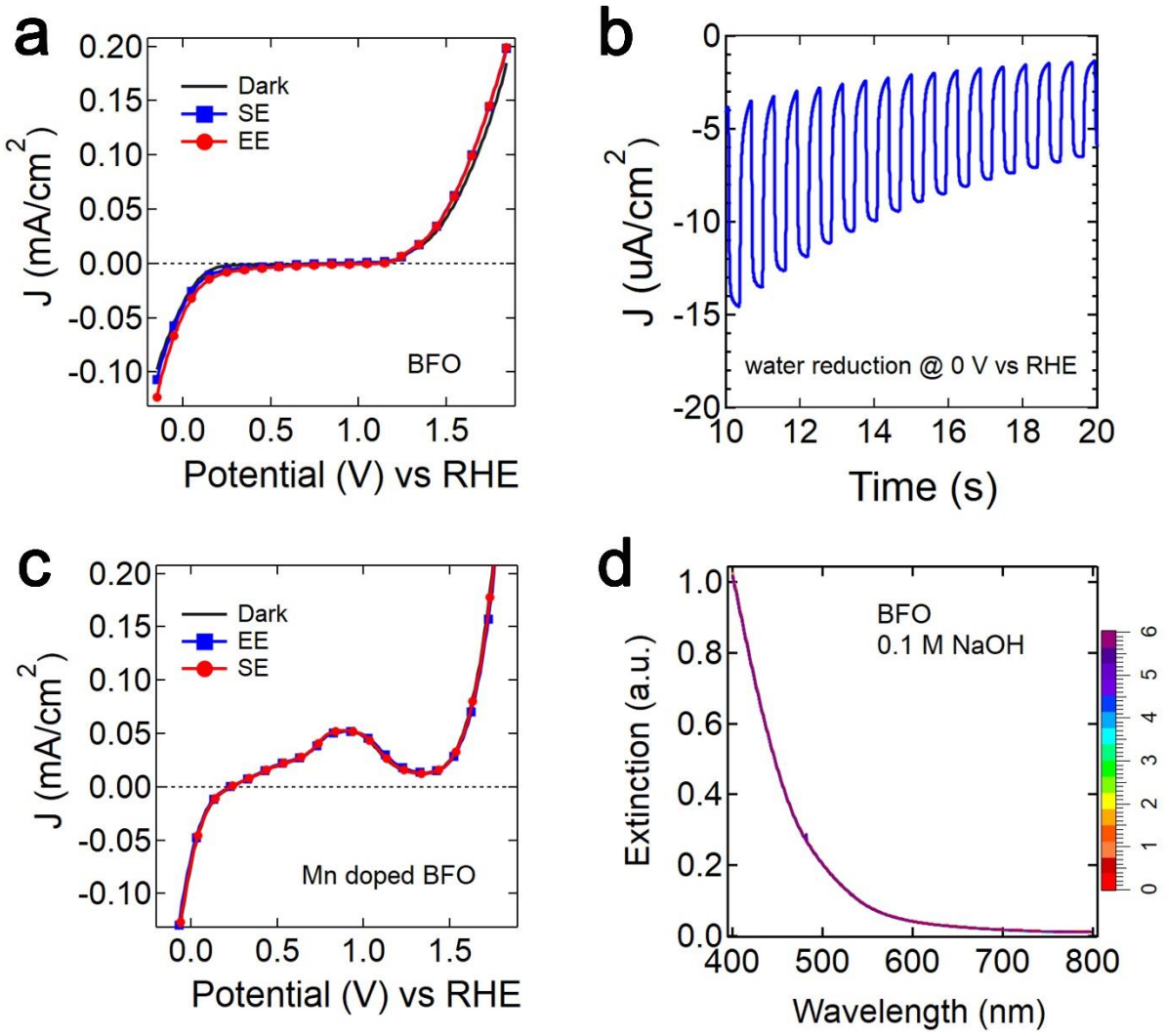

Figure 3. 13 Photoelectrochemical properties of pristine and Mn doped BFO films. J-V measurements for pristine BFO films in 0.1 M phosphate buffer with 0.1 M sulfite as hole scavenger, b) J-t measurement with chopped illumination at 0V vs RHE, c) J-V measurements for 10% Mn alloyed BFO films in 0.1 M phosphate buffer with 0.1 M sulfite as hole scavenger, and stability of pristine BFO films in 0.1 M NaOH solution (pH 13).

BFO does not provide stable photocurrents at anodic potentials, however it does provide stable photocurrent densities of 5-10 $uAcm^{-2}$ for water reduction, suggesting it to be a p type semiconductor. 105 Mn alloyed BFO films did not provide a clear electrochemical window suggesting the presence of midgap defect state formation due to Mn alloying. These states might be responsible for shift in indirect band gap upon alloying. The alloyed films did not provide a stable photocurrent and showed poor photoactivity which can be attributed to the excess defects in the band gap region. BFO showed to be a very stable material at pH 13 under 0.1 M NaOH as expected from its Pourbeux diagram.

3.3.4. Conclusion

We designed a simple spin coating-based process for fabrication of bismuth ferrite nanoporous films. The morphology is tunable, and films exhibit great chemical stability in alkaline pH. The direct bandgap of the films can be tuned from 2.5 to 2.2 eV and indirect band gap can be tuned from 2.2 to 1.4 eV by alloying with different B site metal ions like chromium , manganese, and cobalt. However, alloying leads to the formation of high in-gap defects that adversely affect the photoactivity of this material. Efforts can be made to tune the fabrication process to minimize the defect density upon alloying to maintain the photoactivity while reducing bandgap.

3.4. Iron tungstate ($FeWO_4$)

Iron tungstate (FeWO) is another promising candidate for photoelectrochemical water oxidation due to its remarkable stability in both acid as well as base, ~ 2eV direct band gap and earth abundant catalytic constituent metals. However, so far, the fabrication is limited to either nanocrystal colloids or planer thin films made by sputtering. Here we have designed a protocol for solution-based processing of nanostructured thin film of FeWO, characterized and tested it for a potential photoanode for photoelectrochemical water oxidation.

3.4.1. Film fabrication and characterization

Iron tungstate (FeWO) belongs to the ferberite class of minerals with a monoclinic (P2/c) structure. Iron and tungsten are in +2 and +6 oxidation states, respectively. Figure 3.14a shows the layered monoclinic structure of iron tungstate. FeWO films were fabricated by double annealing of a spin cast molecular ink. A typical ink had 0.5 g water, 1 g ethylene glycol and 0.5 ml glacial acetic acid as solvent. 1 mmol ammonium meta tungstate hydrate and 1 mmol ferric nitrate nonahydrate were used a metal precursor. 400 mg Pluronic F-108 was added as structure directing agent. System was sonicated for 1.5 hours to get a transparent orangish viscous molecular ink. This ink was spin casted on a FTO casted glass substrate. This film was annealed in two stages. First, it was annealed at 450 °C in air for 30 minutes to oxidize all the carbonaceous species to CO_2, thus, templating a high surface area Fe-W oxide film. Second, annealing this film in 5% hydrogen in nitrogen at 610 °C for one hour to reduce Iron from (III) to (II) oxidation state and form crystalline iron tungstate. These films were then cooled naturally to room temperature and were used for further characterization.

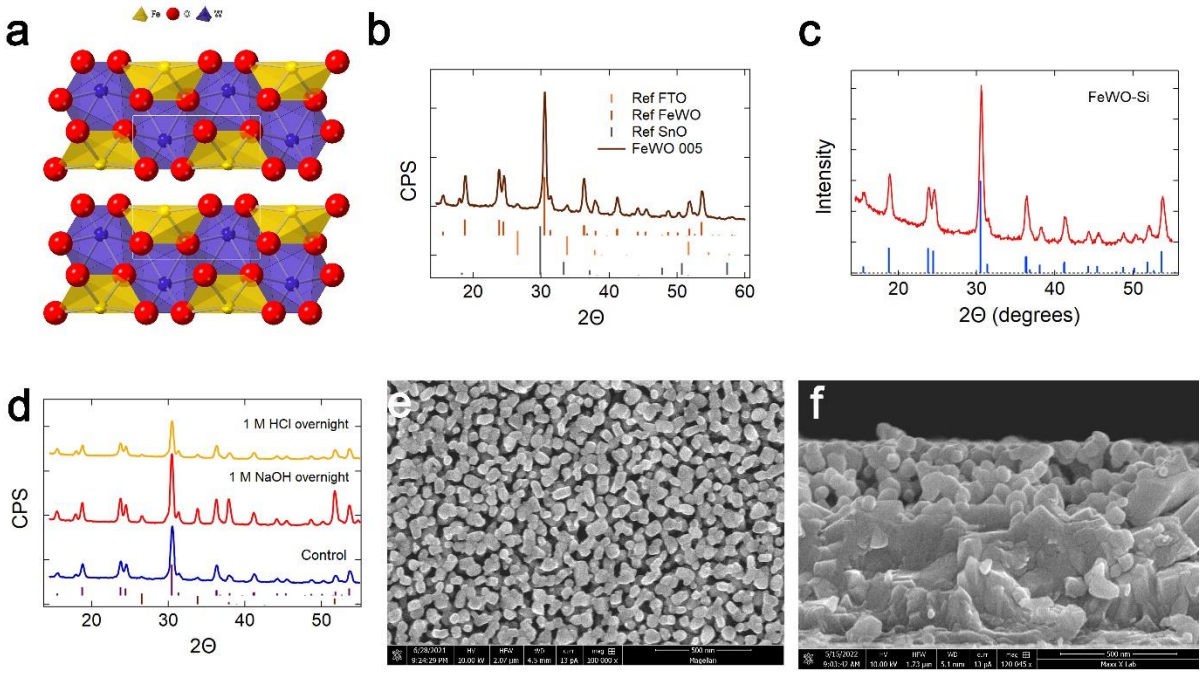

Figure 3.14 Crystal and morphological properties of Iron tungstate films. a) FeWO unit cell, b) GIXRD pattern for a FeWO film grown on FTO coated glass, c) GIXRD pattern for a FeWO film grown on silicon, d) crystal stability in pH 0 solution (1 M HCl) and pH 14 solution (1M NaOH), e) plan view SEM image and, f) cross section SEM image.

Figure 3.14b shows the GIXRD pattern of FeWO films grown on FTO coated glass substrate. Most of the peaks match for ferberite Iron tungstate with PDF card # 01-074-1130, however, peaks at 18°, 26° and 34° are phase impurities. These extra peaks are absent in films prepared on silicon (Figure 3.14C) as a substrate suggesting that it has to do with the substrate or interface. Blank FTO annealed at 610 °C for 1 hour in 5% hydrogen in nitrogen did not show any extra peaks suggesting the extra peaks form at the interface in the presence of Iron and tungsten.

FeWO shows excellent chemical stability in both highly acidic as well as highly alkaline solutions. Figure 3.14d show the GIXRD patterns of the FeWO films kept immersed in 1 M HCl and 1M NaOH overnight. Both films retain good crystallinity. The reason behind the exceptional stability of this material in the whole pH range lies in the stability of its constituent binary oxides in the

complementary section of pH range. According to its Pourbeux diagram, FeWO forms at neutral pH. However, once formed, it can readily form and Fe_2O_3 protective layer in base and WO_3 protective layer in acid, thus cover both ends of the pH range. Figure 3.14e and f show the plan view and cross section SEM images of a typical FeWO film. The grain size is 52 ± 7 nm and the film thickness is 256 ± 12 nm. Both grain size and film thickness are highly tunable by tuning metal ion concentration, amount of polymer, annealing time and annealing temperatures.

3.4.2. Optical properties

Figure 3.15a shows the absorptance, reflectance, and transmittance spectra of a standard FeWO film grown on FTO coated glass substrate. The absorption edge lies around 800 nm. The absorptivity is of the order of 10^4 cm^{-1} for wavelengths below 540 nm. Th material is theoretically predicted to be an indirect bandgap semiconductor which reflects in the linear Tauc plot fitting for $(\alpha hv)^{0.5}$ vs hv. The direct band gap is around 2 eV.

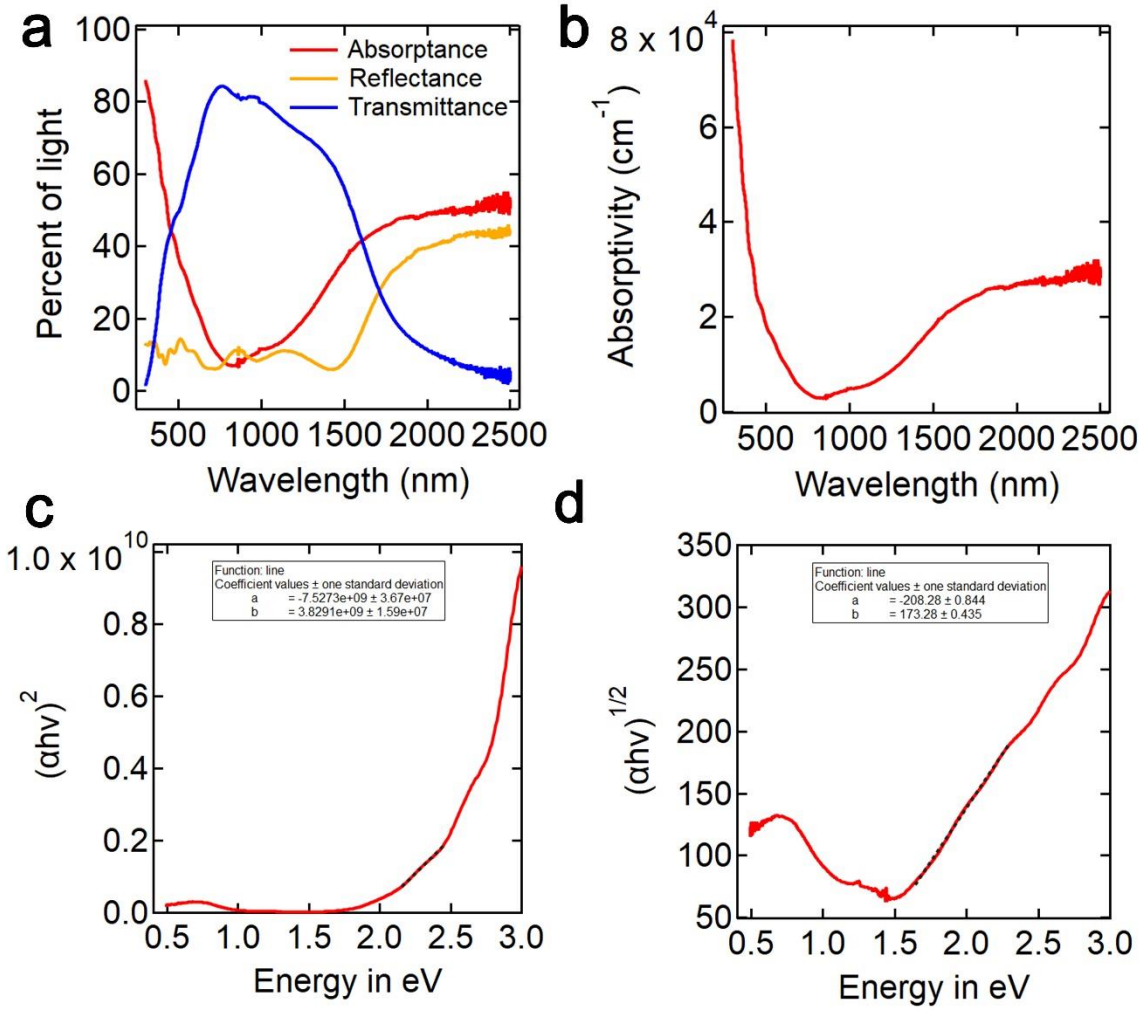

Figure 3.15 Optical properties of Iron tungstate films. a) absorptance, transmittance and reflectance spectra of standard FeWO films grown on FTO coated glass substrate, b) absorptivity spectra of the same film, c) direct band gap Tauc plot fitting, and d) indirect bandgap Tauc plot fitting.

3.4.3. PEC device testing

The photoelectrochemical testing of FeWO films were carried out in 0.1 M phosphate buffer (pH 7) with 0.1 M sulfite as hole scavenger. Figure 3.16a shows the cyclic voltammetry with FeWO films as working electrodes. These films show a small reversible redox process around 0.25 V vs RHE, which might be due to surface tungsten. Films show small, but highly stable positive photocurrent under chopped illumination and bias at 1.23 V vs RHE.

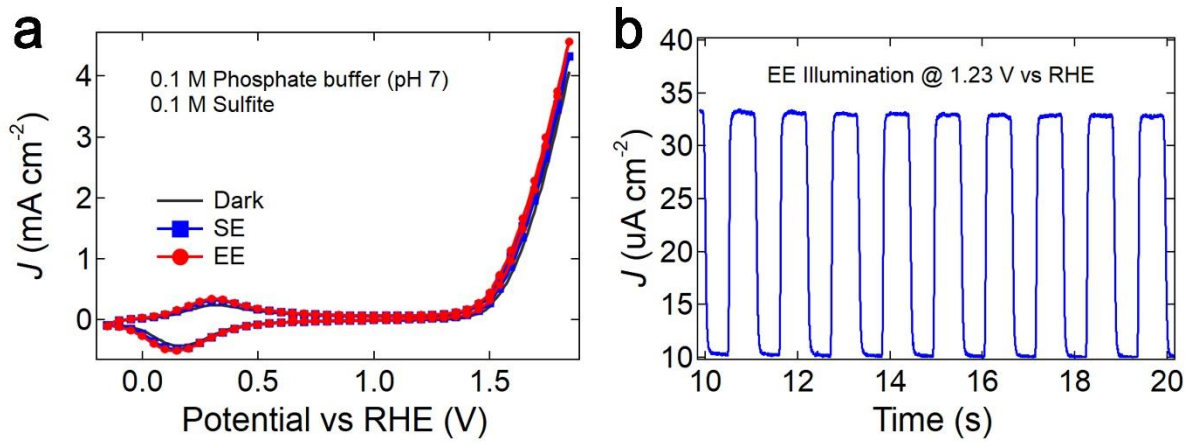

Figure 3.16 Photoelectrochemical properties of FeWO films. a) CV measurement for FeWO films grown on FTO coated glass substrate with 0.1 M phosphate buffer as electrolyte and 0.1 M sulfite as hole scavenger and b) J-t measurements at 1.23 V vs RHE under chopped illumination.

3.4.4. Conclusion

Here we have fabricated a high surface area nanostructured iron tungstate film which is a first report of a solution processible high surface area FeWO film. These films show a 2-eV direct band gap and 1.5 eV indirect band gap. They absorb decent part of visible and UV section of solar spectrum. They exhibit excellent stability in both highly acidic as well as highly alkaline solutions. The positive photocurrent is small but highly stable. The next goal for the development of FeWO electrode is to improve the photocurrent by tuning the electronic properties of these film by primarily doping, but also by texturing or by forming junctions.

4. Deterministic Dimerization of Gold Nanoparticles for Precision Plasmonics

A portion of this chapter has been adapted from a research article (Engelbrekt, C.; Gargasya, Y.; Law, M. Silica Shell Growth on Vitreophobic Gold Nanoparticles Probed by Plasmon Resonance Dynamics. J. Phys. Chem. C 2021, 125 (45), 25119-25125.)

4.1. Main idea

Colloidal metal nanocrystals with strong and tunable LSPR bands in long wave - ultraviolet, visible and near-infra red have received great attention in last few decades for fundamental studies and applications such as chemical sensing, photocatalysis, disease detection, photothermal therapy and surface enhanced spectroscopy. Two nanoparticles (Figure 4.1a) coming close leads to a strong plasmonic coupling, an appearance of a red shifted longitudinal plasmonic band and nm^3 region od strong electric field enhancement (hot spot) in the NC gap. These hotspots form the basis of surface enhanced Raman spectroscopy. Despite the fundamental and practical importance of gold nanoparticle dimers, the large-scale single pot synthesis of monodisperse NC dimers stays a challenge.

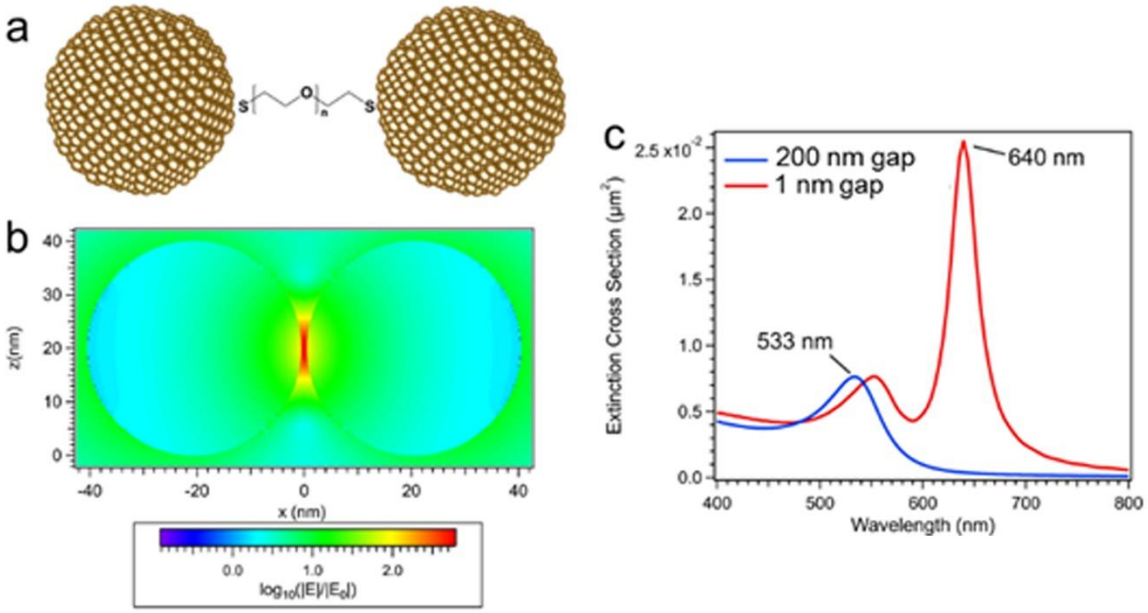

Figure 4.1 FDTD calculations for gold nanoparticle dimers. a) Schematic diagram of a gold nanoparticle dimer,) calculated electric field enhancements for a gold nanoparticle (40 nm nanoparticle size, 1 nm gap size, and electric field enhancement of 600 times in the gap) calculated far field extinction spectra of two gold nanoparticles at 1 and 200 nm gap.

While dimerization is routine in atomic and molecular chemistry, NC dimerization is particularly challenging as unlike a molecule, a NC can have 10^2-10^4 binding sites of similar reactivity and thus, it is difficult to bind it selectively to just one other NC. The two approaches usually followed are asymmetric functionalization and arrested aggregation. In the asymmetric functionalization gold nanocrystal dimerization occurs at the solid-liquid or liquid-liquid interface to break symmetry . However, the processes tend to be complicated and yields poor. Arrested aggregation involves first initiating NC linking using species like DNA,[112] amide bond formation,[113] dithiols,[114] antisolvents[115] and neutral nonbinding ligands[116] etc., and then arresting the aggregation by using silica growth,[117] polymers,[118] or phospholipids.[119] This method provides a dispersion of oligomers which requires a post synthesis separation to achieve dimers.

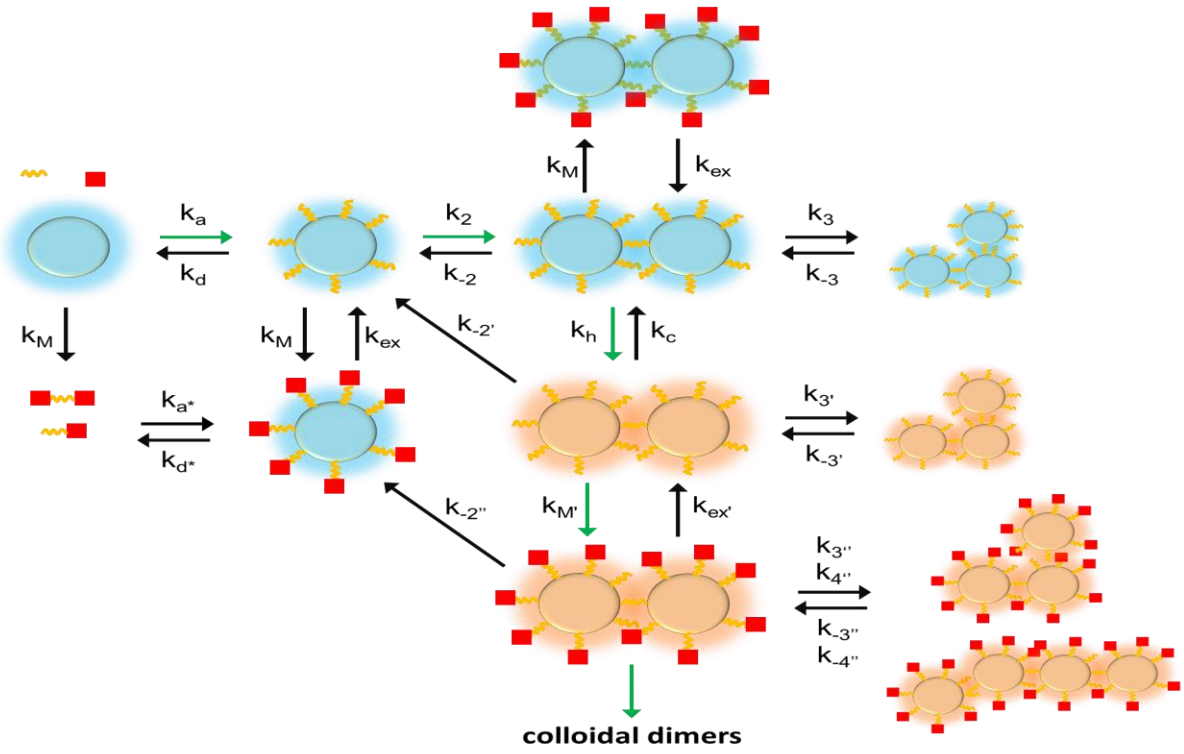

Figure 4.2 Schematics of light driven gold nanoparticle dimerization Kinetics

The goal of this chapter is to develop a simple, single pot synthesis of monodisperse gold NC dimers with controlled gap size. To achieve this goal, we will initiate the aggregation in gold nanocrystals while illuminating the sample with light (with wavelength > 630 nm) to selectively excite the dimers. This photonic excitation will eventually convert into lattice heat in ~ ns which will accelerate the passivation chemistry selectively on the dimer surface. Given, a dimer is the first step in aggregation and our approach can potentially inhibit the aggregation at dimer stage, we can achieve the target of 100% NC dimerization following this approach.

4.2. Gold nanocrystal synthesis

Gold nanocrystal synthesis primarily, has two components. First- reduction of gold salt with a reducing agent, which decides the rate of formation of gold atoms, and second - presence of a ligand, which dictates the relative stability of crystal facets of gold. Together, these two factors lead to nanocrystals with controlled size and shapes like spheres[120], trigonal prims[121], nanorods[122], pentagonal bipyramids[123], truncated decahedra[124], etc. Below are the syntheses for faceted nanocrystals with physically labile and easily exchangeable citrate and perfectly round nanospheres stabilized by a CTAC double layer.

4.2.1. Citrate capped gold nanocrystals

Citrate capped gold nanocrystals were synthesized by a kinetically controlled seeded growth synthesis.[125] In a typical synthesis, 2.2 mM trisodium citrate (150 ml) was heated to boiling under vigorous stirring. A water-cooled condenser was utilized to minimize solvent loss. 25 mM Tetrachloroauric acid (1 ml) was quickly injected once citrate solution started bubbling. The solution color quickly changed from colorless to yellow to bluish grey and stabilized at light pink in 10 minutes. The resulting solution had gold seeds (~ 10 nm, 10^{12}NC's/ml).

Immediately after 10 minutes, the temperature was lowered to 90° C to encourage growth over nucleation and 25 mM $HAuCl_4$ (1ml) was quickly injected. The procedure was repeated twice after an interval of 30 minutes. Upon completion, 55 ml of solution was removed from the reaction mixture and was replaced with 53 ml of water and 2 ml of 60 mM trisodium citrate solution to maintain the pH and nanocrystal stability. This process was repeated multiple times to achieve nanoparticles with subsequently larger sizes.

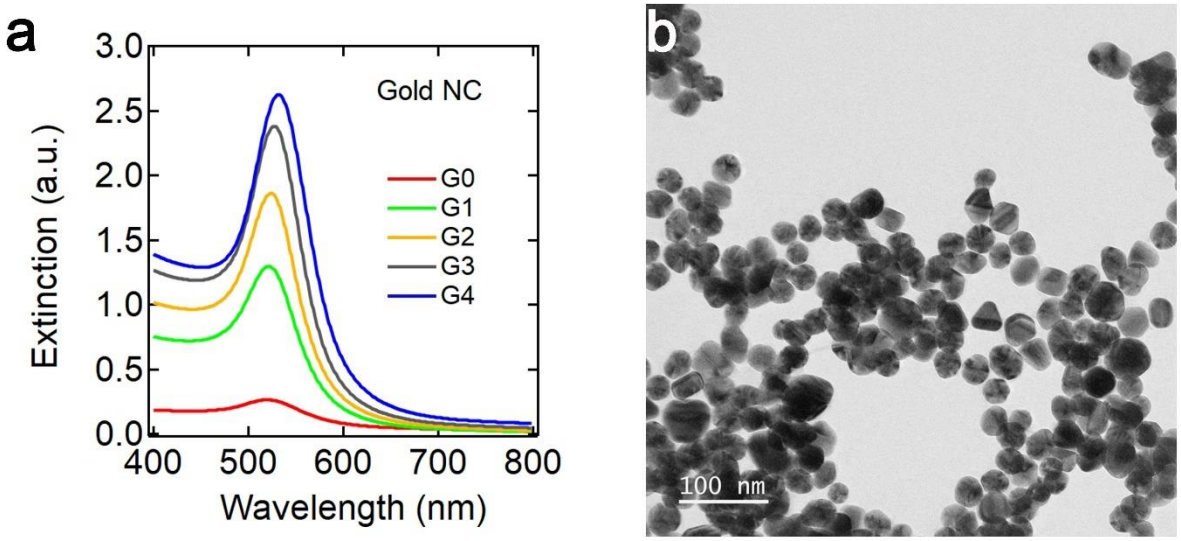

Figure 4.3 Optical and morphological characterization of citrate capped gold nanoparticles. a) Extinction spectra of gold nanoparticles of different sizes and b) TEM image of 30 nm gold nanoparticles.

Oligoethylene glycol dithiol was used as the linker for this application as it is Raman silent (in the region of general interest), water soluble, has a very strong binding with the gold, and has a tunable molecular length from 0.5 nm to 3 nm by tuning the number of ethylene glycol units in the molecule. Hexaethylene glycol dithiol (HEGDT) was molecule size of 2 nm was utilized in this study as linker. Bellow section attempts to understand the aggregation process of gold nanocrystals in the presence of a dithiol and the role of factors like dithiol concentration, presence of other monothiols, and pH on the rate of aggregation.

4.2.2. HEGDT concentration effect

In a typical sample, 1 ml as synthesized 30 nm gold NC colloids were added to water with variable concentrations of HEGDT. The system was monitored for aggregation over time with UV Visible spectrophotometer. (Figure 4.5) There is no aggregation below a certain concentration threshold which is almost 5 uM for this system. The aggregation rates increase upon increasing HEGDT concentrations until they hit a maximum after which further increase in HEGDT concertation lowers the rate of aggregation. This happens ash the rate of aggregation depends on the product of the concentrations of free gold site and a sticky HEGDT attached to a gold NC.

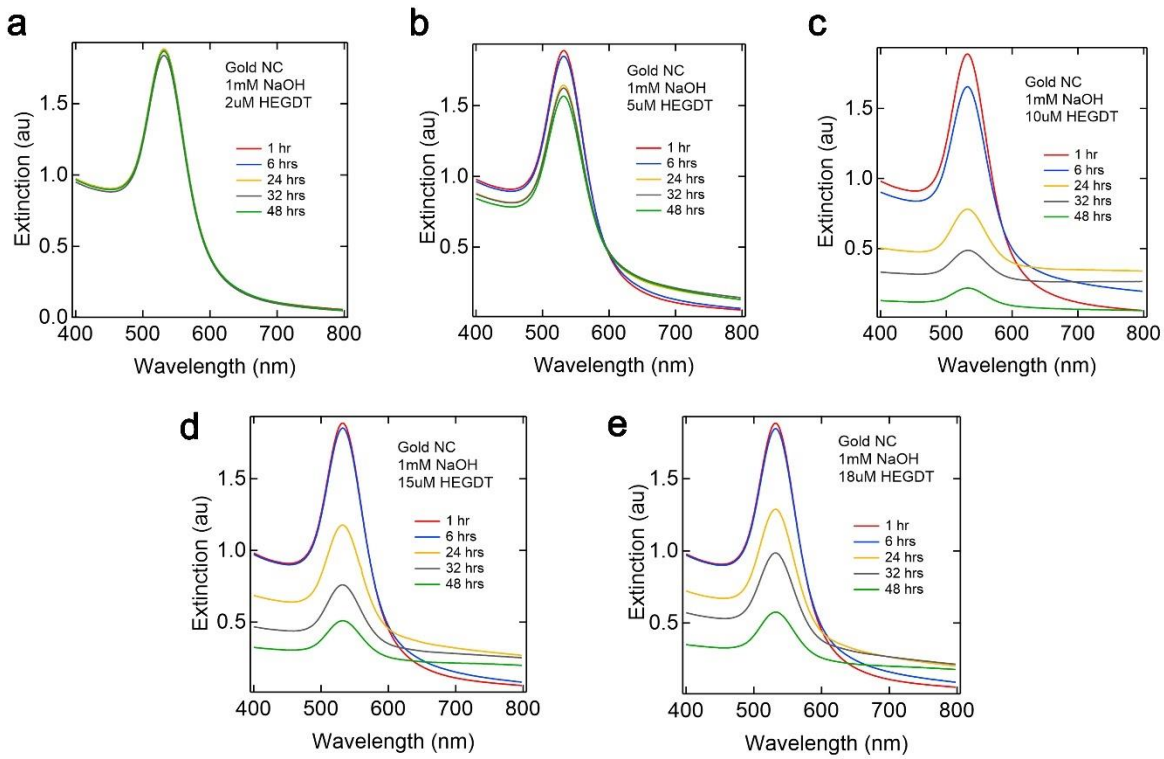

Figure 4.4 Gold NPs aggregation kinetics as a function of HEGDT concentration. a) 2 uM HEGDT, 5 uM HEGDT, c) 10 uM HEGDT, d) 15 uM HEGDT, and e) 18 uM HEGDT.

At low HEGDT concentration There are not enough sticky HEGDT ends with other side attached to a gold NC and at high concentration, there are not enough vacant gold site to bind to. Thus, rate of aggregation is maximum somewhere in the middle. This is an effect which has been reported in the past too.[126]

4.2.3. Thiol cocktail effect

Another handle that can be used to tune the aggregation rates is the presence of a monothiol to compete for the gold atom sites on NCs. Mercapto propionic acid can be an appropriate molecule for this job. Its size, charge and NC stabilization mechanism is same as sodium citrate. However, adding MPA to the gold NC colloid leads to immediate aggregation due to zeta potential destabilization. The current methods to do ligand exchange from citrate to

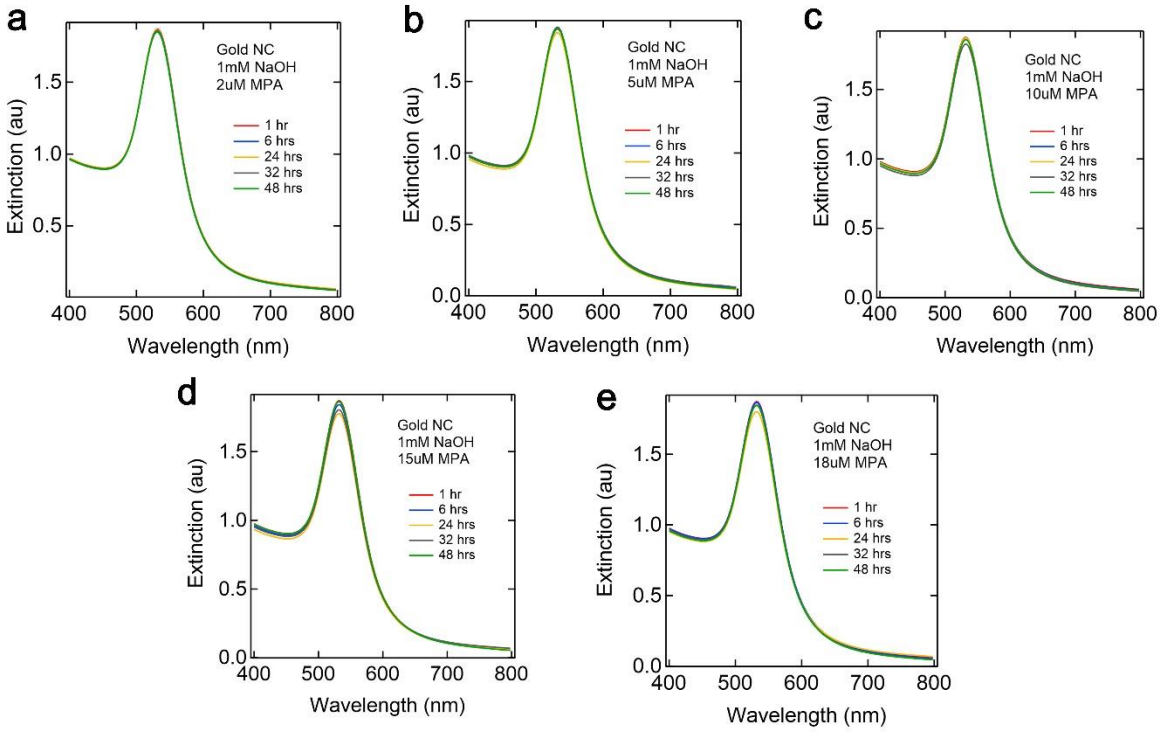

Figure 4.5 Stability of gold NPs upon addition of MPA. a) 2uM, b) 5uM, c) 10 uM, d) 15 uM, and e) 18 uM.

MPA are time consuming and require multiple centrifugation and slow ligand exchange, first to polyethylene glycol thiol and then to MPA in ~48 hours. We found that with addition of 1 mM NaOH solution to the gold colloid, MPA ligand exchange does not cause any aggregation and leads to a stable gold NC colloid at different MPA concentrations. (Figure 4.6)

Effect of MPA was studied at two different net thiol concentrations of 200 uM (Figure 4.7) and 20 um (Figure 4.8). HEGDT to Total thiol percentages were varied from 10%, 25%, 50%, 75%, and 90%, with 0% and 100% shown in the last two figures. It was noted that aggregation started with at least 50% HEGDT in the system, after which the rate of aggregation increased with an increase in the percentage of HEGDT in the solution reaching a maximum at 90% where the aggregation behavior was close to 100% HEGDT as expected.

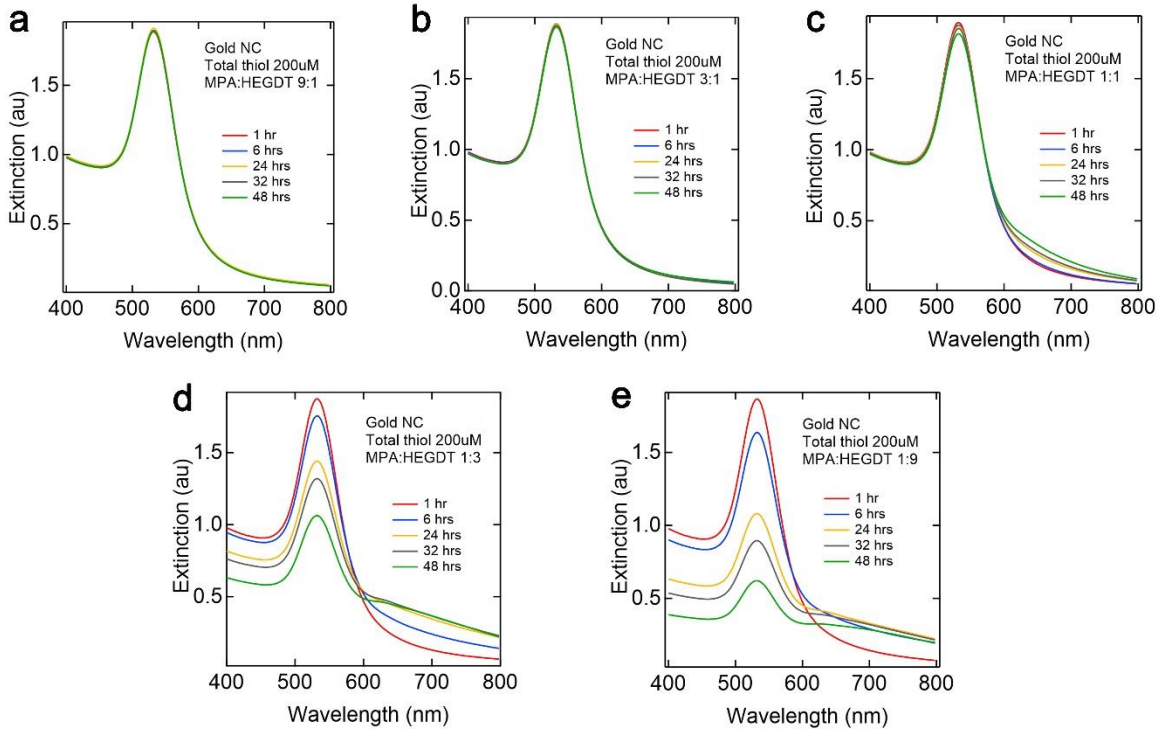

Figure 4.6 Cocktail effect under 200uM net thiol concentration. a) 10% HEGDT, b) 25% HEGDT, c) 50% HEGDT, d) 75% MPA, and e) 90% HEGDT.

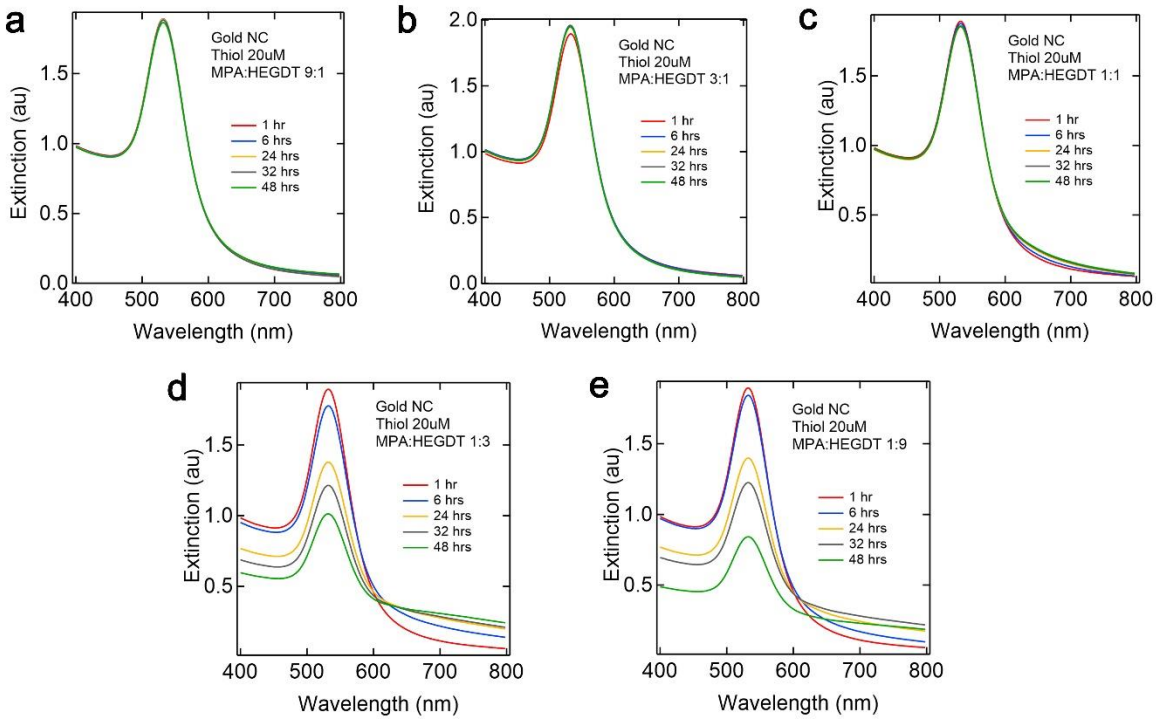

Figure 4.7 Cocktail effect under 20 uM net thiol concentration. a) 10% HEGDT, b) 25% HEGDT, c) 50% HEGDT, d) 75% MPA, and e) 90% HEGDT.

Another interesting effect observed was no effect of net thiol concentration on aggregation behavior. With net thiol concentration either 20 uM or 200 uM, aggregation started at 50% HEGDT, suggesting a very statistical nature of aggregation in the presence of a competing mono thiol. Thus, MPA concentration can be further used to tune the aggregation rates if needed.

4.2.4. pH effect

Given that the citrate capped gold nanocrystals are negative charge stabilized, it is expected that their zeta potential and thus, stability can be tuned by adding protons (common acid HCl) to the system. Figure 4.9 shows an increase in the rate of aggregation upon addition of acid. Excess of protons lead to decrease in zeta potential that allows gold nanocrystals to come close in proximity

before getting repulsed by the surface charge. This gives a higher opportunity for thiols to bind to gold nanocrystals and link them together.

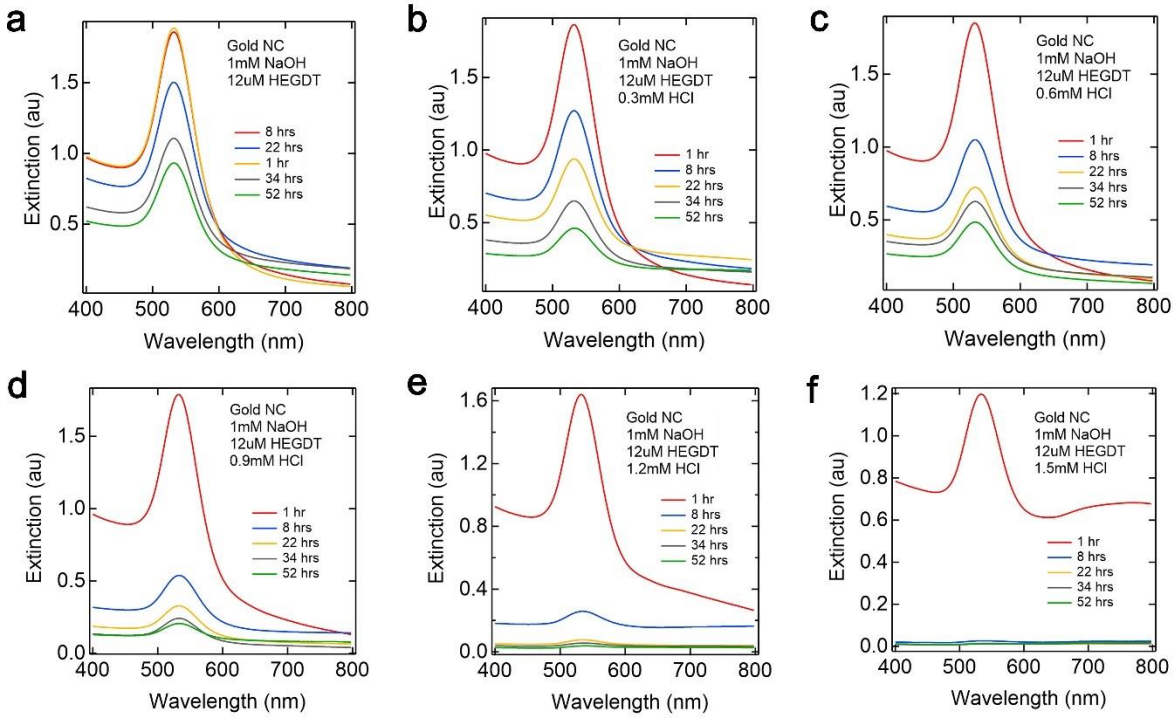

Figure 4.8 pH effect on aggregation rate of gold NPs with 100% HEGDT. a) 0 mM HCl**,** b) 0.3 mM HCl, c) 0.6 mM HCl, d) 0.9 mM HCl, e) 1.2 mM HCl, and f) 1.5 mM HCl

This is an excellent handle that can be used to increase the rate of aggregation. A 60% HEGDT shows very low rates of aggregation however, the rates enhance significantly upon addition of just 0.3 mM HCl.(Figure 4.10). similarly, a 50% HEGDT system is also expected to show very weak aggregation rates but addition of just 0.3 mM HCl is enough to accelerate the aggregation. This becomes even more important in systems where no aggregation was supposed to happen for example HEGDT percentages less than 50% (25% and 10%). Figures 4.12 and 4.13 show that aggregation can be initiated even in these systems if we add more acid to the system

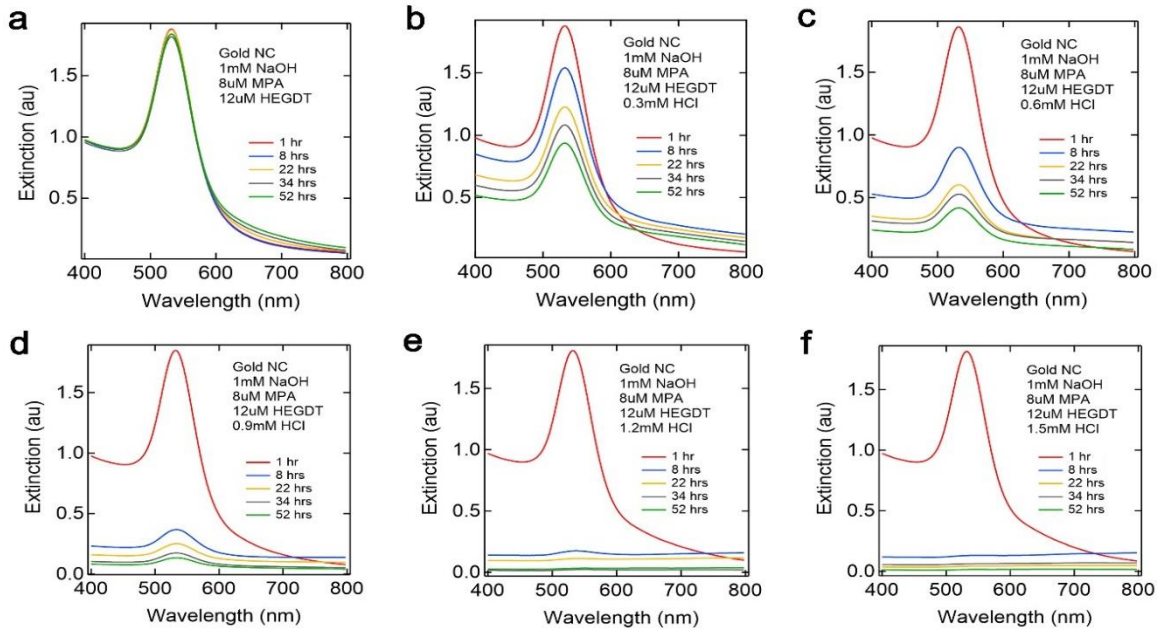

Figure 4.9 pH effect with 40-60 MPA-HEGDT. a) 0 mM HCl**,** b) 0.3 mM HCl, c) 0.6 mM HCl, d) 0.9 mM HCl, e) 1.2 mM HCl, and f) 1.5 mM HCl

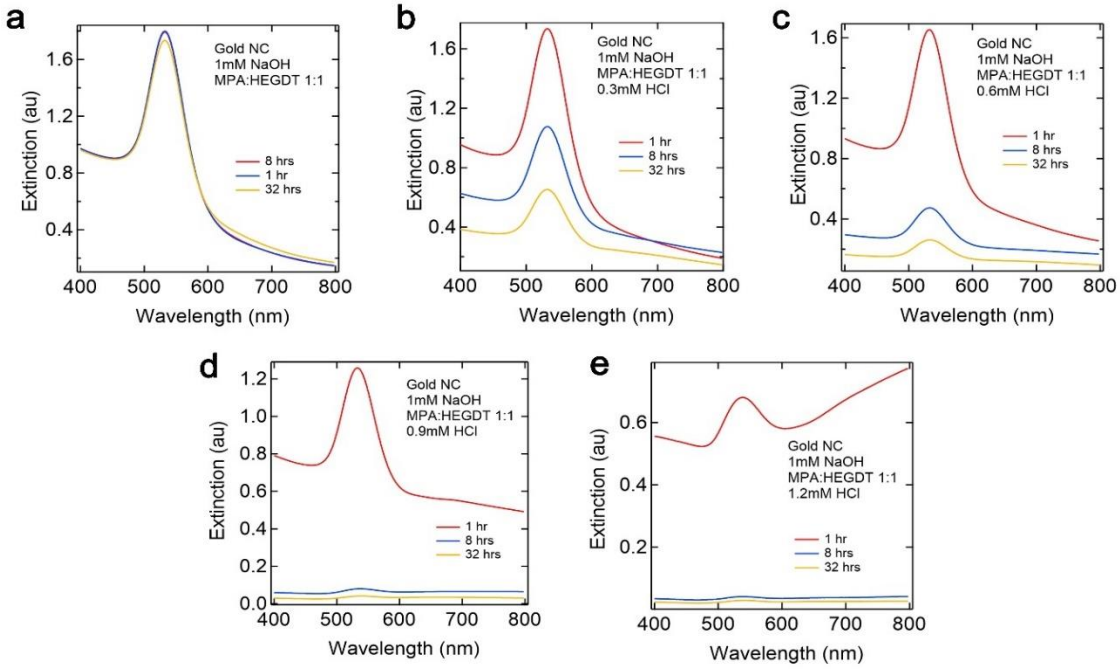

Figure 4.10 pH effect on 50-50 MPA -HEGDT system. a) 0 mM HCl**,** b) 0.3 mM HCl, c) 0.6 mM HCl, d) 0.9 mM HCl, and e) 1.2 mM HCl.

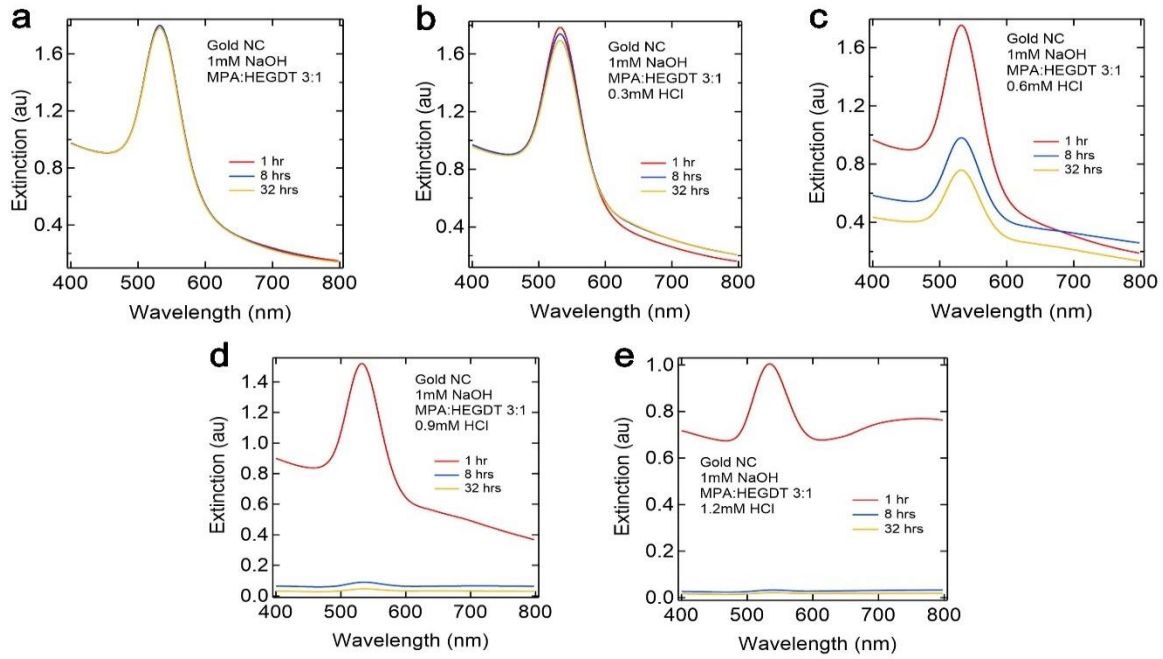

Figure 4.11 pH effect on 75-25 MPA - HEGDT system. a) 0 mM HCl**,** b) 0.3 mM HCl, c) 0.6 mM HCl, d) 0.9 mM HCl, and e) 1.2 mM HCl.

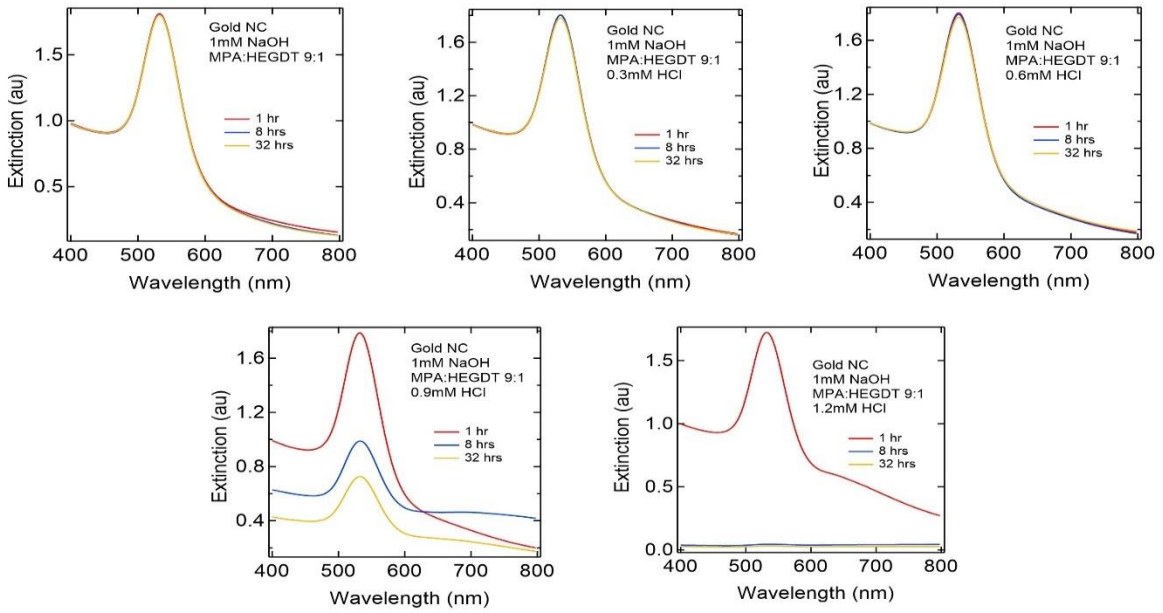

Figure 4.12 pH effect on 90-10 MPA - HEGDT system. a) 0 mM HCl**,** b) 0.3 mM HCl, c) 0.6 mM HCl, d) 0.9 mM HCl, and e) 1.2 mM HCl.

So, a system with just 25% HEGDT can be aggregated in the presence of 0.6 mM HCl and a system with barely 10% HEGDT can be aggregated in the presence of 0.9 mM HCl. It should be noted that we started with 1mM NaOH to ensure that MPA does not cause any aggregation and addition of 0.9 mM HCl brings the system still keep the pH of the colloid greater than 4.75, below which the gold colloid gets unstable.

Thus, we can tune the rate of aggregation with multiple handles like HEGDT concentration, presence of a monothiol, addition of acid, concentration of gold NCs etc.

4.3. Passivation chemistries

The passivation of nanocrystal surface can be done either by an accelerated molecular reaction with all the sticky thiol ends or by growing a solid oxide and burying a dimer in it. Thiol ene click reactions were chosen for the molecular approach and silica growth on gold nanoparticles was chosen for the accelerated solid oxide growth on gold NC dimers. Both approaches bring their own advantages and challenges. The advantage of the molecular approach is that it allows the Raman active molecules to reach the hot spot and so analyte can be intruded at any stage in the system. However, since the mechanism behind passivation chemistry acceleration is thermal, there is a chance that a lot of dimers may undergo necking or coalescence during the illumination, especially when gold atoms are known to be very labile and move continuously on the surface. The advantages with using silica growth as passivation chemistry is robustness and mechanical and thermal stability that it can provide to the newly formed dimer. However, there is a high chance that it might block the hotspot for analyte. A good bypass to this problem is either to introduce analyte during the dimer synthesis or make an extremely porous silica coat that stabilize the gold dimer but leaves avenues for the molecules to diffuse into the hot spots.

4.4. Thiol ene click chemistry

Thiol ene click chemistries are of particular interest for passivating sticky HEGDT ends as these chemistries are highly efficient, leave no by product, activation energies can be tuned by tuning the electron withdrawing group attached to ene and is largely carried out at near neutral pH where gold colloid is stable. Figure 4.14 shows the schematic diagram and reaction of thiol ene click reactions. Common enes used for click reactions can be classified in three categories. 1) ene in conjugation with two electron withdrawing groups + ring strain, example maleimide These molecules tend to be the most reactive for thiol ene click reactions and react within minutes upon exposure to thiols. 2) ene in conjugation with one electron withdrawing groups, for example acrylates, which react with thiol within days. These are promising class of enes with low reactivity at room temperature and high reactivity at an elevated temperature. 3) The third category is an ene without any electron withdrawing group in conjugation . These molecules do not react with thiols

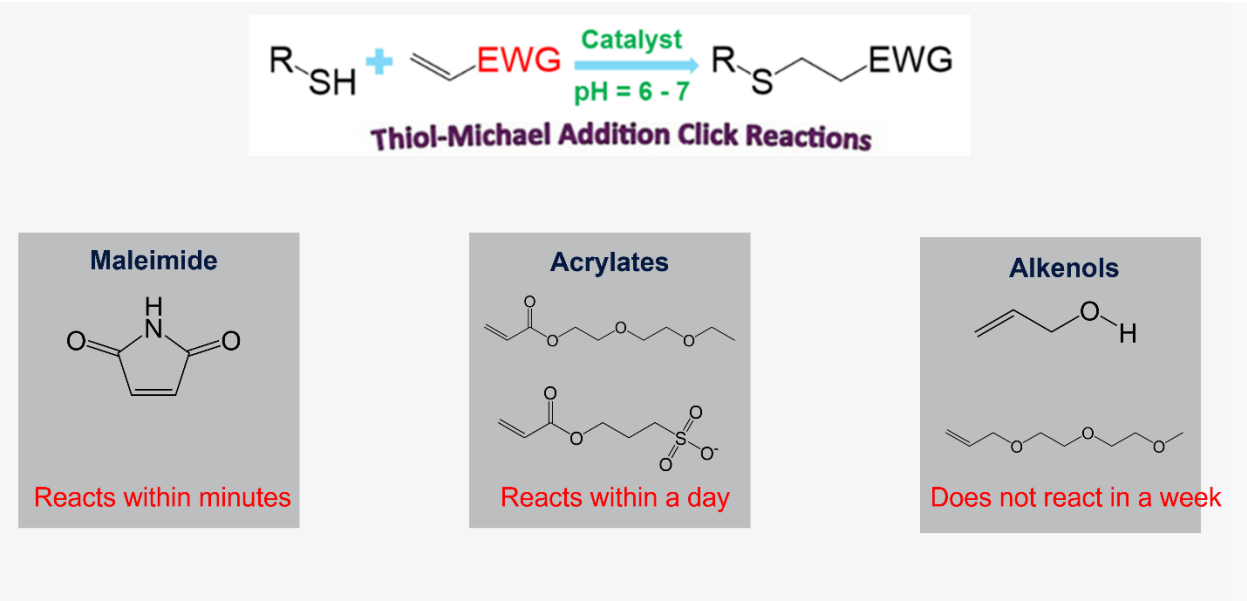

Figure 4.13 Schematic diagram of various classes of thiol ene click reactions

even in weeks and might need a catalyst in addition to high temperature to react with thiols. For our experiments, we have used molecule – **Diethyleneglycol Ethyl Ether acrylate (DEE)** from second category. The acrylate part of the molecule reacts with thiol whereas ethylene glycol improves its water solubility.

4.4.1. Passivation chemistry at room temperature

The concentration of DEE was kept around 10 mM in water, near its solubility limit to ensure that its reactivity is not limited by diffusion. Figure 4.14 shows the impact of DEE on aggregation rate of gold NCs at room temperature. Addition of DEE minimizes the rate of aggregation at room temperature, this corroborates the NMR data suggesting a slow but quantifiable rate of HEGDT-DEE reaction which takes around 24 hours to complete at room temperature.

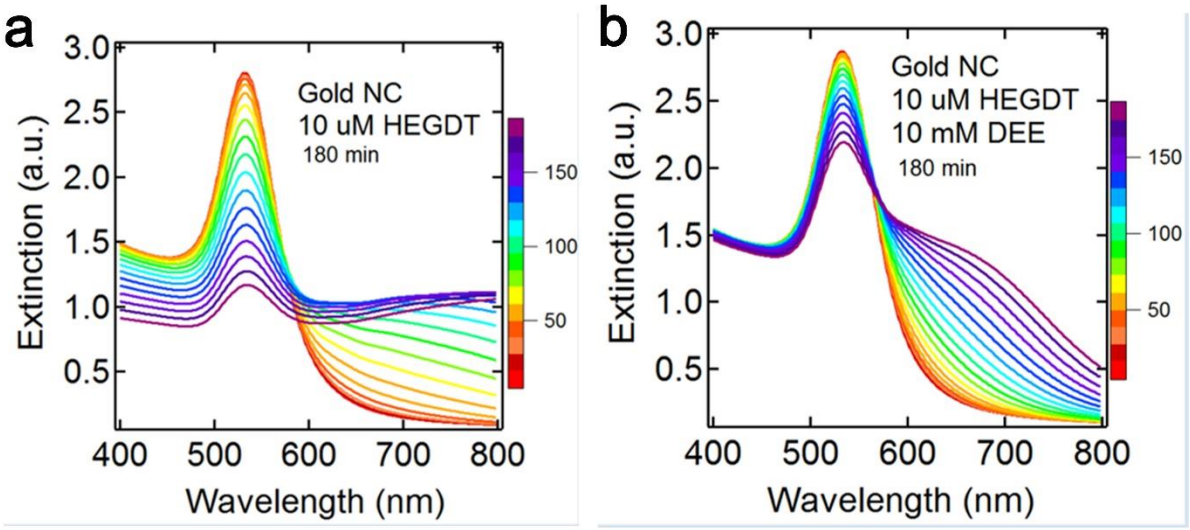

Figure 4.14 Ene effect at room temperature. a) Gold NC with 10uM HEGDT at room temperature and b) Gold NC with 10uM HEGDT and 10 Mm DEE at room temperature.

4.5. Silica growth on gold surface

Growing silica can be another approach for passivating and protecting a gold nanoparticle dimer. Nanotechnology based on colloidal silica started in 1968 with the work of Stöber, Fink, and Bohn, who presented a protocol for controllable synthesis of silica sols now known as the Stöber method.[127] Three decades later, Mulvaney, Giersig, and Liz-Marzán demonstrated silica growth on gold colloids *via* a modification of the Stöber method.[128]The process entailed three separate steps: (1) ligand exchange from citrate to aminosilane, (2) slow formation of a thin silica shell from active silica in water, and (3) further growth *via* alkoxysilane hydrolysis and condensation in ethanol. It was argued that the vitreophobic character of the citrate-terminated AuNP surface prevents the formation of conformal silica shells, prompting the replacement of citrate with aminosilane to provide a vitreophilic surface.[128] This report laid the foundation for the field of gold-silica core–shell nanoparticle (Au@SiO_2 NP) synthesis and applications. Since 1996, a number of modifications to the original report have been developed. The group of Xia directly coated commercial AuNPs with silica, omitting the two first steps of the previous protocol.[129]The Xia method, in which tetraethyl orthosilicate (TEOS) is hydrolyzed in a mixture of isopropyl alcohol (IPA) and water using ammonia as a catalyst, is frequently used for Au@SiO_2 NP synthesis. Many variations on these previous methods have been developed for various systems, and all consist of the same general components, that is, a silica precursor (sodium silicate, [128130131132], tetramethyl, [130] -ethyl, [133134135136137138139140141142143] or -propyl[130] orthosilicate, or diglyceroxysilane,[141] a water/organic solvent mixture (ethanol [133134135128130131128137138144139140141142] methanol,[130] or IPA,[145129143] and base, (NaOH[134130144140] or NH_4OH[133135128137141142143]). AuNPs of different shape and surface functionalization have been coated with silica. Commonly, silica shells are formed directly on spherical citrate-capped AuNPs (cit-AuNPs).[133135129137142143] or after

exchange of the original ligand with vitreophilic ligands such as (3-aminopropyl)-[134128130] or (3-mercaptopropyl)-trimethoxysilane[130](APTMS or MPTMS) or polymers such as polyvinylpyrrolidone.[133138141]

The optical properties depend strongly on the thickness and morphology of the silica shell, and significant efforts have been made on understanding these relations.[145129] To the best of our knowledge, only one paper reports the time dependence of this process, and with relatively low time resolution (1 h).[142] Here, we employ time-resolved ultraviolet–visible (UV–vis) spectroscopy to monitor the formation of silica shells on AuNPs with ∼1.5 min time resolution. By applying a simple analytical model to the spectra, the time dependence of the physically motivated parameters describing the LSPR and the bulk silica can be extracted. The silica shell formation mechanism is studied through analysis of the formation kinetics under different reaction conditions. This analysis is supported by dynamic light scattering and *ex situ* electron microscopy imaging of Au@SiO_2 NPs at different stages of silica growth. The combination of high time resolution and the analytical model is crucial for the kinetic analysis that identifies a surface reaction preceding the formation of silica which may be rate limiting for shell formation. The early growth of silica is also shown to be non-uniform, with initial nucleation and growth on vertices/edges, and growth to several nanometers in thickness before coalescing into a conformal shell. This observation stresses the need for chemical surface modification on vitreophobic AuNPs to achieve uniform thin silica shell coatings.

Our approach further demonstrates how *in situ* UV–vis absorption spectroscopy and LSPR analysis can be used to obtain detailed kinetics information about chemical reactions on colloidal AuNP surfaces. This approach can be applied broadly and may enable better synthesis control of composite AuNP-based nanomaterials.

4.5.1. Preparation of Au@SiO_2 NPs

Silica shells were grown on AuNPs (Figure 4.16a and A3.3) in an alkaline IPA–water mixture. A small volume of TEOS was injected to initiate Au@SiO_2 NP formation, which was completed in 15 min to 2 h, depending on TEOS concentrations and temperature. Figure 4.15

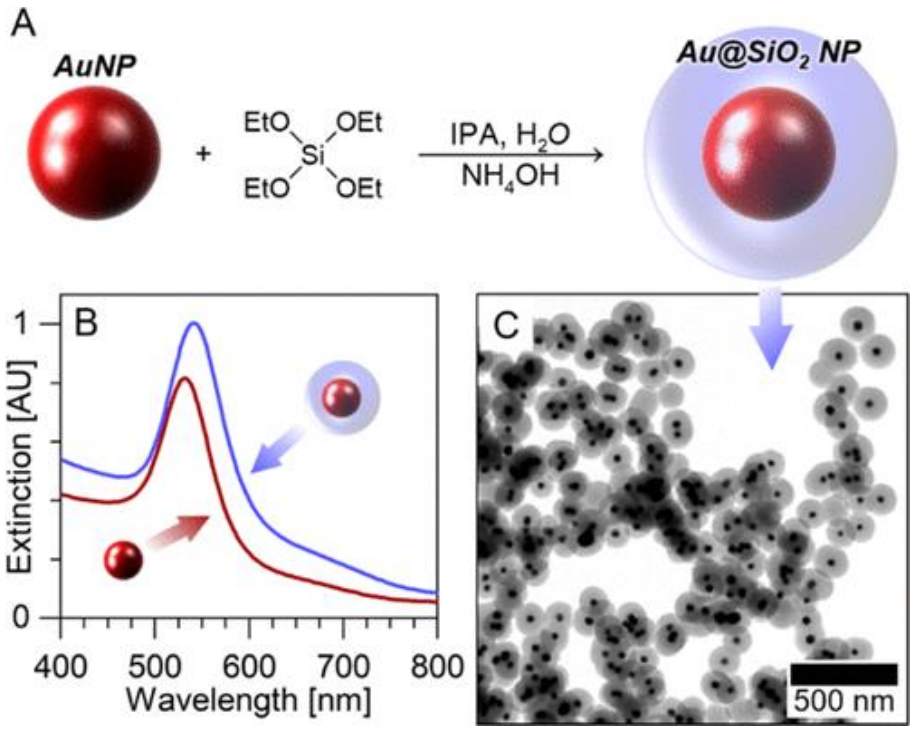

Figure 4.15 Preparation of Au@SiO2 NPs. (A) Silica shells are formed around the cit-AuNPs from *via* TEOS hydrolysis and condensation. (B) Optical extinction spectra of the cit-AuNPs (green) and Au@SiO_2 NPs (blue). (C) Representative transmission electron micrograph of the final uniform core–shell product.

4.5.2. Analysis of *in-situ* UV Vis spectra

To monitor the Au@SiO_2 formation, UV–vis extinction spectra were continuously recorded while the shells grew on the colloidal AuNPs in a glass cuvette. A representative *in situ* spectral series (Figure 4.16.a) shows three distinct stages of silica growth. The spectral changes during these stages are highlighted in Figure 4.16c–e. In the first stage, the LSPR peak intensity and energy

both decrease slightly (labeled red in the spectral series). In the second stage, a large and rapid increase in peak intensity occurs (labeled orange). The third stage is characterized by a slow increase in intensity across the entire spectrum (yellow and blue). We note that the initial drop in peak extinction has not been previously reported and may contain information about the early steps of silica shell formation.

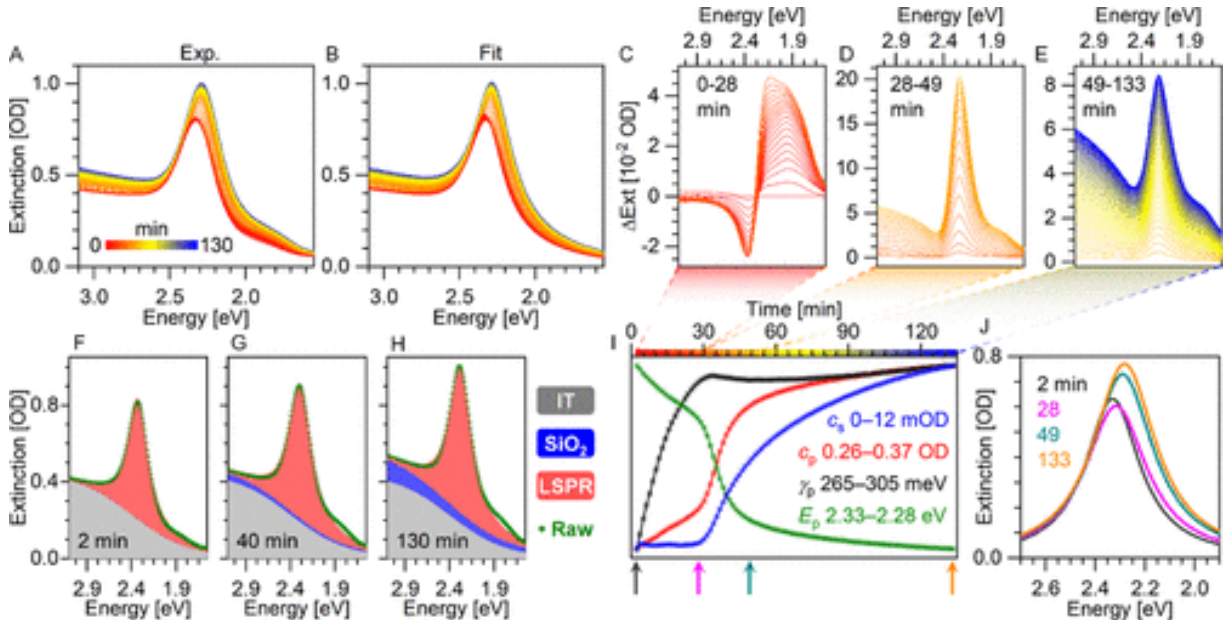

Figure 4.16 Analysis of in situ UV–vis spectra shown for standard reaction conditions (20 ± 1 °C, 2 mM TEOS). A) Experimental and (B) fitted *in situ* spectra. (C–E) Difference spectra showing the change occurring in each distinct stage. (F–H) Recorded spectra (green symbols) and contributions from the interband transition (gray shading), LSPR (red shading), and SiO_2 (blue shading) at three different times during reaction. (I) Time dependence of the fitting parameters. The color scale on the *x*-axis correlates to the color scheme of the spectra in (A–E). The *y*-axis values are different for each fitting parameter (see the legend). (J) LSPR spectra extracted from fits of the first spectrum (gray) and the spectra at the end of each stage. The corresponding time points are indicated with colored arrows in (I).

To better understand the spectral behavior and derive its time dependence, a model of the extinction spectrum was applied. The *in situ* spectra were modeled with three contributions: the LSPR, the gold sp ← d interband transition, and scattering from the silica shell. These

contributions are represented by a Lorentzian distribution, a logistic function (broadened step function), and an exponential growth function, respectively, as shown in equation below.

$$A(E) = \overbrace{\frac{1/2\pi c_p \cdot \gamma_p}{(E - E_p)^2 + \left(\frac{\gamma_p}{2}\right)^2}}^{\text{plasmon}} + \overbrace{\frac{c_i}{1 + e^{-(E - E_i/\gamma_i)}}}^{\text{interband}} + \overbrace{c_s(e^{b_s E} - y_s)}^{\text{silica}}$$

Equation 3.1

The parameters for the interband transition, that is, c_i, γ_i, and E_i, are determined by fitting the first spectrum, where silica has not yet formed and does not contribute. These parameters are then fixed for all the following spectra in an experiment. Similarly, the shape of the silica contribution is determined by fitting spectra of silica particle formation in the absence of AuNPs (Figure A3.5). Here, the spectrum is solely determined by the silica contribution and found to be well represented by an exponential growth function (extinction *vs* energy). The shape of the silica extinction spectrum (represented by the parameters b_s and y_s) did not change during silica growth, so these parameters were fixed in the fits of silica growth on the AuNPs. Overall, there are four time-dependent parameters to be extracted from each spectrum, namely, the three parameters for the plasmon (c_p, γ_p, and E_p) and one for the scattering intensity (amount) of the silica (c_s). As seen in Figure 4.16a,b and A3.6, this model very accurately reproduces the experimental data except for the weak shoulder at ~1.8 eV that is related to a small amount of aggregation induced by the change in the AuNP environment upon addition of IPA and NH_4OH. The aggregation process was effectively instantaneous and had completed before the addition of TEOS, so it did not contribute to the dynamics of silica formation. The accuracy of the fitting model and the time dependence of the parameters were further tested by fitting a series of spectra calculated using Mie theory (Figure A3.7). The model reproduces the calculated spectra well and provides shell thickness-dependent parameters that agree well with time-dependent parameters extracted from fitting of the experimental spectra (Figure 4.16i).

Examples of deconvoluted *in situ* spectra are presented in Figure 4.16f–h, showing the LSPR on top of the interband transition to which a contribution from silica is added. Figure 4.16i shows the evolution of the four fitting parameters from equation 4.1 during a representative Au@SiO_2 NP synthesis with ~80 s time resolution. Here, the three distinct stages are clearly observed. Stage 1 (S1) is dominated by plasmon broadening, stage 2 (S2) is dominated by rapid plasmon redshift and intensity increase, and stage 3 (S3) is dominated by a continuous increase in the silica contribution. The fits show that the decrease in LSPR peak intensity in S1 (Figure 4.16a) does not arise from a reduced intensity of the LSPR (c_p does not decrease) but rather from peak broadening and redshifting down the sloping interband transition (Figure 4.16j).

S2 and S3 correlate well with observations of LSPR dependence on silica thickness by Liz-Marzán and Mulvaney,[128] and others.[129,134,135,137,146] Initially, a redshift occurs followed by increased intensity. This can be explained by changes to the dielectric function of the medium, ε_m, as the silica shell is growing and can be reproduced by Mie theory (as seen in figure A3.7 and shown previously[128]). Changes to ε_m do not explain the behavior observed during S1, which has not yet been described in the literature.

4.5.3. Kinetics analysis of Au@SiO_2 NP formation

In order to better understand the chemistry of S1–S3, the reaction kinetics were investigated by varying the TEOS concentration (1–15 mM) and reaction temperature (20–60 °C). The limits for these parameters were set by the stability of the AuNP sol. The time dependence of all parameters at all experimental conditions is given in Figure A3.8-12. In Figure 4.17, the effect of reaction conditions on the evolution of the LSPR energy is represented by the E_p time curves and on the formation of silica by the c_s time curves. While these parameters do not have direct interpretations

as concentrations of reactants or products, apparent process rates can be extracted from the time curves, and their dependence on experimental conditions is evaluated. The inverse sigmoidal shape of the E_p time curves can be viewed as three approximately linear segments with intersections that indicate the transitions between reaction stages, that is, t_1 (S1 → S2) and t_2 (S2 → S3). These transition times together with the maximum rate of the LSPR energy shift (middle of S2) can be conveniently extracted by fitting the first derivative of $E_p(t)$ with a Gaussian function with full width at half-maximum, w, and center, t_{max}, as illustrated in Figure A3.13. An additional kinetic parameter describing S3 is taken as the maximum rate of increase in silica scattering, that is, the maximum of the first derivative of the c_s time traces.

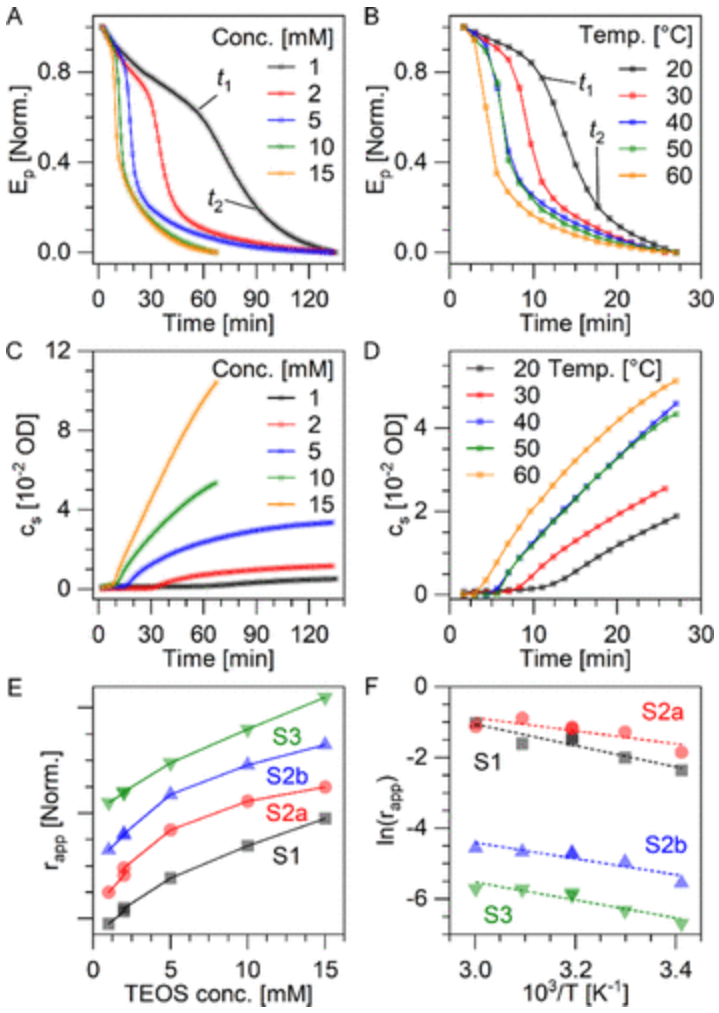

Figure 4.17 Kinetics analysis of Au@SiO2 NP formation. (A,B) Normalized time-dependence of LSPR energy, E_p, (C,D) silica scattering intensity, c_s, and (E,F) kinetic parameters, at varying [TEOS] at r.t. (left column), and various reaction temperatures at 10 mM TEOS (right column). In (A,B), the transitions times t_1 and t_2 are indicated with markers for the slowest reaction (black). In (E,F), r_{app} are determined by the duration of S1 (black), the duration of S2 (red), the max rate of change of S2 (blue), and the max rate of change of S3 (green).

The four apparent rates, r_{app}, are thus defined as below.

$$r_{S1} = t_1^{-1} = \frac{1}{t_{max} - 0.5w}$$

$$r_{S2a} = t_2 - t_1 = \frac{1}{t_{max} + 0.5w}$$

$$r_{S2b} = \max|dE_p/dt|$$

$$r_{S3} = \max|dc_s/dt|$$

These four kinetic parameters can be considered as apparent rates for S1, S2, and S3, that is, the inverse of the duration of S1 and S2 and the maximum rates of change for S2 and S3. Plotting the rates against the TEOS concentration provides insights into the reaction order, Figure 4.17e. S1 and S3 display approximately linear dependence on the TEOS concentration, indicating that these processes are of first order in TEOS. However, the S2 (and to some extent S1) rates show a diminishing increase with increasing TEOS concentrations. This can be understood as S2 representing a surface reaction occurring on the AuNPs that is limited by the reactant concentration on the surface rather than that in solution. The reaction order thus approaches zero at high TEOS concentrations since the fixed number of surface sites on the AuNPs are all occupied, and an increase in the TEOS concentration no longer leads to a rate increase. This surface reaction (S2) may be attributed to the formation of silica through condensation, as shown in Figure 4.16a, agreeing with the emergence of SiO_2 scattering in this phase. This further indicates that S1 describes a step that precedes silica formation, which may be the association of silica precursor species with the AuNP surface and formation of partly hydrolyzed/condensed pre-silica networks.

The rate dependence on temperature was studied in a similar fashion between 20 and 60 °C at a fixed TEOS concentration of 10 mM (right column in Figure 4.17). The Arrhenius-style plot in Figure 4.18f shows that the temperature dependence of the rates are slightly larger for S1 than S2 and S3. This is in good agreement with the generally accepted vitreophobic nature of citrate-stabilized AuNPs and the larger energy barrier associated with the adsorption of silica precursors on the citrate-terminated surface than with growth of the resulting vitreophilic silica shell. Our data thus indicate that the rate of $Au@SiO_2$ formation is limited by adsorption of molecular silica precursors and/or formation of pre-silica networks. The LSPR broadening of the colloid during S1 further support this interpretation, in agreement with previous reports showing a strong correlation

between the LSPR width and the nature of the chemical interface at the surface of the plasmonic metal.[147148] This mechanism of LSPR broadening was associated with both charge transfer to adsorbates and induction of surface dipoles.[148]

4.5.4. Time dependance of silica growth

A comparison of the Au@SiO_2 NP morphology at different temperatures was made by quenching the silica formation reaction by 10-fold dilution in water after 30 min (Figure A3.14). At 20 °C, 30 min corresponds to the beginning of S3. These NPs showed only thin or partial SiO_2 shells. These shells provided insufficient stabilization, and the NPs had therefore aggregated during centrifugation. However, thick SiO_2 shells had formed after 30 min at 40 °C, where the reaction had progressed well into S3. These observations suggest that SiO_2 formation starts in S2 and continues through S3.

The correlation between optical properties and NP size/morphology was further verified by *in situ* monitoring of the hydrodynamic NP diameter and TEM imaging of quenched reaction products around the S2/S3 transition (Figure 4.18 and A3.16). The hydrodynamic diameter, d_h, does not change significantly during S1. In fact, d_h follows very closely the time curve of c_s, supporting the correlation between c_s and the growth of the SiO_2 shell. The quenched reaction products exhibited highly non-uniform SiO_2 shells at early reaction times. As the final Au@SiO_2 NPs appear nearly perfectly spherical, this was unexpected. The non-uniform growth was especially obvious on the small fraction of AuNPs that are anisotropic (*e.g.*, truncated prisms), as seen in Figure 4.18 b-f. During S2, SiO_2 forms in patches that are localized at AuNP vertices and edges, indicating that nucleation happens preferentially at sites of high local curvature. This may be due to curvature-dependent chemical properties of the ligand shell[149] or lower local ligand densities, which has been used in similar systems to selectively coat gold nanorod tips.[140,150] We note that SiO_2

nucleation in solution (rather than on the AuNP surface) followed by attachment to the NP surface is unlikely. First, empty SiO_2 particles in the final product are rare (~10%), and primary SiO_2 nuclei are only found associated with the AuNPs, and second, SiO_2 formation (the rise of c_s) is significantly slower in the absence of AuNPs, indicating the primarily heterogeneous SiO_2 nucleation on AuNP surfaces.

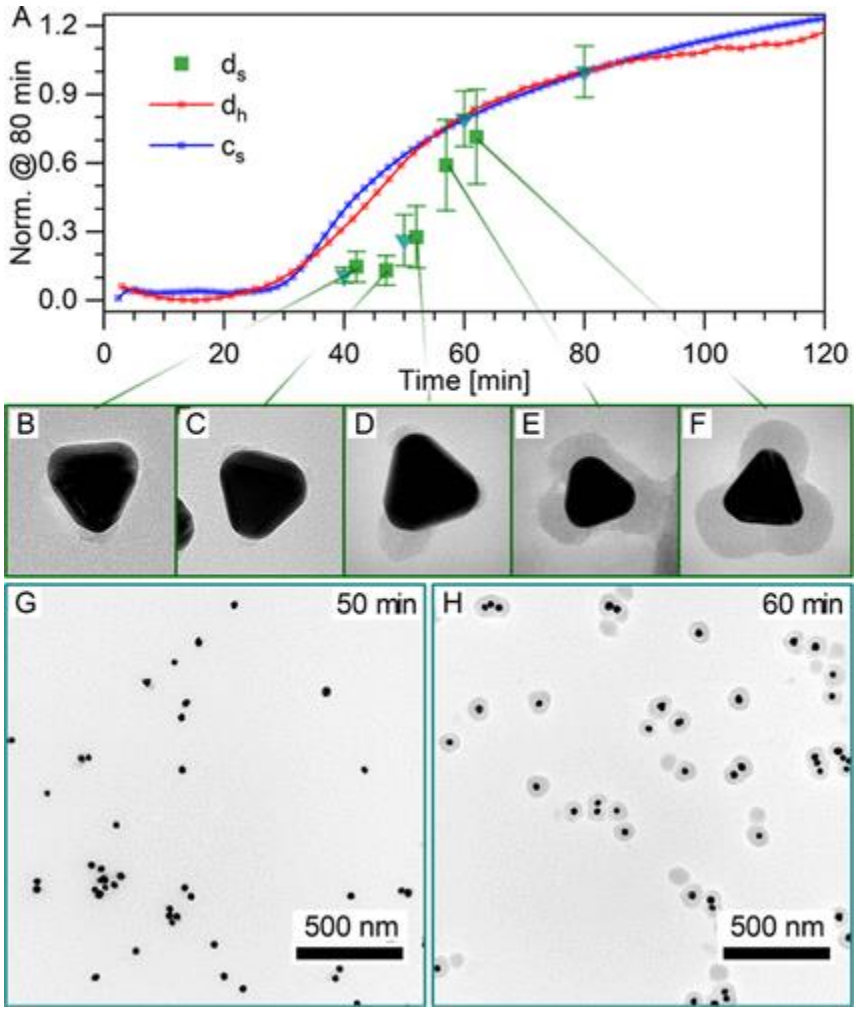

Figure 4.18 Silica coating mechanism at initial stage. (A) Comparison of the time-dependence of silica shell thickness determined by TEM, d_s (symbols), hydrodynamic diameter, d_h (red), and the silica component from *in situ* spectra, c_s (blue). (B–F) TEM micrographs of individual-faceted AuNPs at different times of Au@SiO_2 formation in complete darkness (green squares in A). (G,H) TEM micrographs of fractions taken during an *in situ* spectroscopy experiment (cyan triangles in A). [TEOS] = 2 mM.

Through *in situ* UV–vis spectroscopy, we have identified three reaction stages in the formation of Au@SiO_2 NPs *via* SiO_2 growth on cit-AuNPs and associated them with distinct processes. S1 appears as an induction phase where no SiO_2 forms, but the sensitive LSPR probe reports significant changes on the AuNP surface. We assign the LSPR broadening to adsorption of silica precursor species on the citrate-terminated gold surface, such as orthosilicate anions, and formation of low-density pre-silica networks of partly condensed structures. This process is a prerequisite for shell formation and may influence the properties of the core–shell product, highlighting the importance of being able to probe this step and the merits of our approach. The subsequent condensation and densification, forming SiO_2 patches, change the dielectric function of the surroundings, causing the LSPR to redshift and intensify during S2, as has been reported previously.[134135129128137146] This process is accelerated on vertices possibly because their lower density of citrate ligands facilitates the adsorption of SiO_2 precursor species. In the final stage (S3), the SiO_2 shell grows approximately isotropically until it terminates when the TEOS is consumed. The LSPR only changes slightly in this phase as further Shell growth happens too far from the AuNP surface to affect the plasmon

4.6. Temperature accelerated passivation

The primary idea is to selectively excite the gold NC dimers, allow conversion of electronic energy into lattice heat and then use this heat to accelerate passivation chemistries selectively on NC dimer surface to arrest their further aggregation. It is a good check to ensure that passivation rates can be successfully increased upon increasing the temperature and this can be utilized to arrest the aggregation. Below is the data to ensure both click chemistry as well as silica growth can passivate the nanocrystals and arrest the aggregation at an elevated temperature.

4.6.1. Click chemistry led passivation

HEGDT DEE reaction at . The peak at 8.5 ppm is standard sodium oxalate. The peaks between 6 and 6.5 are the alkene peaks of DEE. HEGDT -DEE reaction is bimolecular and is most likely second order reaction. The concentrations die in an inverse [x] fashion and it should not complete ever. It does not complete in a week, but majority of concentration reduces substantially in around 17 hours. DEE reacts substantially with HEGDT at 80 C within first 5 minutes and not an appreciable change happens in DEE concentration after heating it for 55 minutes more. Point to be noted is that there will always be some unreacted HEGDT left even at 80C.

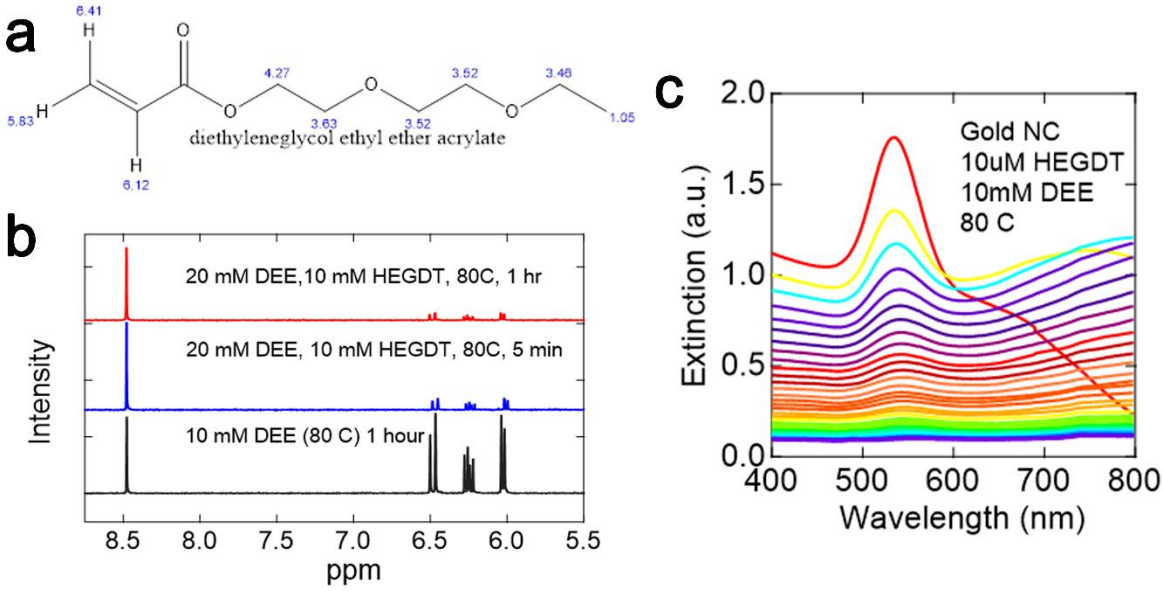

Figure 4.19 HEGDT-DEE reaction at 80 °C. a) chemical structure of DEE with ^{1}H NMR chemical shifts, b) NMR data for HEGDT-DEE reaction at 80 °C, and c) passivation profile at 80 °C (for 3 hours)

Upon increasing the temperature this system gets complicated. Multiple rates increase with increased temperature for example, HEGDT -DEE reaction rate, thiol place exchange reaction rate, Brownian motion of nanocrystals and aggregates, etc. Net effect is the result of all these processes.

It should be noted that electrostatically, the desired product – DEE passivated NC oligomers are electrostatically less stable than the citrate capped monomer due to lack/absence of negative charge.

Our hypothesis was that incomplete reaction between HEGDT and DEE will lead to enhanced thiol place exchange reaction at an elevated temperature. eventually, so I worked out things like cocktail effect with cocktailing monothiol providing charge stability and is far smaller in size than HEGDT-DEE combo and thus, would take preference in case of thiol place exchange reactions. Since, cocktail effect slows down the aggregation rates, pH effect was worked out to tune the aggregation rates as per our needs.

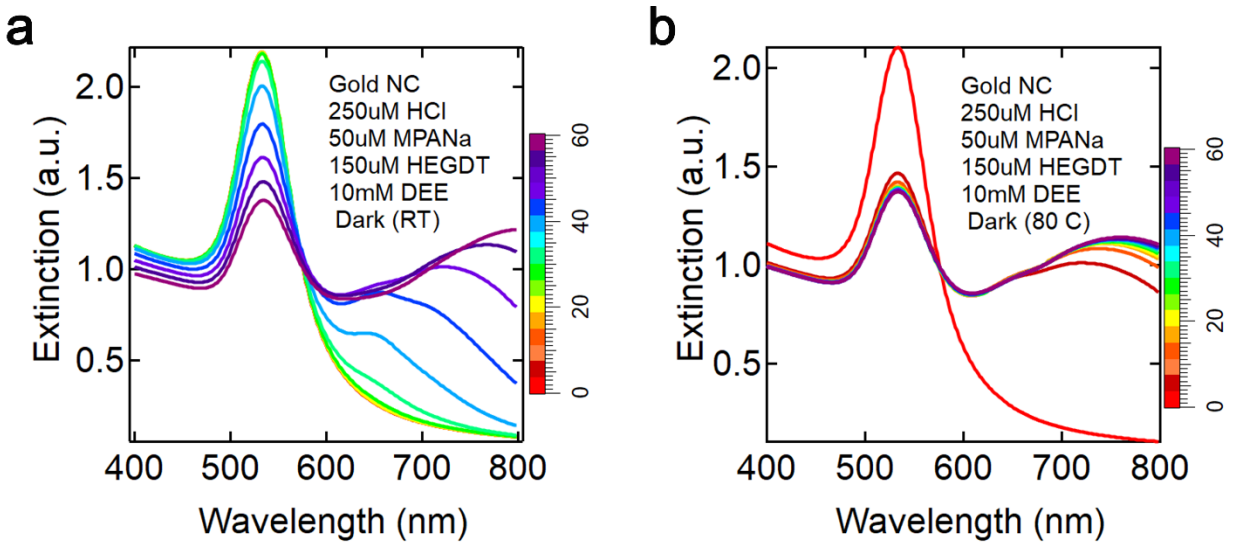

Figure 4.20 Aggregation profile with acrylate, cocktail, and pH effect at a) room temperature and b) at 80 °C.

On increasing temperature, aggregation rates increase substantially at first within first 10 minutes, but then stabilize due to the combination of HEGDT-DEE click reaction and place exchange of longer HEGDT or HEGDT-DEE combo with smaller MPA. It should be noted that with substantial

MPA on the surface, our product is almost equally stable (electrostatically) as our reactant, if not more.

4.6.2. Silica growth led passivation

The conditions for silica growth were optimized to ensure no silica growth at room temperature. TEOS concentration was kept high at 10 mM and NaOH catalyst concentrations were tuned to 0.5 mM to control the silica growth rate. At room temperature, aggregation goes normally however at an elevated bulk temperature of 80 °C, aggregation stops within first 15 minutes. It should be noted the bulk heating happens through conduction or convection and may take a few minutes for the system to be a steady state, whereas the local heating due to illumination is expected to happen in nanoseconds. Another point to note is that dithiol linking is specific to gold and it does not bind or aggregate silica coated gold.

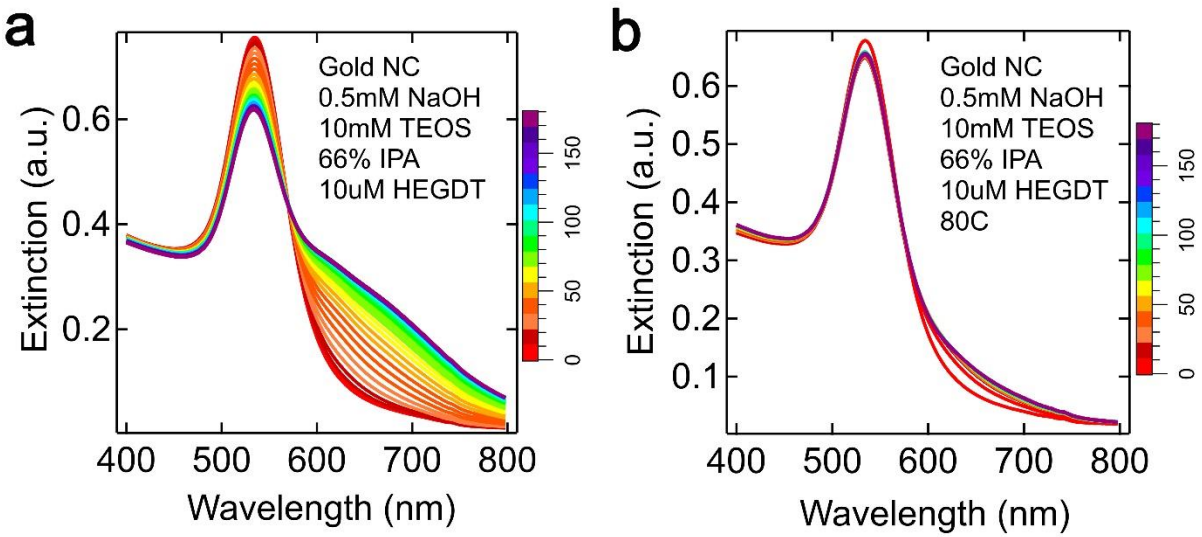

Figure 4.21 Thermal driven arrest of gold NP aggregation via silica growth on NP surface. Aggregation profile with gold NC, linker and silica precursor at a) room temperature and b) at 80 °C.

4.7. Illumination accelerated passivation

We need a light source that can delivers sufficient pulse energy (0.15 mJ) to increase the peak surface temperature of the dimers T_{peak} by ~100 °C ($\Delta T_{peak} = E_{abs}/C$, where E_{abs} is the pulse energy absorbed by a dimer and C is the heat capacity of the dimer)[151] and trigger the passivating surface reaction. A pulsed laser is required because the power density of continuous wave light sources is too low to significantly increase the dimer surface temperature unless the beam is focused on just a small region of the sample.[152] Pulsed illumination also achieves much higher temperature confinement around the dimers, minimizing bulk heating of the solution.[151] The hot dimers will cool within a few ns after each pulse,[93] but this should be enough time for at least a few thiol-ene reactions to occur on each dimer when the alkene concentration is sufficiently high (10-100 mM). Alkene molecules in proximity to a hot dimer can diffuse 5-10 nm during this time, guaranteeing collisions with the dimer surface. We estimate that if an average of just one thioether linkage forms per pulse, the dimers will be passivated and protected from further aggregation in ~30 s (using a 1

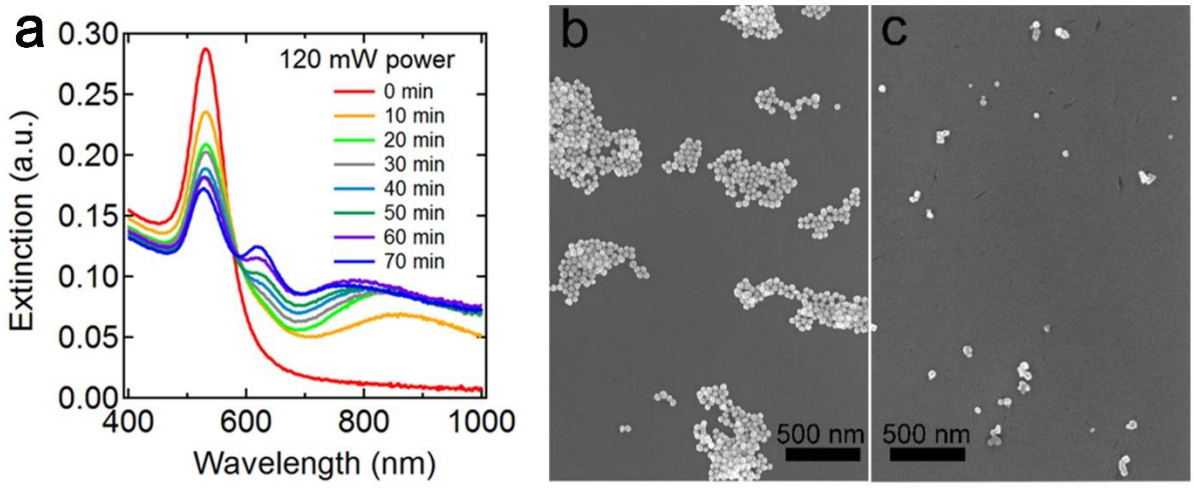

Figure 4.22 Laser driven arrest of gold NP aggregation. a) extinction spectra of a system of gold nanocrystals, 10uM HEGDT and 10mM DEE under illumination with 120 mW 640 nm fs laser, b) SEM images of gold aggregates from a system kept in dark, and c) SEM images of a system under illumination

kHz rep rate). As discussed below, this is significantly faster than the time needed for a dimer to collide with a monomer or another dimer to form unwanted larger oligomers.

A system with gold NC, 10uM HEGDT and 10mM DEE was illuminated with 120mW, 640 nm, 1 kHz, femtosecond laser. A broad hump in the IR and a shoulder around 640 nm start to form within 10 minutes of illumination. The shoulder around 640 nm develops into a full peak at time progresses. The broad hump in the near infrared first increases and then blue shifts. (Figure 4.21a)

Figure 4.21b shows the systems kept in the dark whereas figure 4.21c shows the system kept under illumination for 70 minutes.

4.8. Outstanding challenges

There are several outstanding challenges that still need redressal for achieving deterministic dimerization of gold nanocrystals. First, femtosecond laser does passivate the gold NC surface, however it also causes morphological damage by causing necking and coalescence in the particles that can be observed both in SEM images as well as in the broad IR band. Second, gold nanocrystals are not completely monodispersed and dimers with very large or very small size might still undergo further aggregation. Third, currently the particle heating happens in picosecond and majority of this heat is dissipated into the solution by nanoseconds. The two fall outs are 1) we cannot use slower reactions like silica growth with this mode of illumination and 2) In order to get a large lifetime for a hot dimer, we'll need very high peak powers that can lead to effect like non thermal necking, hot electrons generation reacting with surface ligands, thus leading to illumination induced disaggregation. One solution to this challenge can be the use of 80 MHz broad band light sources. The broadband nature will compensate for any polydispersity in the gold NCs. Lower peak power will minimize the chances of illumination and hot electrons related

damage and high rep rate will ensure that thermal energy builds up from pulse to pulse, thus allowing even slower chemistries like oxide growth to be used for passivation.

4.9. Experimental

Materials: $HAuCl_4 \cdot 3H_2O$ (Aldrich, ≥99.9%), trisodium citrate (TSC, MP Biomedicals, LLC, 99.8%), 2-propanol (IPA, Fischer Scientific, HPLC grade), TEOS (Aldrich, 99.999%), and 28–30% NH_4OH in water (Fischer Chemicals) were used as received. Ultrapure water (18.2 MΩ) was obtained from a Milli-Q system from Millipore.

Au NP Synthesis: Synthesis of spheroidal AuNPs with controlled size was based on the protocol by Bastús *et al*.[153] First, AuNP seeds were prepared by injection, and subsequent reduction, of aqueous $HAuCl_4$ into TSC solution with final concentrations of 165 μM and 2.2 mM, respectively, at 95–100 °C and heating for 25 min. Then, a seeded-growth process was undertaken by sequentially injecting $HAuCl_4$, removing a fraction of the growth solution after three $HAuCl_4$ injections, and adding more TSC solution. This produced a series of fractions of AuNPs of increasing size, Figure A3.1. A fraction consisting of 36 ± 9 nm AuNPs was used for the present study.

Au@SiO_2 NP Synthesis: For a 6 mL total volume of Au@SiO_2 sol prepared with 10 mM of TEOS, 0.7 mL of ultrapure water was added to 1 mL of AuNPs under stirring, followed by 4.1 mL of IPA and 150 μL of 14.5 M NH_4OH (28% ammonia water). After mixing for 2–5 min, 60 μL of 1 M TEOS (in IPA) was injected. To adjust the TEOS concentration, the added volume of 1 M TEOS was modified, and that of IPA adjusted to compensate. Au@SiO_2 NP formation was performed at room temperature (r.t., 20 ± 1 °C) unless otherwise stated. Representative transmission electron microscopy (TEM) samples at given reaction times were obtained by quenching the reaction by extracting 100 μL of the reaction mixture and injecting it into an Eppendorf tube with 1–1.5 mL

of water. The colloid was sedimented by centrifugation (16k rcf, 15 min), the supernatant reaction mixture was discarded, and the colloids redispersed in ultrapure water, which was then dropcast onto a TEM grid. For Au@SiO_2 NP synthesis in complete darkness, the synthesis was carried out in a dark laboratory in a foil-wrapped vial. Fractions were extracted into Al foil-wrapped Eppendorf tubes, and the TEM samples were covered while drying to exclude light.

Characterization: UV–vis extinction spectroscopy was carried out using a LAMBDA 950 spectrophotometer from PerkinElmer. For *in situ* spectroscopy, AuNP sol, ultrapure water, IPA, and NH_4OH were mixed in this order in a glass vial with constant stirring to ensure quick mixing and avoid AuNP destabilization due to IPA and NH_4OH addition. After stirring for 2–5 min, the desired amount of TEOS was added to the vial, the solution was quickly mixed with a pipette, poured into a glass cuvette, and then capped and immediately placed in the spectrometer, at which point continuous UV–vis measurements were initiated. The time delay between addition of TEOS and recording of the first spectrum was typically 10–20 s. For syntheses at controlled temperature, the sample cuvette was placed in a metal compartment cooled/heated by water from a circulating bath (Grand LT Ecocool 150),Figure A3.4.

TEM data were acquired on a JEOL 2800 microscope equipped with a 4k × 4k Gatan Oneview camera at 200 kV accelerating voltage at the Irvine Materials Research Institute, UC Irvine. Data were processed using ImageJ.[154]

In situ hydrodynamic size information was obtained with a Malvern Zetasizer Nano DLS instrument at the Laser Spectroscopy Labs, UC Irvine.

Appendix 1 (A1)

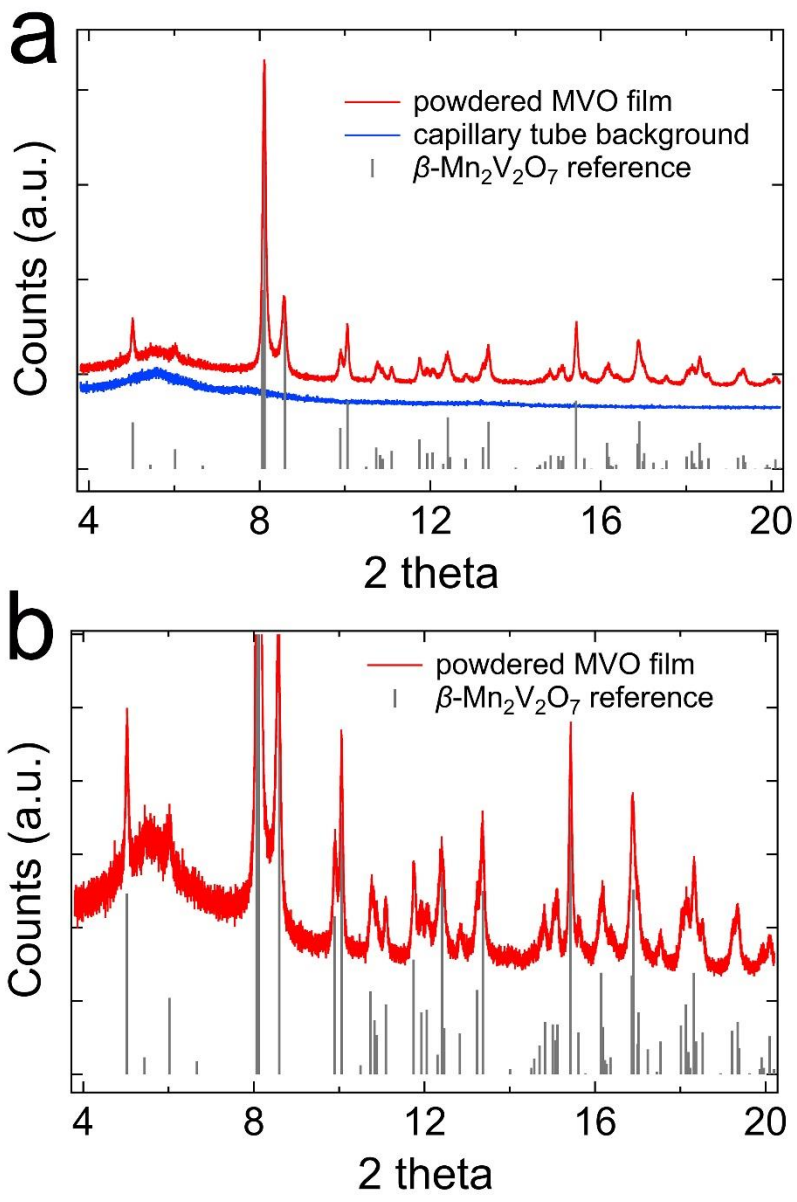

Figure A1. 1 High-resolution synchrotron powder XRD of a powderized β-MVO film. The film was 580 nm thick, made on FTO-coated glass substrates using a 30 minute calcination at 500 °C (the "standard" films). λ = 0.458092 Å. All peaks index to β-MVO (grey bars).

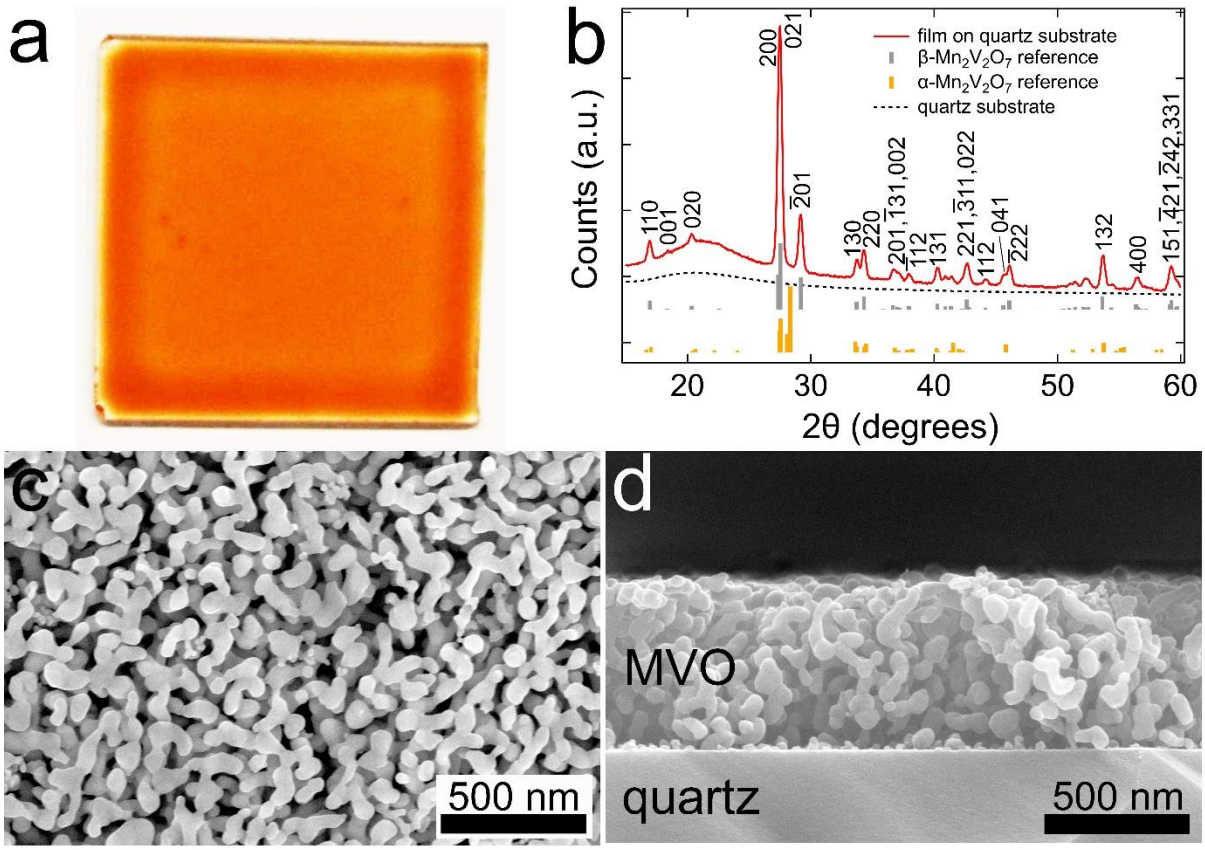

Figure A1.2 Characterization of nanostructured MVO films on quartz substrates. (a) Photograph of a 570 ± 35 nm thick MVO film on a 1×1 inch quartz substrate. (b) XRD pattern of a duplicate film. All peaks index to β-$Mn_2V_2O_7$ (PDF# 01-089-0484, grey bars) and the sample appears to be phase pure. The broad peak at 23° is due to the quartz substrate. (c-d) Plan view and cross-section SEM images of the film.

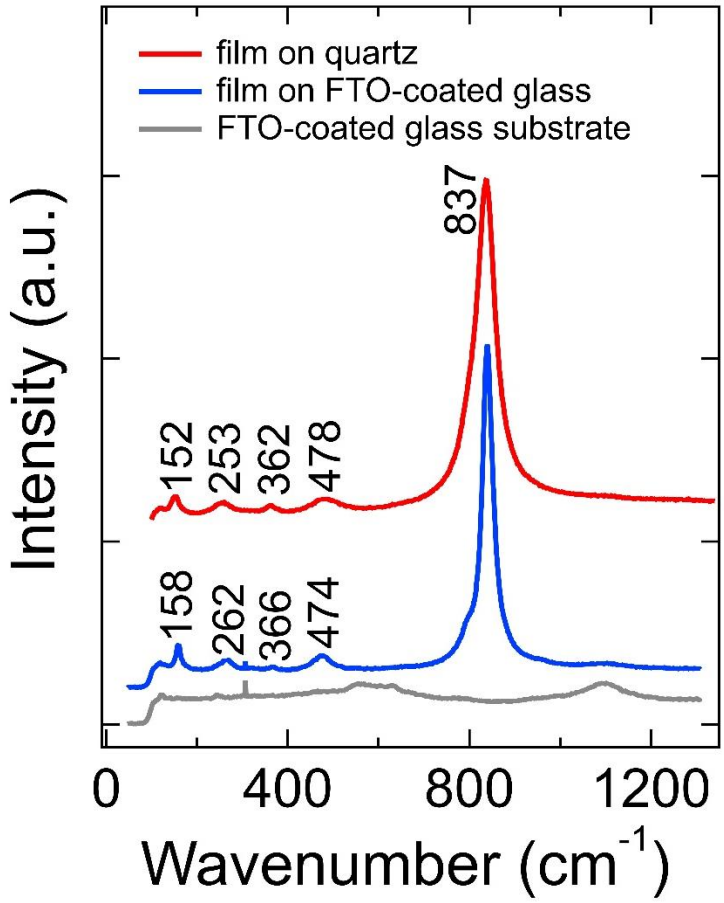

Figure A1.3 Raman spectra of β-MVO films on FTO-coated glass and quartz substrates. The spectrum of a bare FTO-coated glass substrate is also shown.

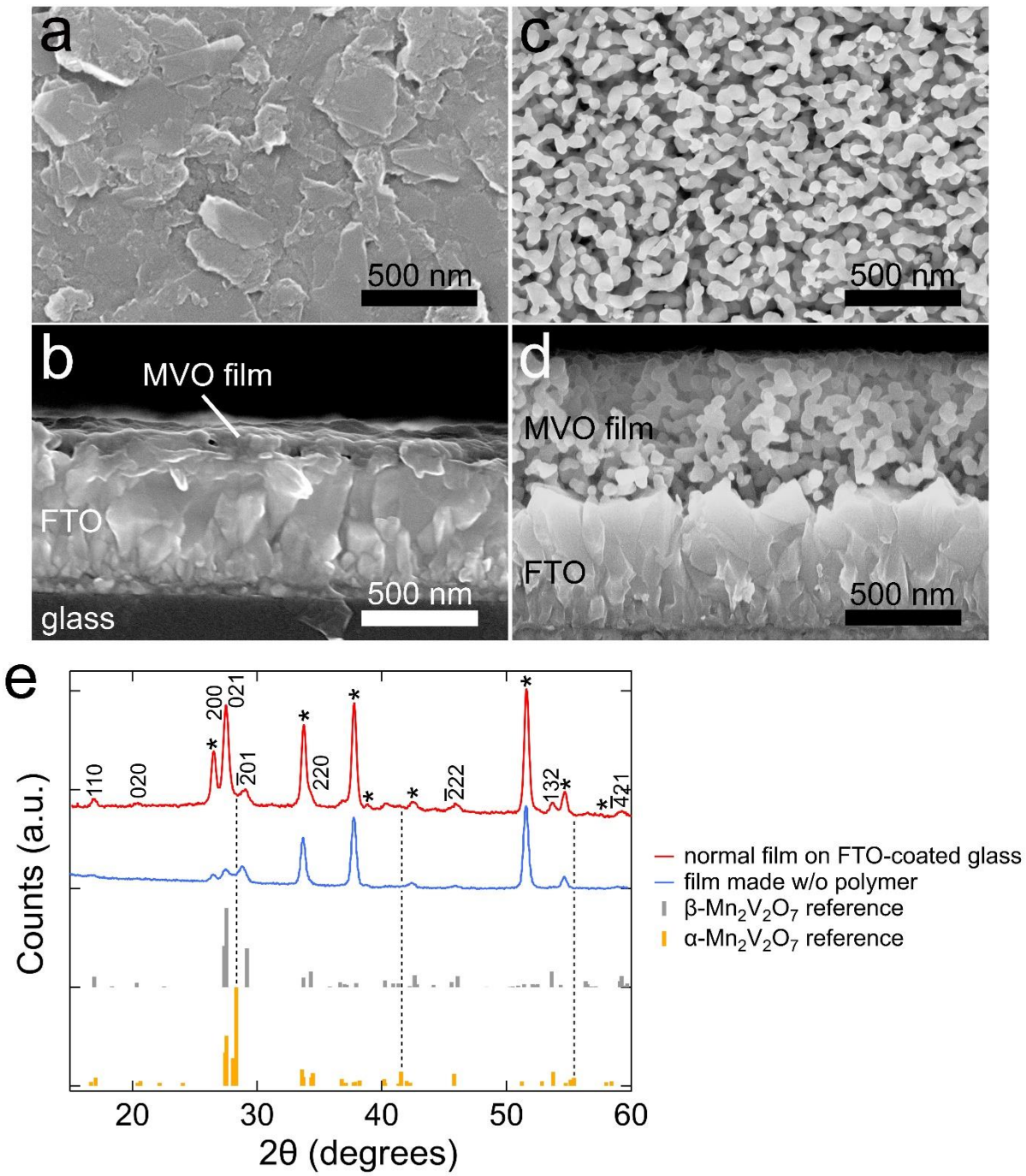

Figure A1.4 Characterization of a representative MVO film made without the Pluronic F-108 triblock copolymer. (a-b) Plan view and cross-section SEM images of an MVO film made without the polymer. The film is nonporous and thin. The substrate is FTO-coated glass. (c-d) Corresponding SEM images of a standard β-MVO film. (e) XRD patterns of the two films. Reference patterns for β-MVO (grey bars) and α-MVO (orange bars) are also shown.

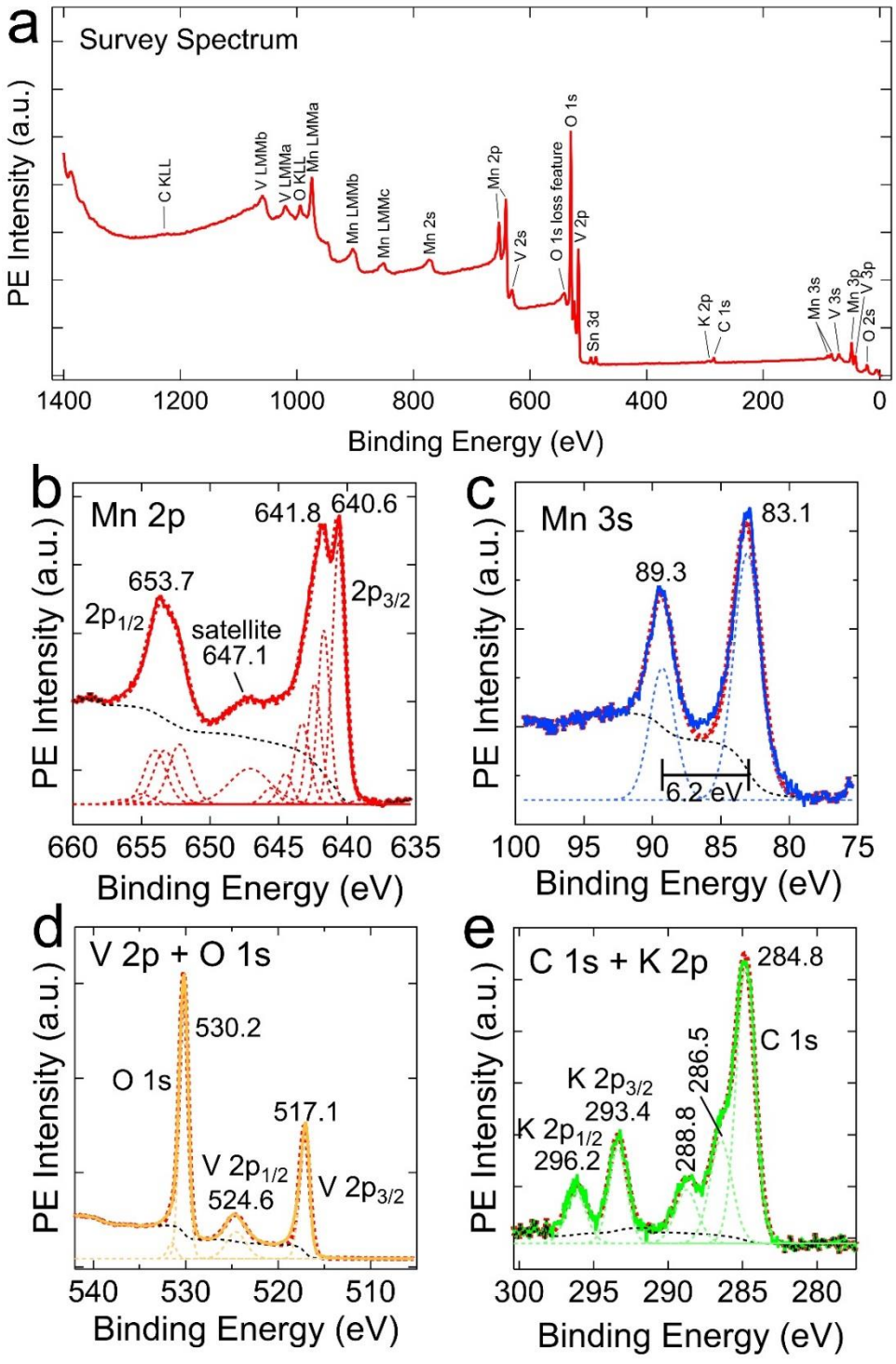

Figure A1.5 XPS analysis of a standard β-MVO film on an FTO-coated glass substrate. (a) Indexed survey scan. The only elements detected were Mn, V, O, C, K (origin unknown), and Sn (from the substrate). (b) Mn 2p region. (c) Mn 3s region. (d) V 2p and O 1s region. (e) C 1s and K 2p region. Each high-resolution spectrum shows the raw data (solid lines), background (dashed black line), peaks (colored dashed lines), and sum (heavy dashed red line). A Mn:V atomic ratio of 1.09 was measured for this sample (see Table 2).

Table A1.1 Ink composition and fabrication conditions for the different MVO films.

Film Thickness/ Grain Size (nm)	Mn (mmol)	V (mmol)	HNO_3 (g)	H_2O/EG (g)	F-108 (g)	Annealing		Spin Speed (sec)
						Temp (°C)	Time (min)	
260/61	1	1	0.32	1.5/1.5	0.4	500	30	5000 (20) 6000 (40)
575/64	1	1	0.32	1.5/1.5	0.4	500	30	2000(20) 3000(40)
1000/61	1	1	0.32	1.0/1.0	0.4	500	30	2000(20) 3000(40)
3200/66	1	1	0.32	0.5/0.5	0.4	500	30	1500(20) 2200(40)
4650/66	1	1	0.32	0.5/0.5	0.4	500	30	750(20) 1200(40)
557/39	1	1	0.32	1.5/1.5	0.4	500	15	2000(20) 3000(40)
537/89	1	1	0.32	1.5/1.5	0.4	500	60	2000(20) 3000(40)
570/110	1	1	0.32	1.5/1.5	0.4	500	120	2000(20) 3000(40)

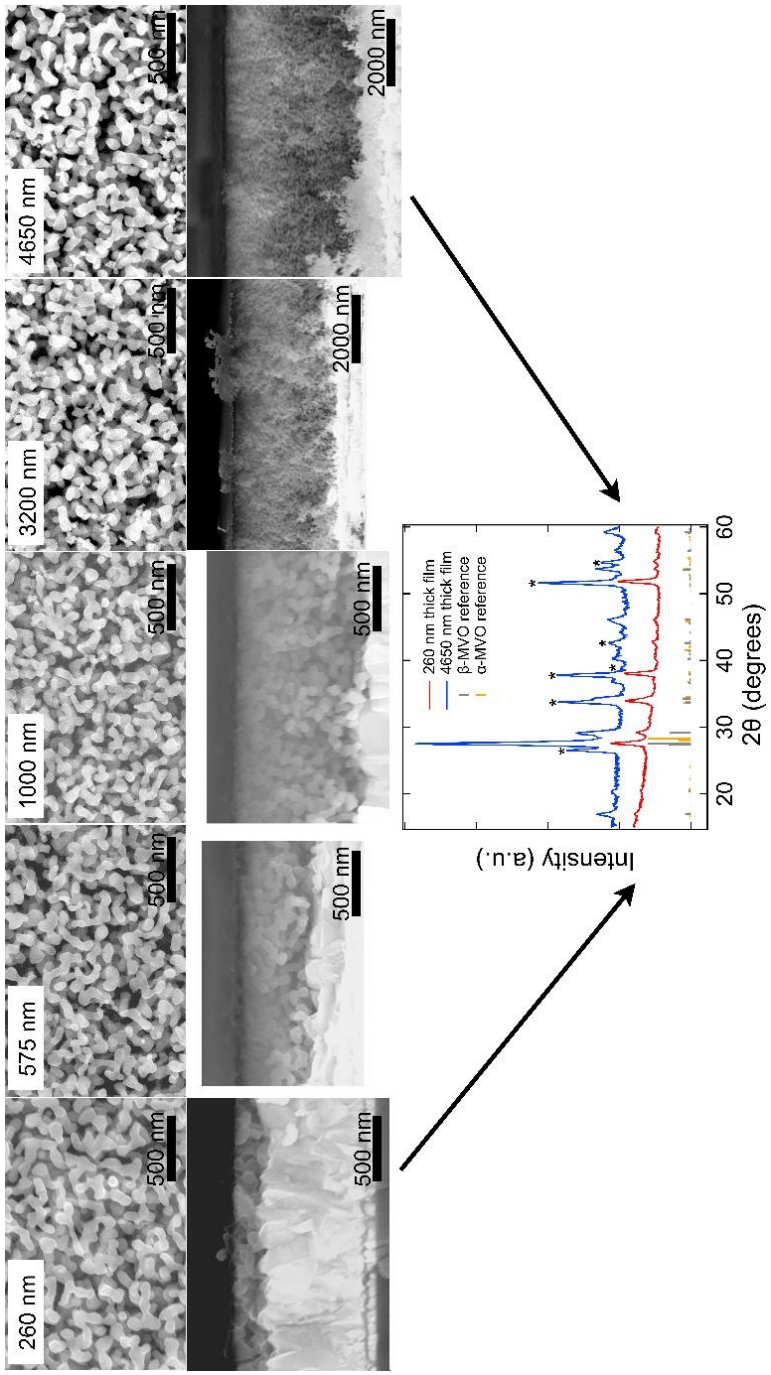

Figure A1.6 β-MVO films of different thickness. (top) Plan view and cross-section SEM images of films with a thickness of 260, 575, 1000, 3200, and 4650 nm. All films have an average crystallite diameter of 55-65 nm and were grown on FTO-coated glass substrates. (*bottom*) Grazing-incidence XRD patterns of the thinnest and thickest films (red and blue traces, respectively). Both films are phase-pure β-MVO. Asterisks denote substrate peaks. Reference patterns for β-MVO (grey bars) and α-MVO (orange bars) are also shown. The angle of incidence was 0.2° and 1.5° for the 260 and 4650 nm thick films, respectively. Film thickness was tuned by changing the solvent volume and spin coating parameters (Table S1)

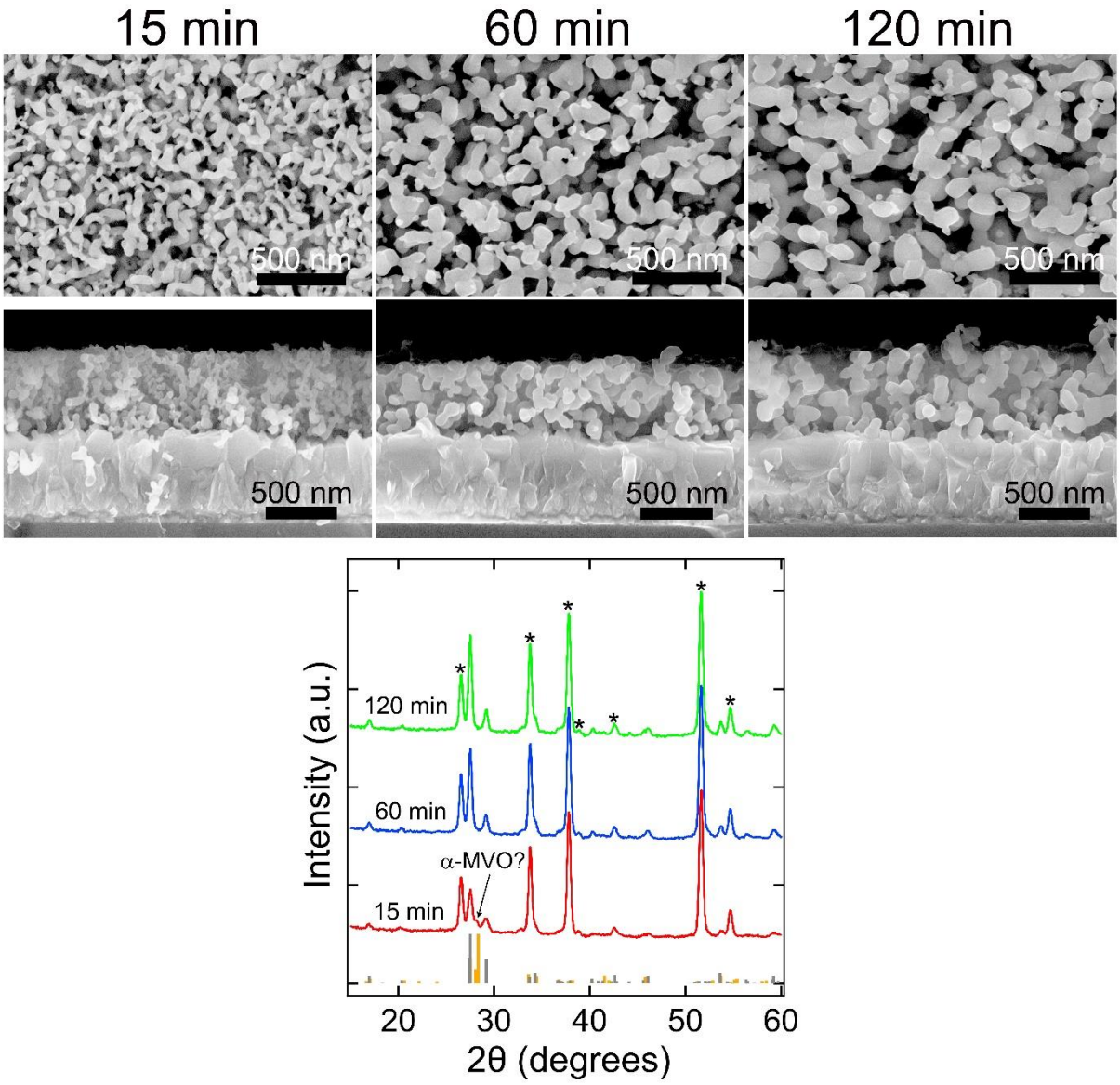

Figure A1.7 β-MVO films with different crystallite size. (top) Plan view and cross-section SEM images of films calcined at 500 ºC for either 15, 60, or 120 minutes, resulting in an average crystallite diameter of ~39 nm, ~89 nm, and ~110 nm, respectively. The films have a thickness of 520-580 nm and were made from a single sample deposited on an FTO-coated glass substrate and then diced into three pieces prior to calcination. (*bottom*) XRD patterns of the three films. All films are phase-pure β-MVO except for a small shoulder at ~28.2º in the 15-min calcined film that may be due to α-MVO (labelled in the figure). Asterisks denote substrate peaks. Reference patterns for β-MVO (grey bars) and α-MVO (orange bars) are also shown.

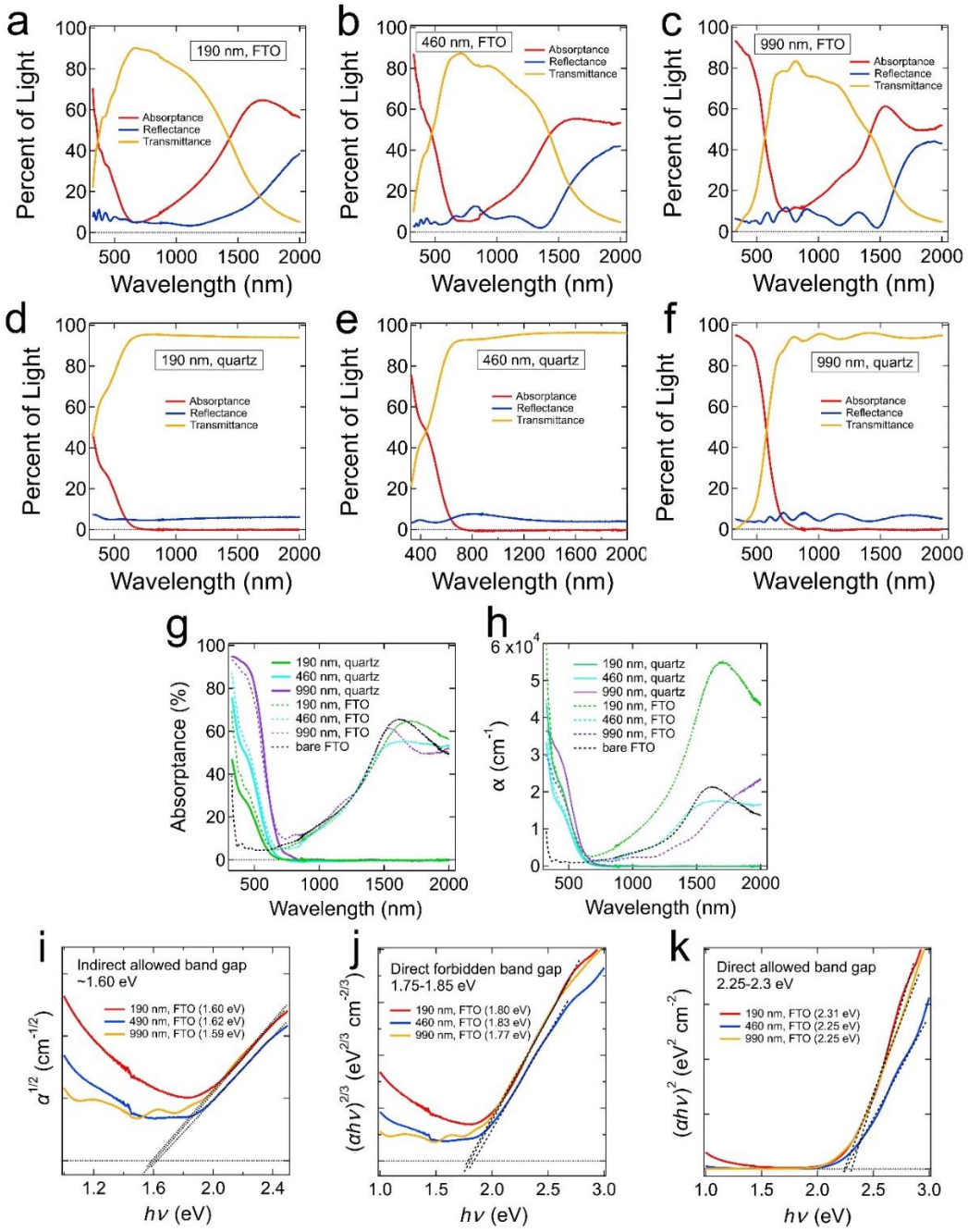

Figure A1.8 Optical properties of MVO films on FTO. (a-f) Absorptance, reflectance, and transmittance spectra of MVO films of various thickness grown on FTO-coated glass and quartz substrates. (g) Compiled absorptance spectra of these samples. The spectrum of a bare FTO-coated glass substrate is also shown for reference. Figure S9 shows the full data for the bare substrate. (h) Absorptivity spectra of the samples and the bare FTO-coated glass substrate. The absorptivity of the MVO samples was calculated using only the MVO film thickness, without including the thickness of the FTO layer. The absorptivity of the bare FTO substrate was calculated using the thickness of the FTO layer (~500 nm). (i-k) Fitted Tauc plots for the MVO films on FTO-coated glass substrates.

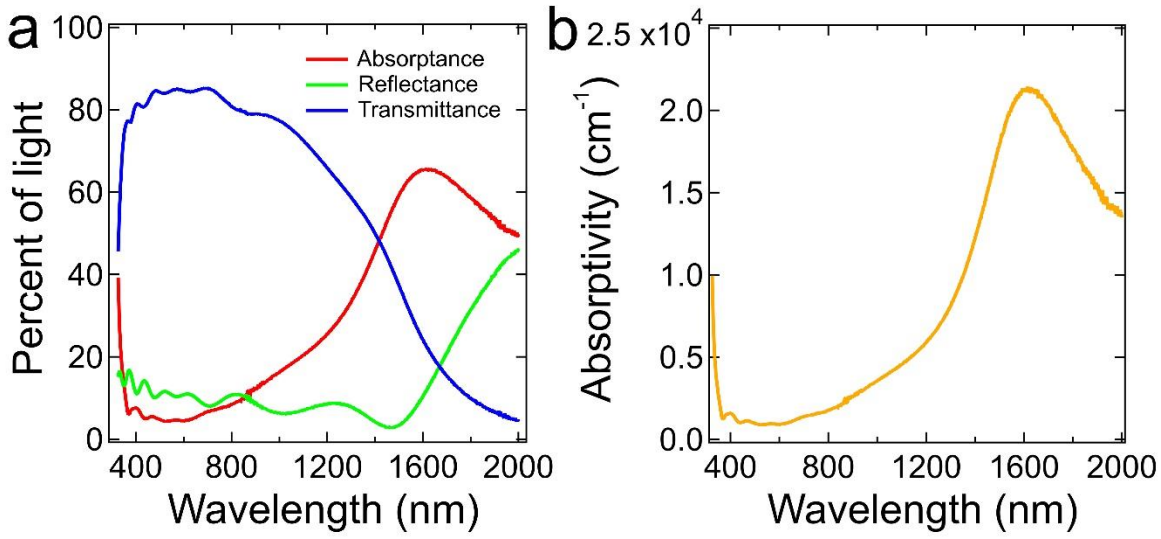

Figure A1.9 (a) Measured transmittance, reflectance, and absorptance spectra and (b) absorptivity spectrum of a clean FTO-coated glass substrate.

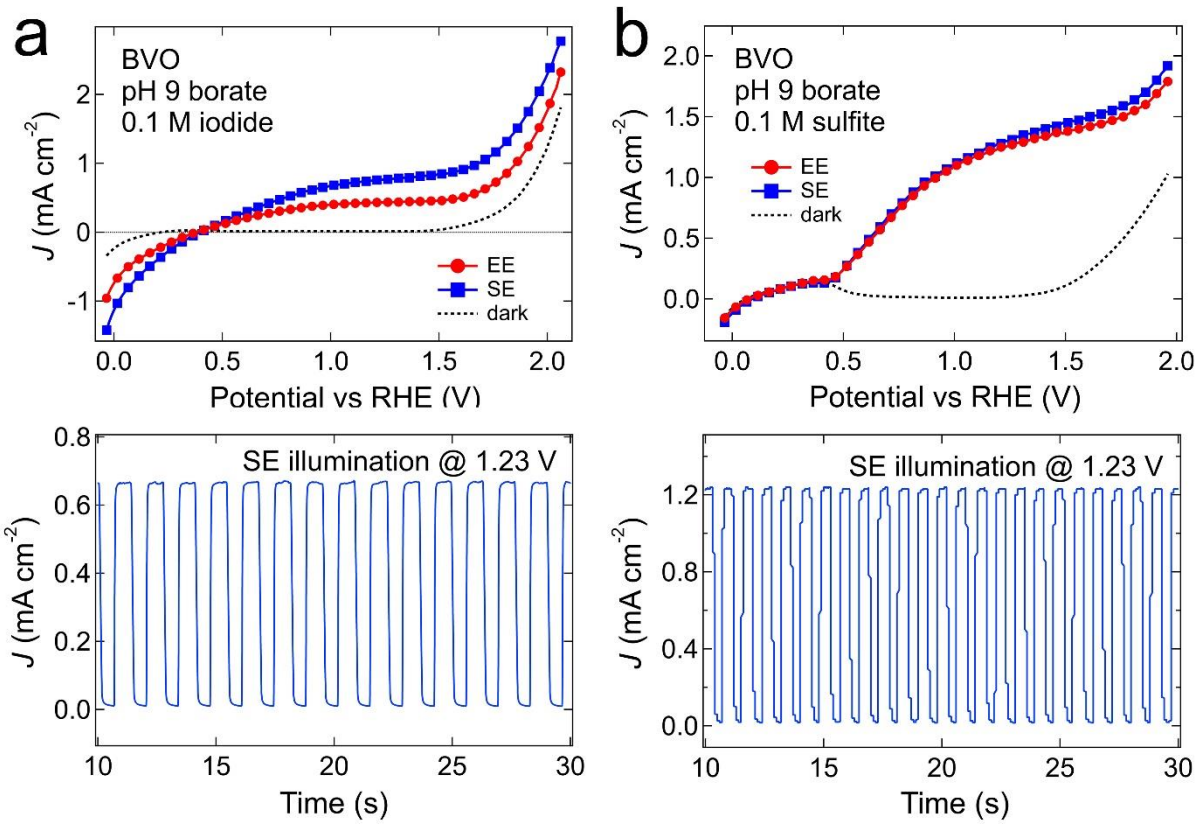

Figure A1.10 Photoelectrochemical J-E and J-t data for BiVO4 (BVO) films measured in 0.1 M aqueous borate buffer (pH 9) with (a) 0.1 M potassium iodide and (b) 0.1 M sodium sulfite as a hole scavenger. The J-t data were acquired at 1.23 V vs. RHE using chopped illumination

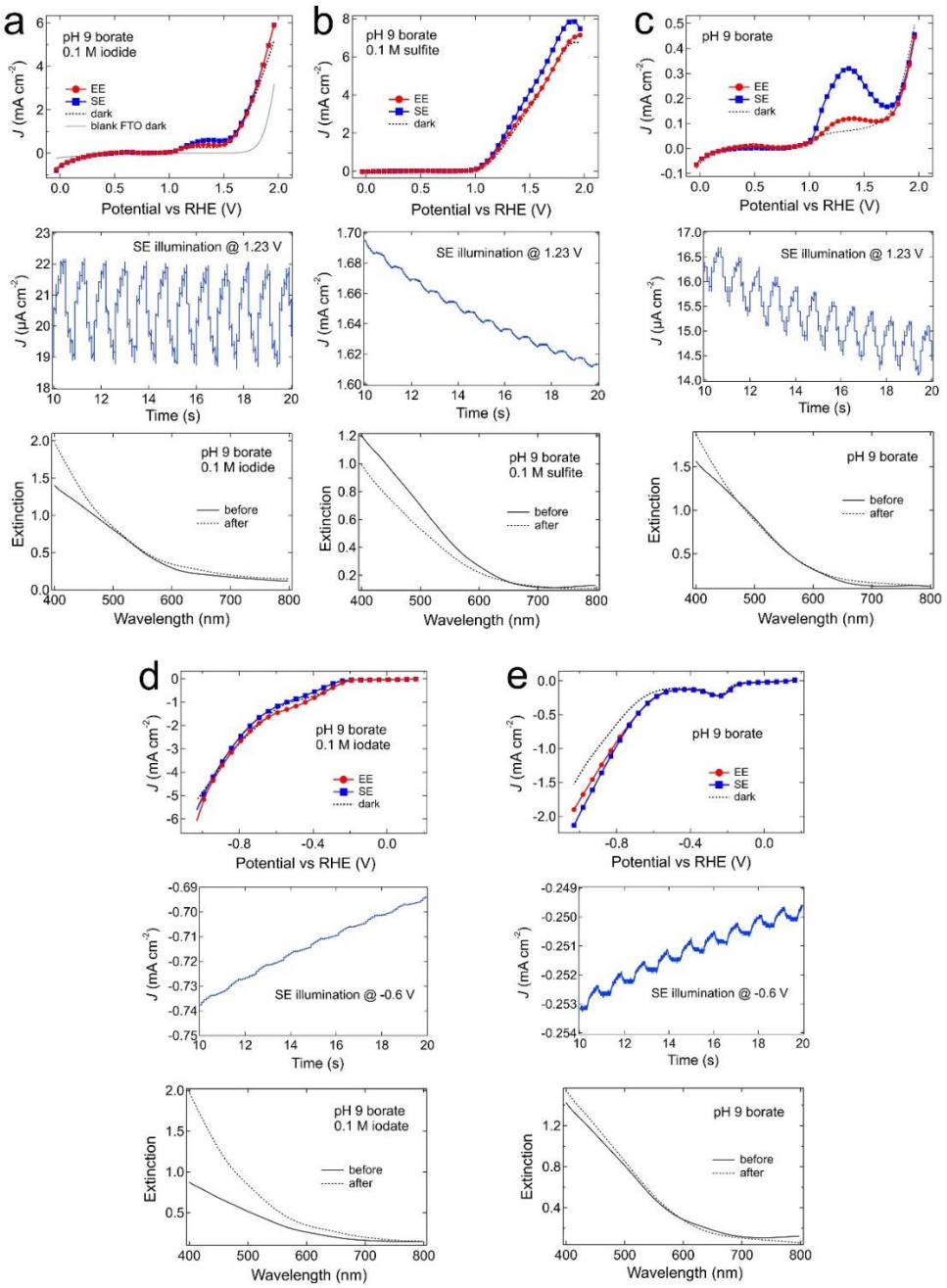

Figure A1.11 Photoelectrochemical (PEC) data for MVO films in 0.1 M aqueous borate buffer at pH 9. Current-potential (*J*-*E*) and current-time (*J*-*t*) plots and optical extinction spectra immediately before and after PEC measurements for (a) iodide oxidation, (b) sulfite oxidation, (c) water oxidation, (d) iodate reduction, and (e) water reduction. *J*-*E* data were acquired at a potential sweep rate of 50 mV/s. *J*-*t* data were acquired at either 1.23 V vs. RHE (for oxidations) or -0.6 V vs. RHE (for reductions) using chopped illumination (1.25 Hz) in the SE geometry. PEC data required ~20 minutes to collect per sample, so Δt ~ 20 minutes for each set of optical spectra. All of the MVO films were 580 ± 60 nm thick except for the film tested in iodate, which was ~450 nm thick. See Methods for other details.

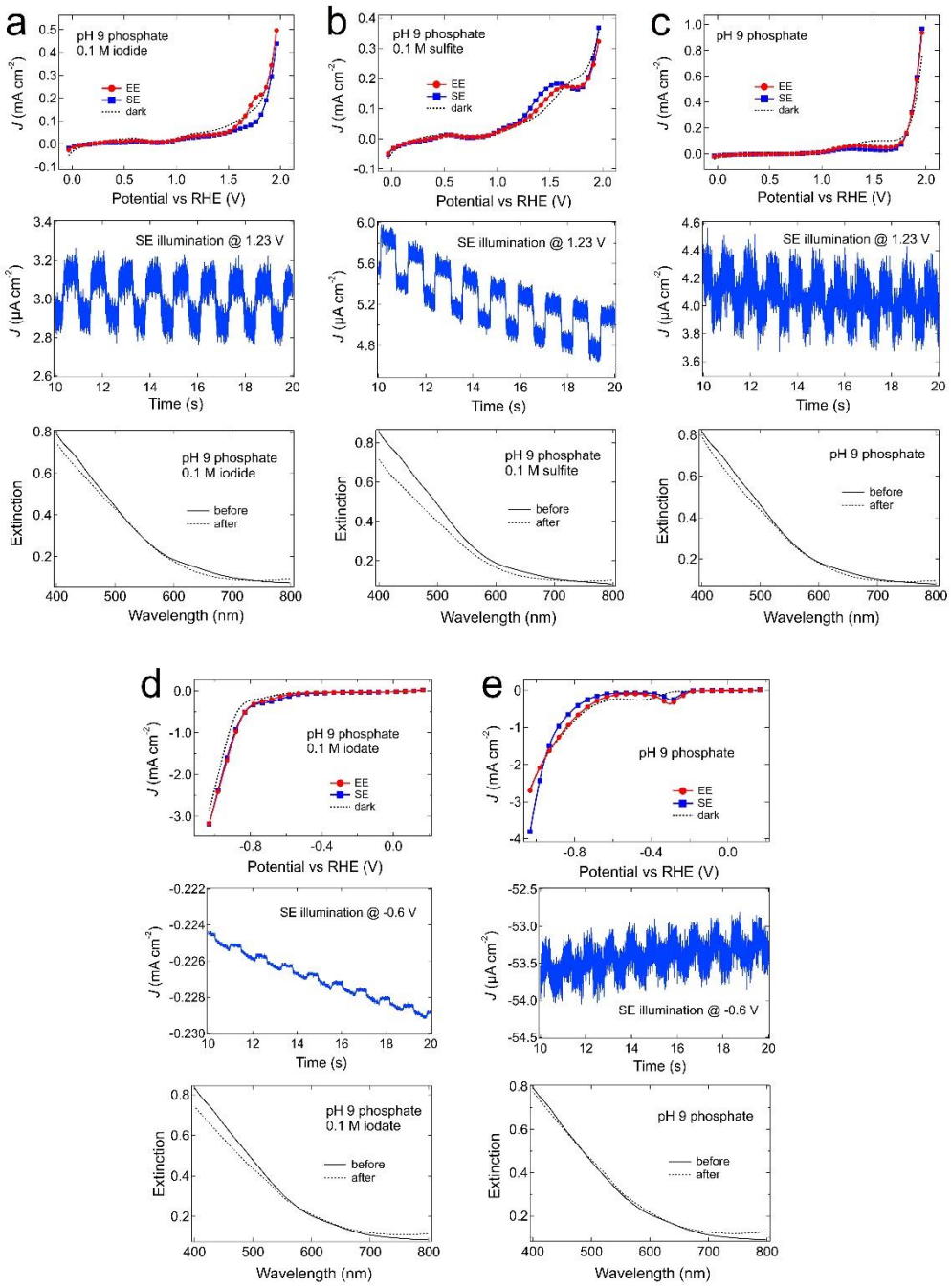

Figure A1.12 Photoelectrochemical (PEC) data for MVO films in 0.1 M aqueous phosphate buffer at pH 9. Current-potential (*J-E*) and current-time (*J-t*) plots and optical extinction spectra immediately before and after PEC measurements for (a) iodide oxidation, (b) sulfite oxidation, (c) water oxidation, (d) iodate reduction, and (e) water reduction. *J-E* data were acquired at a potential sweep rate of 50 mV/s. *J-t* data were acquired at either 1.23 V vs. RHE (for oxidations) or -0.6 V vs. RHE (for reductions) using chopped illumination (1.25 Hz) in the SE geometry. PEC data required ~20 minutes to collect per sample, so Δt ~ 20 minutes for each set of optical spectra. All of the MVO films were 400 ± 60 nm thick. See Methods for other details.

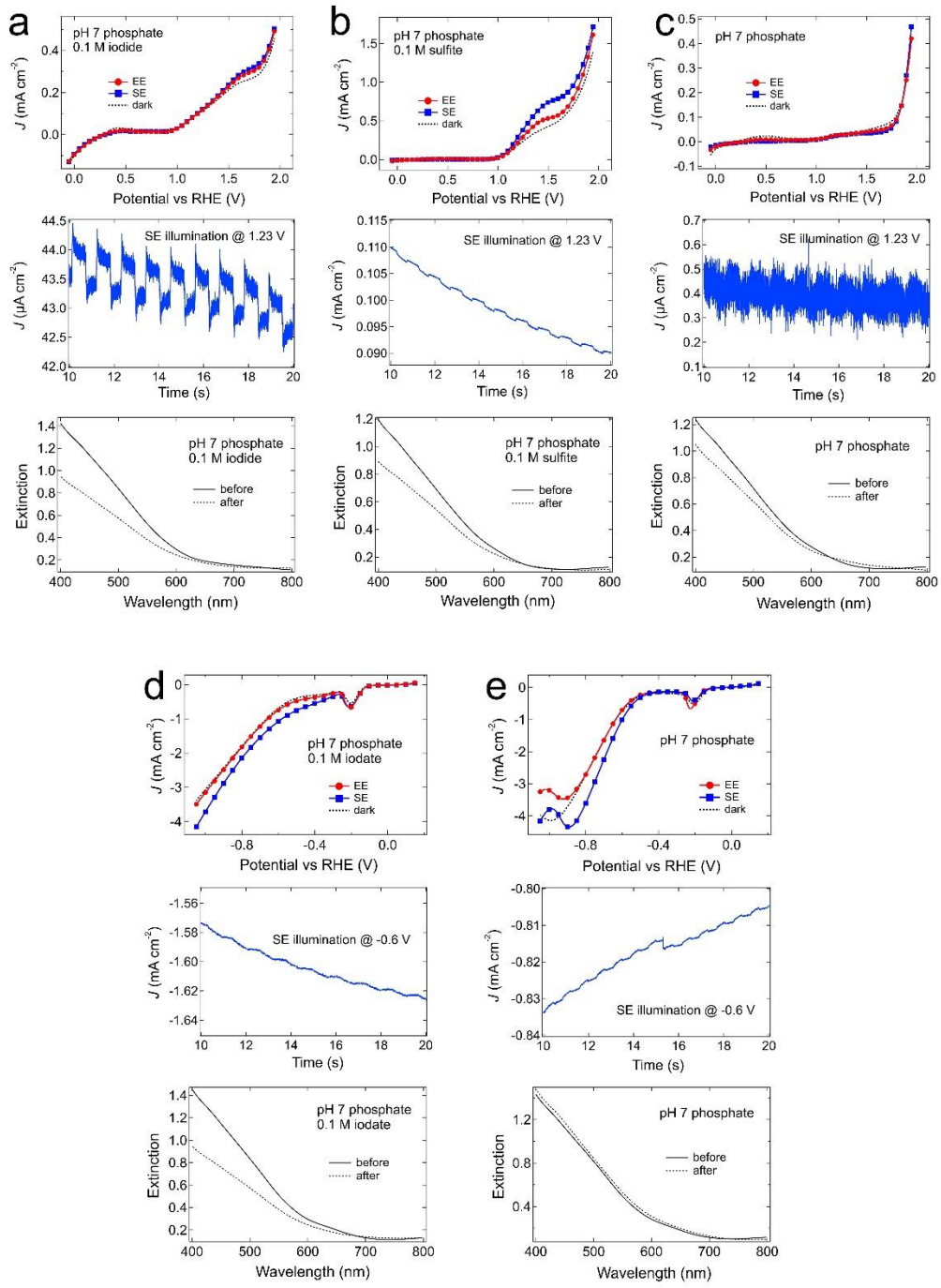

Figure A1.13 Photoelectrochemical data for MVO films in 0.1 M aqueous phosphate buffer at pH 7. Current-potential (J-E) and current-time (J-t) plots and optical extinction spectra immediately before and after PEC measurements for (a) iodide oxidation, (b) sulfite oxidation, (c) water oxidation, (d) iodate reduction, and (e) water reduction. *J-E* data were acquired at a potential sweep rate of 50 mV/s. *J-t* data were acquired at either 1.23 V vs. RHE (for oxidations) or -0.6 V vs. RHE (for reductions) using chopped illumination (1.25 Hz) in the SE geometry. PEC data required ~20 minutes to collect per sample, so Δt ~ 20 minutes for each set of optical spectra. All of the MVO films were 580 ± 60 nm thick. See Methods for other details.

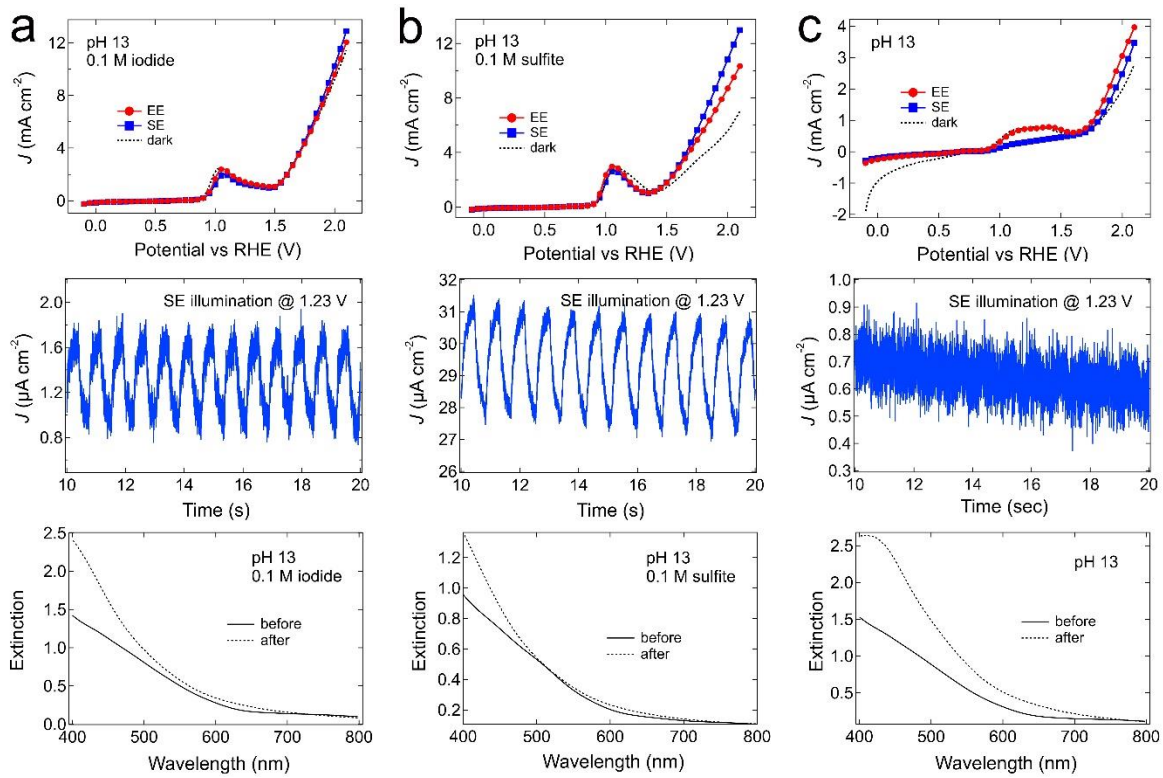

Figure A1.14 Photoelectrochemical data for MVO films in 0.1 M aqueous NaOH solution (pH 13). Current-potential (*J*-*E*) and current-time (*J*-*t*) plots and optical extinction spectra immediately before and after PEC measurements for (a) iodide oxidation, (b) sulfite oxidation, and (c) water oxidation. *J*-*E* data were acquired at a potential sweep rate of 50 mV/s. *J*-*t* data were acquired at 1.23 V vs. RHE using chopped illumination (1.25 Hz) in the SE geometry. PEC data required ~20 minutes to collect per sample, so Δt ~ 20 minutes for each set of optical spectra. All of the MVO films were 580 ± 60 nm thick except for the film tested in iodate, which was ~480 nm thick. See Methods for other details.

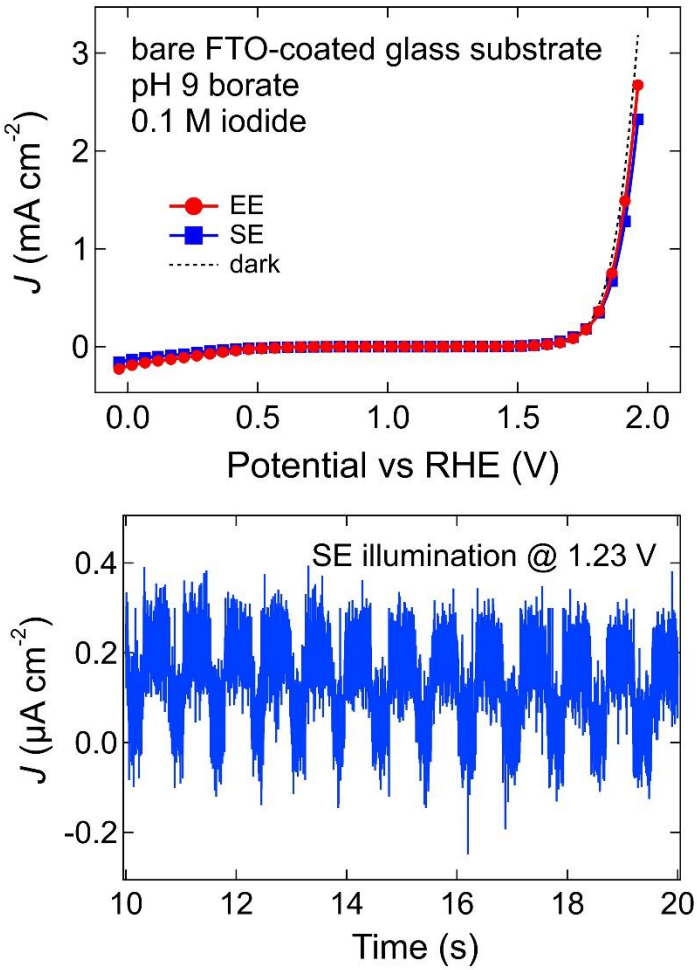

Figure A1.15 Photoelectrochemical data for a blank FTO-coated glass substrate (no MVO film) in 0.1 M aqueous borate buffer containing 0.1 M iodide at pH 9. *J-E* data were acquired at a potential sweep rate of 50 mV/s. *J-t* data were acquired at 1.23 V vs. RHE using chopped illumination (1.25 Hz) in the SE geometry. The photocurrent was only ~0.3 µA cm^{-2}. See Methods for experimental details.

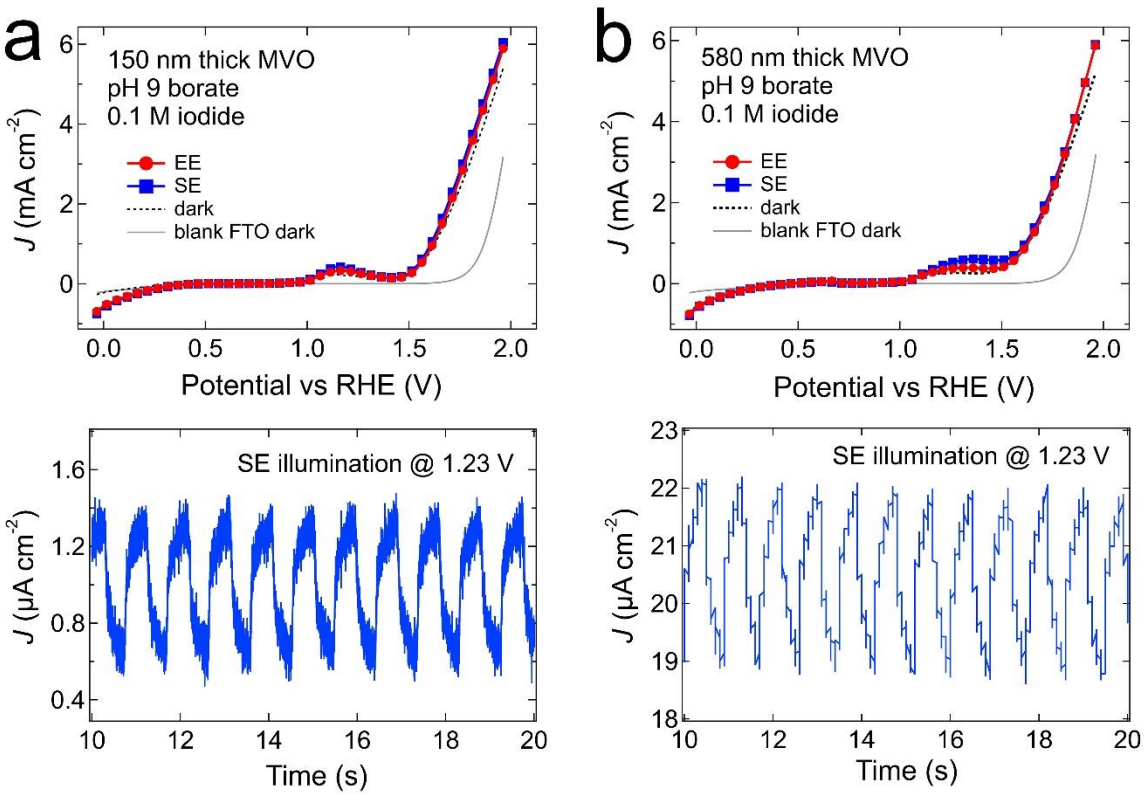

Figure A1.16 Photoelectrochemical (PEC) data for MVO films of different thickness. Current-potential (*J*-*E*) and current-time (*J*-*t*) data for iodide oxidation in pH 9 borate buffer for films with a thickness of (a) 150 nm and (b) 580 nm. *J*-*E* data were acquired at a potential sweep rate of 50 mV/s. *J*-*t* data were acquired at 1.23 V vs. RHE using chopped illumination (1.25 Hz) in the SE geometry. See Methods for other details.

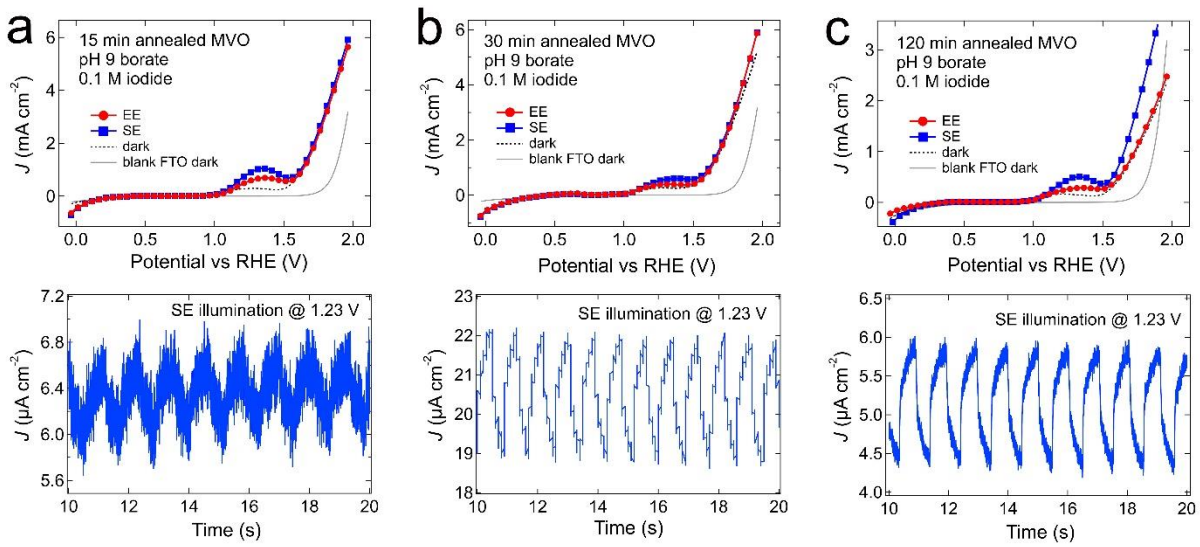

Figure A1.17 Photoelectrochemical (PEC) data for MVO films as a function of MVO annealing time. Current-potential (*J-E*) and current-time (*J-t*) data for iodide oxidation in pH 9 borate buffer for films annealed at 500 ºC for (a) 15 minutes, (b) 30 minutes, and (c) 120 minutes. *J-E* data were acquired at a potential sweep rate of 50 mV/s. *J-t* data were acquired at 1.23 V vs. RHE using chopped illumination (1.25 Hz) in the SE geometry. All of the MVO films were 580 ± 60 nm thick. See Methods for other details.

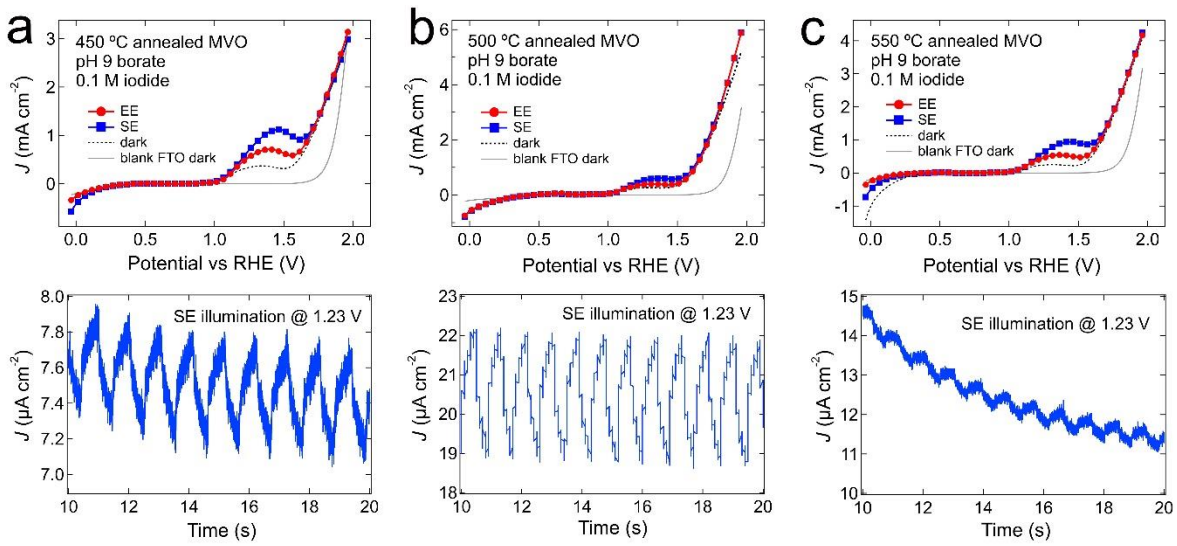

Figure A1.18 Photoelectrochemical (PEC) data for MVO films as a function of MVO annealing temperature. Current-potential (*J*-*E*) and current-time (*J*-*t*) data for iodide oxidation in pH 9 borate buffer for films annealed at (a) 450 ºC, (b) 500 ºC, and (c) 550 ºC for 30 minutes. *J*-*E* data were acquired at a potential sweep rate of 50 mV/s. *J*-*t* data were acquired at 1.23 V vs. RHE using chopped illumination (1.25 Hz) in the SE geometry. All of the MVO films were 580 ± 60 nm thick. See Methods for other details.

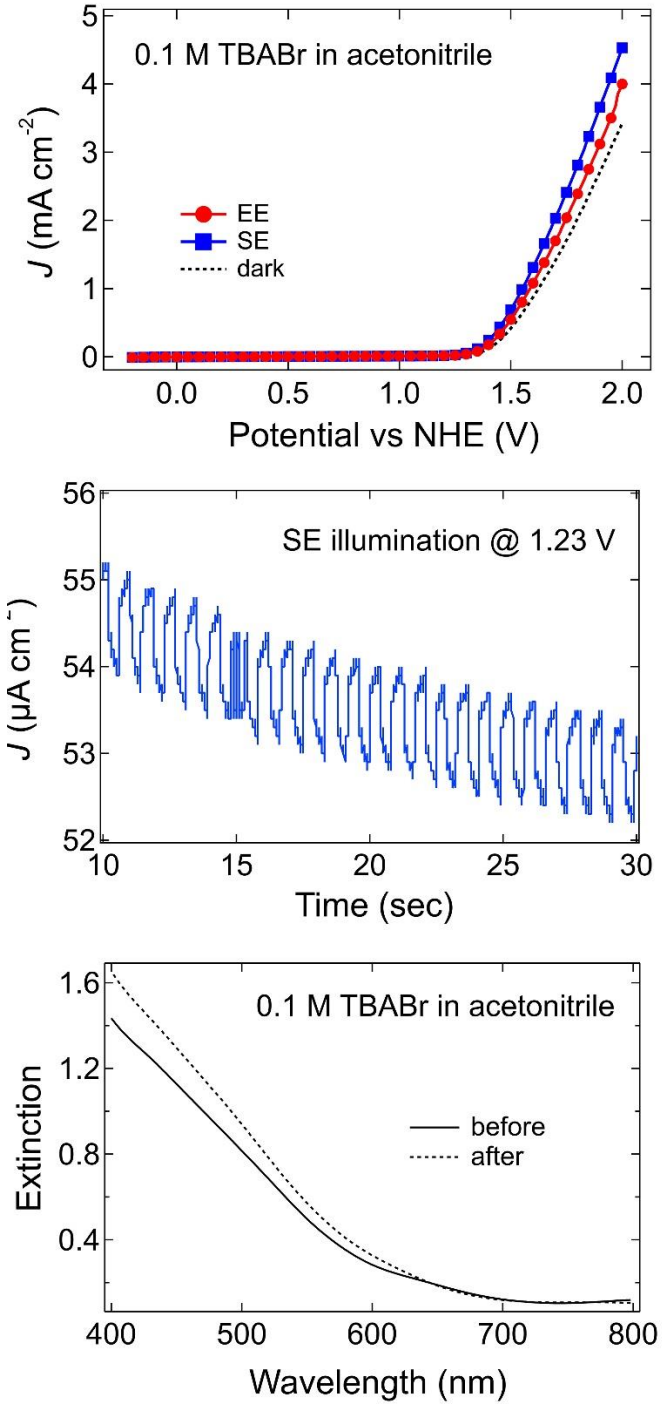

Figure A1.19 Non-aqueous photoelectrochemical data for an MVO film in 0.1 M tetrabutylammonium bromide (TBABr) in dry acetonitrile. Current-potential (*J-E*), current-time (*J-t*), and optical extinction spectra immediately before and after PEC measurements for bromide oxidation. *J-E* data were acquired at a potential sweep rate of 50 mV/s. *J-t* data were acquired at 1.23 V vs. NHE using chopped illumination (1.25 Hz) in the SE geometry. PEC data required ~20 minutes to collect per sample, so Δt ~ 20 minutes for the two optical spectra. The MVO film was 580 ± 60 nm thick. See Methods for other details.

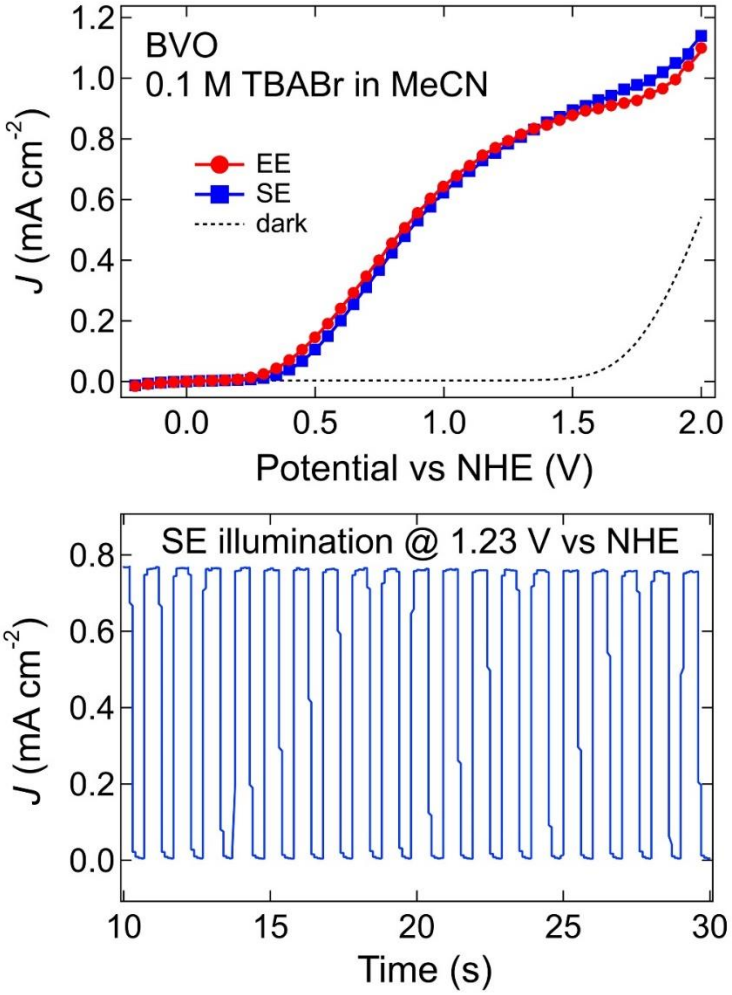

Figure A1.20 Photoelectrochemical J-E and J-t data for a BiVO4 (BVO) film measured in 0.1 M tetrabutylammonium bromide in acetonitrile. A photocurrent of ~0.75 mA cm^{-2} was measured at 1.23 V vs. NHE (1 Sun AM1.5G illumination). The *J-t* data were acquired at 1.23 V vs. NHE using chopped illumination (1.25 Hz) in the SE geometry.

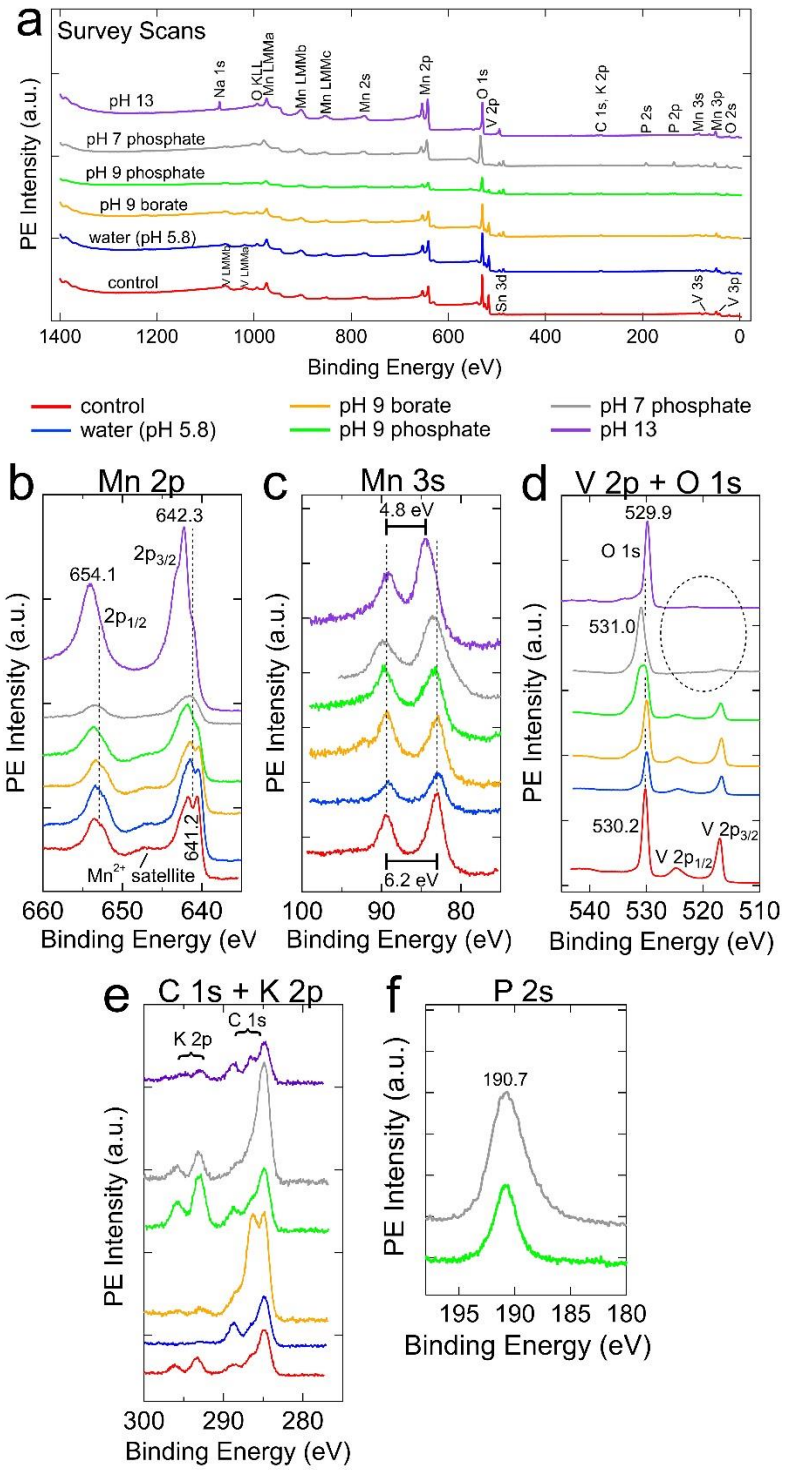

Figure A1.21 XPS data for standard β-MVO films immersed in various aqueous solutions for 20 hours unbiased in the dark. The solutions did not contain added Mn or V species. (a) Indexed survey scans. The only elements detected were Mn, V, O, C, K (origin unknown), Sn (from the substrate), P in the two films immersed in phosphate buffer, and Na on the film aged in 0.1 M NaOH. (b) Mn 2p region. The films aged in pure water (pH 5.8) and 0.1 M borate solution at pH 9 have nearly the same spectrum as the dry control film. The film aged in 0.1 M phosphate solution

at pH 9 shows the appearance of higher-energy $2p_{3/2}$ and $2p_{1/2}$ peaks consistent with partial conversion of Mn^{2+} to Mn^{3+}, possibly in the form of amorphous Mn_2O_3, Mn_3O_4, and/or Mn(III)-containing phosphates.[155,100,99] The film aged in 0.1 M phosphate solution at pH 7 appears to contain mostly Mn^{3+}, but broadening of the Mn 3s peaks (see below) suggests that substantial Mn^{2+} is still present. Finally, the spectrum of the film treated in 0.1 M NaOH (pH 13) is characteristic of Mn^{4+}, which is mostly likely present in the form of amorphous $MnO(OH)_2$ and MnO_2. (c) Mn 3s region. The energy separation between the two multiplet-split components decreases from 6.2 eV (characteristic of Mn^{2+}) for the control film to 4.8 eV (characteristic of Mn^{4+}) for the film aged at pH 13.[98] There is also substantial peak broadening in the film aged in pH 7 phosphate solution that is consistent with the presence of both Mn^{3+} and Mn^{2+}. (d) V 2p and O 1s region. The O 1s spectrum of the control film features a strong, narrow peak originating from the lattice oxygen of MVO. There is also a very weak high-energy tail probably caused by surface hydroxides. This tail becomes a small shoulder at ~532 eV in the film aged in water. The shoulder is more prominent for the film treated in borate solution. Immersion in pH 9 phosphate solution results in the appearance of an O 1s peak at 531 eV due to PO_3^{4-}.[156] Both phosphate and metal oxide lattice oxygen are present in this sample, as is the high-energy shoulder. Meanwhile, the vanadium peaks are significantly reduced in intensity, consistent with partial loss of vanadium and formation of Mn phosphates. The film aged in pH 7 phosphate solution exhibits a single oxygen peak at 531.0 eV due to phosphate. The metal oxide peak is largely gone. The high-energy shoulder is still present but weaker. Furthermore, the vanadium signal is almost gone (dashed oval). This is consistent with extensive conversion of the sample to Mn phosphates. Aging at pH 13 causes loss of all vanadium signal and a sharp oxygen peak at 529.9 eV with weak high-energy features that we assign to the bulk oxygen of MnO_2 plus surface hydroxides. (e) C 1s and K 2p region. (f) P 2s region. The binding energy of 190.7 eV is consistent with phosphate (PO_3^{4-}).[157] See Table 2 in the text for the Mn:V atomic ratio of each sample.

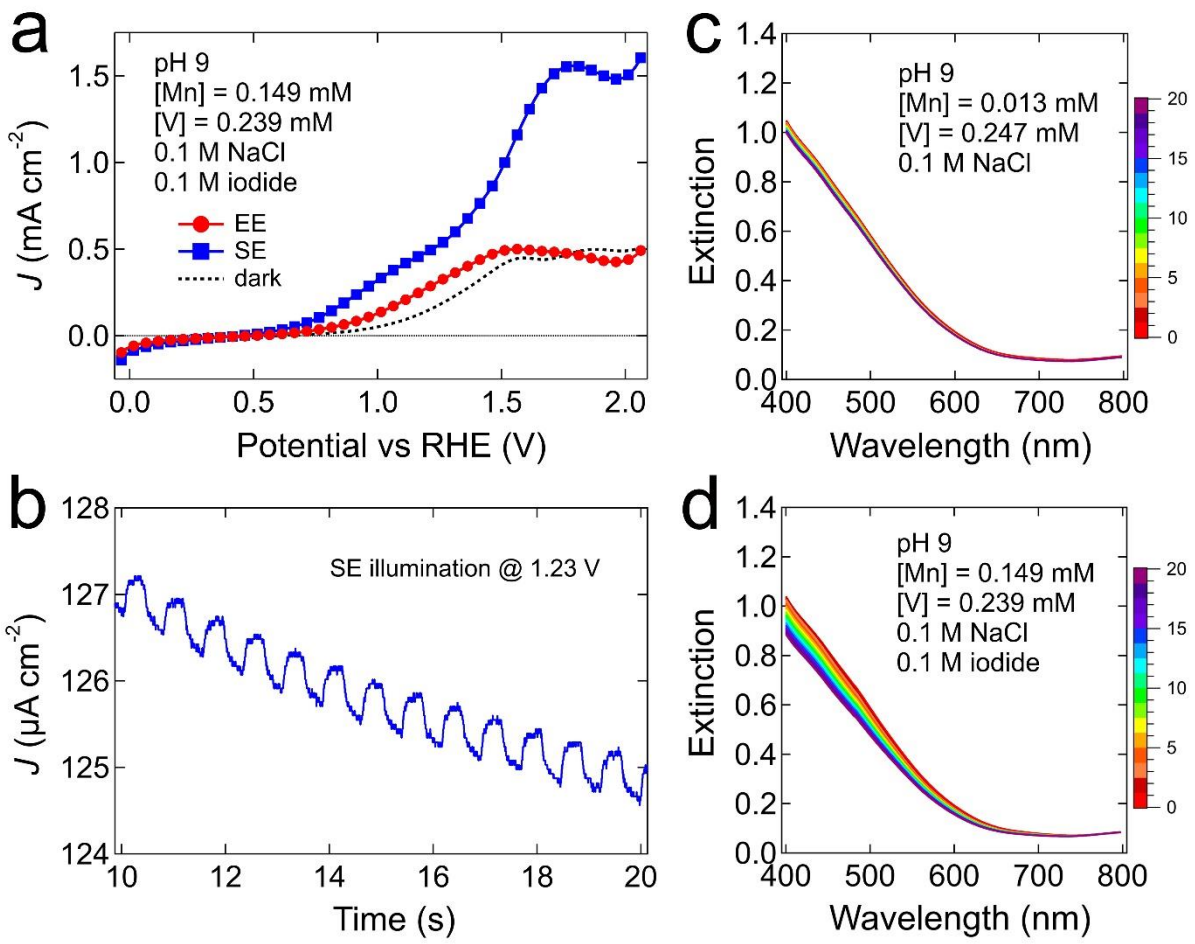

Figure A1.22 (a) Current-potential (J-E) and (b) current-time (J-t) plots for iodide oxidation by β-MVO films in Mn- and V-saturated electrolyte. The electrolyte composition was 0.149 ± 0.006 mM Mn, 0.239 ± 0.008 mM V, 0.1 M NaCl, and 0.1 M KI at pH 9. *J-E* data were acquired at a sweep rate of 50 mV/s. *J-t* data were acquired at 1.23 V vs. RHE using chopped illumination (1.25 Hz) in the SE geometry. (c) Representative spectral time series for films aged unbiased in the dark for 20 hours in 0.1 M NaCl containing 0.013 ± 0.001 mM Mn and 0.247 ± 0.009 mM V at pH 9 and (d) 0.1 M NaCl containing 0.1 M KI, 0.149 ± 0.006 mM Mn and 0.239 ± 0.008 mM V at pH 9 (the same electrolyte used in panels (a-b)). Scans were acquired every 15 minutes for 20 hours. The MVO films were 520 ± 60 nm thick. See Methods for other details.

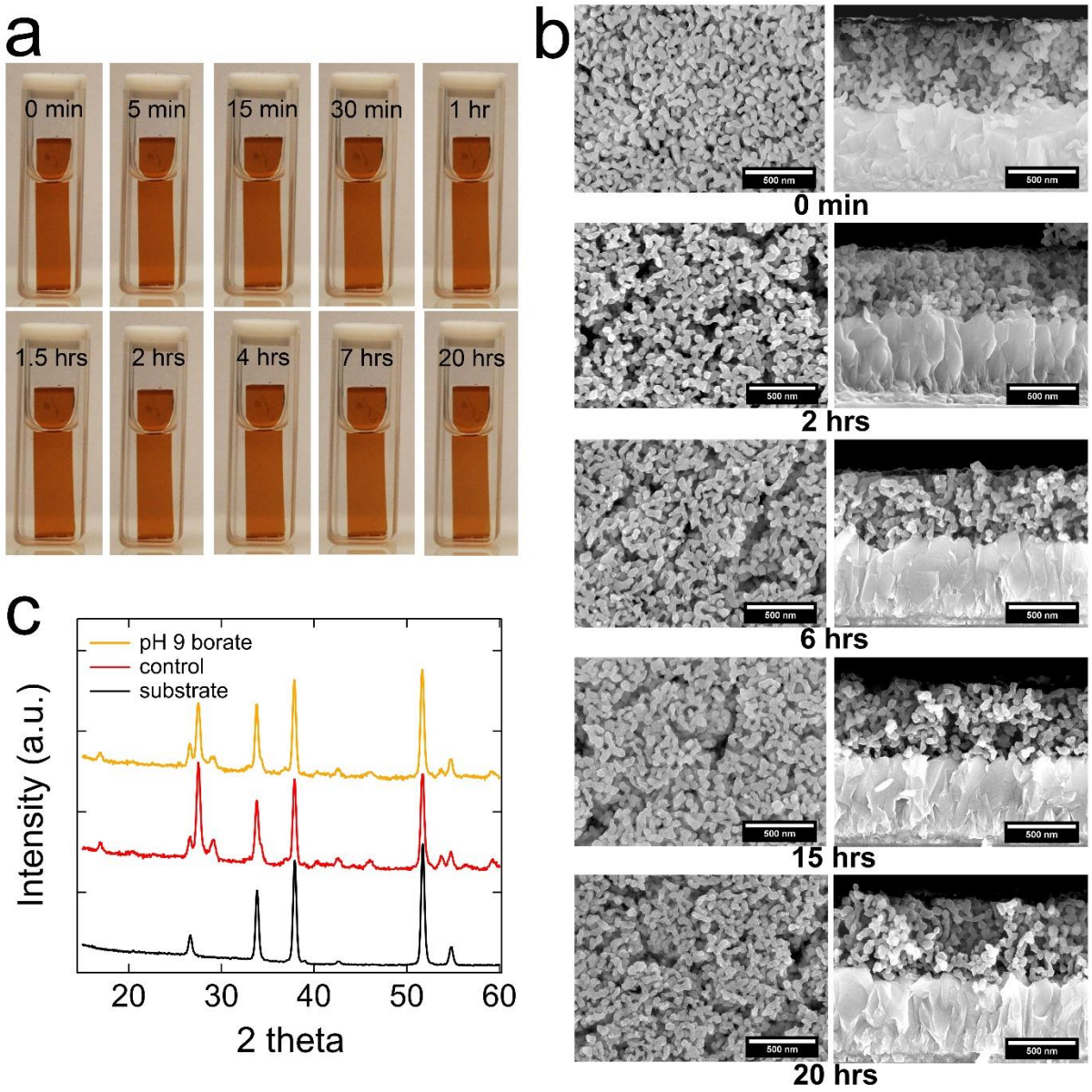

Figure A1.23 MVO film stability in pH 9 borate buffer solution in the absence of light and applied bias. No Mn or V was added to the initial solution. (a) Photographic time series of a film from 0 min to 20 hours of immersion in the solution. (b) Plan-view and cross-section SEM images of films aged in solution for 0 min, 2 hrs, 6 hrs, 15 hrs, and 20 hrs. Some minor surface roughening and etching of the crystallites occurs, but the gross film morphology is unchanged. (c) XRD patterns of an MVO film before immersion (red), an MVO film after 20 hrs of immersion (orange), and a clean FTO-coated glass substrate (black). The pattern of the aged film is nearly identical to that of the control film, with no new peaks.

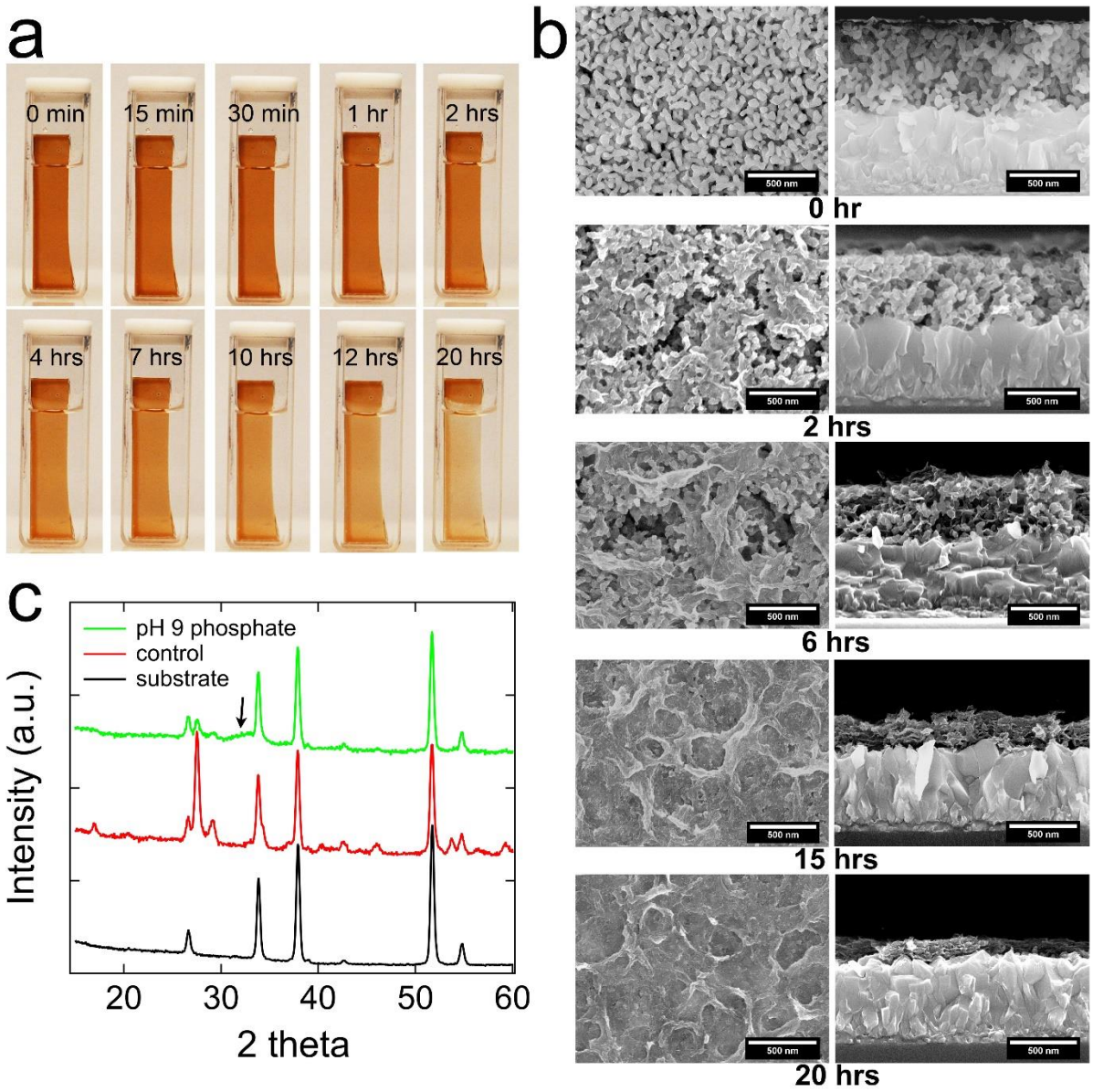

Figure A1.24 MVO film stability in pH 9 phosphate buffer solution in the absence of light and applied bias. No Mn or V was added to the initial solution. (a) Photographic time series of a film from 0 min to 20 hours of immersion in the solution. The color of the immersed part of the film begins to fade within several hours and becomes significantly lighter after 20 hours, consistent with partial dissolution and/or phase transformation. (b) Plan-view and cross-section SEM images of films aged in solution for 0 min, 2 hrs, 6 hrs, 15 hrs, and 20 hrs. The nanostructured film is gradually etched and slowly collapses into a dense, thinner layer within 15-20 hours. (c) XRD patterns of an MVO film before immersion (red), an MVO film after 20 hrs of immersion (green), and a clean FTO-coated glass substrate (black). The pattern of the aged film shows much smaller MVO peaks and the appearance of a weak, very broad feature at ~33 degrees (labelled with an arrow), which we assign to the 222 reflexion of α-Mn_2O_3 (PDF # 00-041-1442). Overall, these changes are qualitatively the same as in pH 7 phosphate solution, only slower.

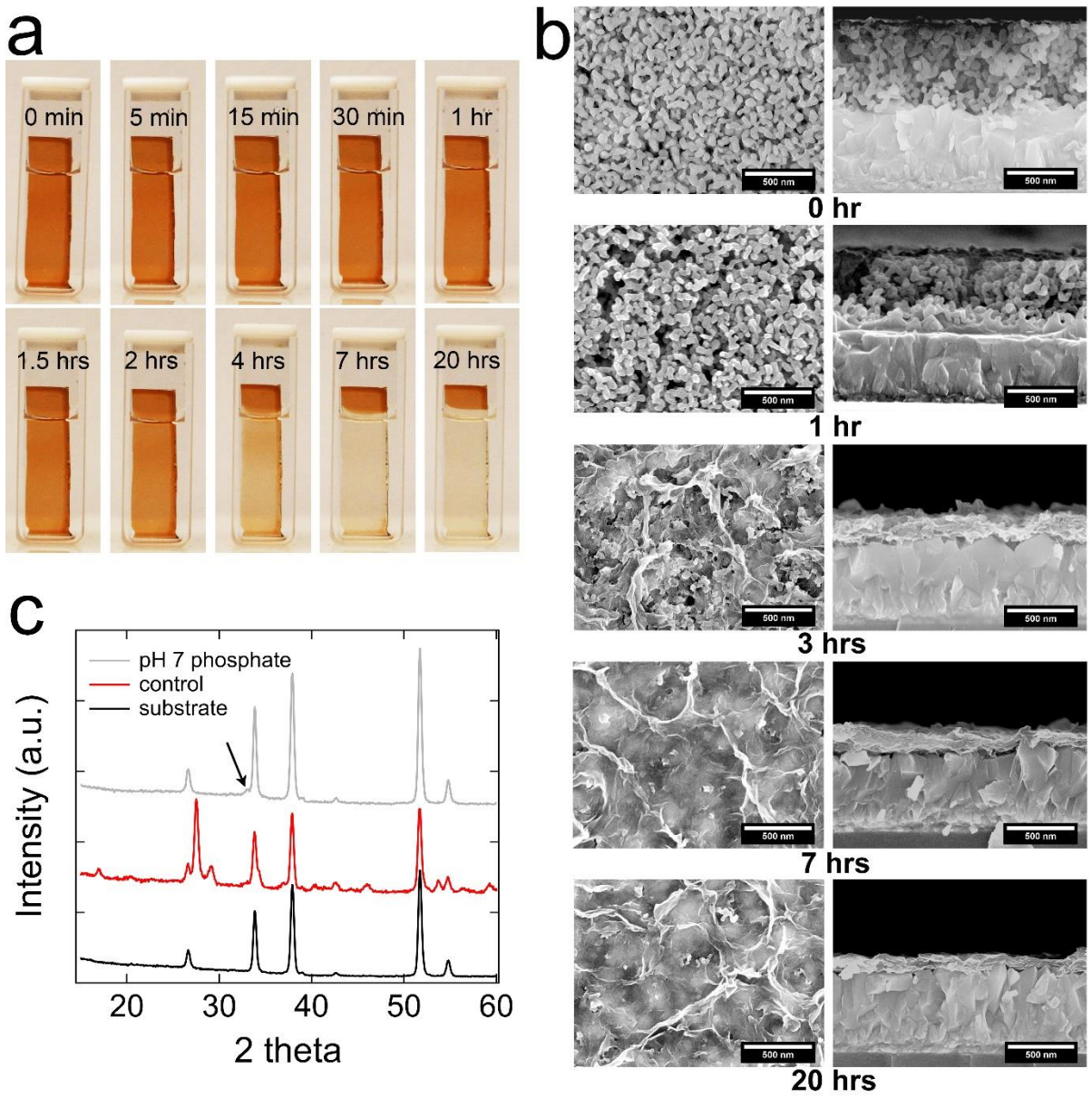

Figure A1.25 MVO film stability in pH 7 phosphate buffer solution in the absence of light and applied bias. No Mn or V was added to the initial solution. MVO film stability in pH 7 phosphate buffer solution in the absence of light and applied bias. No Mn or V was added to the initial solution. (a) Photographic time series of a film from 0 min to 20 hours of immersion in the solution. The color of the immersed part of the film begins to fade within 1-2 hours and becomes very faint after 20 hours, consistent with dissolution and/or phase transformation. (b) Plan-view and cross-section SEM images of films aged in solution for 0 min, 5 min, 15 min, 4 hrs, and 20 hrs. The nanostructured film collapses into a dense, much thinner layer within a few hours. This layer continues to slowly thin out to at least 20 hours. (c) XRD patterns of an MVO film before immersion (red), an MVO film after 20 hrs of immersion (grey), and a clean FTO-coated glass substrate (black). The pattern of the aged film shows a complete loss of MVO peaks and the appearance of a weak shoulder at 33.0 degrees (labelled with an arrow), which we assign to the 222 reflexion of α-Mn_2O_3 (PDF # 00-041-1442).

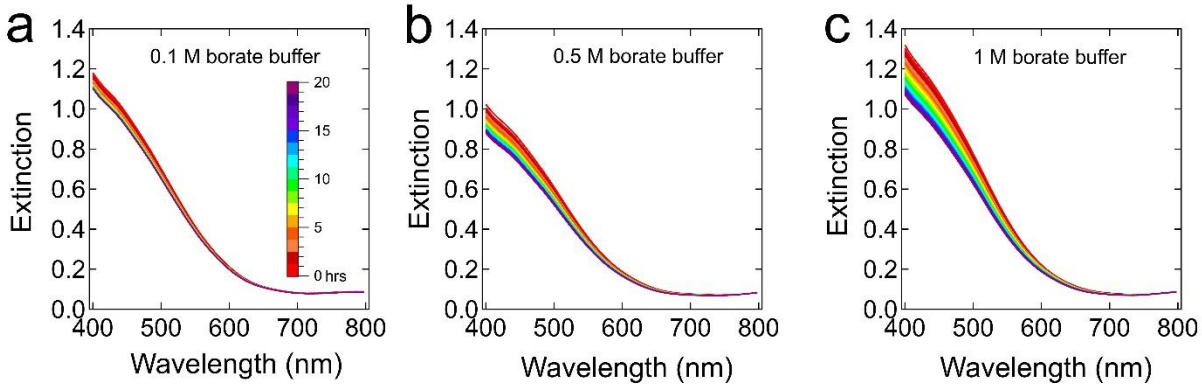

Figure A1.26 . Effect of borate ion concentration on film stability. **S26**Spectral time series for a standard MVO film immersed in (a) 0.1 M, (b) 0.5 M and (c) 1 M borate buffer at pH 9 for 20 hours. [Mn] = [V] = 0.

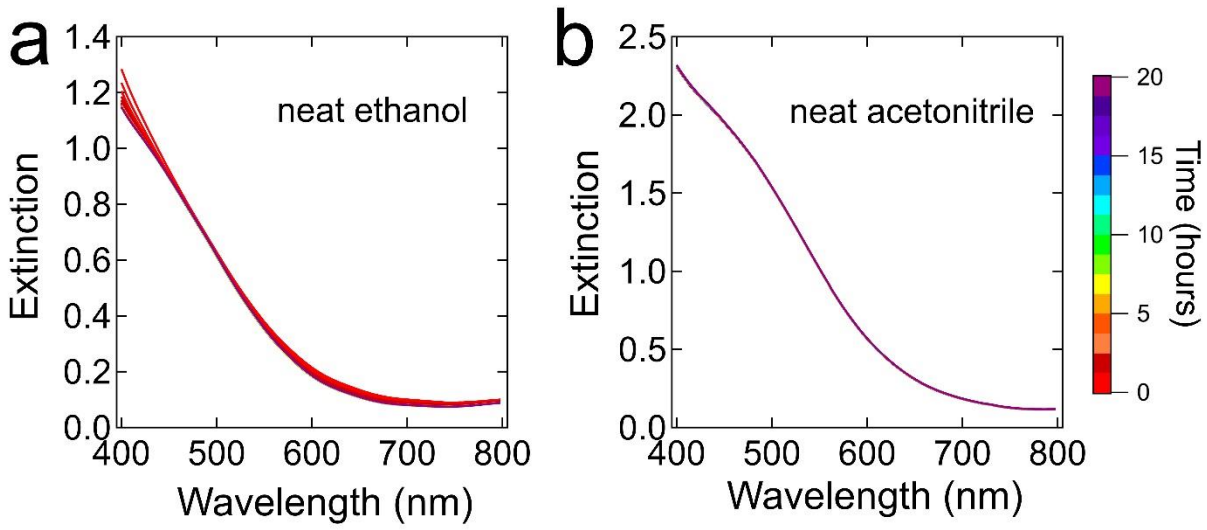

Figure A1.27 Film stability in pure ethanol and acetonitrile. Spectral time series for a standard MVO film immersed in (a) neat ethanol and (b) neat acetonitrile for 20 hours. [Mn] = [V] = 0.

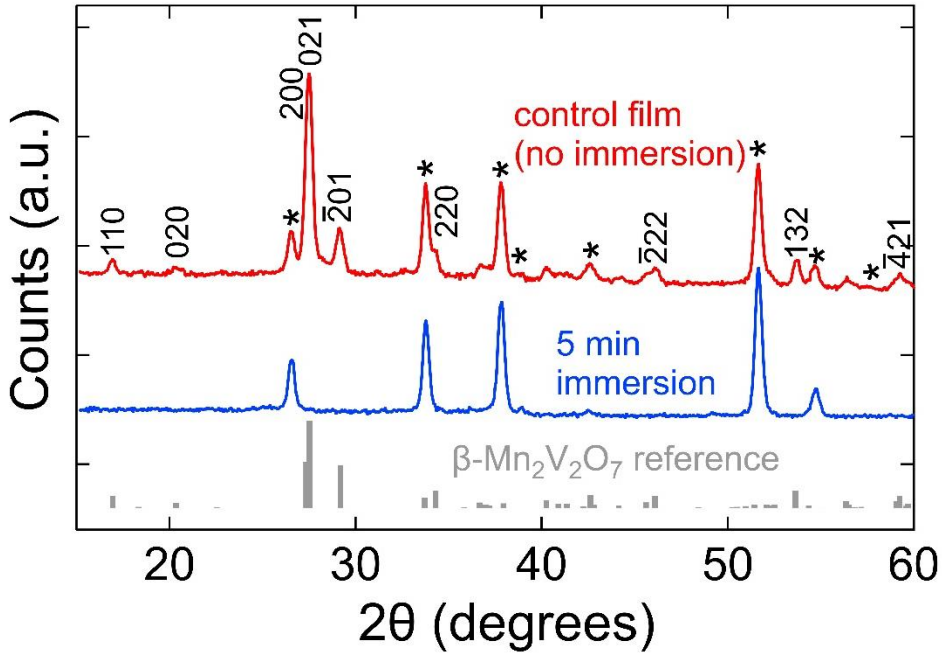

Figure A1.28 GIXRD pattern of a β-MVO film aged in pH 13 electrolyte for 5 minutes. The MVO peaks disappear. The angle of incidence was 0.79° for the aged film and 0.85° for the control film. The β-MVO reference pattern (grey bars) is also shown.

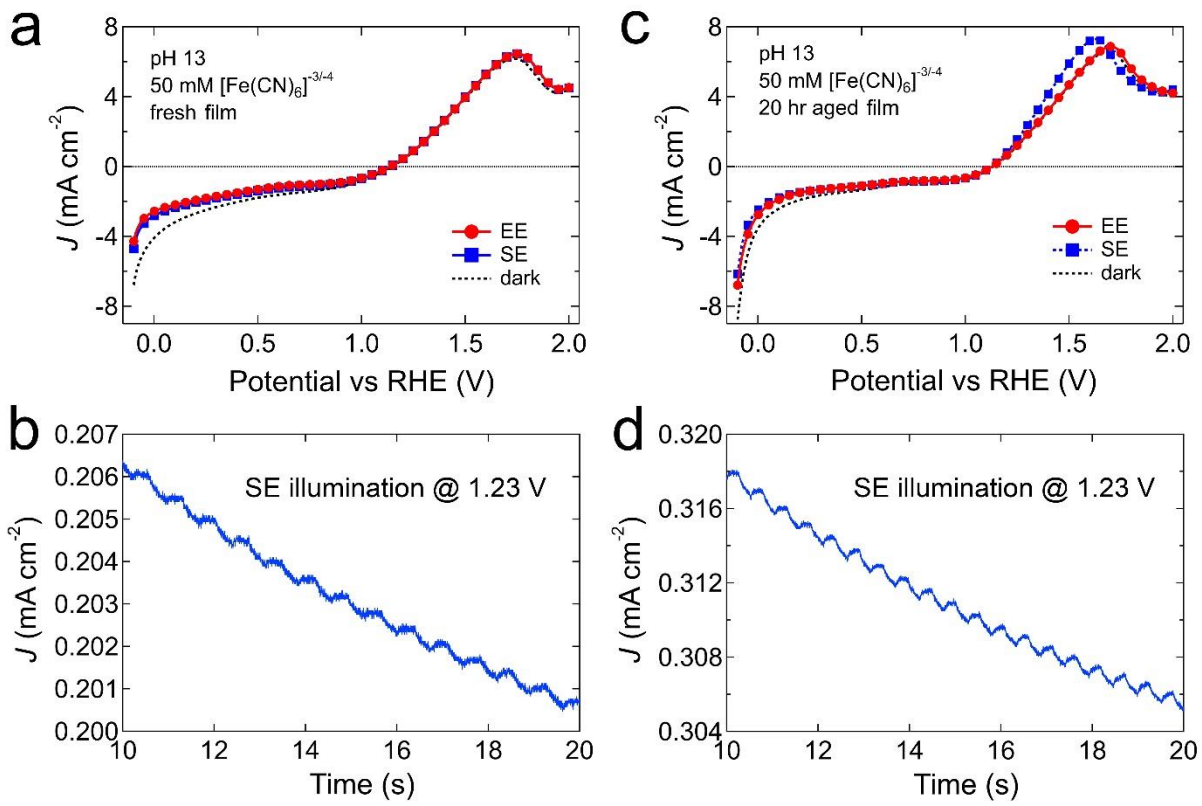

Figure A1.29 Representative photoelectrochemical data for MVO films in 0.1 M aqueous NaOH (pH 13) containing 50 mM [Fe(CN)6]3-/4- redox couple. Current-potential (*J-E*) and current-time (*J-t*) plots for (a-b) a fresh film and (c-d) a film after 20 hours of immersion in the electrolyte (dark and unbiased). *J-E* data were acquired at a potential sweep rate of 50 mV/s. *J-t* data were acquired at 1.23 V vs. RHE using chopped illumination (1.25 Hz) in the SE geometry. Data acquisition for the fresh film started within 3-4 minutes of immersion in the electrolyte and required ~15 minutes to complete, during which time the film degraded significantly (see Fig. 5). The MVO films were 580 ± 60 nm thick. See Methods for other details.

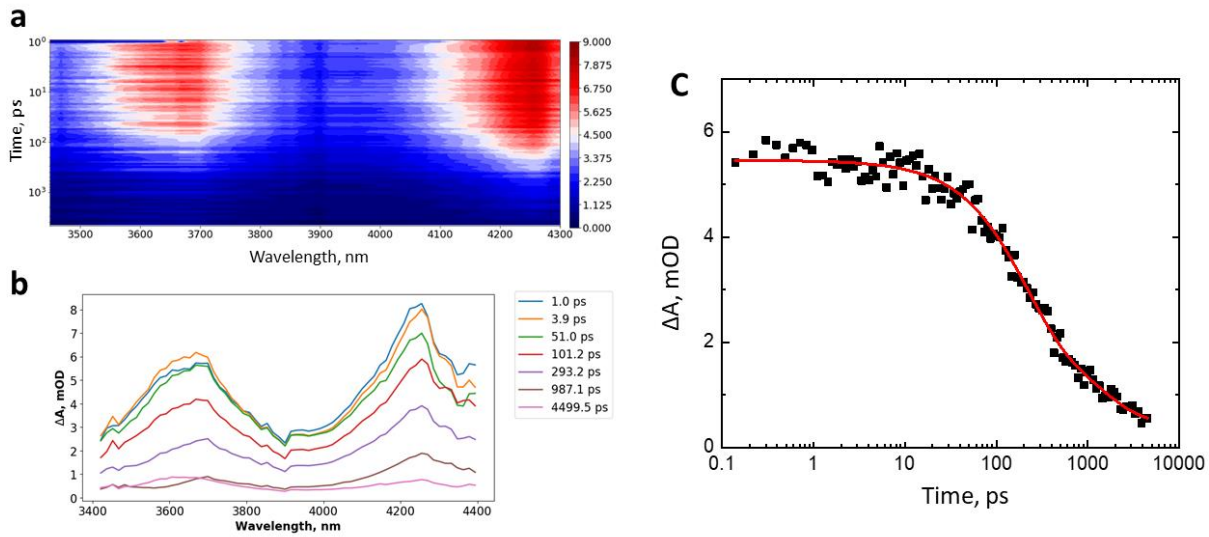

Figure A1.30 . (a-b) Mid-IR transient absorption spectra and (c) kinetics for a dry MVO film pumped at 400 nm and probed at 4.2 μm. The spectral features are convoluted with the features of the mid-IR continuum probe.

Table A1.2 Fit parameters for mid-IR PIA kinetics.

	A_1	t_1 (ps)	A_2	t_2 (ps)
4200 nm decay	65%	197 (24)	35%	1389 (616)

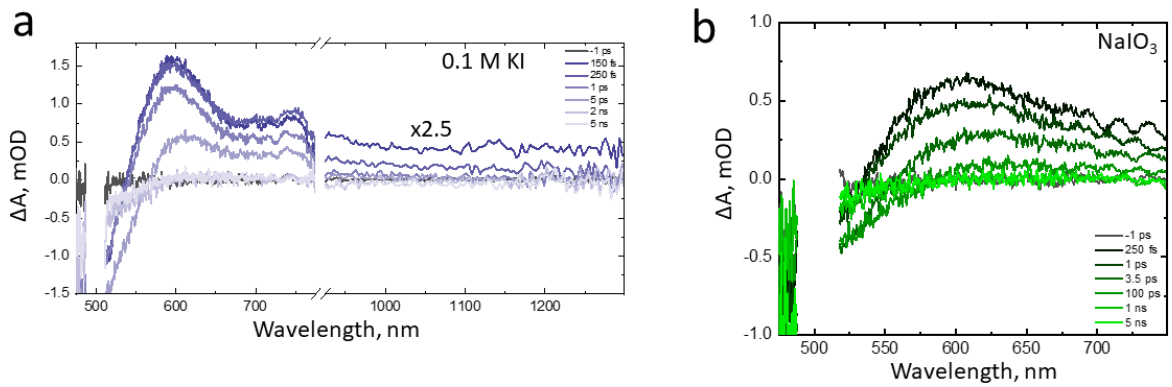

Figure A1.31 Transient absorption spectra at selected delay times for an MVO film immersed in (a) 0.1 M KI in 0.1 M borate buffer at pH 9 and (b) 0.1 M NaIO3 in 0.1 M borate buffer at pH 9.

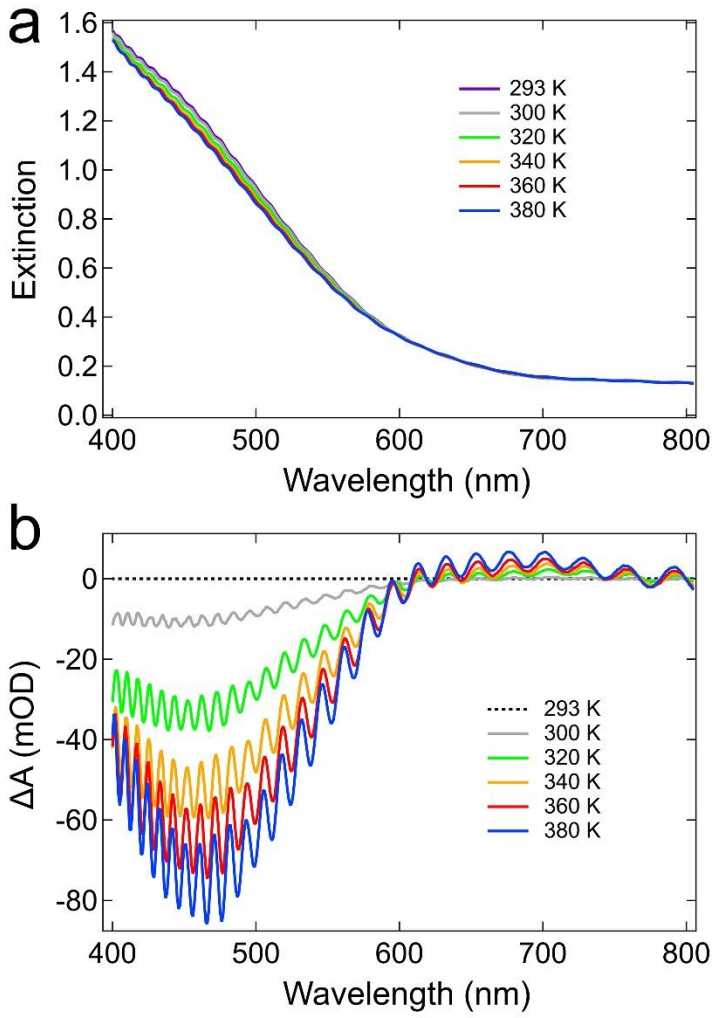

Figure A1.32 (a) Steady-state variable-temperature optical extinction spectra of a β-MVO film on a sapphire substrate from 293-380 K. (b) Corresponding difference spectra. Fringes in the spectra are due to Fabry-Perot interference.

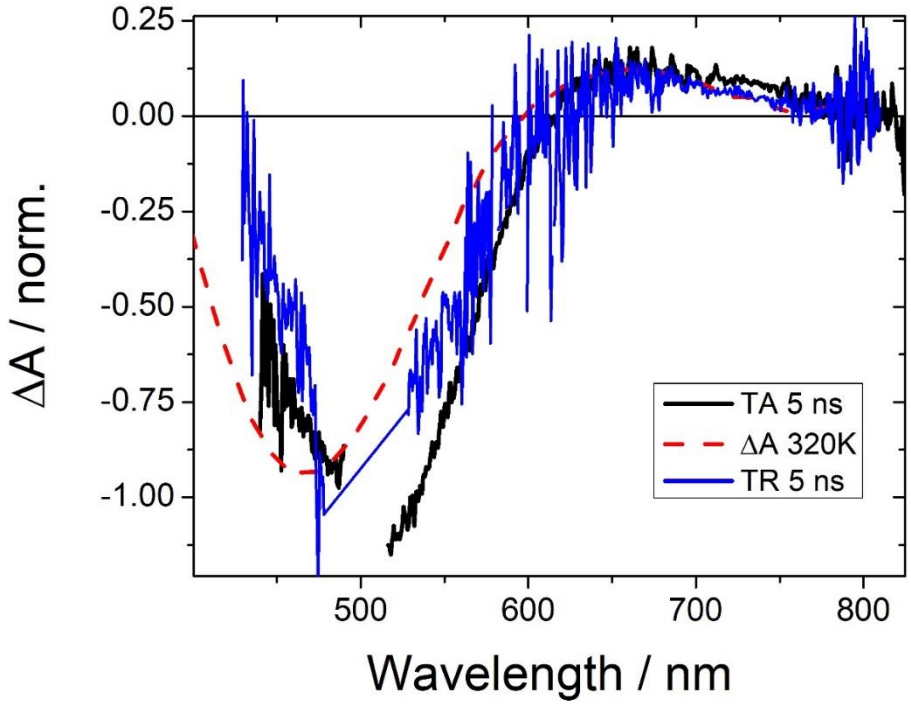

Figure A1.33 Comparison of the long-lived transient absorption (TA) spectrum (black), transient reflectivity (TR) spectrum (blue), and steady-steady extinction difference spectrum at 320 K (red) for a dry MVO film.

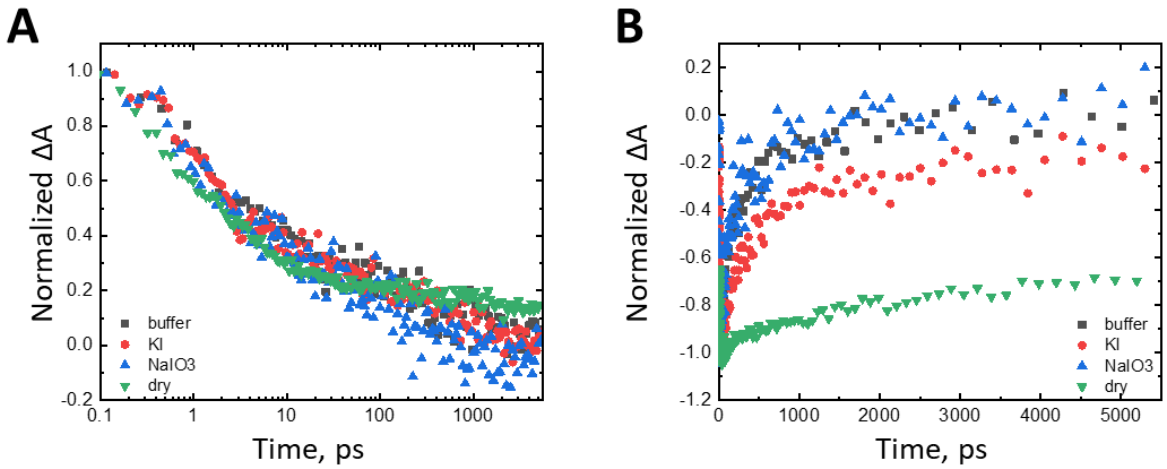

Figure A1.34 Kinetics of (a) the PIA at a 715 nm probe wavelength and (b) the GSB at 520 nm under various sample conditions.

Table A1.3 Fit parameters for PIA decay at 1100 nm.

	dry	0.1 M borate (pH 9)	buffer + 0.1 M KI
A_1	93%	87%	100%
t_1 (ps)	0.43 (0.03)	0.43 (0.03)	0.101 (0.02)
A_2	7%	13%	-
t_2 (ps)	176 (40)	377 (66)	-

Appendix 2 (A2)

Table 3.1 Film thickness as a function of growth current

S no	Growth time (min)	Film thickness (nm)
1	3	250
2	6	600
3	9	900
4	12	1200
5	15	1500

Appendix 3 (A3)

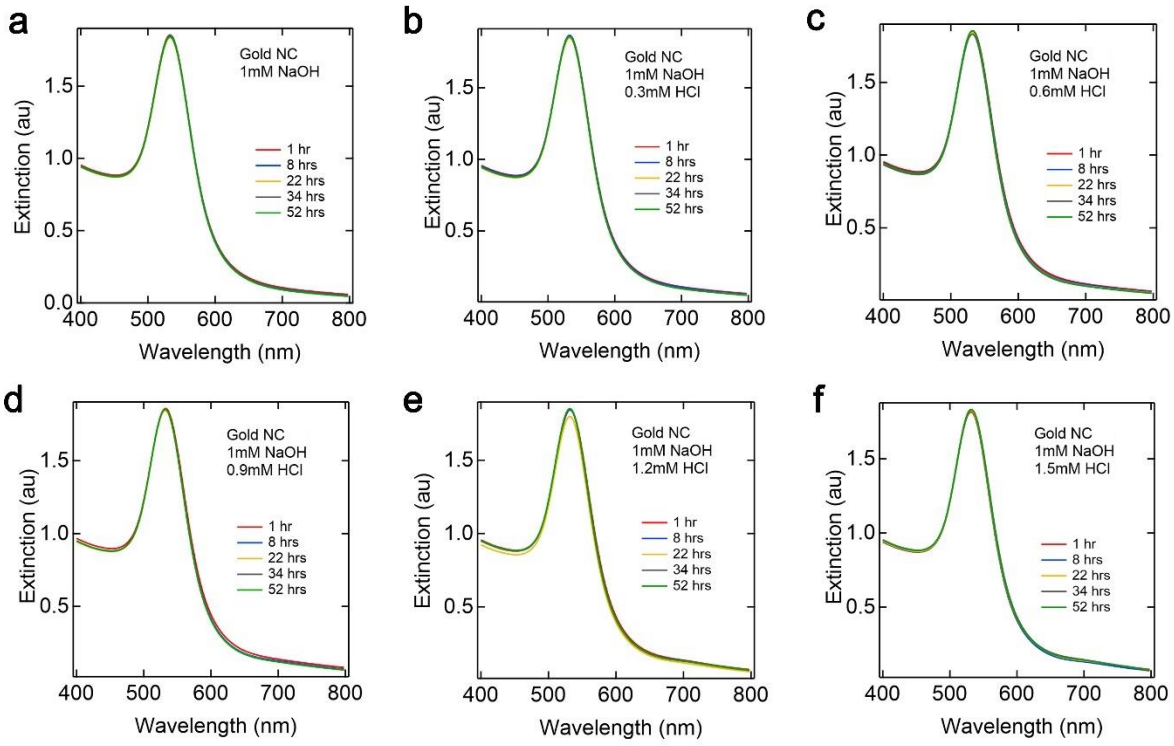

Figure A3.1 Acid effect on citrate capped gold nanoparticles.

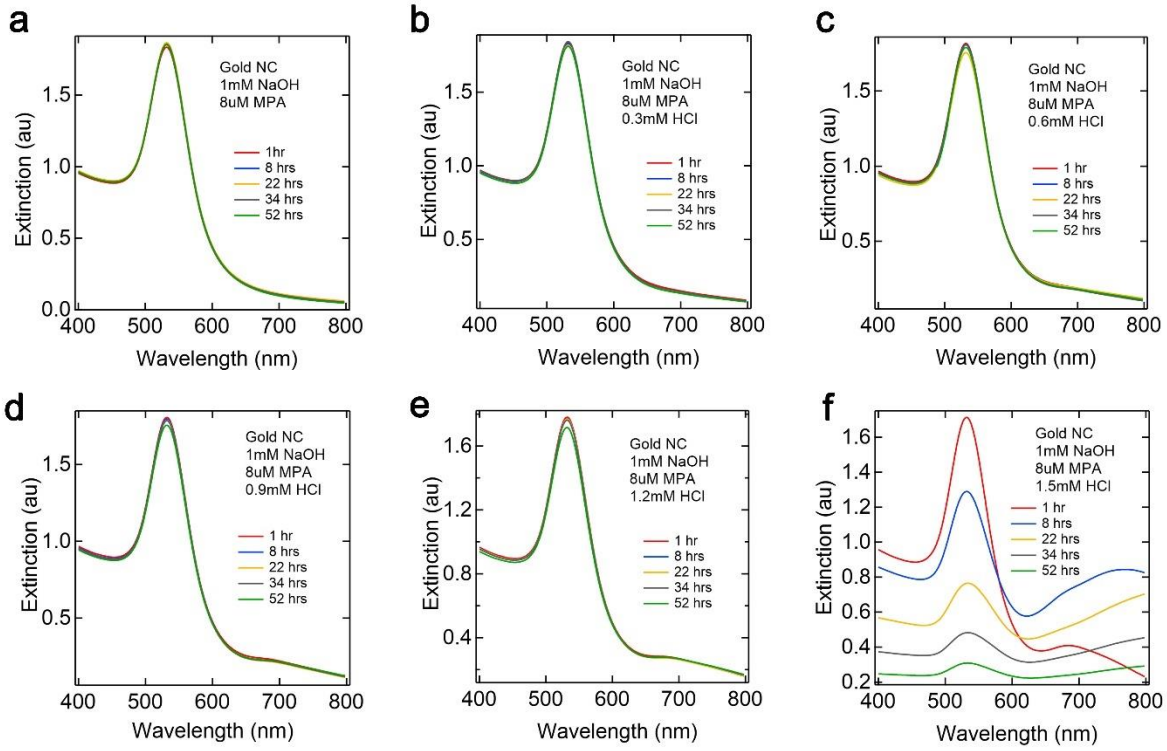

Figure A3.2 Acid effect on MPA capped gold nanocrystals

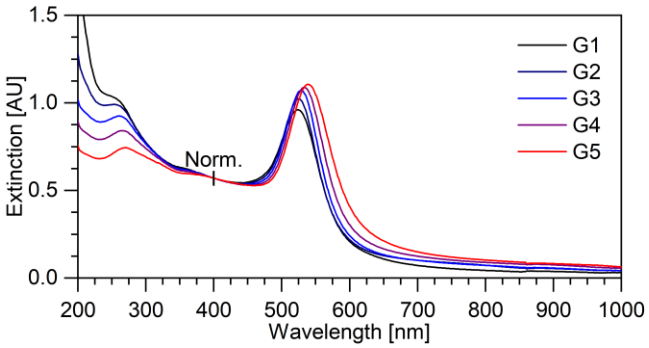

Figure A3.3 UV-vis extinction spectra of the different fractions obtained during seeded growth of citrate-capped AuNPs. The fraction G3 was used for the study of SiO2 growth on AuNPs.

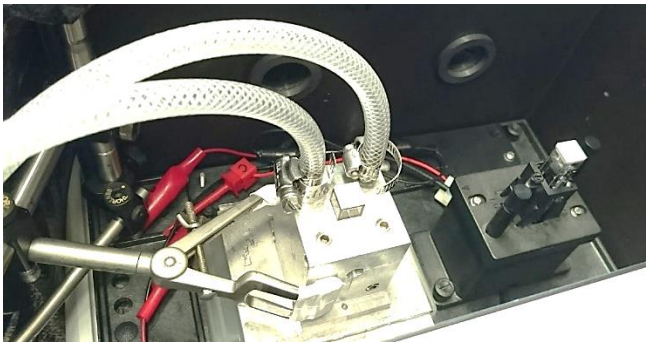

Figure A3.4 Photograph of the temperature-controlled sample compartment in the UV-vis spectrometer.

The *in situ* spectra of silica NP formation are fitted with the following expression:

$$A(E) = \overbrace{c_s\left(e^{b_s E} - y_s\right)}^{\text{silica}}$$

The spectral shape (determined by b_s and y_s) is independent of time and initial TEOS concentration.

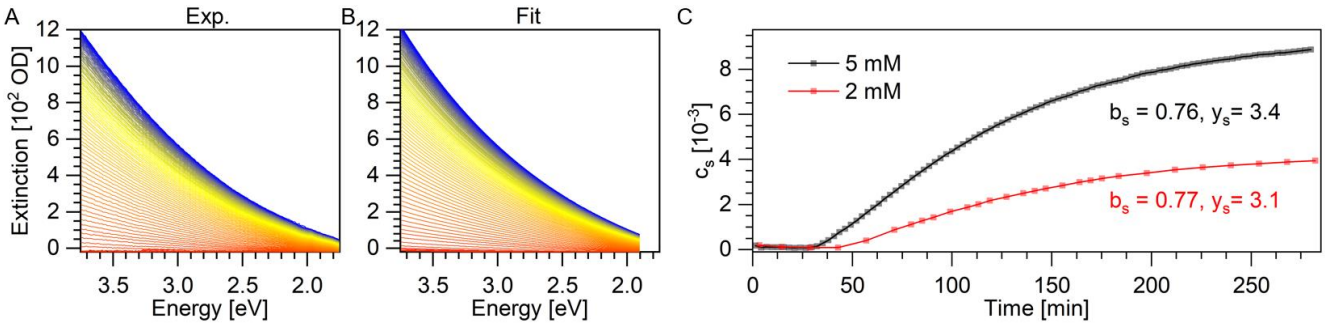

Figure A3.5 In situ UV-vis spectroscopy of SiO2 NP formation in the absence of AuNPs. (A) Experimental and (B) fitted spectra during SiO2 NP formation with 5 mM TEOS. (C) Time-dependence of cs with 5 mM (black) and 2 mM (red) TEOS, along with the fitted values of t

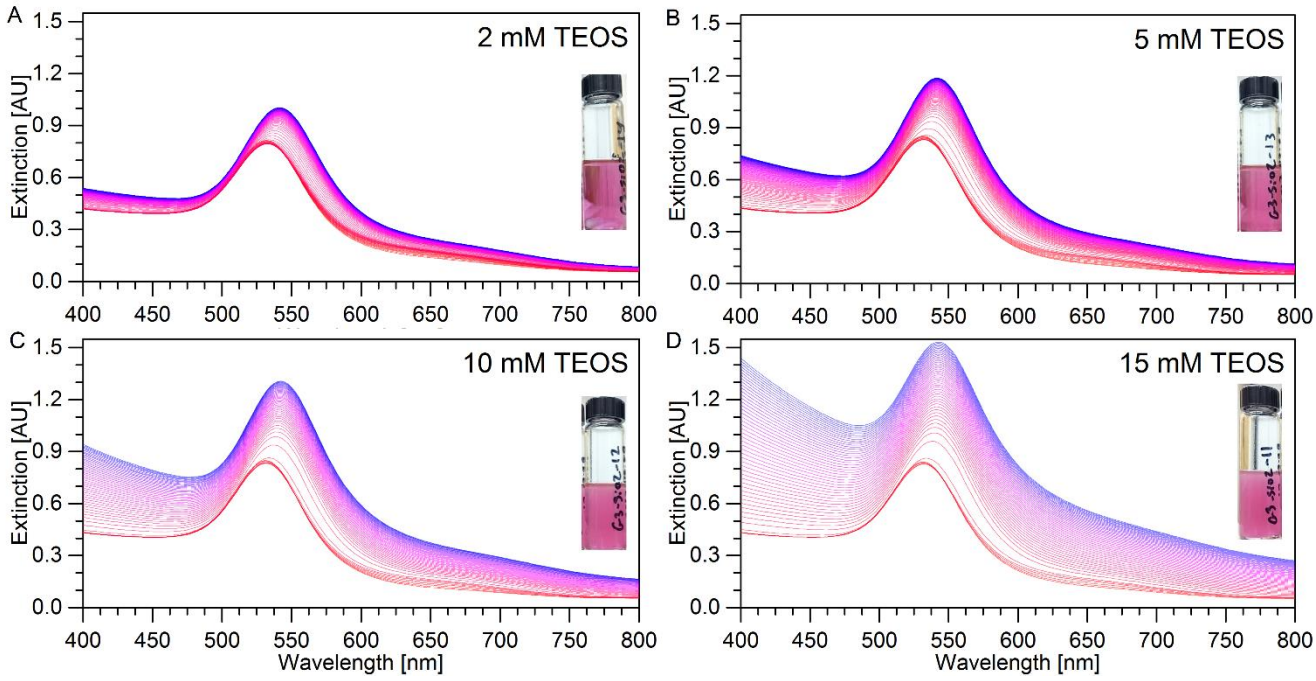

Figure A3.6 Raw In situ UV-vis data for Au@SiO2 NP formation with initial TEOS concentrations of (A) 2 mM, (B) 5 mM, (C) 10 mM, and (D) 15 mM. Insets show photographs of the final product dispersions.

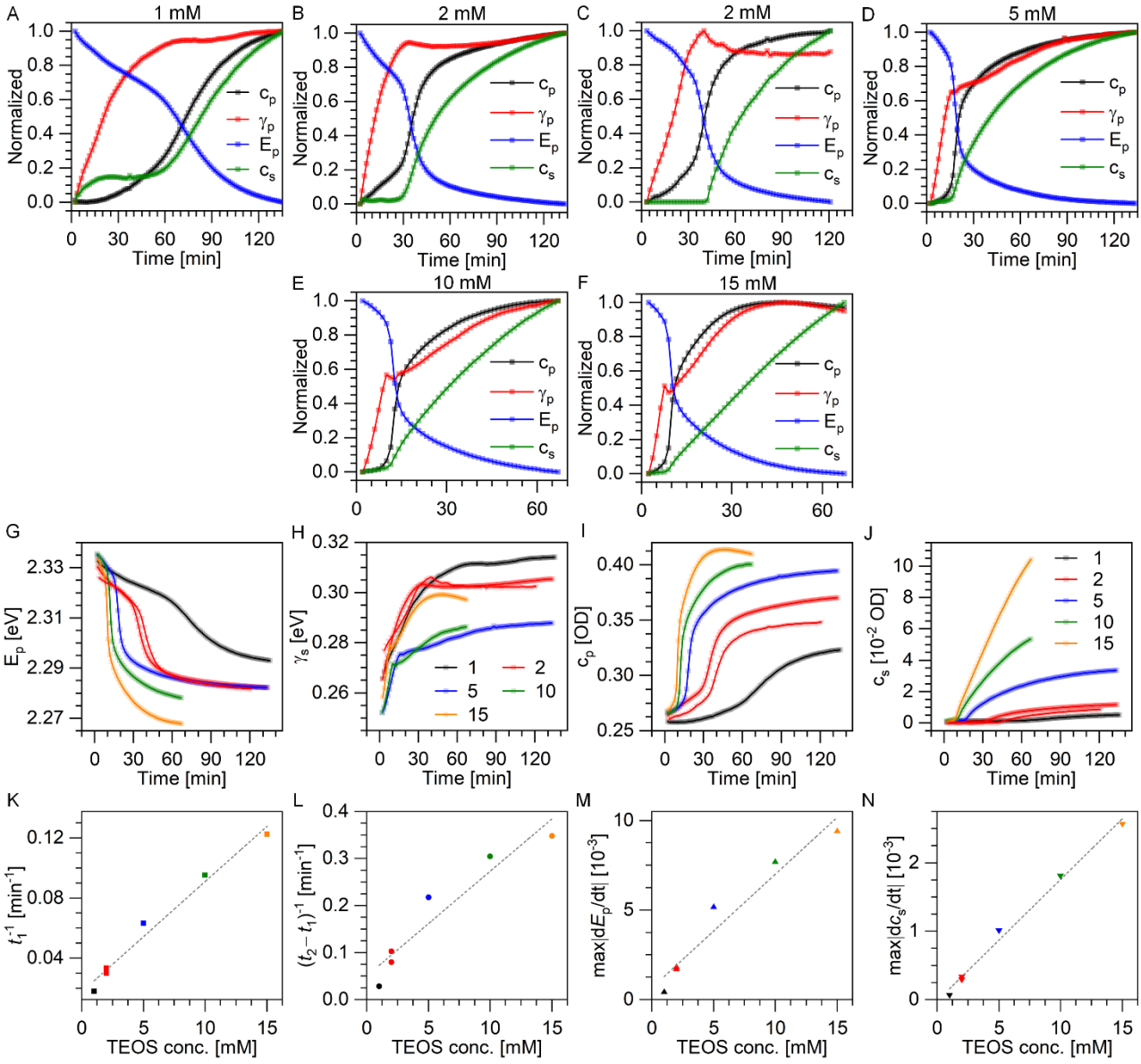

Figure A3.7 Time-dependence of the fitting parameters for Au@SiO2 NP formation at various TEOS concentrations. (A-F) Overlays of normalized curves for individual experiments. (G-J) Overlays of curves for individual fitting parameters from different experiments. Rate vs. TEOS concentration of apparent rates extracted from the (K-M) E_p and (N) c_s time dependence. Dashed lines represent linear fits corresponding to first-order kinetics.

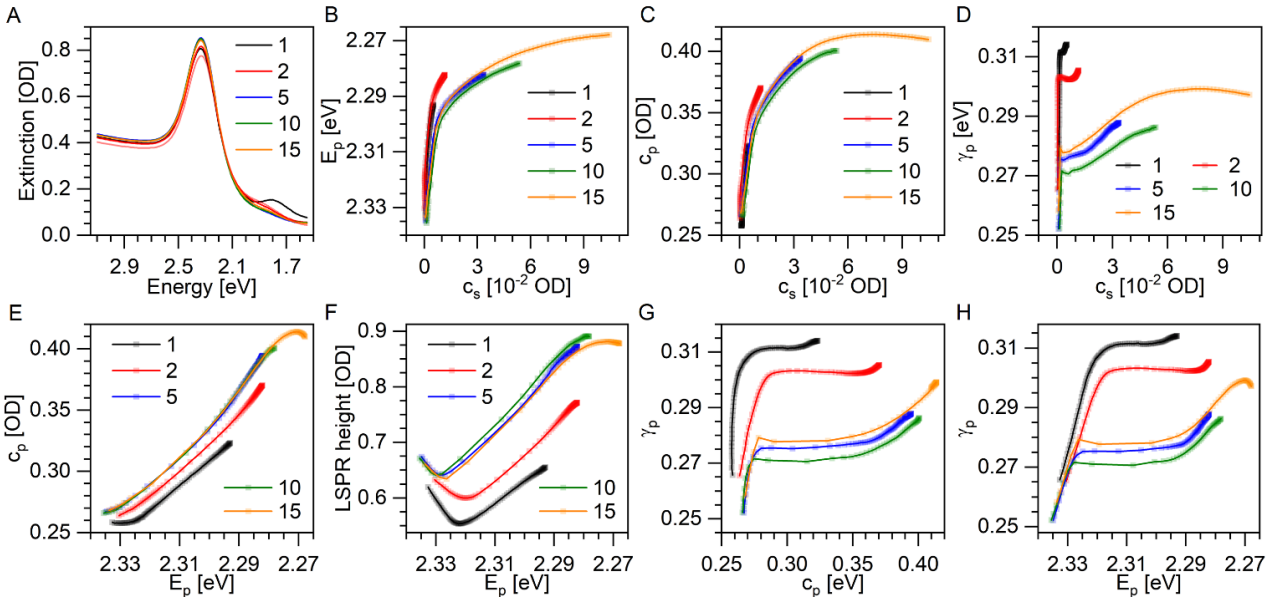

Figure A3.8 (A) Initial UV-vis extinction spectra at different [TEOS] (in mM). Slight aggregation gives rise to small deviations in initial fitting parameters, especially γp. (B-H) Correlations between fitting parameters. Stages of Au@SiO2 NP formation appear as domains with coupled parameter behavior.

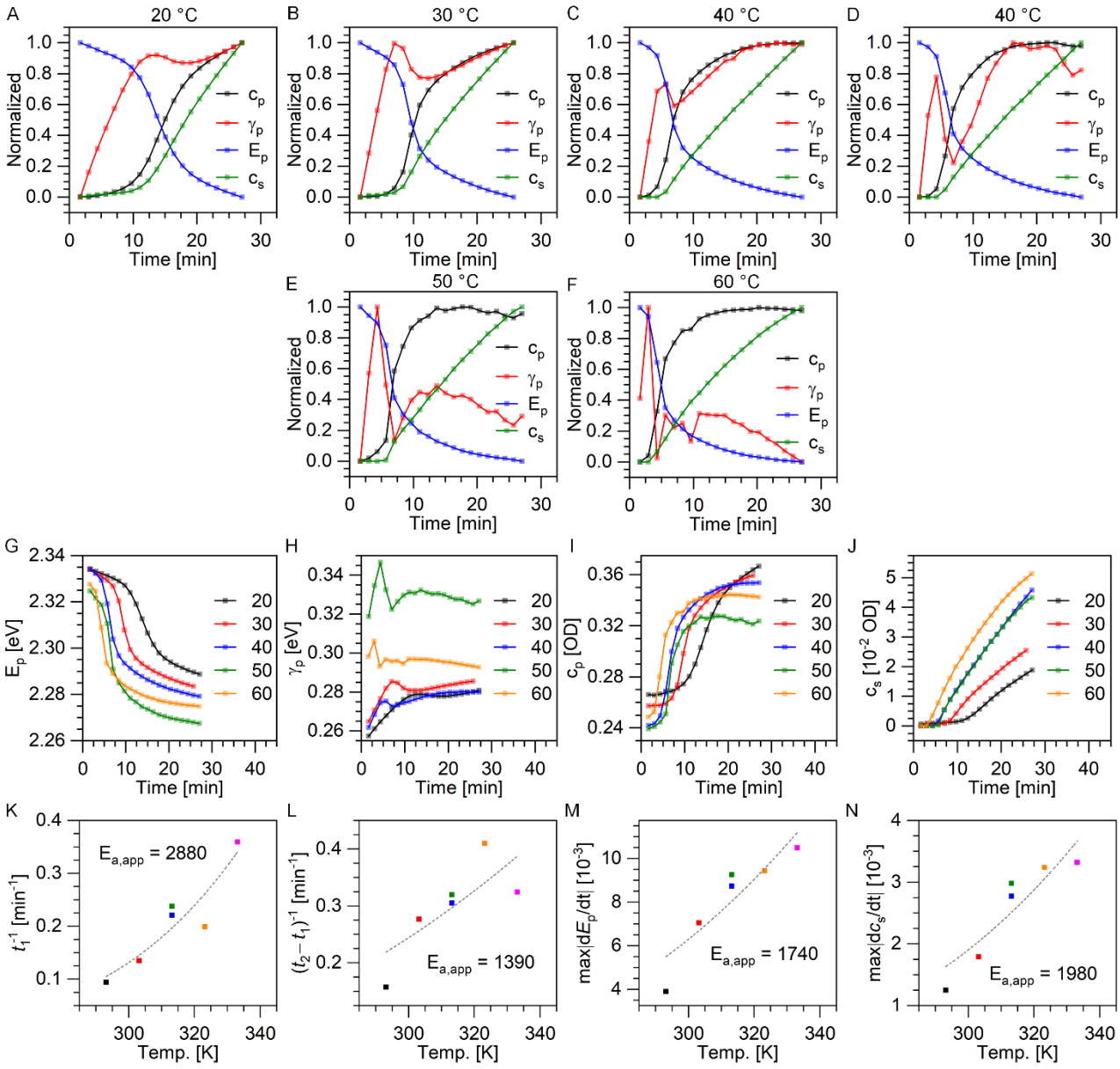

Figure A3.9 Time-dependence of fitting parameters for Au@SiO2 NP formation at various temperatures. (A-F) Overlays of normalized curves for individual experiments. (G-J) Overlays of curves for individual fitting parameters from different experiments. Arrhenius plots of apparent rates extracted from the (K-M) E_p and (N) c_s time dependence. Dashed lines represent Arrhenius fits and the apparent activation energies, $E_{a,app}$, in arbitrary units are given in the panels.

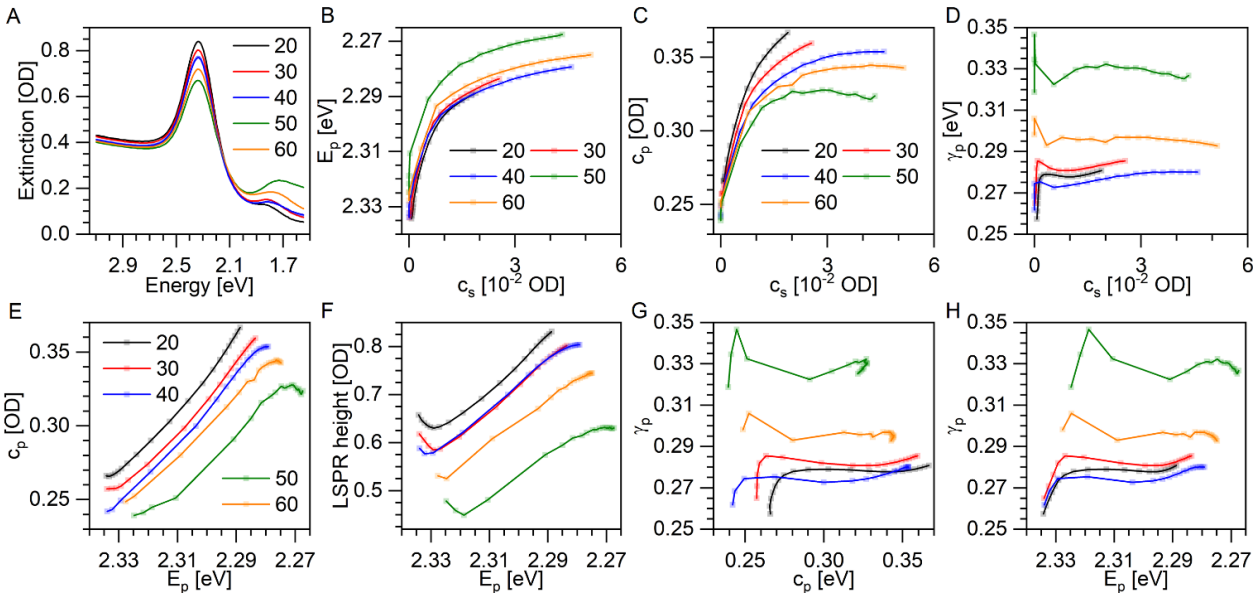

Figure A3.10 . (A) Initial UV-vis extinction spectra at various temperatures (in °C). Slight aggregation gives rise to small deviations in the initial fitting parameters, especially γp. (B-H) Correlations between fitting parameters. The stages of Au@SiO_2 NP formation appear as domains with coupled parameter behavior.

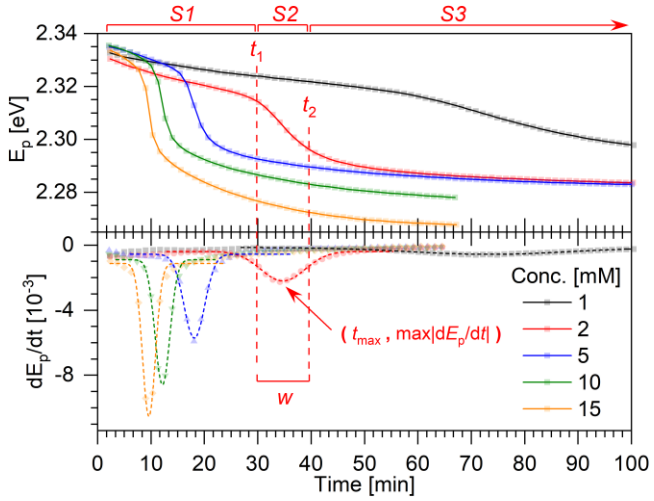

Figure A3.11 Extraction of rate information from the Ep time curves. (A) E_p vs time for different TEOS concentrations (same as Figure S5E). (B) First derivative of the curves in (A) with Gaussian peak fits (dashed lines). The transitions between stages are identified as the left and right sides of the full-width at half maximum, *w*, as indicated for the 2 mM TEOS case (red). The duration of S1 is from 0 to t_1, and the duration of S2 is *w*. The maximum rate of change during S2 is defined as the peak maximum as indicated for the 2 mM TEOS case.

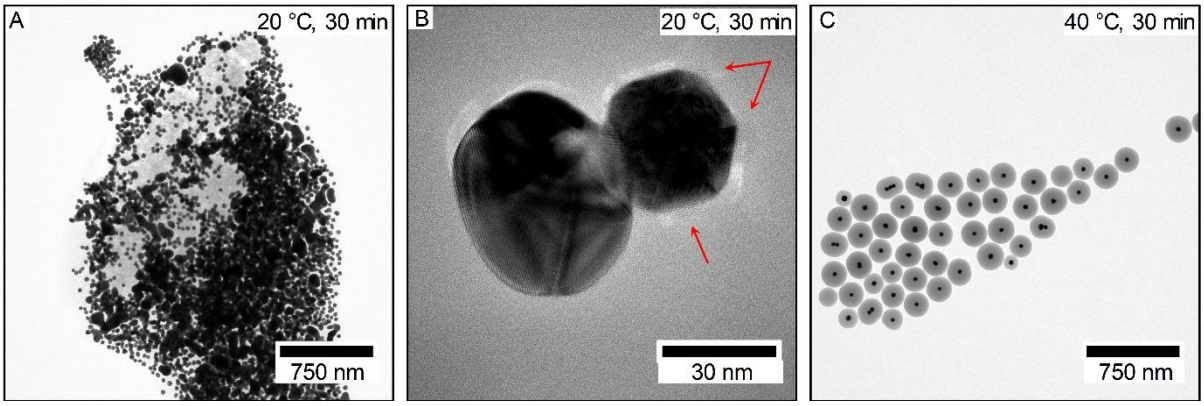

Figure A3.12 TEM micrographs of quenched reaction products after 30 min with 10 mM TEOS and (A-B) 20 °C or (C) 40 °C. Panel B shows small SiO2 deposits on the AuNPs, indicated by red arrows.

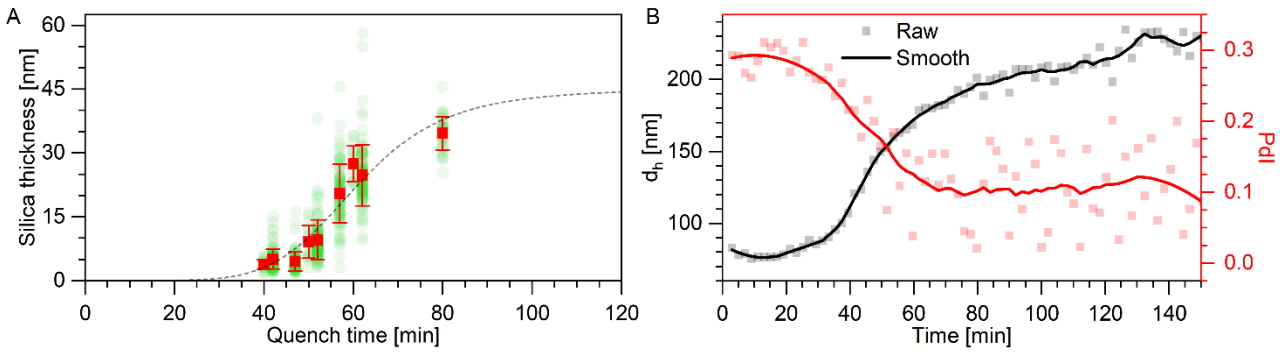

Figure A3.13 (A) SiO2 thickness vs. reaction time as measured from TEM images. Semitransparent green circles represent individual data points. Red squares are averages with error bars indicating one standard deviation. The dashed line represents a fit with a logistic function where initial and final SiO_2 thicknesses are fixed at 0 and 45 nm, respectively. (B) Time-dependent hydrodynamic diameter (black) and polydispersity index (red) from *in situ* Zetasizer measurements. [TEOS] = 2 mM.

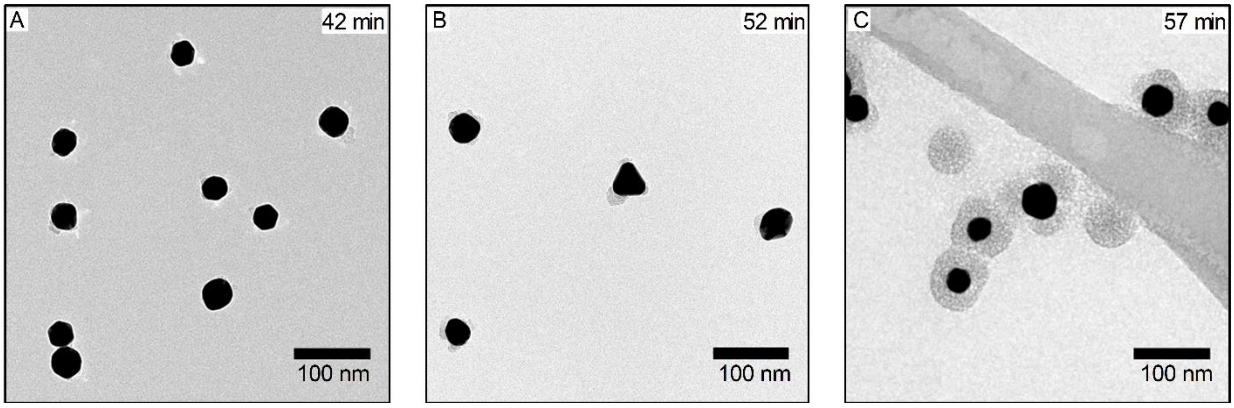

Figure A3.14 TEM micrographs of quenched reaction products from a reaction in complete darkness with 2 mM TEOS. The reaction was quenched after (A) 42 min, (B) 52 min, and (C) 57 min.

Bibliography

(1) Crabtree, G. W.; Lewis, N. S. Solar Energy Conversion. *Phys. Today* **2007**, *60* (3), 37–42. https://doi.org/10.1063/1.2718755.

(2) *International Energy Outlook - U.S. Energy Information Administration (EIA)*. https://www.eia.gov/outlooks/ieo/tables_side_xls.php (accessed 2022-05-31).

(3) British Petroleum. *Statistical Review of World Energy 2021*; 2021; Vol. 70.

(4) Leung, D. Y. C.; Caramanna, G.; Maroto-Valer, M. M. An Overview of Current Status of Carbon Dioxide Capture and Storage Technologies. *Renewable and Sustainable Energy Reviews*. 2014. https://doi.org/10.1016/j.rser.2014.07.093.

(5) Sullivan, M. A.; Stenger, D.; Roma, A.; Tynan, M. The Future of Nuclear Power. *Electr. J.* **2014**, *27* (4). https://doi.org/10.1016/j.tej.2014.04.008.

(6) Goldemberg, J.; Johansson, T. B. *World Energy Assessment: Overview 2004 Update.*; 2004.

(7) Carbon Dioxide Capture and Storage — IPCC.

(8) Kummu, M.; de Moel, H.; Ward, P. J.; Varis, O. How Close Do We Live to Water? A Global Analysis of Population Distance to Freshwater Bodies. *PLoS ONE* **2011**, *6* (6), e20578. https://doi.org/10.1371/journal.pone.0020578.

(9) Ardo, S.; Rivas, D. F.; A. Modestino, M.; Greiving, V. S.; F. Abdi, F.; Llado, E. A.; Artero, V.; Ayers, K.; Battaglia, C.; Becker, J.-P.; Bederak, D.; Berger, A.; Buda, F.; Chinello, E.; Dam, B.; Palma, V. D.; Edvinsson, T.; Fujii, K.; Gardeniers, H.; Geerlings, H.; Hashemi, S. M. H.; Haussener, S.; Houle, F.; Huskens, J.; D. James, B.; Konrad, K.; Kudo, A.; Patil Kunturu, P.; Lohse, D.; Mei, B.; L. Miller, E.; F. Moore, G.; Muller, J.; L. Orchard, K.; E. Rosser, T.; H. Saadi, F.; Schüttauf, J.-W.; Seger, B.; W. Sheehan, S.; A. Smith, W.; Spurgeon, J.; H. Tang, M.; Krol, R. van de; K. Vesborg, P. C.; Westerik, P. Pathways to Electrochemical Solar-Hydrogen Technologies. *Energy Environ. Sci.* **2018**, *11* (10), 2768–2783. https://doi.org/10.1039/C7EE03639F.

(10) Greg. *Electrolyzer overview: Lowering the cost of hydrogen and distributing its production*. pv magazine USA. https://pv-magazine-usa.com/2020/03/26/electrolyzer-overview-lowering-the-cost-of-hydrogen-and-distributing-its-productionhydrogen-industry-overview-lowering-the-cost-and-distributing-production/ (accessed 2022-05-12).

(11) Vartiainen, E.; Breyer, C.; Moser, D.; Román Medina, E.; Busto, C.; Masson, G.; Bosch, E.; Jäger-Waldau, A. True Cost of Solar Hydrogen. *Sol. RRL* **2022**, *6* (5), 2100487. https://doi.org/10.1002/solr.202100487.

(12) Keene, S.; Chandran, R. B.; Ardo, S. Calculations of Theoretical Efficiencies for Electrochemically-Mediated Tandem Solar Water Splitting as a Function of Bandgap Energies and Redox Shuttle Potential. *Energy Environ. Sci.* **2019**, *12* (1), 261–272. https://doi.org/10.1039/C8EE01828F.

(13) Fabian, D. M.; Hu, S.; Singh, N.; Houle, F. A.; Hisatomi, T.; Domen, K.; Osterloh, F. E.; Ardo, S. Particle Suspension Reactors and Materials for Solar-Driven Water Splitting. *Energy Environ. Sci.* **2015**. https://doi.org/10.1039/c5ee01434d.

(14) Fountaine, K. T.; Lewerenz, H. J.; Atwater, H. A. Efficiency Limits for Photoelectrochemical Water Splitting. *Nat. Commun.* **2016**, *7*, 1–9. https://doi.org/10.1038/ncomms13706.

(15) Fujishima, A.; Honda, K. Electrochemical Photolysis of Water at a Semiconductor Electrode. *Nature* **1972**. https://doi.org/10.1038/238037a0.

(16) Apolinário, A.; Lopes, T.; Costa, C.; Araújo, J. P.; Mendes, A. M. Multilayered WO3 Nanoplatelets for Efficient Photoelectrochemical Water Splitting: The Role of the Annealing Ramp. *ACS Appl. Energy Mater.* **2019**, *2* (2), 1040–1050. https://doi.org/10.1021/acsaem.8b01530.

(17) Lee, D. K.; Choi, K. S. Enhancing Long-Term Photostability of BiVO4photoanodes for Solar Water Splitting by Tuning Electrolyte Composition. *Nat. Energy* **2018**. https://doi.org/10.1038/s41560-017-0057-0.

(18) Hong, C.-Y.; Hung, M.-M.; Yang, T.-T.; Wang, Y.-C.; Lin, Y.-C.; Yu, P. Photovoltaic Characteristics of GaAs Solar Cells with Selective Filters. In *2015 IEEE 42nd Photovoltaic Specialist Conference (PVSC)*; 2015; pp 1–3. https://doi.org/10.1109/PVSC.2015.7356116.

(19) Jin, J.; Walczak, K.; Singh, M. R.; Karp, C.; Lewis, N. S.; Xiang, C. An Experimental and Modeling/Simulation-Based Evaluation of the Efficiency and Operational Performance Characteristics of an Integrated, Membrane-Free, Neutral PH Solar-Driven Water-Splitting System. *Energy Environ. Sci.* **2014**, *7* (10). https://doi.org/10.1039/c4ee01824a.

(20) Biagioni, P.; Huang, J.; Hecht, B. Nanoantennas for Visible and Infrared Radiation. **2012**. https://doi.org/10.1088/0034-4885/75/2/024402.

(21) Maier, S. A. *Plasmonics: Fundamentals and Applications*; 2007. https://doi.org/10.1007/0-387-37825-1.

(22) Kittel C. *Introduction to Solid State Physics, 8th Edition, Berkeley*; 1996.

(23) Bohren, C. F. *Absorption and Scattering of Light by Small Particles*; 1983. https://doi.org/10.1088/0031-9112/35/3/025.

(24) Amendola, V.; Pilot, R.; Frasconi, M.; Maragò, O. M.; Iatì, M. A. Surface Plasmon Resonance in Gold Nanoparticles: A Review. *Journal of Physics Condensed Matter*. 2017. https://doi.org/10.1088/1361-648X/aa60f3.

(25) Müller, H. Optical Properties of Metal Clusters. *Z. Für Phys. Chem.* **1996**. https://doi.org/10.1524/zpch.1996.194.part_2.278.

(26) Amendola, V. Surface Plasmon Resonance of Silver and Gold Nanoparticles in the Proximity of Graphene Studied Using the Discrete Dipole Approximation Method. *Phys. Chem. Chem. Phys.* **2016**, *18* (3). https://doi.org/10.1039/c5cp06121k.

(27) Amendola, V.; Rizzi, G. A.; Polizzi, S.; Meneghetti, M. Synthesis of Gold Nanoparticles by Laser Ablation in Toluene: Quenching and Recovery of the Surface Plasmon Absorption. *J. Phys. Chem. B* **2005**, *109* (49). https://doi.org/10.1021/jp055783v.

(28) Zijlstra, P.; Paulo, P. M. R.; Yu, K.; Xu, Q. H.; Orrit, M. Chemical Interface Damping in Single Gold Nanorods and Its near Elimination by Tip-Specific Functionalization. *Angew. Chem. - Int. Ed.* **2012**, *51* (33). https://doi.org/10.1002/anie.201202318.

(29) Aruda, K. O.; Tagliazucchi, M.; Sweeney, C. M.; Hannah, D. C.; Schatz, G. C.; Weiss, E. A. Identification of Parameters through Which Surface Chemistry Determines the Lifetimes of Hot Electrons in Small Au Nanoparticles. *Proc. Natl. Acad. Sci. U. S. A.* **2013**, *110* (11). https://doi.org/10.1073/pnas.1222327110.

(30) Garcia, M. A.; De La Venta, J.; Crespo, P.; Llopis, J.; Penadés, S.; Fernández, A.; Hernando, A. Surface Plasmon Resonance of Capped Au Nanoparticles. *Phys. Rev. B - Condens. Matter Mater. Phys.* **2005**, *72* (24). https://doi.org/10.1103/PhysRevB.72.241403.

(31) Malola, S.; Lehtovaara, L.; Enkovaara, J.; Häkkinen, H. Birth of the Localized Surface Plasmon Resonance in Monolayer-Protected Gold Nanoclusters. *ACS Nano* **2013**, *7* (11). https://doi.org/10.1021/nn4046634.

(32) Mayer, K. M.; Hafner, J. H. Localized Surface Plasmon Resonance Sensors. *Chemical Reviews*. 2011. https://doi.org/10.1021/cr100313v.

(33) Zolotavin, P.; Alabastri, A.; Nordlander, P.; Natelson, D. Plasmonic Heating in Au Nanowires at Low Temperatures: The Role of Thermal Boundary Resistance. *ACS Nano* **2016**, *10* (7). https://doi.org/10.1021/acsnano.6b02911.

(34) Bouillard, J. S. G.; Dickson, W.; O'Connor, D. P.; Wurtz, G. A.; Zayats, A. V. Low-Temperature Plasmonics of Metallic Nanostructures. *Nano Lett.* **2012**, *12* (3). https://doi.org/10.1021/nl204420s.

(35) Langille, M. R.; Personick, M. L.; Zhang, J.; Mirkin, C. A. Defining Rules for the Shape Evolution of Gold Nanoparticles. *J. Am. Chem. Soc.* **2012**, *134* (35), 14542–14554. https://doi.org/10.1021/ja305245g.

(36) Zohar, N.; Chuntonov, L.; Haran, G. The Simplest Plasmonic Molecules: Metal Nanoparticle Dimers and Trimers. *J. Photochem. Photobiol. C Photochem. Rev.* **2014**, *21*, 26–39. https://doi.org/10.1016/j.jphotochemrev.2014.10.002.

(37) *Interparticle Coupling Effect on the Surface Plasmon Resonance of Gold Nanoparticles: From Theory to Applications | Chemical Reviews*. https://pubs.acs.org/doi/full/10.1021/cr0680282 (accessed 2022-05-22).

(38) Link, S.; El-Sayed, M. A. Optical Properties and Ultrafast Dynamics of Metallic Nanocrystals. *Annu Rev Phys Chem* **2003**.

(39) Losquin, A.; Zagonel, L. F.; Myroshnychenko, V.; Rodríguez-González, B.; Tencé, M.; Scarabelli, L.; Förstner, J.; Liz-Marzán, L. M.; García De Abajo, F. J.; Stéphan, O.; Kociak, M. Unveiling Nanometer Scale Extinction and Scattering Phenomena through Combined Electron Energy Loss Spectroscopy and Cathodoluminescence Measurements. *Nano Lett.* **2015**, *15* (2). https://doi.org/10.1021/nl5043775.

(40) Kats, M. A.; Yu, N.; Genevet, P.; Gaburro, Z.; Capasso, F. Effect of Radiation Damping on the Spectral Response of Plasmonic Components. *Opt. Express* **2011**, *19* (22). https://doi.org/10.1364/oe.19.021748.

(41) Griffiths, D. J. *Introduction to Electrodynamics*; 2017. https://doi.org/10.1017/9781108333511.

(42) Sönnichsen, C.; Franzl, T.; Wilk, T.; Von Plessen, G.; Feldmann, J. Plasmon Resonances in Large Noble-Metal Clusters. *New J. Phys.* **2002**, *4*. https://doi.org/10.1088/1367-2630/4/1/393.

(43) Brongersma, M. L.; Halas, N. J.; Nordlander, P. Plasmon-Induced Hot Carrier Science and Technology. *Nature Nanotechnology*. 2015. https://doi.org/10.1038/nnano.2014.311.

(44) Perner, M.; Bost, P.; Lemmer, U.; Von Plessen, G.; Feldmann, J.; Becker, U.; Mennig, M.; Schmitt, M.; Schmidt, H. Optically Induced Damping of the Surface Plasmon Resonance in Gold Colloids. *Phys. Rev. Lett.* **1997**, *78* (11). https://doi.org/10.1103/PhysRevLett.78.2192.

(45) Voisin, C.; Fatti, N. Del; Christofilos, D.; Vallee, F. Ultrafast Electron Dynamics and Optical Nonlinearities in Metal Nanoparticles. *J. Phys. Chem. B* **2001**. https://doi.org/10.1021/jp0038153.

(46) Saavedra, J. R. M.; Asenjo-Garcia, A.; García De Abajo, F. J. Hot-Electron Dynamics and Thermalization in Small Metallic Nanoparticles. *ACS Photonics* **2016**, *3* (9). https://doi.org/10.1021/acsphotonics.6b00217.

(47) Alabastri, A.; Tuccio, S.; Giugni, A.; Toma, A.; Liberale, C.; Das, G.; Angelis, F. De; Fabrizio, E. Di; Zaccaria, R. P. Molding of Plasmonic Resonances in Metallic Nanostructures: Dependence of the Non-Linear Electric Permittivity on System Size and Temperature. *Materials* **2013**, *6* (11). https://doi.org/10.3390/ma6114879.

(48) Mie, G. Beiträge Zur Optik Trüber Medien, Speziell Kolloidaler Metallösungen. *Ann. Phys.* **1908**, *330* (3). https://doi.org/10.1002/andp.19083300302.

(49) Purcell, E. M.; Pennypacker, C. R. Scattering and Absorption of Light by Nonspherical Dielectric Grains. *Astrophys. J.* **1973**, *186*. https://doi.org/10.1086/152538.

(50) Draine, B. T. The Discrete-Dipole Approximation and Its Application to Interstellar Graphite Grains. *Astrophys. J.* **1988**, *333*. https://doi.org/10.1086/166795.

(51) Goodman, J. J.; Flatau, P. J.; Draine, B. T. Application of Fast-Fourier-Transform Techniques to the Discrete-Dipole Approximation. *Opt. Lett.* **1991**, *16* (15). https://doi.org/10.1364/ol.16.001198.

(52) Drain, B. T.; Piotr, F. J. *User Guide for the Discrete Dipole Approximation Code DDSCAT 7.3*; 2013.

(53) Zhao, J.; Pinchuk, A. O.; McMahon, J. M.; Li, S.; Ausman, L. K.; Atkinson, A. L.; Schatz, G. C. Methods for Describing the Electromagnetic Properties of Silver and Gold Nanoparticles. *Acc. Chem. Res.* **2008**, *41* (12), 1710–1720. https://doi.org/10.1021/ar800028j.

(54) Jackson, J. D. *Classical Electrodynamics, Third Edition, Vol. 67*; 1999.

(55) Khlebtsov, N. Scattering From Model Nonspherical Particles: Theory and Applications to Environmental Physics, Second Edition. *Eos Trans. Am. Geophys. Union* **2008**, *89* (39), 365–365. https://doi.org/10.1029/2008EO390007.

(56) Howes, P. D.; Chandrawati, R.; Stevens, M. M. Colloidal Nanoparticles as Advanced Biological Sensors. *Science* **2014**, *346* (6205). https://doi.org/10.1126/science.1247390.

(57) Tokel, O.; Inci, F.; Demirci, U. Advances in Plasmonic Technologies for Point of Care Applications. *Chem. Rev.* **2014**, *114* (11), 5728–5752. https://doi.org/10.1021/cr4000623.

(58) Zhou, W.; Gao, X.; Liu, D.; Chen, X. Gold Nanoparticles for In Vitro Diagnostics. *Chem. Rev.* **2015**, *115* (19), 10575–10636. https://doi.org/10.1021/acs.chemrev.5b00100.

(59) Lee, K.-S.; El-Sayed, M. A. Gold and Silver Nanoparticles in Sensing and Imaging: Sensitivity of Plasmon Response to Size, Shape, and Metal Composition. *J. Phys. Chem. B* **2006**, *110* (39), 19220–19225. https://doi.org/10.1021/jp062536y.

(60) Zheng, W.; Li, H.; Chen, W.; Ji, J.; Jiang, X. Recyclable Colorimetric Detection of Trivalent Cations in Aqueous Media Using Zwitterionic Gold Nanoparticles. *Anal. Chem.* **2016**, *88* (7), 4140–4146. https://doi.org/10.1021/acs.analchem.6b00501.

(61) Chen, L.; Li, J.; Chen, L. Colorimetric Detection of Mercury Species Based on Functionalized Gold Nanoparticles. *ACS Appl. Mater. Interfaces* **2014**, *6* (18), 15897–15904. https://doi.org/10.1021/am503531c.

(62) Niu, H.; Wang, S.; Zhou, Z.; Ma, Y.; Ma, X.; Cai, Y. Sensitive Colorimetric Visualization of Perfluorinated Compounds Using Poly(Ethylene Glycol) and Perfluorinated Thiols Modified Gold Nanoparticles. *Anal. Chem.* **2014**, *86* (9), 4170–4177. https://doi.org/10.1021/ac403406d.

(63) Jiang, Y.; Zhao, H.; Zhu, N.; Lin, Y.; Yu, P.; Mao, L. A Simple Assay for Direct Colorimetric Visualization of Trinitrotoluene at Picomolar Levels Using Gold Nanoparticles. *Angew. Chem. Int. Ed.* **2008**, *47* (45), 8601–8604. https://doi.org/10.1002/anie.200804066.

(64) Guarise, C.; Pasquato, L.; De Filippis, V.; Scrimin, P. Gold Nanoparticles-Based Protease Assay. *Proc. Natl. Acad. Sci.* **2006**, *103* (11), 3978–3982. https://doi.org/10.1073/pnas.0509372103.

(65) Mirkin, C. A.; Letsinger, R. L.; Mucic, R. C.; Storhoff, J. J. A DNA-Based Method for Rationally Assembling Nanoparticles into Macroscopic Materials. *Nature* **1996**, *382* (6592). https://doi.org/10.1038/382607a0.

(66) Li, H.; Rothberg, L. Colorimetric Detection of DNA Sequences Based on Electrostatic Interactions with Unmodified Gold Nanoparticles. *Proc. Natl. Acad. Sci. U. S. A.* **2004**, *101* (39). https://doi.org/10.1073/pnas.0406115101.

(67) Medley, C. D.; Smith, J. E.; Tang, Z.; Wu, Y.; Bamrungsap, S.; Tan, W. Gold Nanoparticle-Based Colorimetric Assay for the Direct Detection of Cancerous Cells. *Anal. Chem.* **2008**, *80* (4). https://doi.org/10.1021/ac702037y.

(68) Mastrotto, F.; Caliceti, P.; Amendola, V.; Bersani, S.; Pall Magnusson, J.; Meneghetti, M.; Mantovani, G.; Alexander, C.; Salmaso, S. Polymer Control of Ligand Display on Gold Nanoparticles for Multimodal Switchable Cell Targeting. *Chem. Commun.* **2011**, *47* (35), 9846–9848. https://doi.org/10.1039/C1CC12654G.

(69) Moskovits, M. Surface-Enhanced Raman Spectroscopy: A Brief Retrospective. *J. Raman Spectrosc.* **2005**, *36* (6–7), 485–496. https://doi.org/10.1002/jrs.1362.

(70) Lakowicz, J. R. Radiative Decay Engineering: Biophysical and Biomedical Applications. *Anal. Biochem.* **2001**, *298* (1), 1–24. https://doi.org/10.1006/abio.2001.5377.

(71) Darby, B. L.; Auguié, B.; Meyer, M.; Pantoja, A. E.; Le Ru, E. C. Modified Optical Absorption of Molecules on Metallic Nanoparticles at Sub-Monolayer Coverage. *Nat. Photonics* **2016**, *10* (1), 40–45. https://doi.org/10.1038/nphoton.2015.205.

(72) Ichimura, T.; Hayazawa, N.; Hashimoto, M.; Inouye, Y.; Kawata, S. Local Enhancement of Coherent Anti-Stokes Raman Scattering by Isolated Gold Nanoparticles. *J. Raman Spectrosc.* **2003**, *34* (9), 651–654. https://doi.org/10.1002/jrs.1047.

(73) Zhang, Y.; Zhen, Y.-R.; Neumann, O.; Day, J. K.; Nordlander, P.; Halas, N. J. Coherent Anti-Stokes Raman Scattering with Single-Molecule Sensitivity Using a Plasmonic Fano Resonance. *Nat. Commun.* **2014**, *5* (1), 4424. https://doi.org/10.1038/ncomms5424.

(74) Butet, J.; Martin, O. J. F. Surface-Enhanced Hyper-Raman Scattering: A New Road to the Observation of Low Energy Molecular Vibrations. *J. Phys. Chem. C* **2015**, *119* (27), 15547–15556. https://doi.org/10.1021/acs.jpcc.5b04128.

(75) Turley, H. K.; Hu, Z.; Silverstein, D. W.; Cooper, D. A.; Jensen, L.; Camden, J. P. Probing Two-Photon Molecular Properties with Surface-Enhanced Hyper-Raman Scattering: A Combined Experimental and Theoretical Study of Crystal Violet. *J. Phys. Chem. C* **2016**, *120* (37), 20936–20942. https://doi.org/10.1021/acs.jpcc.6b02746.

(76) Montoya, J. H.; Seitz, L. C.; Chakthranont, P.; Vojvodic, A.; Jaramillo, T. F.; Nørskov, J. K. Materials for Solar Fuels and Chemicals. *Nat. Mater.* **2017**, *16* (1), 70–81. https://doi.org/10.1038/nmat4778.

(77) Abdi, F. F.; Berglund, S. P. Recent Developments in Complex Metal Oxide Photoelectrodes. *Journal of Physics D: Applied Physics*. 2017. https://doi.org/10.1088/1361-6463/aa6738.

(78) Zhou, L.; Shinde, A.; Guevarra, D.; Haber, J. A.; Persson, K. A.; Neaton, J. B.; Gregoire, J. M. Successes and Opportunities for Discovery of Metal Oxide Photoanodes for Solar Fuels Generators. *ACS Energy Lett.* **2020**, *5* (5). https://doi.org/10.1021/acsenergylett.0c00067.

(79) Yan, Q.; Li, G.; Newhouse, P. F.; Yu, J.; Persson, K. A.; Gregoire, J. M.; Neaton, J. B. Mn 2 V 2 O 7 : An Earth Abundant Light Absorber for Solar Water Splitting. **2015**, 1–6. https://doi.org/10.1002/aenm.201401840.

(80) Skorupska, K.; Parkinson, B. A. Combinatorial Synthesis and Screening of Oxide Materials for Photoelectrochemical Energy Conversion. In *Photoelectrochemical Solar Fuel Production: From Basic Principles to Advanced Devices*; 2016. https://doi.org/10.1007/978-3-319-29641-8_10.

(81) Ninova, S.; Strach, M.; Buonsanti, R.; Aschauer, U. Suitability of Cu-Substituted β -Mn2V2O7and Mn-Substituted β -Cu2V2O7for Photocatalytic Water-Splitting. *J. Chem. Phys.* **2020**, *153* (8). https://doi.org/10.1063/5.0019306.

(82) Zhou, L.; Shinde, A.; Guevarra, D.; Richter, M. H.; Stein, H. S.; Wang, Y.; Newhouse, P. F.; Persson, K. A.; Gregoire, J. M. Combinatorial Screening Yields Discovery of 29 Metal Oxide Photoanodes for Solar Fuel Generation. *J. Mater. Chem. A* **2020**, *8* (8). https://doi.org/10.1039/c9ta13829c.

(83) Seenivasan, S.; Moon, H.; Kim, D. H. Investigation of Bulk Carrier Diffusion Dynamics Using β-Mn2V2−xMoxO7 Photoanodes in Solar Water Splitting. *Appl. Surf. Sci.* **2021**, *540*. https://doi.org/10.1016/j.apsusc.2020.148376.

(84) Liao, J. H.; Leroux, F.; Piffard, Y.; Guyomard, D.; Payen, C. Synthesis, Structures, Magnetic Properties, and Phase Transition of Manganese(II) Divanadate: Mn2V2O7. *J. Solid State Chem.* **1996**, *121* (1), 214–224.

(85) Sannigrahi, J.; Giri, S.; Majumdar, S. Magnetic and Dielectric Properties of Mn2V2O7. *Solid State Commun.* **2016**, *228*, 10–15. https://doi.org/10.1016/j.ssc.2015.11.020.

(86) Sannigrahi, J.; Adroja, D. T.; Perry, R.; Gutmann, M. J.; Petricek, V.; Khalyavin, D. Commensurate to Incommensurate Magnetic Phase Transition in Honeycomb-Lattice Pyrovanadate Mn2 V2 O7. *Phys. Rev. Mater.* **2019**, *3* (11). https://doi.org/10.1103/PhysRevMaterials.3.113401.

(87) He, Z.; Ueda, Y.; Itoh, M. Martensitic-like Transition in Mn2V2O7 Single Crystals. *Solid State Commun.* **2008**, *147* (3–4), 138–140. https://doi.org/10.1016/j.ssc.2008.04.038.

(88) Sun, Y. C.; Ouyang, Z. W.; Xiao, Y.; Su, Y.; Feng, E.; Fu, Z.; Jin, W. T.; Zbiri, M.; Xia, Z. C.; Wang, J. F.; Rao, G. H. Honeycomb-Lattice Antiferromagnet Mn2V2O7: A Temperaturedependent x-Ray Diffraction, Neutron Diffraction and ESR Study. *Mater. Res. Express* **2017**, *4* (4). https://doi.org/10.1088/2053-1591/aa67d6.

(89) Wu, H. C.; Hsieh, D. J.; Yen, T. W.; Sun, P. J.; Kakarla, D. C.; Her, J. L.; Matsuda, Y. H.; Chang, C. K.; Lai, Y. C.; Gooch, M.; Deng, L. Z.; Webber, K. G.; Lee, C. A.; Chou, M. M. C.; Chu, C. W.; Yang, H. D. Pressure and Magnetic Field Effects on Ferroelastic and Antiferromagnetic Orderings in Honeycomb-Lattice M N2 V2 O7. *Phys. Rev. B* **2020**, *102* (7). https://doi.org/10.1103/PhysRevB.102.075130.

(90) Sambandam, B.; Soundharrajan, V.; Song, J.; Kim, S.; Jo, J.; Duong, P. T.; Kim, S.; Mathew, V.; Kim, J. Investigation of Li-Ion Storage Properties of Earth Abundant B-Mn2V2O7prepared Using Facile Green Strategy. *J. Power Sources* **2017**, *350*, 80–86. https://doi.org/10.1016/j.jpowsour.2017.03.054.

(91) Xia, D.; Xu, S.; Wang, W.; Wang, D.; Wu, M.; Gong, F. Pure-Phase β-Mn2V2O7interconnected Nanospheres as a High-Performance Lithium Ion Battery Anode. *Chem. Commun.* **2020**, *56* (58). https://doi.org/10.1039/d0cc02458a.

(92) Xia, D.; Gao, H.; Li, M.; Gong, F.; Li, M. Transition Metal Vanadates Electrodes in Lithium-Ion Batteries: A Holistic Review. *Energy Storage Materials*. 2021. https://doi.org/10.1016/j.ensm.2020.10.023.

(93) Ravindra, P.; Athresh, E.; Ranjan, R.; Raghavan, S.; Avasthi, S. Effect of Annealing on Performance of Solar Cells with New Oxide Absorber Mn2V2O7; 2018. https://doi.org/10.1109/pvsc.2017.8366546.

(94) Zhao, L.; Lin, S.; Bi, K.; Liang, C.; Du, Y.; Liu, J.; Yang, H.; Fan, D.; Wang, Y.; Lei, M. Manganese Vanadium Oxide Hollow Microspheres: A Novel Electrocatalyst for Oxygen Reduction Reaction. *J. Solid State Electrochem.* **2017**, *21* (6), 1743–1749. https://doi.org/10.1007/s10008-017-3548-9.

(95) Xin, Y.; Li, H.; Zhang, N.; Li, Q.; Zhang, Z.; Cao, X.; Hu, P.; Zheng, L.; Anderson, J. A. Molecular-Level Insight into Selective Catalytic Reduction of NOx with NH3 to N2 over a Highly Efficient Bifunctional Va-MnOx Catalyst at Low Temperature. *ACS Catal.* **2018**, *8* (6). https://doi.org/10.1021/acscatal.8b00196.

(96) Xing, X.; Liu, R.; Cao, K.; Kaiser, U.; Zhang, G.; Streb, C. Manganese Vanadium Oxide-N-Doped Reduced Graphene Oxide Composites as Oxygen Reduction and Oxygen Evolution Electrocatalysts. *ACS Appl. Mater. Interfaces* **2018**, *10* (51). https://doi.org/10.1021/acsami.8b16578.

(97) Nair, V.; Perkins, C. L.; Lin, Q.; Law, M. Textured Nanoporous Mo:BiVO 4 Photoanodes with High Charge Transport and Charge Transfer Quantum Efficiencies for Oxygen Evolution. *Energy Environ. Sci.* **2016**, *9* (4), 1412–1429. https://doi.org/10.1039/C6EE00129G.

(98) Ilton, E. S.; Post, J. E.; Heaney, P. J.; Ling, F. T.; Kerisit, S. N. XPS Determination of Mn Oxidation States in Mn (Hydr)Oxides. *Appl. Surf. Sci.* **2016**, *366*, 475–485. https://doi.org/10.1016/j.apsusc.2015.12.159.

(99) Biesinger, M. C.; Payne, B. P.; Grosvenor, A. P.; Lau, L. W. M.; Gerson, A. R.; Smart, R. St. C. Resolving Surface Chemical States in XPS Analysis of First Row Transition Metals, Oxides and Hydroxides: Cr, Mn, Fe, Co and Ni. *Appl. Surf. Sci.* **2011**, *257* (7), 2717–2730. https://doi.org/10.1016/j.apsusc.2010.10.051.

(100) Nesbitt, H. W.; Banerjee, D. Interpretation of XPS Mn(2p) Spectra of Mn Oxyhydroxides and Constraints on the Mechanism of MnO 2 Precipitation. *Am. Mineral.* **1998**, *83* (3–4), 305–315. https://doi.org/10.2138/am-1998-3-414.

(101) Mesmer, R. E.; Baes, C. F.; Sweeton, F. H. Acidity Measurements at Elevated Temperatures. VI. Boric Acid Equilibria. *Inorg. Chem.* **1972**, *11* (3). https://doi.org/10.1021/ic50109a023.

(102) Jin, J.; Walczak, K.; Singh, M. R.; Karp, C.; Lewis, N. S.; Xiang, C. An Experimental and Modeling/Simulation-Based Evaluation of the Efficiency and Operational Performance Characteristics of an Integrated, Membrane-Free, Neutral PH Solar-Driven Water-Splitting System. *Energy Environ. Sci.* **2014**, *7* (10). https://doi.org/10.1039/c4ee01824a.

(103) Ravensbergen, J.; F. Abdi, F.; H. van Santen, J.; N. Frese, R.; Dam, B.; van de Krol, R.; T. M. Kennis, J. Unraveling the Carrier Dynamics of BiVO4: A Femtosecond to Microsecond Transient Absorption Study. *J. Phys. Chem. C* **2014**, *118* (48), 27793–27800. https://doi.org/10.1021/jp509930s.

(104) K. Cooper, J.; E. Reyes-Lillo, S.; H. Hess, L.; Jiang, C.-M.; B. Neaton, J.; D. Sharp, I. Physical Origins of the Transient Absorption Spectra and Dynamics in Thin-Film Semiconductors: The Case of BiVO4. *J. Phys. Chem. C* **2018**, *122* (36), 20642–20652. https://doi.org/10.1021/acs.jpcc.8b06645.

(105) Liu, J.; Leng, J.; Wang, S.; Zhang, J.; Jin, S. Artifacts in Transient Absorption Measurements of Perovskite Films Induced by Transient Reflection from Morphological Microstructures. *Journal of Physical Chemistry Letters*. 2019. https://doi.org/10.1021/acs.jpclett.8b03704.

(106) Suzuki, Y.; H. K. Murthy, D.; Matsuzaki, H.; Furube, A.; Wang, Q.; Hisatomi, T.; Domen, K.; Seki, K. Rational Interpretation of Correlated Kinetics of Mobile and Trapped Charge Carriers: Analysis of Ultrafast Carrier Dynamics in BiVO4. *J. Phys. Chem. C* **2017**, *121* (35), 19044–19052. https://doi.org/10.1021/acs.jpcc.7b05574.

(107) Ran, Z.; Wang, X.; Li, Y.; Yang, D.; Zhao, X. G.; Biswas, K.; Singh, D. J.; Zhang, L. Bismuth and Antimony-Based Oxyhalides and Chalcohalides as Potential Optoelectronic Materials. *Npj Comput. Mater.* **2018**. https://doi.org/10.1038/s41524-018-0071-1.

(108) Govindaraju, G. V.; Wheeler, G. P.; Lee, D.; Choi, K. S. Methods for Electrochemical Synthesis and Photoelectrochemical Characterization for Photoelectrodes. *Chem. Mater.* **2017**. https://doi.org/10.1021/acs.chemmater.6b03469.

(109) Lee, D. K.; Choi, K. S. Enhancing Long-Term Photostability of BiVO4photoanodes for Solar Water Splitting by Tuning Electrolyte Composition. *Nat. Energy* **2018**. https://doi.org/10.1038/s41560-017-0057-0.

(110) Reis, S.; Araujo, E. Impact of Defects on the Electrical Properties of BiFeO3 Thin Films. *Ferroelectrics* **2020**, *556*, 70–78.

(111) Schrade, M.; Masó, N.; Perejón, A.; Pérez-Maqueda, L. A.; West, A. R. Defect Chemistry and Electrical Properties of $BiFeO_3$. *J Mater Chem C* **2017**, *5* (38), 10077–10086. https://doi.org/10.1039/C7TC03345A.

(112) Alivisatos, A. P.; Johnsson, K. P.; Peng, X.; Wilson, T. E.; Loweth, C. J.; Bruchez, M. P.; Schultz, P. G. Organization of "nanocrystal Molecules" Using DNA. *Nature* **1996**, *382* (6592), 609–611. https://doi.org/10.1038/382609a0.

(113) Krüger, C.; Agarwal, S.; Greiner, A. Stoichiometric Functionalization of Gold Nanoparticles in Solution through a Free Radical Polymerization Approach. *J. Am. Chem. Soc.* **2008**, *130* (9), 2710–2711. https://doi.org/10.1021/ja0763495.

(114) Indrasekara, A. S. D. S.; Paladini, B. J.; Naczynski, D. J.; Starovoytov, V.; Moghe, P. V.; Fabris, L. Dimeric Gold Nanoparticle Assemblies as Tags for SERS-Based Cancer Detection. *Adv. Healthc. Mater.* **2013**, *2* (10), 1370–1376. https://doi.org/10.1002/adhm.201200370.

(115) Wang, H.; Schaefer, K.; Moeller, M. In Situ Immobilization of Gold Nanoparticle Dimers in Silica Nanoshell by Microemulsion Coalescence. *J. Phys. Chem. C* **2008**, *112* (9), 3175–3178. https://doi.org/10.1021/jp7113658.

(116) Nepal, D.; Park, K.; Vaia, R. A. High-Yield Assembly of Soluble and Stable Gold Nanorod Pairs for High-Temperature Plasmonics. *Small* **2012**, *8* (7), 1013–1020. https://doi.org/10.1002/smll.201102152.

(117) Cho, E. C.; Choi, S.-W.; Camargo, P. H. C.; Xia, Y. Thiol-Induced Assembly of Au Nanoparticles into Chainlike Structures and Their Fixing by Encapsulation in Silica Shells or Gelatin Microspheres. *Langmuir* **2010**, *26* (12), 10005–10012. https://doi.org/10.1021/la100127w.

(118) Yang, M.; Chen, G.; Zhao, Y.; Silber, G.; Wang, Y.; Xing, S.; Han, Y.; Chen, H. Mechanistic Investigation into the Spontaneous Linear Assembly of Gold Nanospheres. *Phys. Chem. Chem. Phys.* **2010**, *12* (38), 11850–11860. https://doi.org/10.1039/C0CP00127A.
(119) Stewart, A. F.; Lee, A.; Ahmed, A.; Ip, S.; Kumacheva, E.; Walker, G. C. Rational Design for the Controlled Aggregation of Gold Nanorods via Phospholipid Encapsulation for Enhanced Raman Scattering. *ACS Nano* **2014**, *8* (6), 5462–5467. https://doi.org/10.1021/nn4044589.
(120) Hanske, C.; González-Rubio, G.; Hamon, C.; Formentín, P.; Modin, E.; Chuvilin, A.; Guerrero-Martínez, A.; Marsal, L. F.; Liz-Marzán, L. M. Large-Scale Plasmonic Pyramidal Supercrystals via Templated Self-Assembly of Monodisperse Gold Nanospheres. *J. Phys. Chem. C* **2017**, *121* (20). https://doi.org/10.1021/acs.jpcc.6b12161.
(121) Scarabelli, L.; Coronado-Puchau, M.; Giner-Casares, J. J.; Langer, J.; Liz-Marzán, L. M. Monodisperse Gold Nanotriangles: Size Control, Large-Scale Self-Assembly, and Performance in Surface-Enhanced Raman Scattering. *ACS Nano* **2014**, *8* (6). https://doi.org/10.1021/nn500727w.
(122) Sánchez-Iglesias, A.; Jenkinson, K.; Bals, S.; Liz-Marzán, L. M. Kinetic Regulation of the Synthesis of Pentatwinned Gold Nanorods below Room Temperature. *J. Phys. Chem. C* **2021**, *125* (43). https://doi.org/10.1021/acs.jpcc.1c07284.
(123) Sánchez-Iglesias, A.; Winckelmans, N.; Altantzis, T.; Bals, S.; Grzelczak, M.; Liz-Marzán, L. M. High-Yield Seeded Growth of Monodisperse Pentatwinned Gold Nanoparticles through Thermally Induced Seed Twinning. *J. Am. Chem. Soc.* **2017**, *139* (1). https://doi.org/10.1021/jacs.6b12143.
(124) Carbó-Argibay, E.; Rodríguez-González, B.; Pastoriza-Santos, I.; Pérez-Juste, J.; Liz-Marzán, L. M. Growth of Pentatwinned Gold Nanorods into Truncated Decahedra. *Nanoscale* **2010**, *2* (11). https://doi.org/10.1039/c0nr00239a.
(125) Bastús, N. G.; Comenge, J.; Puntes, V. Kinetically Controlled Seeded Growth Synthesis of Citrate-Stabilized Gold Nanoparticles of up to 200 Nm: Size Focusing versus Ostwald Ripening. *Langmuir* **2011**. https://doi.org/10.1021/la201938u.
(126) Luan, Z.; Salk, T.; Abelson, A.; Jean, S.; Law, M. Reversible Aggregation of Covalently Cross-Linked Gold Nanocrystals by Linker Oxidation. *J. Phys. Chem. C* **2019**, *0* (ja), null-null. https://doi.org/10.1021/acs.jpcc.9b06976.
(127) Stöber, W.; Fink, A.; Bohn, E. Controlled Growth of Monodisperse Silica Spheres in the Micron Size Range. *J. Colloid Interface Sci.* **1968**, *26* (1). https://doi.org/10.1016/0021-9797(68)90272-5.
(128) M. Liz-Marzán, L.; Giersig, M.; Mulvaney, P. Synthesis of Nanosized Gold−Silica Core−Shell Particles. *Langmuir* **1996**, *12* (18), 4329–4335. https://doi.org/10.1021/la9601871.
(129) Lu, Y.; Yin, Y.; Li, Z. Y.; Xia, Y. Synthesis and Self-Assembly of Au@SiO2 Core-Shell Colloids. *Nano Lett.* **2002**, *2* (7). https://doi.org/10.1021/nl025598i.
(130) Nooney, R. I.; Thirunavukkarasu, D.; Chen, Y.; Josephs, R.; Ostafin, A. E. Self-Assembly of Mesoporous Nanoscale Silica/Gold Composites. *Langmuir* **2003**, *19* (18). https://doi.org/10.1021/la034522e.
(131) Park, Y.-S.; Liz-Marzán, L. M.; Kasuya, A.; Kobayashi, Y.; Nagao, D.; Konno, M.; Mamykin, S.; Dmytruk, A.; Takeda, M.; Ohuchi, N. X-Ray Absorption of Gold

Nanoparticles with Thin Silica Shell. *J. Nanosci. Nanotechnol.* **2020**, *6* (11). https://doi.org/10.1166/jnn.2006.17970.

(132) Liz-Marzán, L. M.; Mulvaney, P. Au@SiO2 Colloids: Effect of Temperature on the Surface Plasmon Absorption. *New J. Chem.* **1998**, *22* (11). https://doi.org/10.1039/a801214h.

(133) Huang, Y. F.; Ma, K. H.; Kang, K. Bin; Zhao, M.; Zhang, Z. L.; Liu, Y. X.; Wen, T.; Wang, Q.; Qiu, W. Y.; Qiu, D. Core-Shell Plasmonic Nanostructures to Fine-Tune Long "Au Nanoparticle-Fluorophore" Distance and Radiative Dynamics. *Colloids Surf. Physicochem. Eng. Asp.* **2013**, *421*. https://doi.org/10.1016/j.colsurfa.2012.12.050.

(134) Kobayashi, Y.; Inose, H.; Nakagawa, T.; Gonda, K.; Takeda, M.; Ohuchi, N.; Kasuya, A. Control of Shell Thickness in Silica-Coating of Au Nanoparticles and Their X-Ray Imaging Properties. *J. Colloid Interface Sci.* **2011**, *358* (2). https://doi.org/10.1016/j.jcis.2011.01.058.

(135) Mine, E.; Yamada, A.; Kobayashi, Y.; Konno, M.; Liz-Marzán, L. M. Direct Coating of Gold Nanoparticles with Silica by a Seeded Polymerization Technique. *J. Colloid Interface Sci.* **2003**, *264* (2). https://doi.org/10.1016/S0021-9797(03)00422-3.

(136) Gorelikov, I.; Matsuura, N. Single-Step Coating of Mesoporous Silica on Cetyltrimethyl Ammonium Bromide-Capped Nanoparticles. *Nano Lett.* **2008**, *8* (1). https://doi.org/10.1021/nl0727415.

(137) Lee, H. B.; Yoo, Y. M.; Han, Y. H. Characteristic Optical Properties and Synthesis of Gold-Silica Core-Shell Colloids. *Scr. Mater.* **2006**, *55* (12). https://doi.org/10.1016/j.scriptamat.2006.08.044.

(138) Zhao, Y.; Yang, D.; Hu, H.; Chen, L.; Xu, Y.; Qu, L.; Yang, P.; Zhang, Q. A Simple Approach to the Synthesis of Eccentric Au@SiO2 Janus Nanostructures and Their Catalytic Applications. *Surf. Sci.* **2016**, *648*. https://doi.org/10.1016/j.susc.2015.10.044.

(139) Meena, S. K.; Goldmann, C.; Nassoko, D.; Seydou, M.; Marchandier, T.; Moldovan, S.; Ersen, O.; Ribot, F.; Chanéac, C.; Sanchez, C.; Portehault, D.; Tielens, F.; Sulpizi, M. Nanophase Segregation of Self-Assembled Monolayers on Gold Nanoparticles. *ACS Nano* **2017**, *11* (7). https://doi.org/10.1021/acsnano.7b03616.

(140) Hinman, J. G.; Eller, J. R.; Lin, W.; Li, J.; Li, J.; Murphy, C. J. Oxidation State of Capping Agent Affects Spatial Reactivity on Gold Nanorods. *J. Am. Chem. Soc.* **2017**, *139* (29). https://doi.org/10.1021/jacs.7b06391.

(141) Vanderkooy, A.; Chen, Y.; Gonzaga, F.; Brook, M. A. Silica Shell/Gold Core Nanoparticles: Correlating Shell Thickness with the Plasmonic Red Shift upon Aggregation. *ACS Appl. Mater. Interfaces* **2011**, *3* (10). https://doi.org/10.1021/am200825f.

(142) Qu, Q.; Liu, S. Coating Time Effect on Surface Structures of Silica-Encapsulated Gold Nanoparticles. In *Advanced Materials Research*; 2009; Vol. 79–82. https://doi.org/10.4028/www.scientific.net/AMR.79-82.935.

(143) Ye, J.; Van de Broek, B.; De Palma, R.; Libaers, W.; Clays, K.; Van Roy, W.; Borghs, G.; Maes, G. Surface Morphology Changes on Silica-Coated Gold Colloids. *Colloids Surf. Physicochem. Eng. Asp.* **2008**, *322* (1–3). https://doi.org/10.1016/j.colsurfa.2008.03.033.

(144) Wang, F.; Cheng, S.; Bao, Z.; Wang, J. Anisotropic Overgrowth of Metal Heterostructures Induced by a Site-Selective Silica Coating. *Angew. Chem. - Int. Ed.* **2013**, *52* (39). https://doi.org/10.1002/anie.201304364.

(145) Rodríguez-Fernández, J.; Pastoriza-Santos, I.; Pérez-Juste, J.; García De Abajo, F. J.; Liz-Marzán, L. M. The Effect of Silica Coating on the Optical Response of Sub-Micrometer Gold Spheres. *J. Phys. Chem. C* **2007**, *111* (36). https://doi.org/10.1021/jp073853n.
(146) Kobayashi, Y.; Inose, H.; Nakagawa, T.; Gonda, K.; Takeda, M.; Ohuchi, N.; Kasuya, A. Synthesis of Au-Silica Core-Shell Particles by Sol-Gel Process. *Surf. Eng.* **2012**, *28* (2). https://doi.org/10.1179/1743294411Y.0000000069.
(147) Moon, S. W.; Tsalu, P. V.; Ha, J. W. Single Particle Study: Size and Chemical Effects on Plasmon Damping at the Interface between Adsorbate and Anisotropic Gold Nanorods. *Phys. Chem. Chem. Phys.* **2018**, *20* (34). https://doi.org/10.1039/c8cp03231a.
(148) Foerster, B.; Spata, V. A.; Carter, E. A.; Sönnichsen, C.; Link, S. Plasmon Damping Depends on the Chemical Nature of the Nanoparticle Interface. *Sci. Adv.* **2019**, *5* (3). https://doi.org/10.1126/sciadv.aav0704.
(149) Walker, D. A.; Leitsch, E. K.; Nap, R. J.; Szleifer, I.; Grzybowski, B. A. Geometric Curvature Controls the Chemical Patchiness and Self-Assembly of Nanoparticles. *Nat. Nanotechnol.* **2013**, *8* (9), 676–681. https://doi.org/10.1038/nnano.2013.158.
(150) Wu, B.; Liu, D.; Mubeen, S.; Chuong, T. T.; Moskovits, M.; Stucky, G. D. Anisotropic Growth of TiO2 onto Gold Nanorods for Plasmon-Enhanced Hydrogen Production from Water Reduction. *J. Am. Chem. Soc.* **2016**, *138* (4), 1114–1117. https://doi.org/10.1021/jacs.5b11341.
(151) Baffou, G.; Rigneault, H. Femtosecond-Pulsed Optical Heating of Gold Nanoparticles. *Phys. Rev. B* **2011**, *84* (3), 035415. https://doi.org/10.1103/PhysRevB.84.035415.
(152) Keblinski, P.; Cahill, D. G.; Bodapati, A.; Sullivan, C. R.; Taton, T. A. Limits of Localized Heating by Electromagnetically Excited Nanoparticles. *J. Appl. Phys.* **2006**, *100* (5), 054305. https://doi.org/10.1063/1.2335783.
(153) G. Bastús, N.; Comenge, J.; Puntes, V. Kinetically Controlled Seeded Growth Synthesis of Citrate-Stabilized Gold Nanoparticles of up to 200 Nm: Size Focusing versus Ostwald Ripening. *Langmuir* **2011**, *27* (17), 11098–11105. https://doi.org/10.1021/la201938u.
(154) Schneider, C. A.; Rasband, W. S.; Eliceiri, K. W. NIH Image to ImageJ: 25 Years of Image Analysis. *Nature Methods*. 2012. https://doi.org/10.1038/nmeth.2089.
(155) Gupta, R. P.; Sen, S. K. Calculation of Multiplet Structure of Core P-Vacancy Levels. *Phys. Rev. B* **1974**, *10* (1), 71–77. https://doi.org/10.1103/PhysRevB.10.71.
(156) Ernens, D.; Langedijk, G.; Smit, P.; de Rooij, M. B.; Pasaribu, H. R.; Schipper, D. J. Characterization of the Adsorption Mechanism of Manganese Phosphate Conversion Coating Derived Tribofilms. *Tribol. Lett.* **2018**, *66* (4). https://doi.org/10.1007/s11249-018-1082-2.
(157) Franke, R.; Chassé, T.; Streubel, P.; Meisel, A. Auger Parameters and Relaxation Energies of Phosphorus in Solid Compounds. *J. Electron Spectrosc. Relat. Phenom.* **1991**, *56* (4). https://doi.org/10.1016/0368-2048(91)85035-R.